

Advanced Techniques for Ultrasound-based Condition Monitoring

Dissertation

zur Erlangung des akademischen Grades

Dr.-Ing.

eingereicht an der
Mathematisch-Naturwissenschaftlich-Technischen Fakultät
der Universität Augsburg

von

Marcel Achzet

Augsburg, Januar 2025



Erstgutachter:

Prof. Dr. Markus Sause

Zweitgutachter:

Prof. Dr.-Ing. Nils Meyer

Tag der mündlichen Prüfung:

02. April 2025

Contents

1	Introduction	1
2	Theoretical Background	5
2.1	Physics of Ultrasound	5
2.2	Signal Analysis Techniques	15
2.3	Signal Processing	22
2.3.1	Data Organization	25
2.3.2	Time-Domain Analysis	26
2.3.3	Frequency Analysis	27
2.3.4	Time-Frequency Analysis	28
2.3.5	Feature Extraction	30
2.3.6	Feature Selection	39
3	Experimental Setup	43
3.1	Gearbox Test Bench	44
3.2	Setup for Rheological Investigations	50
3.3	Infusion and Injection Processes: VAP and T-RTM	52
3.4	Data Acquisition System and Sensor Placement	59
4	Enhanced Techniques for Ultrasound based Condition Monitoring	69
4.1	Feature Adaption	74
4.2	Feature Selection	78
4.3	Global Reconstruction	85
5	Application	99
5.1	Feature Adaption: Rheological Measurements	99
5.2	Feature Selection: Gearbox Test Bench	109
5.3	Global Reconstruction	121
6	Discussion	135
6.1	Feature Adaption	135
6.2	Feature Selection	139
6.3	Global Reconstruction	144
7	Summary and Outlook	149

Contents

Glossary 151

Acronyms 153

References 155

Acknowledgments 165

1 Introduction

In today's industrial environment, designing and managing processes sustainably is increasingly important. With growing concerns about climate change, resource depletion, and environmental impact, industries face greater pressure to adopt practices that reduce their ecological footprint.

Sustainable process design is becoming essential for ensuring long-term viability and meeting environmental regulations. A key aspect of this approach is effective condition monitoring (CM), which helps optimize resource use, minimize waste, and improve overall efficiency [1–4].

CM refers to activities aimed at assessing the technical state of machines or systems, including monitoring, diagnostics, evaluation, and prognostics. It involves the collection, processing and interpretation of various data, such as temperature, pressure, flow rate, or chemical composition [5].

Based on this data, CM enables the detection of deviations from the normal state and thus enables real-time adjustments to maintain quality, enhancing efficiency, and reducing costs of operation.

It is widely applied in industries such as manufacturing, chemical processing, and energy production, where precise control over operational parameters is crucial.

However, its application is less prevalent in sectors where processes are less standardized or where the cost of monitoring equipment is disproportionate and prohibitive.

In these contexts, the advantages of CM must be weighed against the initial investment and complexity of implementation. Nonetheless, with ongoing research, there is potential to expand the application of CM to new areas, particularly by developing cost-effective and adaptable monitoring solutions [6–8].

Several sensing techniques are employed in CM, ranging from traditional methods such as pressure sensors and flow meters to more advanced technologies like infrared spectroscopy and acoustic emissions. Among these, ultrasound-based techniques are popular due to their non-invasive nature and ability to provide detailed insights into the internal structure of solid as well as fluid materials [9–12].

Ultrasonic signals are highly sensitive to various factors, including pressure, temperature, and rheological properties. Thus ultrasonic signals, if properly applied and processed are a versatile tool for monitoring a wide range of process variables. However, this sensitivity also comes with a downside as the complexity of the signals can make it difficult to isolate and accurately monitor specific process variables.

To address these challenges, current research is exploring advanced methods such as machine learning, deep learning, convolutional neural networks, and feature extraction techniques. These approaches are being developed to enhance the processing and interpretation of ultrasound data [13, 14].

In [15] and [16] key challenges are identified in the fields of acoustic monitoring, structural health monitoring (SHM), and non destructive testing (NDT). According to them, difficulties are often posed by noise, environmental variability, data scarcity, and the complexity of current models. Thus, in industrial settings, acoustic monitoring systems often struggle with background noise, making it difficult to accurately detect anomalies. Similarly, SHM systems are affected by environmental factors like temperature changes, which can distort sensor readings and compromise the accuracy of data analysis.

Thus, future research should also aim to advance the complexity and robustness of models, developing more sophisticated approaches that can generalize across different conditions and structures, reducing false positives and missed detections. The integration of AI and machine learning into these models should be further explored to automate data processing tasks and improve the long-term reliability and accuracy of monitoring systems.

Ultrasonic signals often exhibit high complexity and generate large volume of data. This makes preprocessing techniques, specifically feature engineering and selection, play an important role in transforming the raw data into more concise form. This is known as data reduction, which also supports the data's interpretability by emphasizing the most relevant aspects of the signal that correspond to specific process variables.

The effectiveness of advanced analytical models is also dependent on the features fed into these models. Suitable features can enhance the performance of these techniques by providing a more informative and structured input, making it easier for the models to learn the underlying patterns in the data. Moreover, well-chosen features can reduce the risk of overfitting, where a model performs well on training data but fails to generalize to new, unseen data [17, 18].

Considering that different industrial applications have unique requirements and challenges, specifically customizing the feature to suit the applications can significantly improve monitoring outcomes. For instance, in a high-temperature environment, features that account for temperature-related variations in ultrasonic signals may be crucial. Application-specific feature design ensures that the monitoring system is tailored to the specific needs of the process, leading to more accurate and relevant insights.

In this research, the goal was to develop methods for comprehensive monitoring systems that not only achieve high accuracy in the short term but also maintain robustness over the long term without the need for frequent maintenance. Several key challenges have been identified with substantial potential for optimization, particularly in adapting and selecting

application-specific features, and how to assess unmonitored areas outside the physical reach of the sensors.

Thus this work proposes three approaches to realize:

- Defining and adapting features
- Selecting features
- Reconstructing data for unmonitored areas

The first approach focuses on optimizing the parameters of features to enhance the accuracy of predicting specific process variables.

In the context of ultrasonic CM, features are derived from the raw ultrasonic signals, and these features are typically influenced by various parameters, such as window size, frequency range, or threshold levels. The choice of these parameters can significantly affect how well the features capture the relevant information needed to monitor a particular process variable.

Adapting the feature parameters to the specific application is crucial to maximize the potential of individual features, ensuring that any decisions to exclude and select features over others are informed and well-founded.

The second approach deals with a common issue that many predictive models, while they may achieve high accuracy initially, their performance tends to degrade over time. This phenomenon can be observed in various applications, where the conditions under which the model was trained may change, leading to a decline in the model's effectiveness.

To address the issue of performance degradation, this research proposes a tailored approach to feature selection that focuses on creating more robust models. The key idea is to design or record test data to select features that are relevant to the application and resilient to its specific types of changes and drifts [19].

The final challenge is the placement of the sensors and their limited range. Even with the implementation of sensor networks and placement optimization, it is not always possible to cover every area of interest due to the inherent physical constraints of the sensors, limited number of available sensors or geometrical restrictions.

The information extracted from the monitoring process is inherently dependent on the placement and reach of the sensors used. Ultrasonic sensors, while effective in many applications, have a finite range, meaning they can only monitor a limited area primarily determined by the volume directly beneath the transducer's contact point with the object. This constraint poses challenges when trying to achieve comprehensive coverage of the entire process or system being monitored [16].

By overcoming these challenges, this work not only contributes to the theoretical understanding of ultrasound data processing but also provides practical solutions for enhancing

1 Introduction

monitoring systems in industry. These solutions are designed to improve the accuracy and robustness of monitoring systems, ensuring they remain effective even in complex and changing environments.

Ultimately, the research aims to make ultrasound-based techniques more versatile, enabling their adoption in a broader range of industrial applications where precise and reliable CM is crucial.

This work is divided into seven chapters. Chapter 1 serves as the introduction. Chapter 2 and Chapter 3 establishes the physical and mathematical foundation and the experimental setups necessary for understanding the advanced processing techniques introduced in the fourth chapter. Chapter 5 presents the actual application of these techniques to the processes, followed by a discussion of the results and a summary in Chapter 6 and Chapter 7, respectively.

2 Theoretical Background

Understanding the fundamental principles underlying ultrasound-based condition monitoring is crucial to advancing its application and efficacy. This chapter provides a comprehensive overview of the theoretical foundation necessary to support the methodologies and experimental techniques explored in this research.

It begins with an examination of the physics of ultrasound, detailing the mechanisms of wave propagation, reflection, and attenuation in media, as well as the principles of generation and detection using piezoelectric transducers. These foundational concepts are essential for understanding how ultrasonic signals interact with materials and convey information about their internal structures.

Building on this, the chapter introduces the mathematical tools essential for signal analysis, emphasizing the importance of Fourier transforms and filtering techniques in processing high-frequency data. Additionally, key principles of signal preprocessing, such as noise reduction, feature extraction, and alignment, are discussed to highlight their role in enhancing data quality and interpretability.

2.1 Physics of Ultrasound

Propagation

Acoustics as a branch of physics is usually defined as the study of mechanical vibrations and their generation, propagation and impact within certain media. Driven by restoring forces these vibrations can be described as oscillations about the equilibrium state, exhibiting a wave-like behaviour described by the familiar properties of amplitude and frequency. Vibrations of appropriate amplitude and frequency, approximately ranging between 10 Hz and 20 kHz [20], can be perceived by the human ear and thus, are called sound [21]. Then, *ultrasound* refers to certain vibrations of frequencies beyond the audible range above 20 kHz and is frequently used in NDT techniques, commonly known as ultrasonic testing. In many NDT applications, ultrasound offers a favourable balance between resolution and attenuation. Furthermore, since acoustic emission signals generated by microscopic deformations, such as crack growth, typically occur at frequencies in the lower ultrasonic range [22], ultrasonic testing has become a widely used and efficient technique.

2 Theoretical Background

For a theoretical understanding of the formation and propagation of ultrasonic waves in solid media consider the stress components σ_{ik} of a infinitesimal volume element as illustrated in Figure 2.1.

With $dA_1 = dx_2 dx_3$ and neglecting any body forces, the resulting force F_1 on the element

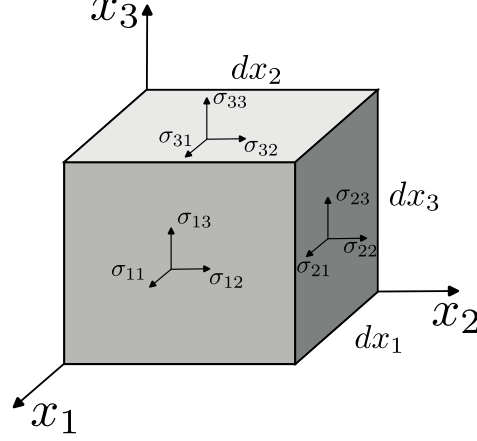


Figure 2.1: Differential three-dimensional element with the components of the stress tensor.

in 1-direction can be written as

$$F_1 = \frac{\partial \sigma_{11}}{\partial x_1} dx_1 \cdot dA_1 + \frac{\partial \sigma_{21}}{\partial x_2} dx_2 \cdot dA_2 + \frac{\partial \sigma_{31}}{\partial x_3} dx_3 \cdot dA_3 = \left(\frac{\partial \sigma_{11}}{\partial x_1} + \frac{\partial \sigma_{21}}{\partial x_2} + \frac{\partial \sigma_{31}}{\partial x_3} \right) \cdot dV. \quad (2.1)$$

Thus, using index notation and Newton's Law, $\vec{F} = m\vec{a} = m\ddot{\vec{u}}$ yields

$$\rho \ddot{u}_i = \frac{\partial \sigma_{ik}}{\partial x_k}, \quad (2.2)$$

with u_i being the displacement component and ρ the density. Hook's Law describes the relation between the stress tensor σ_{ik} and the strain tensor $\epsilon_{lm} = \frac{1}{2} \left(\frac{\partial u_l}{\partial x_m} + \frac{\partial u_m}{\partial x_l} \right)$ and is defined as

$$\sigma_{ik} = C_{iklm} \epsilon_{lm}, \quad (2.3)$$

with C_{iklm} as the elasticity tensor exhibiting 81 components. However, applying symmetric considerations to a given body, the tensor can be reduced to at least 21 components for generally anisotropic bodies [23]. Combining 2.2 and 2.3 results in a differential equation for the displacement components u_i

$$\rho \ddot{u}_i = \frac{1}{2} C_{iklm} \left(\frac{\partial^2 u_l}{\partial x_k \partial x_m} + \frac{\partial^2 u_m}{\partial x_k \partial x_l} \right). \quad (2.4)$$

Equation 2.5 represents a plane harmonic wave and is given by

$$u_i = A_i \exp(i(k_j x_j - \omega t)), \quad (2.5)$$

where A_i is the amplitude of particle displacement, ω as the angular frequency and k_j denoting the unit wave vector, yields the Christoffel equation defined as

$$(C_{iklm}k_k k_l - \rho\omega^2 \delta_{im})u_m = 0. \quad (2.6)$$

and can be rewritten as

$$(\Gamma_{im} - \rho c^2 \delta_{im})u_m = 0 \quad (2.7)$$

with $c = \frac{\omega}{k}$, $k_i = |k|n_i$ and $\Gamma_{im} = C_{iklm}n_k n_l$ [24]. Following [25], Equation 2.7 is used to describe plane harmonic waves propagating in anisotropic media by setting the determinant of the coefficient matrix equal to zero.

To demonstrate this approach consider isotropic materials. In this case, the fourth-order elasticity tensor C_{iklm} is often reformulated using Voigt notation. This compact representation maps the tensor components to a 6×6 matrix by exploiting the symmetries of the stress and strain tensors. For isotropic materials, the resulting stiffness matrix depends only on the two independent components Λ and μ , known as the Lamé Constants which show the following relations to the elastic parameters for an isotropic material

$$E = \frac{\mu(3\Lambda + 2\mu)}{\Lambda + \mu} \quad (2.8)$$

$$\nu = \frac{\Lambda}{2(\Lambda + \mu)} \quad (2.9)$$

$$G = \mu \quad (2.10)$$

with the Young's modulus E , the Poisson's ratio ν and the shear modulus G , the stiffness matrix C can be written as:

$$C = \begin{bmatrix} \Lambda + 2\mu & \Lambda & \Lambda & 0 & 0 & 0 \\ \Lambda & \Lambda + 2\mu & \Lambda & 0 & 0 & 0 \\ \Lambda & \Lambda & \Lambda + 2\mu & 0 & 0 & 0 \\ 0 & 0 & 0 & \mu & 0 & 0 \\ 0 & 0 & 0 & 0 & \mu & 0 \\ 0 & 0 & 0 & 0 & 0 & \mu \end{bmatrix}$$

Now, based on a harmonic wave with a wave vector of $\vec{k} = \frac{k}{\sqrt{2}} [1 \ 1 \ 0]$ the terms for Γ_{im} in Equation 2.7 can be calculated. Then, setting the determinate of $|\Gamma_{im} - \rho c^2 \delta_{im}|$ to zero gives two eigenvalues with the values for c being

$$c_1 = \sqrt{\frac{\Lambda + 2\mu}{\rho}} = \sqrt{\frac{E(1 - \nu)}{(1 + \nu)(1 - 2\nu)\rho}}, \quad c_2 = \sqrt{\frac{\mu}{\rho}} = \sqrt{\frac{G}{\rho}}. \quad (2.11)$$

2 Theoretical Background

The general solution for the corresponding normed eigenvectors are

$$\hat{u}_1 = \frac{1}{\sqrt{2}} [1 \quad 1 \quad 0] \quad \hat{u}_2 = \frac{1}{\sqrt{2a^2 + b^2}} [-a \quad a \quad b] \quad (2.12)$$

The dot products $\hat{k} \cdot \hat{u}_1 = 1$ and $\hat{k} \cdot \hat{u}_2 = 0$ help to identify the orientation between wave vector and displacement vector. While \hat{u}_1 points in the direction of \vec{k} and thus indicating a longitudinal wave, \hat{u}_2 is perpendicular to \vec{k} indicating a transverse wave, with velocities of $c_l = c_1$ and $c_t = c_2$, respectively. For solid, isotropic materials, where $0 > \mu > 0.5$, the relation

$$c_l \sqrt{\frac{1 - 2\mu}{2 - 2\mu}} = c_t \quad (2.13)$$

yields that $c_l > c_t$ [20]. Figure 2.2 illustrates the particle movement of a longitudinal and transverse wave. The euclidean distance between two particles of the same phase, is defined as the wavelength λ , which relates to the wave vector k as $\lambda = \frac{2\pi}{|k|}$. Similarly, the frequency f of a wave is defined as the number of times a particle passes through the same phase per unit of time. It is related to the period T and angular frequency ω by the following relationships:

$$f = \frac{1}{T} = \frac{\omega}{2\pi}.$$

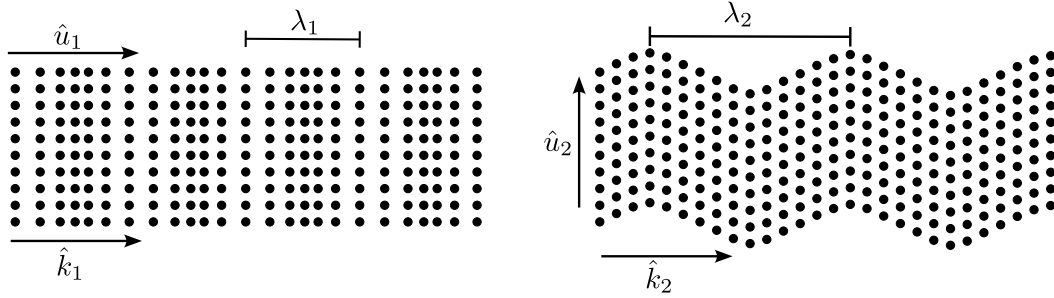


Figure 2.2: Schematic propagation of a longitudinal (left) and a transverse (right) wave along the wave vector \hat{k}_1, \hat{k}_2 and with the wavelengths λ_1, λ_2 , respectively.

Note that, in case of a group of waves with different frequencies, its propagation is associated with a wave packet which velocity is described by the group velocity v_g given by [25]

$$v_g = \frac{d\omega}{dk} = c_p + k \frac{dc_p}{dk}. \quad (2.14)$$

with $c_p(k) = \frac{\omega(k)}{k}$ being the phase velocity. For lossless, isotropic media the group velocity coincides with the velocity of energy transportation and the phase velocity. In general, for anisotropic material, c_p depends on the wave vector \vec{k} , so that $c_g \neq c_p$ resulting in dispersion. Active ultrasonic testing often uses short pulses of sound that are no longer composed of a single frequency. The effects of dispersion are often evident in a gradual extension of the impulse in space. However, reducing the initial impulse length requires a broader frequency range.

In ultrasonic testing the acoustic waves frequently encounter interfaces at the boundaries of the specimen or within it caused by impurities or porosity. The amplitude of the particle's displacement ξ , the sound impedance $Z = \rho c$ and the sound pressure $p = Z\omega\xi$ are useful parameters to describe the influence of interfaces on the propagation of acoustic waves. The reflection factor R and transmission factor T are defined as

$$R = \frac{p_r}{p_i}, \quad T = \frac{p_t}{p_i} \quad (2.15)$$

with p_r , p_t and p_i as the sound pressure of the reflected, transmitted and incident wave at an interface. To derive the dependency from the acoustic impedance Z , consider Figure 2.3. It shows a plane wave travelling through a material of acoustic impedance Z_1 and then encountering an interface with material of acoustic impedance Z_2 . Using Equation 2.5 for the plane wave and applying boundary conditions eventually yields [25]

$$R = \frac{Z_2 - Z_1}{Z_2 + Z_1}, \quad T = \frac{2Z_2}{Z_2 + Z_1}, \quad (2.16)$$

for a normal beam incidence.

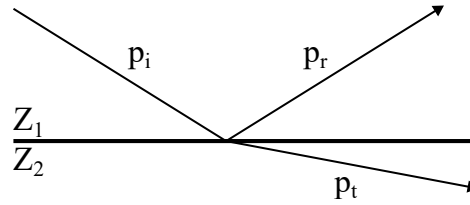


Figure 2.3: Illustration of a sound beam partially reflected and transmitted at an interface.

Attenuation

The sound pressure p is an important quantity in UT as it is proportional to the displacement of the particle and thus a crucial quantity in the detection of acoustic waves. The amplitude of the sound pressure p decreases as the acoustic waves propagate through medium, which is mainly ascribed to three contributions, the geometric spreading, absorption and scattering. For comparison p_{gs} is introduced to describe the influence of geometric spreading, which is unaffected by the carrier medium, and p_a describing absorption and scattering. Using normed values for p_{gs} and p_a the total sound pressure p is calculated via

$$p_{tot} = p_0 p_{gs} p_a, \quad (2.17)$$

with p_0 as the initial sound pressure.

For the geometric spreading p_{gs} consider a spherical wave. Adhering to the law of conservation of energy lead to a decrease of the waves amplitude inversely proportional to the distance travelled. Then, following the Huygens-Fresnel principle the sound pressure

2 Theoretical Background

emitted from emission sources of various shapes can be calculated. A typical emitter used in this work is a piezoceramic which can be described by a plane, circular oscillator. The absolute values of the sound pressure along its rotation axis with z as the distance to the emitter's centre and D as the diameter follow the equation [20, 26]

$$p_{\text{gs}} = |p_0 2 \sin \left(\frac{\pi}{\lambda} \sqrt{\frac{D^2}{4} + z^2} - z \right)|. \quad (2.18)$$

To describe the modulations of the pressure, it is useful to distinguish between near-field $z < N$ and far-field $z > N$ with the near-field length

$$N = \frac{D^2}{4\lambda} \quad (2.19)$$

for a circular emitter. The near-field, strongly influenced by the characteristics of the source, usually exhibit a complex behaviour, whereas the sound pressure monotonically decreases in the far-field. For $D \gg \lambda$ the near-field length corresponds to the last maximum of p in positive z -direction, that is

$$p_{\text{gs,max}} = \left(1 - \frac{\lambda^2}{D^2}\right) N \stackrel{D \gg \lambda}{\approx} N. \quad (2.20)$$

For great distances z the third binomial equation and the small-angle approximation can be used to show that $p \stackrel{z \gg N}{\approx} p_0 \frac{\pi N}{z}$. Figure 2.4 illustrates the sound pressure p_{gs} with this approximation using the parameters $D = 10$ mm, $\lambda = 3.2$ mm and $N = 7.8$ mm frequently encountered in this work. Note that, Equation 2.18 applies to a continuous oscillating source. However, while short pulses influence interference effects in the near field, the far field remains largely unaffected [20].

The consistency of the far field and since the natural focal point, or the point of highest sound pressure of a circular flat-disc oscillator, aligns with the near field length N , it is advisable to position the sensor at a distance larger than N to achieve reliable results.

So far, the sound field is described within a single material with homogenous acoustic properties. To address the impact of interfaces between two distinct materials, it is crucial to note that the frequency f remains constant during transmission. Equation 2.19 with the wavelength defined as $\lambda = \frac{f}{c}$ leads to the relationship between the near field lengths of a material 1 and 2 as follows:

$$\frac{N_1}{N_2} = \frac{c_2}{c_1} \quad (2.21)$$

Generally, for distances d_i that correspond to equivalent points in the sound field for each material, the same proportionality factor holds:

$$\frac{d_1}{d_2} = \frac{c_2}{c_1} \quad (2.22)$$

Applying these equations, the total near field distance N_{tot} can be calculated for a layered structure of two different materials. Assuming d_1 as the thickness of the first material it follows:

$$N_{\text{tot}} = d_1 + (N_1 - d_1) \cdot \frac{c_1}{c_2}. \quad (2.23)$$

Considering an acoustic wave propagating in natural materials, additional effects including

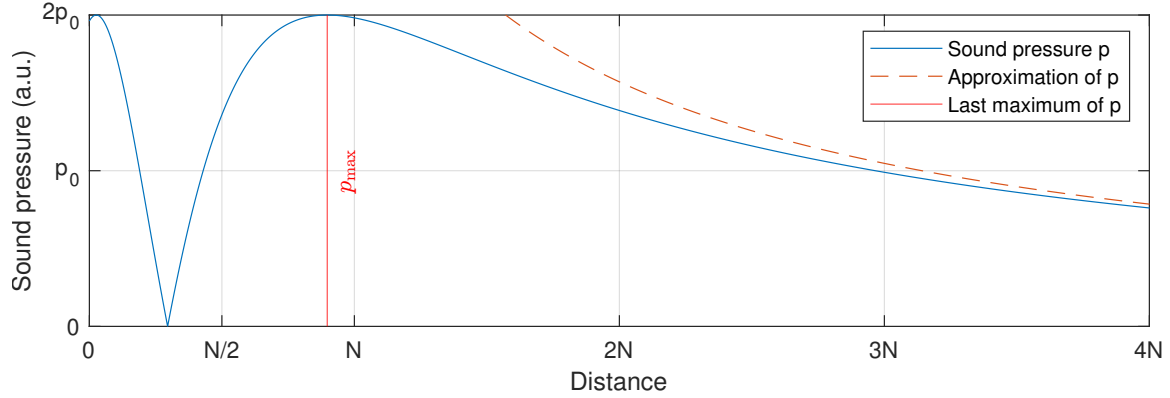


Figure 2.4: Sound pressure p of a circular emitter following Equation 2.18. The distance is illustrated in units of the nearfieldlength N . The red solid line indicates the last maximum p_{max} and the red dashed line indicating the approximation for large distances $> N$.

scattering and true absorption further weaken the amplitude of the sound pressure. Unlike the attenuation through beam divergence, these effects depend on the characteristics of the wave, such as frequency f and wavelength λ . Scattering arises from material inhomogeneities as foreign inclusions, gas pores, or inherent material flaws, where acoustic impedance abruptly changes. These variations cause the sound wave to reflect and refract in different directions into partial waves, which results in a diffuse distribution of the wave intensity. Then, along the paths of the waves their energy is gradually converted into heat. This effect is called true absorption and is caused by various processes detailed in [20, 27, 28]. Mathematically it can be described by introducing viscoelastic properties in Equation 2.4. The impacts of scattering and absorption result in an exponential decay of sound pressure, attributed to the attenuation coefficient α in

$$p_a = p_0 e^{-\alpha z}, \quad (2.24)$$

which is measured in decibels per meter and highly dependent on material properties, such as fiber volume content in composites or grain size in metals, as well as the frequency of sound waves. Generally, scattering increases significantly when the grain size exceeds one-tenth of the wavelength. Therefore, reducing the frequency, and thus increasing the wavelength, can help to mitigate scattering. However, as higher wavelength reduces the resolution, a compromise between attenuation and minimum size of flaw detection has to be made. Using ultrasound with a frequency of 2 MHz the attenuation coefficient α ranges from around $1 \frac{\text{dB}}{\text{m}}$ for light metals to approximately $300 \frac{\text{dB}}{\text{m}}$ for grey cast iron [20]. Figure 2.5 illustrates p_{tot} for different attenuation factors α and shows that the dominant contribution

2 Theoretical Background

highly depends on the magnitude of α and on the distance travelled by the sound waves. To optimize sensor integration for precise measurements, it is imperative to consider this

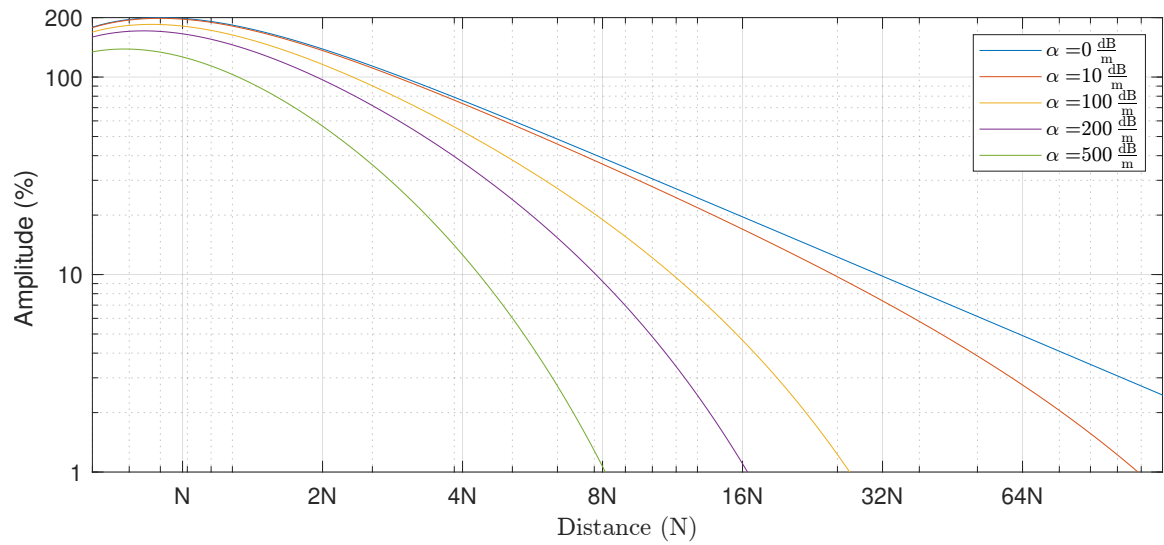


Figure 2.5: The amplitude of p_{tot} over distance in units of the near field length N and for different attenuation factors α . Amplitude 100 % is arbitrarily set to p_0 . When $\alpha = 0$, it indicates pure geometric spreading, where p_{tot} equals p_{gs} .

interplay between the attenuation effects and the specific reflection conditions of the application. For example, for low attenuation factors $\alpha < 1 \frac{\text{dB}}{\text{m}}$ it is a good approximation to consider the sound pressure illustrated in Figure 2.4 and adjust the sensor integration so that the area of high interest of the material to be tested conforms with its maximum sound pressure.

Generation and Detection of Ultrasound

There are a variety of methods to detect and generate ultrasound based on mechanical, electro-dynamics, optical and thermal effects. The most common method however uses the piezo-electric effect due to its capability of producing strong signals with high efficiency and its high performance as emitter as well as receiver [20, 29–31].

The piezoelectric effect is observed in specific solid materials with an asymmetric charge distribution within their elementary cells, leading to the formation of an electrical dipole. Common materials used for the generation and detection of ultrasonic waves are piezoelectric ceramics with a perovskite structure such as lead zirconate titanate (PZT) or barium titanate (BaTiO_3) as illustrated in Figure 2.6. Mechanical stress applied to piezoelectric material changes its dimensions and its dipole distribution. This imbalance of electrical charge leads to an electrical field proportional to the change of thickness [22, 32]. Thus pressure

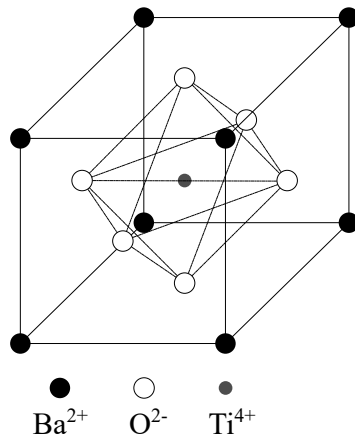


Figure 2.6: Illustration of the crystal lattice of BaTiO_3 as an example of the perovskite structure [33].

p applied to a piezoelectric plate along the x -axis leads to a change in its dimension Δx , creating an electric voltage U_r following the equation

$$U_r = h_{33}\Delta x \quad (2.25)$$

with the piezo-electric deformation constant h_{33} . The arising voltage U_r can also be expressed via the pressure p applied to the piezo plate. In this case, consider the thickness d of the plate following the equation:

$$U_r = g_{33}dp, \quad (2.26)$$

with the piezo-electric pressure constant g_{33} . The incoming ultrasonic waves excite the piezoelectric element, causing it to deform. These deformations generate electrical voltages across the piezoelectric plate, which can be measured to detect the ultrasonic waves.

Conversely the inverse piezoelectric effect occurs, when an external electric field is applied to these materials, which causes them to deform or change shape. The change of thickness

Δx is proportional to the transmitting voltage U_t between the surfaces of the plate according to the equation

$$\Delta x = d_{33} U_t \quad (2.27)$$

with the piezo-electric modulus d_{33} [20]. The inverse piezoelectric effect can be exploited to produce ultrasonic waves by applying an electric field to a piezoelectric plate. This electric field induces oscillatory strains in the plate, compelling it to expand and contract in alignment with the field's direction. These mechanical oscillations then propagate as longitudinal waves through the medium in contact with the plate. The excitation can be realized either through a continuous, oscillating electric field or via short rectangular pulses. The emitted ultrasound waves depend on the resonance characteristics of the piezoelectric plate being excited.

A continuous, oscillating electric field induces a forced oscillation within the piezoelectric plate with the frequency of the excited electric field. The amplitude of this oscillation is governed by the resonance curve of the material. In general, at low frequencies the amplitude corresponds to static case, increasing with higher frequencies and reaching its maximum at the resonance frequency and peaks at its odd multiple. In case of small damping the resonance frequency is approximately the fundamental frequency f_0 of the plate defined as

$$f_0 = \frac{c}{2d} \quad (2.28)$$

with the sound velocity c within the plate and its thickness d . Higher damping causes a broadening of the peak.

Exciting a piezoelectric plate with a short, rectangular pulse induces a free oscillation. Given that a short, rectangular pulse consists of a continuous spectrum of frequencies, the amplitudes of the induced oscillations correspond to the resonance curve. This results in the highest amplitudes at the resonance frequencies and their higher harmonics. In practice, the excitation pulse has a finite length, and to generate a clean and well-defined ultrasound wave, the pulse width of the excitation signal should be carefully controlled. For instance, a rectangular pulse with a duration that matches the inverse of the resonant frequency can effectively excite the piezoelectric plate. However, techniques like frequency sweeps can be beneficial in determining the ideal pulse width for the specific sensor and application. It is not always straightforward to determine the optimal pulse width, as multiple factors need to be considered [34–36].

The piezoelectric effect and its inverse essentially enables the design of ultrasonic transducers capable of converting electrical energy into mechanical energy and vice versa, making it suitable for the generation and detection of ultrasonic waves. The product of these constants defined via the electro-mechanical coupling factor k_{33} in

$$d_{33} h_{33} = \frac{U_r}{U_t} = k_{33}^2 \quad (2.29)$$

can be utilized to assess the efficiency of the conversion of energies [20]. A higher k_{33} value indicates a more efficient transducer, which is crucial for optimizing the performance of ultrasonic systems in various applications.

2.2 Signal Analysis Techniques

In the following, essential mathematical methods for signal processing in ultrasound process monitoring are introduced. The focus is on the mathematical techniques used to process and interpret ultrasound data, with particular emphasis on the Fourier transformation and filters.

The Fourier transformation is fundamental in converting time-domain signals into their frequency-domain representations, revealing critical frequency components for analysis. Filters play a crucial role in removing noise and enhancing signal quality. Together, these methods are indispensable for the accurate processing and interpretation of ultrasound data [37, 38].

Fourier Transform

The Fourier theorem asserts that any time-dependent signal $f(t)$ can be represented as a composition of sinusoidal waves, each with its own frequency and amplitude. To comprehensively analyse the information embedded in sound waves, it is valuable to examine the signal in both time and frequency domains.

Time domain analysis explores the dynamics of a signal, providing insights into variations at specific moments. Frequency domain analysis, on the other hand, decomposes a signal into its fundamental frequencies, unveiling the spectrum of components constituting the signal. Together, these methods offer a detailed perspective on the temporal and spectral characteristics of a signal.

Time-frequency analysis now investigates how a signal's frequency components evolve over time. The Fourier transform (FT) links these domains by representing a function $f(t)$ as a sum of complex exponential functions, each characterized by an angular frequency ω :

$$F(\omega) = \int_{-\infty}^{\infty} f(t)e^{-i\omega t} dt \quad (2.30)$$

Conversely the time signal can be reconstructed using the inverse FT:

$$f(t) = \frac{1}{2\pi} \int_{-\infty}^{\infty} F(\omega)e^{i\omega t} d\omega. \quad (2.31)$$

However, these equations need to be adapted for digital signals, resulting in the discrete Fourier transform (DFT). This adaptation introduces deviations from the exact solutions, as referred to aliasing and leakage. To correctly apply the DFT in signal processing and feature extraction a thorough understanding of its derivation is crucial and summarized in

2 Theoretical Background

the following.

The FT is denoted by $x(t) \leftrightarrow X(\omega)$. The product theorem [37] is defined as:

$$x(t) \cdot y(t) \leftrightarrow X(\omega) * Y(\omega) \quad (2.32)$$

where $*$ denotes convolution integral between the functions $X(t)$ and $Y(\omega)$ given by

$$X(\omega) * Y(\omega) = \int_{-\infty}^{\infty} X(\lambda)Y(\omega - \lambda) d\lambda = \int_{-\infty}^{\infty} X(\omega - \lambda)Y(\lambda) d\lambda. \quad (2.33)$$

Consider a band-limited signal $x(t)$, continuously recorded over time with a maximum non-zero frequency of ω_c . The exemplary signal $x(t)$ and its FT $X(\omega)$, representing an analytical solution of the frequency spectrum, are illustrated in Figure 2.7. However, due to

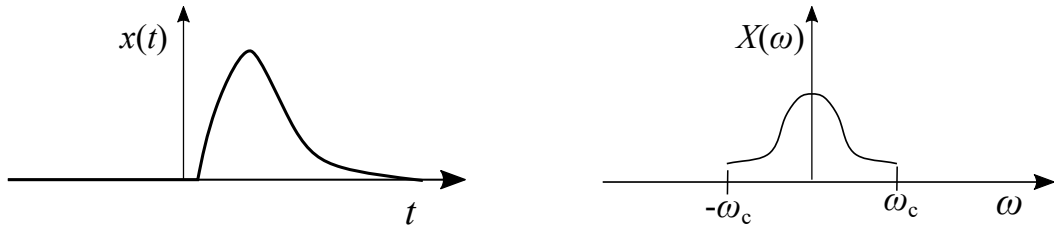


Figure 2.7: Left: Graph of a continuous signal $x(t)$, plotted as a function of time t . Right: Corresponding FT $X(\omega) \leftrightarrow x(t)$ as a function of frequency ω . The frequency ω_c marks the largest frequency occurring in the spectrum.

limited computation and storage capacities the digitizing process requires discretization and truncation of the signal into a finite number of samples.

To introduce discretization mathematically, the signal $x(t)$ is multiplied by an impulse train $s(t)$, which yields a discretized signal $x_s(t)$:

$$x_s(t) = x(t) \cdot s(t) = x(t) \cdot \sum_{n=-\infty}^{\infty} \delta(t - nT), \quad (2.34)$$

where $\delta(t)$ is the delta Dirac function defined as:

$$\delta[n] = \begin{cases} 1 & \text{if } n = 0, \\ 0 & \text{otherwise.} \end{cases} \quad (2.35)$$

The product $x(t) \cdot s(t)$ corresponds to discretization with a sampling frequency of $f = \frac{1}{T}$. The product theorem from Equation 2.32 is used to calculate its FT:

$$x_s[n] = x(t) \cdot \sum_{n=-\infty}^{\infty} \delta(t - nT) \leftrightarrow X_s = X(\omega) * \frac{1}{T} \sum_{n=-\infty}^{\infty} \delta(\omega - n\omega_s) \quad (2.36)$$

$$\leftrightarrow \frac{1}{T} \sum_{n=-\infty}^{\infty} \int_{-\infty}^{\infty} X(\omega - \lambda) \delta(\lambda - n\omega_s) d\lambda \quad (2.37)$$

$$\leftrightarrow \frac{1}{T} \sum_{n=-\infty}^{\infty} X(\omega - n\omega_s) = X_s(\omega), \quad (2.38)$$

where $x_s[n]$ denotes a discrete signal with $n = 0, 1, 2, \dots$. Since the FT of $s(t)$ is a impulse train with a sampling snippet of $\frac{1}{T}$, from Equation 2.38 it follows that the FT X_s of the sampled signal is a $\frac{1}{T}$ -periodic extension of the FT of the corresponding continuous signal $X(t)$.

Figure 2.8 visualizes the process of Fourier transforming the sampled signal $x_s(t)$ and shows, that the sample frequency $\frac{1}{T}$ must be sufficiently large enough to obtain an undistorted representation of the FT within the frequency range $\omega < \omega_c$. However, if the band-limiting

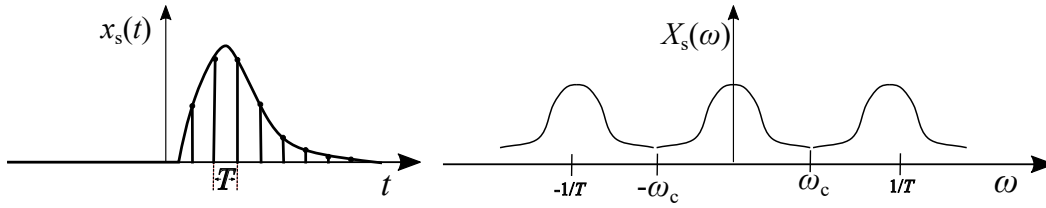


Figure 2.8: Left: Graph of a discretized signal $x_s(t)$ with a sampling frequency of $\frac{1}{T}$. Right: Corresponding FT $X_s(\omega)$ for the case of $|\omega_c| < \frac{1}{2T}$.

frequency ω_c exceeds $\frac{1}{2T}$, the replicas of $X(\omega)$ overlap, thereby distorting the spectrum of the original signal. This phenomenon, known as aliasing, is shown in Figure 2.9. To prevent aliasing, it is crucial to choose a sampling frequency larger than twice the highest frequency present in the signal. This is also known as the Nyquist-Shannon sampling theorem [39], which specifies:

$$2\omega_c \leq f_N \frac{1}{T_{\max}}, \quad (2.39)$$

with f_N being the Nyquist frequency. Thus it is essential that x_s remains band-limited to enable precise reconstruction of the original signal's spectrum. Since real signals are seldom exactly band-limited, careful consideration in the selection of acquisition parameters and the application of appropriate analogue filters is crucial.

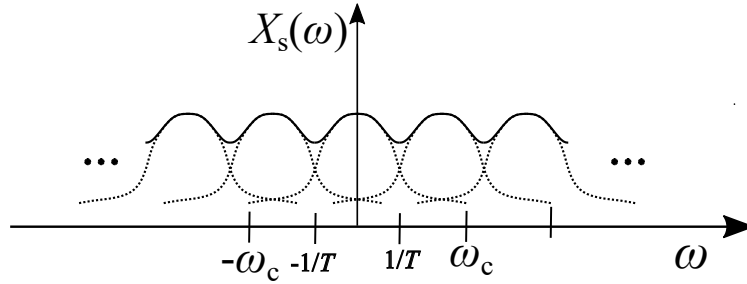


Figure 2.9: FT $X_s(\omega)$ for the case of $|\omega_c| > \frac{1}{2T}$ which results in aliasing and a distortion of the frequency spectrum.

To investigate the effects of truncation multiply the signal with a rectangular window of length N , as expressed by:

$$w[n] = \begin{cases} 1 & \text{for } 0 \leq n \leq N - 1 \\ 0 & \text{otherwise} \end{cases} \quad (2.40)$$

According to the product theorem of Equation 2.32, this operation corresponds in the frequency spectrum to the convolution with the FT of $w[n]$, which is the aliased sinc function, asinc . Thus, with the substitution $\Omega = \omega T$ the Discrete Time Fourier Transform $X_T(\Omega)$ of the truncated signal $x_T[n] = x[n] \cdot w[n]$ is given by

$$x_T[n] \leftrightarrow X_T(\Omega) = X(\Omega) * \text{asinc}(\Omega) \cdot e^{-\frac{i(N-1)}{2}\Omega} \quad (2.41)$$

where the additional linear phase factor $e^{-\frac{i(N-1)}{2}\Omega}$ occurs due to the non-zero centred window function. This procedure causes a further distortion of the FT, referred to as leakage, which can be attenuated by increasing N of the window function as the asinc function gradually approaches the shape of an impulse and thus reducing the sidelobes.

A common technique to reduce leakage is windowing, that is multiplying the signal by a window function different from a simple rectangular window. Common window functions include Hamming and Kaiser window which is compared to the rectangular window in Figure 2.10. Each has different characteristics and is chosen based on the specific requirements for spectral resolution and sidelobe attenuation. The rectangular window has high sidelobes and poor frequency selectivity, while the Hamming window reduces sidelobes through tapering but loses some resolution. The Kaiser window allows tuning via β (e.g., 3) offers better resolution with higher sidelobes, while higher values (e.g. 10) reduces sidelobes at the cost of resolution. This flexibility makes it ideal for balancing resolution and sidelobe suppression.

The FT $X_s(\omega)$ so far is a continuous function and thus needs to be discretized for storage.

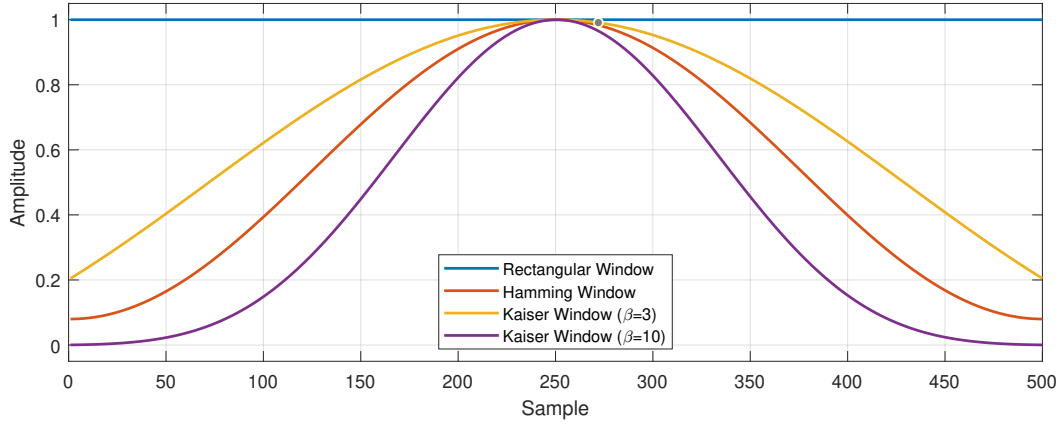


Figure 2.10: Comparison of the rectangular, Hamming and Kaiser window. The sample length is arbitrarily set to 500.

Again, this process is mathematically described by a multiplication with a frequency-domain impulse train. It is given by

$$X_D(\Omega) = X_s(\Omega) \cdot \frac{1}{M} \sum_{m=-\infty}^{\infty} \delta\left(\Omega - \frac{m}{M}\right). \quad (2.42)$$

Thus, the frequency resolution of the FT is

$$\Delta\omega = \frac{1}{MT} = \frac{\omega_s}{M} \quad (2.43)$$

with the sampling frequency ω_s .

The inverse FT is calculated by

$$X_D(\Omega) \leftrightarrow x_D[n] = x_s[n] * \sum_{m=-\infty}^{\infty} \delta(n - mM), \quad (2.44)$$

that implies that $X_D(\Omega)$ is actually the FT of $x_s[n]$, which is periodically extended with a period of M . Depending on the desired resolution, M should be at least equal to N . If $M > N$, the results of the DFT corresponds to the transformation of the signal $x_T[n]$, which has been extended to the length M by adding trailing zeros. This technique, known as zero-padding, can be used to increase the frequency discretization in the frequency-domain. In this study, the discrete fourier transform of a discrete-time vector $x[n]$ of length N is calculated using an optimized algorithm in MATLAB, known as the fast Fourier transform (FFT). This is implemented via a library referred to as FFTW [40]. The MATLAB syntax used is:

$$Y = \text{fft}(X, M); \quad (2.45)$$

This command returns the FFT Y of length M for one period, with the frequency increment of $\frac{f_s}{M}$. Conversely, the command:

$$X = \text{ifft}(Y, n) \quad (2.46)$$

2 Theoretical Background

returns the n -point inverse fourier transform of Y , padding Y with trailing zeros up to length n . For X and Y of length n , these transforms are mathematically expressed as:

$$Y(k) = \sum_{j=1}^n X(j) W_n^{(j-1)(k-1)} \quad (2.47)$$

$$X(j) = \frac{1}{n} \sum_{k=1}^n Y(k) W_n^{-(j-1)(k-1)}, \quad (2.48)$$

where

$$W_n = e^{\frac{-2\pi i}{n}} \quad (2.49)$$

is one of the n roots of unity.

Generally, the FFT results are complex, enabling the extraction of the amplitude A and phase delay ϕ as follows:

$$A_n = \sqrt{Re_n^2 + Im_n^2} \quad (2.50)$$

$$\phi_n = \arctan\left(\frac{Im_n}{Re_n}\right). \quad (2.51)$$

For a real input sequence, the FFT produces a symmetric real component and an antisymmetric imaginary component in the FT. This symmetry extends to the amplitude as well. Given the periodic nature of the DFT, only the first half of the FFT spectrum represents unique frequencies, which means the latter half is redundant and can be discarded.

Filter

Understanding the frequency spectrum provided by the FFT is crucial for many signal processing applications, especially when it comes to filtering. Filters play a vital role in manipulating signals by allowing certain frequencies to pass through while attenuating others. This selective frequency attenuation can be achieved through different types of filters, which can be categorized based on their frequency response and their type of implementation. One can distinguish between four types by frequency response:

- Low-Pass: Passes frequencies below a cutoff frequency, blocks higher ones.
- High-Pass: Passes frequencies above a cutoff frequency, blocks lower ones.
- Band-Pass: Passes frequencies within a frequency range, blocks others.
- Band-Stop: Blocks frequencies within a frequency range, passes others.

The most common types of implementing the filters are analogue and digital filters.

Analogue filters are typically implemented in the signal acquisition process or signal conditioning. They are used to process analogue signals, most commonly voltage signals and require hardware such as resistors, inductors, and capacitors for implementation, making them difficult to modify without redesigning or rebuilding the circuit.

Digital filters, in contrast, process signals after its conversion into digital form via an analogue-to-digital converter. Implemented using software algorithms, digital filters offer flexibility to meet specific application requirements independent of environmental influences like changing temperature [38, 41, 42].

To understand the theory of digital filters consider a discrete signal $x[n]$ with a sampling frequency of f_s . To obtain a filtered output signal $y[n]$ the general mathematical operation is

$$y[n] = \left(\sum_{i=0}^P a_i x[n-i] - \sum_{j=0}^Q b_j y[n-j] \right), \quad (2.52)$$

where P is the feedforward filter order, Q the feedback filter order and a and b its coefficients, respectively. With $b \neq 0$ this equation represents a recurrent or infinite impulse response (IIR) filter. When $b = 0$ the filter is called finite impulse response (FIR) filter.

To understand how filters can be created, consider a low-pass filter using the window design method for an FIR filter. The filter should eliminate all frequencies above f_c . In the frequency domain this corresponds to a simple operation, multiplying the frequency spectrum $X[\omega]$ with a corresponding rectangular function. This removes the unwanted high-frequency components and yields a filtered frequency spectrum. According to the convolution theorem, this operation in the frequency spectrum corresponds to a convolution with the DFT of the rectangular function $a[n]$ in the time domain, resulting in the equation:

$$y[n] = \sum_{i=0}^P a[i] x[n-i], \quad (2.53)$$

where $y[n]$ is the filtered output signal, $x[n]$ is the input signal. $a[n]$ is called the impulse response of the filter, which can be observed using the Dirac delta function in Equation 2.35 as the input signal $x[n] = \delta[n]$. This yields $y[n] = a[n]$. The impulse response for the rectangular window corresponds to its DFT, the origin-symmetric sinc function. These functions are illustrated in Figure 2.11.

To implement the filter, the sinc function must be shifted, sampled, and truncated to achieve a finite length. This truncation is done using a window function, which defines the shape and length of the impulse response. However, truncating the sinc function introduces inaccuracies, manifested as side lobes in the frequency response as illustrated in Figure 2.12. As elaborated in the previous section, the choice of window function significantly impacts the performance of the filter. Different window functions can be used to reduce side lobes and improve the filter's overall effectiveness. Common window functions include the Butterworth, Hamming, Hanning, and Blackman windows. Each of these functions offers a trade-off between main lobe width and side lobe suppression, allowing for the customization of the filter's characteristics based on specific application requirements [38, 43].

In this work the Butterworth filter is frequently used, yielding good results throughout different applications. The Butterworth filter is characterized by a smooth, monotonic

2 Theoretical Background

transition from the passband to the stopband, without any oscillations, where the order of the filter determines the steepness of this transition.

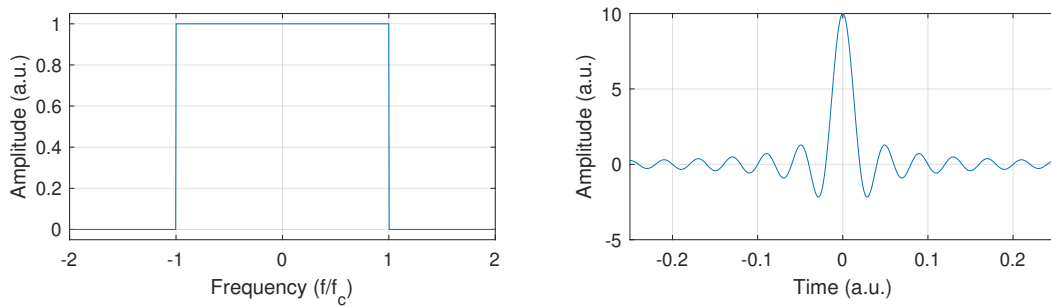


Figure 2.11: Left: Rectangular window with cut-off frequency at f_c . Right: Corresponding inverse FT in the time domain.

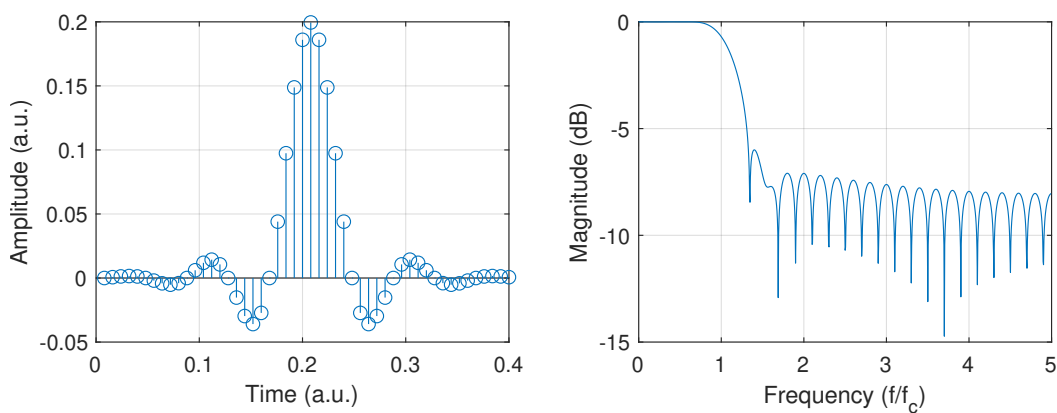


Figure 2.12: Left: Discretized impulse response of the rectangular window. Right: Corresponding frequency response.

2.3 Signal Processing

Central to process monitoring is the transformation of raw signals into actionable information, as extracting meaningful information from raw ultrasound data is not as immediately apparent. Figure 2.13 illustrates the workflow from acquiring raw data to obtaining higher-order information that can be utilized for process monitoring.

In general, signals are primarily categorized into analogue and digital signals. Analogue signals are continuous, varying smoothly over time, and can assume any value within a specified range. These signals are typical for many natural phenomena, such as sound waves, which are of interest in ultrasound-based condition monitoring. Conversely, digital signals exist only at discrete time points, often resulting from the sampling and digitization of analogue signals. Digitization is necessary due to finite storage and computational capacities.

In ultrasound-based condition monitoring, the received signals are generally high-frequency sound waves that materials under test emit, or sound waves actively excited by a transducer. However, these waves often carry unwanted noise and are subject to various distortions and interferences in industrial environments, making signal processing an essential step in process monitoring.

The first step in this process is the detection of ultrasonic waves using sensors, such as piezoelectric sensors, which convert the mechanical vibrations into measurable analogue electrical voltages. Once the analogue voltage signal is acquired, it typically requires analogue filtering and amplification, referred to as signal conditioning, to make it suitable for further processing. This step helps remove unwanted frequencies and enhances signal detectability.

Finally, an analogue-to-digital Converter is used to convert the analogue voltage signal into a digital signal for analysis. It combines sampling and quantization to enable storage and computation with finite capabilities. Sampling is where the continuous signal is measured at specific intervals to create a series of discrete time points, adhering to the Nyquist rate to ensure accurate reconstruction [44]. Quantization follows, assigning each sample a digital value based on a predetermined number of bits and thus discretizing the signal's amplitude [34, 45].

After signal acquisition, the next phase is signal preprocessing, where the signal is prepared for interpretation. This phase includes data cleaning, which removes artifacts or unwanted elements to enhance data quality. Additionally, feature extraction is performed to identify and isolate relevant characteristics or features from the signal, reducing the data volume and supporting the interpretation process.

Finally, the "the interpretation phase", often named diagnostics, applies various models and algorithms to extract higher order information. This could involve employing machine learning models for classification and regression tasks, as well as advanced reconstruction algorithms that not only visualize localized data but also provide deeper insights into the underlying patterns and system behaviour, enhancing interpretability and decision-making. Signal analysis is therefore crucial for effective maintenance. Smartly processing raw ultrasound data helps to identify patterns and anomalies within the ultrasound signals, and enables statements about the state and functioning of the process under investigation.

Preprocessing, referred to the collection of techniques applied to data before signal interpretation, is crucial for preparing raw data by enhancing signal quality, standardizing data formats, reducing noise, and extracting relevant features. Essentially, pre-processing transforms raw data into a refined state, optimized for subsequent analysis [46, 47].

Ultrasound signals, in particular, benefit significantly from preprocessing techniques due to their susceptibility to various types of noise, such as mechanical and electronic noise from the equipment, as well as environmental disturbances. Furthermore, ultrasound data is often voluminous, generating large quantities of data that can strain storage and processing systems.

2 Theoretical Background

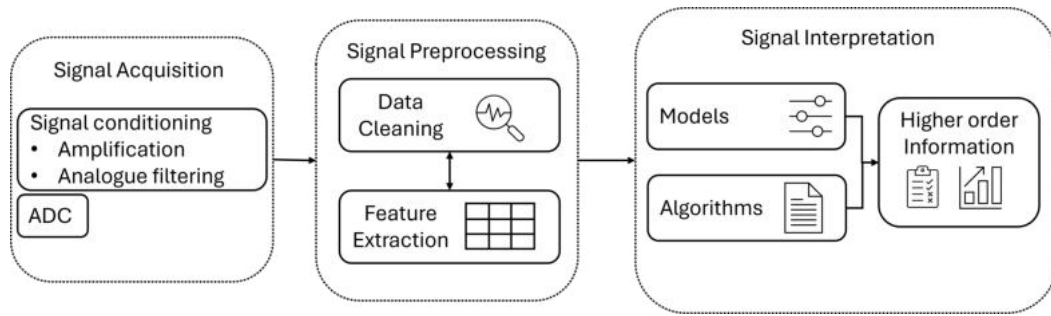


Figure 2.13: An overview of a signal processing workflow involving signal acquisition, preprocessing, and interpretation methods for accurate signal analysis and decision-making.

Suitable preprocessing techniques can help mitigate these issues, filtering out unwanted noise, improving the clarity of the signals and reducing data size while retaining essential information. Figure 2.14 illustrates the process of signal preprocessing used in this work, which is applied between receiving a conditioned signal and ultimately interpreting it. Signal conditioning involves preparing and optimizing raw sensor signals—through processes such as filtering, amplifying, and impedance matching—to enhance signal quality and ensure compatibility with subsequent digital processing systems [34].

The main preprocessing workflow is composed of several essential steps. First, the process of data organization takes place, which includes two key points: data cleaning and data alignment. Data cleaning involves the removal of errors, inconsistencies, and noise from the data to improve its quality and reliability. Data alignment involves resampling, adjusting the signal's sampling rate and synchronizing the data to ensure consistency and accuracy in the subsequent analysis. This supports data storage and further processing.

After data organization, the next crucial step is signal inspection, which involves a preliminary examination of the signal's characteristics to understand the underlying physics of the signal or to identify any obvious patterns or anomalies. There could be several techniques for a more in-depth analysis. The techniques are based on an analysis in the time, frequency or time-frequency domain [48, 49]:

- **Time domain analysis:** This approach focuses on how the signal's amplitude changes over time, providing insight into its temporal behaviour and helping to capture transient events.
- **Frequency domain analysis:** In contrast, this method examines the signal's frequency components, offering a deeper understanding of its periodic characteristics and underlying structures.
- **Time-frequency analysis:** This approach combines elements of both time and frequency domain analyses, allowing for a detailed exploration of how the frequency content of a signal changes over time.

The deeper understanding of the data acquired through initial signal inspections lays the foundation for effective feature extraction.

Feature extraction is a critical part of preprocessing. In this step, specific attributes or characteristics of the data are identified and extracted for further analysis. Feature extraction plays a vital role in simplifying the data, reducing its complexity while preserving the most relevant information. By selecting the most significant features, this step ensures accurate and efficient interpretation [47, 50, 51].

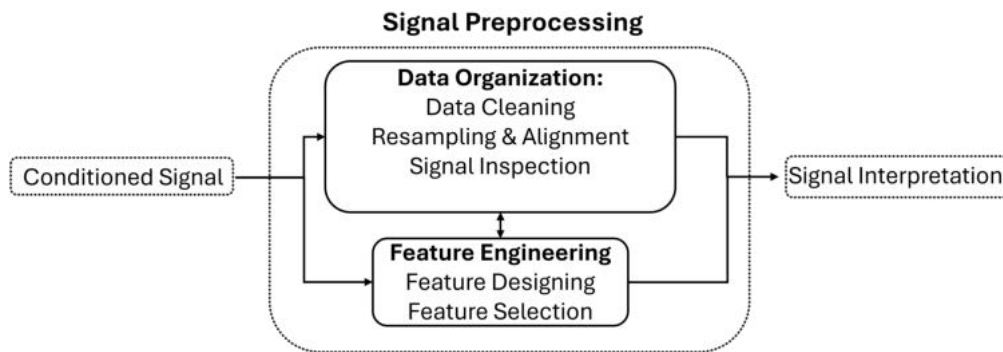


Figure 2.14: Signal preprocessing workflow, beginning with data organization and followed by feature extraction and selection, ultimately leading to signal interpretation.

2.3.1 Data Organization

Data Cleaning and Outlier Removal

After importing well-conditioned signals, the first step is to clean and organize the data. Removing outliers reveals the data's true structure, unaffected by extreme values due to environmental noise or measurement artefacts.

Outlier removal can be applied both to raw data and to calculated features at a later stage. Features such as statistical measures or spectral properties can also contain outliers due to the propagation of anomalies from the raw data. Identifying and addressing outliers at this stage further refines the dataset and ensures more accurate condition monitoring.

Common methods for identifying outliers involve setting a predefined threshold, which is then compared to statistical measures or distributions. For instance, outliers might be defined as sample points that fall outside a specified percentile range or deviate from the mean by a predefined multiples of standard deviations. Once identified, outliers can either be removed from the dataset or their values adjusted. In the context of condition monitoring, where data from different sources often need to be aligned, adjusting values is preferable to removal. This approach preserve the timestamp of the time series or spatial data.

Signal Alignment

Aligning signals to a uniform timestamp is essential when receiving data from multiple sensors. This often requires resampling.

The sample rate, which is changed in the resampling process, affects the accuracy of information transferred at specific frequencies. Adhering to the sampling theorem is essential, as higher frequencies can become distorted, leading to information loss when downsampling. Therefore, before downsampling, the signal must be filtered to eliminate excessive frequency content to prevent distortion. This is achieved by applying a low-pass or anti-aliasing filter. The process is as follows [38]:

- Select a factor M by which to reduce the original sampling rate.
- Apply low-pass filtering: The cutoff frequency should be less than or equal to half of the new sampling rate which is defined as the Nyquist frequency.
- Decimate the signal by retaining only every M^{th} sample of the original signal and discarding the others.

The basics of filter theory, design and its implementation is described above.

2.3.2 Time-Domain Analysis

Time-domain analysis in ultrasound-based condition monitoring involves examining the raw ultrasonic signal as a function of time. This technique benefits from its simplicity, allowing for direct interpretation of the signal without complex transformations, making it suitable for immediate feedback in experiments or a first assessments of data quality [25]. For instance, in ultrasound measurements, the signal can be directly plotted in the time domain to check echo patterns, which indicate whether the sensor is well-aligned and mounted.

Despite its simplicity, plotting the data in the time domain can suffice for basic analyses, such as tracking signal amplitude over time to distinguish different time segments of interest. For example, the top part of Figure 2.15 displays acoustic data recorded from a gearbox in alternating conditions. It illustrates how time-domain analysis can distinguish between the operational modes of the hub based on the acoustic data. The two different conditions emit different sound profiles which can be correlated with the specific mechanical states. Operation in condition 1 produces a louder sound, resulting in higher amplitude segments, clearly visible in the plot. These segments are highlighted in the bottom graph of Figure 2.15.

Time-domain analysis aids in focusing subsequent analyses on relevant time segments. Comparing the signals with other sensor or machine data can further help to highlight significant sections and, if necessary, allow for the discarding of irrelevant data. Abrupt changes in the signals may also indicate significant events and could serve as markers to check data synchronization accuracy.

For example Several time-domain vibration analysis techniques are used for condition monitoring of rolling element bearings, including statistical methods, regression models for analysing non-stationary data, and advanced filtering and noise separation approaches.

These methods improve fault diagnosis by effectively extracting key features and minimizing noise [52, 53].

However, time-domain analysis provides information limited to the signal's amplitude

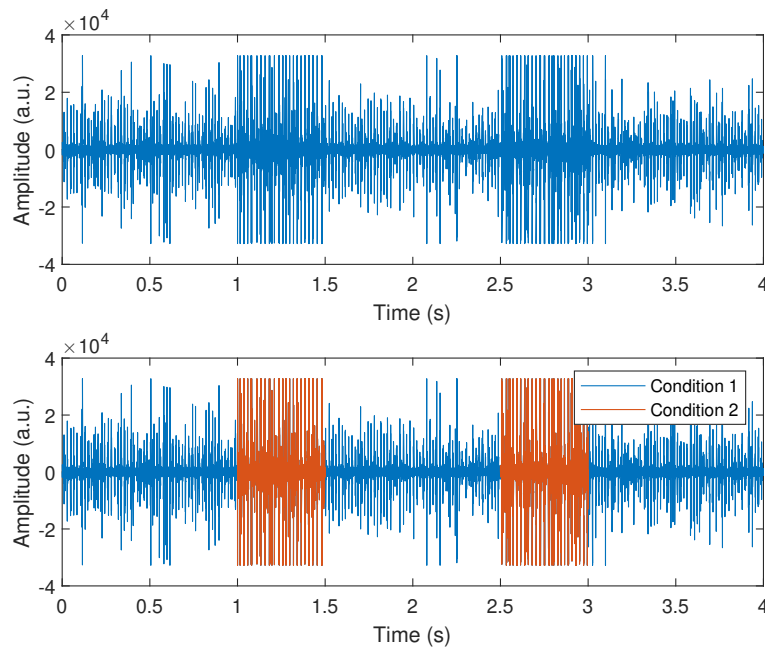


Figure 2.15: Recorded acoustic signals of a bicycle hub monitored using an ultrasonic piezo sensor. Both graphs display the raw amplitude data over time. The bottom graph shows the same signal but additionally differentiates between signals recorded while the hub was in condition 1 (blue) and condition 2 (orange).

and phase over time. Its interpretation becomes challenging when dealing with multiple overlapping signals or noise and interference components that may be superimposed on the primary signal. An analysis in the frequency domain can provide a solution in this context.

2.3.3 Frequency Analysis

In frequency analysis, data is examined within the frequency domain. Data is initially recorded in the time domain and must be transformed into the frequency domain. Techniques such as the FT allow for the visualization of a signal's frequency content, facilitating a deeper understanding of its characteristics and the identification of significant frequency ranges [53, 54].

Relevant frequencies may originate from the process itself, providing insights into the process state or wear. Conversely, irrelevant frequencies or noise that distorts the signal can be identified through frequency spectrum analysis. Once identified, filters can be designed to remove these unwanted frequencies, thereby enhancing the overall signal quality.

Identifying relevant and irrelevant frequency content and interpreting the spectrum can be achieved by theoretical or experimental methods. For a theoretical approach consider the underlying physics of the process. Every mechanical system possesses inherent physical properties such as distribution of mass, stiffness, and damping, which dictate its natural

frequencies and resonance phenomena.

Additionally, considering the operational behaviour is useful. For example, the rotation speed of a gearbox significantly impacts the frequencies of the generated sound waves. Thus, changing the rotational speed produce changes in the frequency spectra due to the direct correlation between mechanical movements and the frequency of vibrations [55, 56]. To effectively identify relevant frequencies within a signal, an experimental approach involves analyzing and comparing the spectra of signals under various sensor and process conditions. By systematically comparing sensor data recorded during different process states, one can attribute changes in the spectral regions to corresponding changes in the process. For example, comparing data collected before and after a change in conditions can reveal key frequency patterns that help identify when the change occurred.

Furthermore, by comparing spectra recorded at different times while maintaining consistent environmental conditions, one can isolate and identify frequency domains that may indicate wear or developing faults.

Conversely, comparing spectra recorded under consistent process parameters but with varying environmental conditions can help identify spectral changes caused by environmental factors. These changes can then be discarded as irrelevant, as they do not reflect the actual state of the process but rather external influences.

The top part of Figure 2.16 shows an exemplary acoustic signal of a bicycle hub operating in an unloaded state from 0 s to 2 s and in a loaded state from 2 s to 4 s. The loaded state means the system is subject to an external resistance, such as weight or friction, while the unloaded state refers to the condition where the system operates without any external resistance or load, allowing it to perform without interference.

In the time domain, the states are indistinguishable. However, the spectrum reveals their differences. The load distorts the spectrum, which is clearly visible on the logarithmic scale. The loaded state leads to a general increase of the frequency amplitudes, particularly in the frequency ranges from 35 kHz to 45 kHz and from 70 kHz to 90 kHz. These ranges are thus a suitable to identify an unknown state as loaded or unloaded as they show the most conspicuous differences.

2.3.4 Time-Frequency Analysis

Although frequency analysis effectively reveals differences in the frequency content of signals, it does not provide information about how these frequencies vary over time. To address this gap, time-frequency analysis methods are employed.

Common frequency analysis such as the FT, while powerful for identifying the overall frequency content of a signal, does not provide temporal information about when these frequencies occur. To overcome this limitation, methods such as spectrograms and scalograms are utilized, both of which decompose signals into their component frequencies while also

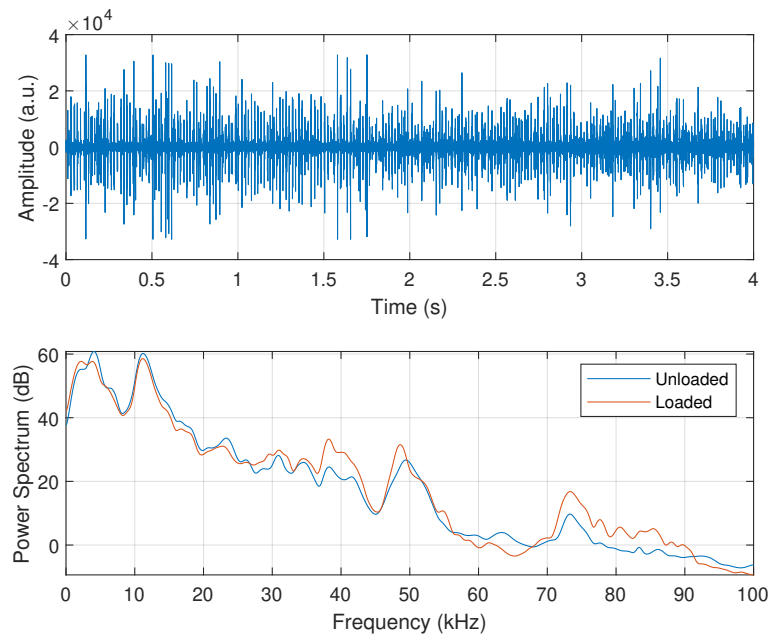


Figure 2.16: Above: Acoustic signal recorded from a bicycle hub, initially in an unloaded state for the first 2 s, followed by a loaded state from 2 s to 4 s. Below: The corresponding frequency spectrums for the unloaded and loaded states, illustrating the distinct acoustic differences of each condition.

considering time information [57, 58].

A spectrogram divides the signal into short, optionally overlapping segments. For each segment, the spectrum is calculated using the FT. A color plot is then used to visualize how the power within different frequency bands changes over time. Usually, the horizontal axis represents time, the vertical axis represents frequency and the color of each data point reflects the amplitude of a specific frequency at a particular moment.

Longer segments will yield better frequency resolution, ideal for identifying subtle frequency components. This comes at the cost of temporal precision due to less available data points within a segment. Conversely, shorter segments offer finer temporal resolution, perfect for capturing rapid changes within the signal but with reduced frequency detail. This trade-off is essential for tailoring the analysis to specific requirements, ensuring that significant events within the signal are captured adequately [59].

A scalogram uses wavelets instead of sine waves. Wavelets are not only localised in frequency but also in the time domain and come in different sizes and shapes, for example frequently used wavelets are Morlet or Haar wavelets and can be chosen appropriate to the application. Being localised not only in the frequency but also time domain makes them particularly useful for analysing non-stationary, erratic signals.

This method decomposes the signal by scaling and shifting the wavelets to match the signal's features at various resolutions. The result is a detailed representation of both time and frequency information, where each point in the scalogram corresponds to a specific time and frequency, with color representing the amplitude or power of the wavelet coefficients.

However, with the extra degrees of freedom, more computational power is necessary [60].

Identifying specific frequencies within a signal is crucial for various applications. Timely detection of frequency changes offers critical insights into machine performance, enabling the identification of operational states, such as gear transitions, and early detection of potential irregularities or faults. These observations are crucial for implementing predictive maintenance strategies and effective fault diagnosis. For instance, the time snippets of loaded and unloaded states in Figure 2.16 may not be directly identifiable with the corresponding spectrum plots. However, the spectrogram in Figure 2.17 provides valuable time-based information. Frequency analysis has successfully identified relevant frequency snippets, particularly effective for distinguishing loaded and unloaded states. These are notably within the frequency snippets from 35 kHz to 45 kHz and from 70 kHz to 90 kHz, where increases in amplitude are observed in the loaded state. This is visibly indicated in the spectrogram by an abrupt colour change at 2 s, demonstrating how frequency analysis can significantly aid in the precise identification of operational states in gear monitoring.

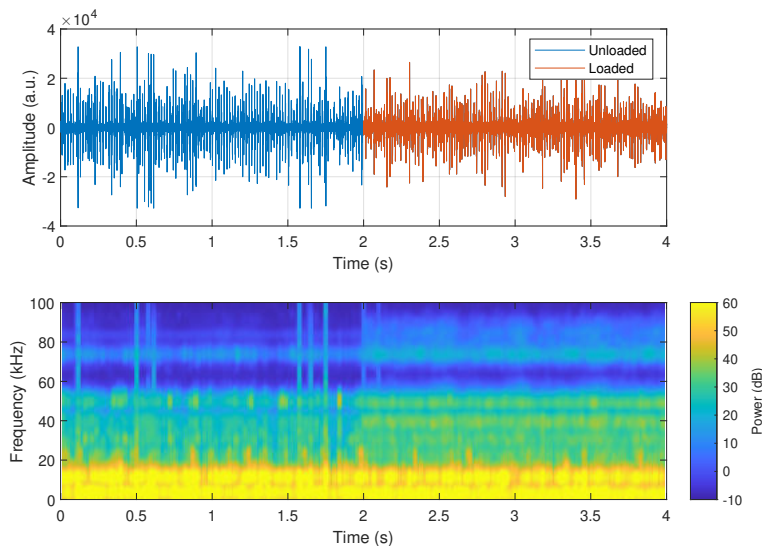


Figure 2.17: The top graph displays the amplitude of the gear signal over time for loaded (orange) and unloaded (blue) states. The bottom figure shows a spectrogram of the signal.

2.3.5 Feature Extraction

This section illustrates the feature extraction process and explains the input parameters, such as snippet length, which are essential for effective feature extraction. It aims to highlight the importance of defining appropriate features tailored to the specific application and the adaption of the parameters. An approach for adapting these parameters is subsequently proposed in Chapter 4.

In ultrasound-based process monitoring features are distinct attributes or characteristics derived from data, which help interpreting information. As an essential base for various subsequent analysis, they can be used to assess, monitor and predict the state of a process as, for example, input for various machine learning models. The features typically relate to characteristics of the ultrasound waves that interact with the materials or components being monitored. These characteristics can include for example amplitude, frequency, echo time delay or a combination of these.

There are several benefits, that come with careful executed feature extraction, enhancing the efficiency and accuracy of data analysis. The main benefits are [18, 51, 61]:

- Signal analysis and decision making can be enhanced through appropriate feature extraction as they capture essential information. Thus, these features provide a data foundation for predictive models.
- Noise and other interferences from environment and measurement system may corrupt the signal. Feature extraction simplifies these signals by isolating the essential characteristics relevant for monitoring and analysis. This makes it easier to interpret the data and draw meaningful conclusions about the state of the process or system being monitored.
- Voluminous and complex acoustic data poses a challenge for efficient processing. Feature extraction helps conserve storage and computational capacities, facilitating real-time monitoring. By focusing on key features, the computational load is lessened, allowing faster processing and immediate response to potential issues detected by ultrasound signals.

Feature extraction can be applied directly to the raw acoustic signal for an initial assessment or after data cleaning. This is illustrated in Figure 2.14.

Before the actual feature extraction takes place, appropriate features need to be identified or engineered. Designing features is the initial phase where domain knowledge is used to conceive new features or use standard features that might be useful for the task at hand. Ideally, all designed features would be relevant to the specific task, but this is not always the case. In fact, through a careful selection process, useful features can be identified that may not have been initially apparent through physical considerations alone. Feature selection then plays a crucial role in choosing the most relevant features from the predefined set, helping to reduce the feature space by eliminating redundant or irrelevant features.

Following [22, 34] before applying the feature extraction, the time-recorded data is divided into predefined time snippets. After identifying a suitable feature set, each snippet is analysed by calculating a sample for each feature using its corresponding feature function. Given an appropriate length for the time snippet, this approach maintains time accuracy while ensuring a sufficiently high number of data points for feature analysis.

Figure 2.18 illustrates this feature extraction process using an ultrasound signal. The top plot shows the signal's amplitude versus time over a duration of 1 s. The signal is divided into equal time intervals, each of length $\Delta t = 0.1$ s. These segments are highlighted by orange vertical lines. The middle and bottom plots display the extracted features from each segment, specifically the root mean square (RMS) and Partial Power, which basically measures the energy proportion within a specific frequency range of a signal [22]. The figure

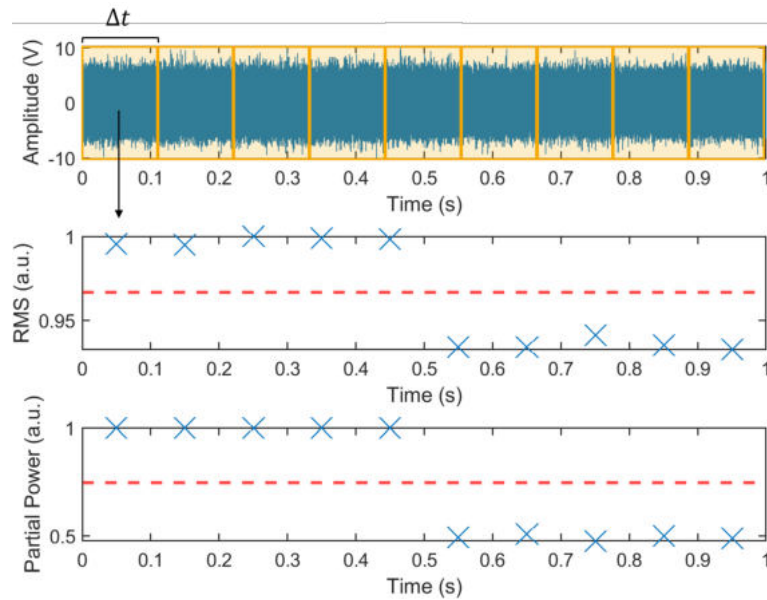


Figure 2.18: Upper plot: Segmentation of a ultrasound signal of a gearbox into equally spaced time intervals Δt . For $t < 0.5$ s the gearbox operates in Gear 1 and switches to Gear 2 at $t = 0.5$ s. The middle and bottom panels show the extracted features.

demonstrates a straightforward method to obtain feature values by directly applying the feature function to the regularly arrayed snippets. However, this process can be extended and adapted based on the application needs. For instance, to increase the time resolution and the density of feature values without decreasing the length of the time intervals, the snippets can be overlapped [34].

Before adjusting individual parameters for the features, it is essential to choose an appropriate snippet length, a general parameter that ideally remains consistent across all features for convenience in signal processing. The time snippets into which the recorded signal is segmented, serve as the basis for feature extraction. The number and duration of these snippets directly influence both the quantity of feature data points and the temporal resolution of the analysis.

Instead of directly applying the feature functions to each snippet, preceding mathematical operations can provide improved results. For instance, each snippet can be further divided into smaller subsnippets, from which feature subsamples are calculated. Applying statistical functions, such as calculating the mean of these subsamples, yields a representative feature

value for the original snippet. This method has been shown to sometimes enhance stability and reduces the impact of outliers or noise within the snippet, leading to more robust analysis.

The length of these snippets and methods of calculating the feature points should be adapted to the process and the intention of analysis. It depends on several factors, which in turn influence each other:

- **Computational resources:** Shorter snippets increase the number of feature samples, which can be computationally intensive and require more storage. Assessing the available computational power and storage capacity is essential to balance the snippet length with practical constraints.
- **Process dynamics:** For processes with rapid changes, shorter snippets are preferable to capture the transient characteristics accurately. Conversely, for slower processes, longer snippets may suffice and reduce the volume of data.
- **Feature stability:** Short snippets provide high time resolution however may lead to high variability in the extracted features due to noise or transient effects. Longer snippets can help in averaging out these variations, providing more stable and reliable features.
- **Analysis objectives:** The intended analysis or application of the features also dictates the snippet length. For instance, real-time monitoring applications require shorter snippets.
- **Signal characteristics:** The inherent properties of the acoustic signal, such as its frequency content and noise level, influence the choice of snippet length. Longer snippets adequately capture the slower variations in low frequency content or can help average out the noise, leading to more stable and reliable feature extraction

In conclusion, there is no general recipe of defining suitable snippet length, which makes feature extraction a rather application specific task.

Designing feature functions is a creative process, unconstrained by specific rules or limitations. A myriad of features have been developed across various disciplines, particularly in scientific time-series analysis. There are frameworks designed to bundle and calculate features simultaneously, such as the highly comparative time-series analysis (hctsa) framework [62]. It offers a comprehensive library of thousands of features specifically tailored for time-series data analysis. However, not all of these features are suitable for specific ultrasound process monitoring. For instance, online monitoring requires high performance, excluding computationally expensive features in such cases.

For designing new features it may be highly beneficial to consider the underlying physics of the process to deduce the interpretation and meaning of the features in the context of

the current application. This can provide insights into the behaviour of the system being monitored and help in diagnosing issues. Features that are well-suited to the application are more likely to capture the important aspects of the data, leading to better performance and more accurate monitoring.

A straightforward approach for optimizing features is to directly assess the correlation between the feature and the response variable. Analysing these correlations and dependencies has several benefits[51, 63]:

- Simplifies initial feature selection: Correlation assessment can quickly identify features that have a strong relationship with the response variable. This simplifies the initial selection of features that are likely to contribute to predictive power.
- Helps in feature engineering and understanding data: High correlation values can indicate which features are most relevant, guiding the process of feature engineering. You can focus on refining features with higher correlations, potentially saving time and effort.
- Reduces overfitting risk: By selecting features with strong correlations, you may reduce the risk of overfitting. Features that are weakly correlated with the response variable may add noise rather than useful information, leading to overfitting.

In ultrasound process monitoring, basic features have been established [22, 34, 64, 65], consistently showing good performance across various applications. These can be used as a standard feature set, complemented with features tailored to the specific application. An overview of frequently used features for ultrasonic signals is provided below.

Time-Domain Features

Time-domain features are extracted directly from the raw ultrasound signal. They provide insights into the characteristics of the monitored process without requiring complex transformations, making them straightforward to compute and interpret in real-time applications.

For an interpretation of the features in the time domain, consider an incident sound wave detected by a piezoelectric sensor. The intensity of the acoustic power J_i [W/m²] of that wave is given by

$$J_i = \frac{1}{2} \frac{p_i^2}{Z_m}, \quad p_i = \sqrt{2J_i Z_m},$$

where p_i is the sound pressure, and Z_m is the acoustic impedance of the medium through which the wave is travelling [20]. To calculate the sound pressure p_p in the piezoelectric

plate generated by an incoming sound wave of pressure p_i , consider the transmission coefficient from Equation 2.15 and Equation 2.16. This leads to:

$$p_p = T \cdot p_i = T \cdot \sqrt{2J_i Z_m} = \frac{Z_p}{Z_p + Z_m} \cdot \sqrt{2J_i Z_m},$$

where T is the transmission coefficient and Z_p is the acoustic impedance of the piezoelectric plate.

Following Equation 2.26, the electric signal measured at the piezoelectric plate, for small deformations, is proportional to the sound pressure p_p . With the proportional constant g_{33} , it follows:

$$U = g_{33} d \cdot p_p = g_{33} d \cdot \frac{Z_p}{Z_p + Z_m} \cdot \sqrt{2J_i Z_m}$$

If the material properties remain constant during the process, it follows:

$$U \propto \sqrt{J_i}$$

and since the recorded values of the signal are proportional to the voltage U , the signal is also proportional to $\sqrt{J_i}$.

- **Statistical Features:**

There are several features used to measure the statistical characteristics of the signal, including the RMS, the arithmetic mean, geomean, and the median.

- The RMS value is the square root of the average of the squared signal values over a specified period:

$$\sqrt{\frac{\sum_i^N x_i^2}{N}}. \quad (2.54)$$

Since $x_i^2 \propto U^2 \propto J$, the square of RMS value provides a comprehensive assessment of the acoustic power, making it particularly effective for distinguishing between states with varying energy levels. For example, defective states in materials can result in stresses or deformations that lead to higher energy emissions.

- The **arithmetic mean** corresponds to the average value of the signal amplitudes, however is highly sensitive to extreme data. It is useful when the signal data is symmetrically distributed without significant outliers.
- The **median**, and **geomean** in contrast are less sensitive to outliers and are useful for datasets with values that span several orders of magnitude, which is often the case with amplitude or power values in ultrasonic signals. It is less sensitive to outliers compared to the arithmetic mean, providing a more representative measure of central tendency for signals of varying ranges.

- **Peak Amplitude:**

The peak amplitude represents the highest value of the ultrasound signal amplitude

observed within a given time window. It indicates the strength of the reflected signal, which is often related to the size and nature of the defect or boundary. A higher peak amplitude generally suggests a more significant reflection, possibly from a larger or more severe defect.

- **Hjorth parameters:**

Caesarendra et al. [66] suggest that Hjorth parameters [67] can serve as effective features in condition monitoring for any time-domain signal, although they were initially used in medical electroencephalography (EEG) signals. Consider a signal $x = x_1, x_2 \dots x_N$ with the discrete derivative $x'_i = \frac{x_i - x_{i-1}}{\Delta t}$. These parameters have meaningful interpretations, particularly for EEG signals, where they help analyse brain activity patterns. However, they are also applicable to other types of time-domain signals by providing distinct values that capture different aspects of signal behaviour. They can effectively describe the dynamics and characteristics of these signals, making them useful for a wide range of applications:

- Hjorth Activity:

$$\text{act}(x) = \text{var}(x) = \sigma^2 = \frac{1}{N} \sum_{i=1}^N (x_i - \bar{x})^2,$$

with \bar{x} as the arithmetic mean value. Activity measures the variance of the signal, representing the power or the energy of the signal.

- Hjorth Mobility:

$$\text{mob}(x) = \sqrt{\frac{\text{act}(x')}{\text{act}(x)}}$$

Mobility measures the standard deviation of the signal's first derivative divided by the standard deviation of the original signal. It reflects the mean frequency or the speed of the signal's changes.

- Hjorth Complexity:

$$\text{com}(x) = \frac{\text{mob}(x')}{\text{mob}(x)}$$

Complexity is the ratio of the Mobility of the first derivative of the signal to the Mobility of the signal itself. It reflects the similarity of the signal to a pure sine wave, indicating how much the signal resembles a simple harmonic oscillation.

- **Combining features:**

Combining different features can lead to more robust and reliable results in ultrasonic signal analysis. Specifically, integrating features with complementary or opposite responses can enhance the robustness and accuracy of the analysis. For instance the **Crest Factor**, defined as the ratio of the peak amplitude of a signal to its RMS value. The crest factor can isolate changes in the signal's peakiness from general increases in energy. This means that even if the overall energy (as represented by RMS) increases,

the crest factor can still detect significant changes in the peak amplitude. This can be also described as self nominating nature. In systems where the overall energy can vary due to normal operational conditions (e.g., changes in load, speed, or operating environment), the crest factor helps maintain sensitivity to fault conditions.

Frequency-Domain Features

Frequency-domain features are obtained by transforming the time-domain signal into the frequency domain, typically using the FFT. In the following consider a signal $x[n] = x_1, x_2 \dots x_N$ and its FFT \hat{x} with \hat{x}_j corresponding to the frequency f_j .

- **Statistical Features:**

Many general statistics can be extracted from the FFT:

- Mean frequency:

$$MF(\hat{x}) = \frac{1}{N} \sum_{j=1}^N \hat{x}_j \quad (2.55)$$

The frequency mean indicates the average frequency component in the signal.

- Mean Square Frequency:

$$MSF(\hat{x}) = \frac{1}{N} \sum_{j=1}^N \hat{x}_j^2 \quad (2.56)$$

The mean square frequency spectral provides a measure of the signal's power.

- Root Mean Square Frequency (\hat{x}_{RMS}):

$$\hat{x}_{RMS} = \sqrt{\frac{1}{N} \sum_{j=1}^N \hat{x}_j^2} \quad (2.57)$$

The root mean square frequency reflects the effective power of the signal.

- Root Variance Frequency:

$$RVF(\hat{x}) = \sqrt{MSF(\hat{x}) - MF(\hat{x})^2} \quad (2.58)$$

The root variance frequency represents the variability around the mean frequency, indicating signal dispersion.

- Spectral Centroid:

$$\hat{x}_c = \frac{\sum_{j=1}^N \hat{x}_j f_j}{\sum_{j=1}^N \hat{x}_j} \quad (2.59)$$

The spectral centroid corresponds to the center of mass of the spectrum, calculated as the weighted average of the frequencies present in the signal. It

indicates where the majority of the signal's power is concentrated in the frequency domain. Shifts in the spectral centroid can indicate changes in material properties or the presence of defects.

- Spectral Skewness:

$$skew(\hat{x}) = \frac{1}{\sigma^3} \frac{1}{N} \sum_{j=1}^N (\hat{x}_j - \bar{\hat{x}})^3 \quad (2.60)$$

The spectral skewness measures the asymmetry of the spectral distribution.

- Spectral Kurtosis:

$$kurt(\hat{x}) = \frac{1}{\sigma^4} \frac{1}{N} \sum_{j=1}^N (\hat{x}_j - \bar{\hat{x}})^4 \quad (2.61)$$

The spectral kurtosis measures the tailedness of the spectral distribution.

- **Partial Power:**

$$\frac{\sum_{f=f_1}^{f_2} \hat{x}_f^2}{\sum_{f=f_{start}}^{f_{end}} \hat{x}_f^2},$$

where f_1 and f_2 are the boundaries of the current range and f_{start} and f_{end} are the boundaries of the total range.

The partial power feature is defined as the ratio of energy or power within a designated frequency range to the total energy. Multiple frequency bands can be defined, which may be overlapping or separate, and tailored to the specifics of the monitoring process. The placement of these frequency boundaries is critical. Normalizing the energy within these bands to the total energy ensures that this feature remains consistent and effective across different scenarios [22].

- **Peak Frequencies:**

$$f_{peak} = f \max(\hat{x})$$

The peak frequency is the frequency at which the power spectrum is highest. To extract multiple peak frequencies, first identify the highest peak and define a dead area around it, setting these values to zero. Then, find the next highest peak in the modified spectrum. Repeat this process, each time defining a new dead area around the latest peak, to sequentially extract multiple significant frequency components.

- **Combination:**

Combining the centroid frequency f_c and the peak frequencies f_p , the feature **weighted peak frequency** $f_w = \sqrt{f_c \cdot f_p}$ [22] captures both the overall distribution of the frequency spectrum via the centroid and the prominent components via the peaks. This combination ensures that the feature is sensitive to both broad and specific changes in the signal. The centroid frequency tends to be more stable and less

susceptible to noise compared to individual peak frequencies. By incorporating the centroid frequency, the weighted peak frequencies inherit this stability, reducing the overall variability of the feature.

2.3.6 Feature Selection

One of the primary objectives of CM is to save time and reduce costs by accurately predicting and identifying the state of the monitored system. This allows for timely interventions to prevent downtime or more severe issues.

For example, studies [68–70] have demonstrated that accurate and reliable CM systems can enhance the cost-effectiveness of wind turbines in energy production. According to the studies, CM systems can substantially reduce life cycle costs, particularly in the monitoring of gearboxes and generators. However, achieving accurate and reliable diagnostics is crucial for effectively applying CM systems and the success of wind turbine condition monitoring depends heavily on the selection of appropriate signal processing and data analysis techniques.

An effective and reliable condition monitoring system optimizes hardware maintenance cycles while ensuring long-term stability by minimizing the frequency of software updates. Central to this is developing a robust initial model with a solid foundation and strong predictive capabilities, which is supported by a suitable preselection of features.

To achieve this, consider the following points:

- **Computation Time:** Assess how time-consuming the feature is to calculate and if the application requires real-time capability.
- **Domain knowledge:** Initially evaluate the potential importance of the feature for the application. Physical domain knowledge is useful for predicting feature performance.
- **Correlation to other features:** A robust model should be free from bias, which can be introduced by using too many features of the same nature. Avoid features that are similar and show high correlations. Useful tools for this include correlation matrices, dendrograms, or hierarchical trees with clustering algorithms.

In addition, there are several common feature selection algorithms which can be categorised in three groups [71]:

- **Filter Type Methods:** These methods use statistical techniques to evaluate the relationship between each feature and the target variable independently of any machine learning model. Being model-agnostic they are simple, fast, and computationally efficient.
- **Wrapper Methods:** These methods evaluate the usefulness of feature subsets by actually training and testing a specific machine learning model. These methods consider feature interactions and can lead to higher accuracy since the selection is based on model performance, however computationally expensive.

- **Embedded Methods:** These methods perform feature selection as part of the model training process. The algorithm inherently selects the most relevant features while building the model. More efficient than wrapper methods since feature selection and model training are combined. They often achieve good performance by considering feature dependencies.

- **Filter Methods:**
 - **Analysis of Variance (ANOVA):** Used to analyze the data distribution across different groups. It tests the null hypothesis that the data is drawn from a normal distribution with a single mean against the alternative hypothesis that the data is drawn from distributions with different mean values for each group. The corresponding F-value is calculated, and the associated p-value is used to rank the features. Applied to feature selection, a feature with a high score indicates a clear separation of mean values for each label. This suggests that the feature has a strong impact on the response variable, making it suitable for machine learning algorithms that aim to cluster and categorize labels. However, it is important to note that ANOVA does not account for the distribution around the individual mean values for each group.

 - **The Kruskal-Wallis test:** Assumes that all samples originate from populations with the same continuous distribution, except for possible differences in location due to group effects. Additionally, it requires that all observations are mutually independent. Unlike ANOVA, which uses the actual numeric values of the data, the Kruskal-Wallis test computes the test statistics based on the ranks of the data. To determine ranks, the data are ordered from smallest to largest across all groups, and each value is assigned a rank based on its position in this ordered list.

 - **The Chi-Square Test:** Used to determine whether there is a significant association between two categorical variables. It tests the null hypothesis that there is no relationship between the variables, against the alternative hypothesis that there is a relationship. The test compares the observed frequencies in each category to the frequencies that would be expected if there were no association between the variables. To apply the test to continuous variables or features they need to be discretized or binned. The test statistic, called the Chi-Square statistic, is calculated by summing the squared differences between the observed and expected frequencies, divided by the expected frequencies. The resulting value is then compared to a critical value from the Chi-Square distribution to determine the p-value, which indicates the significance of the observed association.

 - **R-squared:** Measures the proportion of variance in the dependent variable that can be predicted from the independent variables.

- ReliefF: Evaluates the importance of features based on how well they differentiate between instances that are near to each other, considering both nearest neighbors of the same class and different classes to estimate the feature weights.
 - Laplacian Score: Evaluates feature importance by preserving the local structure of the data, using the Laplacian matrix of the graph formed by the data points to score features.
 - Infinite Feature Selection (Inf-FS): Uses an infinite path approach to select features based on their importance, scoring features by their ability to connect different samples in an infinite random walk model.
 - Minimum Redundancy Maximum Relevance (mRMR): Selects features that are highly relevant to the target variable but minimally redundant among themselves, using mutual information to measure relevance and redundancy.
- **Wrapper Methods:**
 - Fitted Discriminant Analysis (FDA): Used for classifying observations into pre-defined groups based on predictor variables. It involves finding a set of linear combinations of the predictor variables or features that best separate the groups. These linear combinations are identified to maximize the distance between the means of the groups and minimize the variation within each group. FDA then ranks the features that contribute most to these linear combinations, thereby distinguishing between the groups. Unlike ANOVA, FDA considers the distribution within each group, providing a more nuanced analysis. However, this method does not assess the performance of features individually; instead, it evaluates their effectiveness in combination with each other.
 - Neighbourhood Component Analysis: Learns a feature weighting by optimizing a stochastic neighbour assignment objective, finding a linear transformation of the input features that maximizes the accuracy of nearest neighbour classification.
 - **Embedded Methods:**
 - Classification Tree: Uses decision tree models to evaluate the importance of features, measuring feature importance based on how often a feature is used to split the data and how much it improves the model's performance.
 - Classification Ensemble: Combines multiple classification models to improve the robustness and accuracy of feature selection, evaluating feature importance by aggregating the importance scores from different models in the ensemble.
 - Random Forest Classification Tree: An ensemble of decision trees where each tree is trained on a random subset of features and data samples, measuring feature importance by averaging the decrease in impurity (e.g., Gini impurity or entropy) brought by each feature across all trees.

2 Theoretical Background

Choosing the right feature selection method depends on various factors including the nature of the dataset, the complexity of the model, computational resources, and the specific objectives of the analysis.

3 Experimental Setup

This chapter introduces the experimental setups that serve as the foundation for the development of the advanced techniques proposed for ultrasound process monitoring. While the techniques, discussed in Chapter 4, are designed for broad applicability, they were specifically developed to address challenges encountered during the monitoring of these setups. To provide the necessary context for understanding the methods, the experimental setups are described here before delving into the theoretical framework of the advanced techniques.

The experimental setups detailed in this chapter are used for validating the advanced signal analysis techniques subsequently discussed. These techniques are applied to four distinct processes, each described sequentially in this chapter, with a focus on the selection and integration of sensor systems.

In the following section, a gearbox demonstrator, equipped with passive ultrasonic sensors is examined. It serves for the validation of the proposed feature selection technique. In this setup, structure-borne noise are analysed with the aim of developing a robust classification model for distinguishing between different gears.

Next, the setups, the rheometer and the thermoplastic resin transfer moulding (T-RTM), process are presented successively. For both setups the same sensor and measurement system are utilized. This consistency is intentional, as the rheometer experiments are conducted under controlled laboratory conditions, primarily serve as validation tests to apply their findings to the more industrially relevant T-RTM experiments. Thus, the setup is specifically tailored and optimized for the T-RTM process, and this configuration is applied to the other experiment.

For the vacuum assisted process (VAP) experiment, the use of any ultrasonic monitoring system was not necessary, as it was specifically designed for optical monitoring to validate the global reconstruction method. Therefore, ultrasonic sensors were deemed redundant and were replaced by optical measurements, effectively simulating virtual sensors.

Finally, this chapter provides a detailed description of the ultrasound (US) data acquisition measurement system utilized for the rheometer and T-RTM processes. This system is described in more detail due to its capability to perform more complex active measurements, where the sensors function not only as receivers but also as transmitters, in contrast to the passive measurements used in the gearbox experiments. The chapter also discusses the process of determining optimal sensor placement to enhance signal clarity, streamline signal

processing, and improve overall outcomes. Focusing on active sensors applied to multilayer structures with planar interfaces, it concludes with a graphical method for identifying the most effective sensor placement.

3.1 Gearbox Test Bench

It is useful to investigate new developed algorithms in a controlled environment with clear defined operation states.

For this purpose a gear demonstrator was developed with the experimental setup depicted in Figure 3.1, which is located at a showroom, instead of noisy industrial environments. Thus the gear demonstrator serves as the ideal test object to investigate and test the developed methods for acoustic monitoring.

Within the controlled laboratory environment, this setup offers the advantage of maintaining stable parameters, such as a constant temperature, over extended periods. This allows for description of degradation effects, specifically wear and tear, without the interference of larger, unpredictable incidents that might occur in an industrial environment.

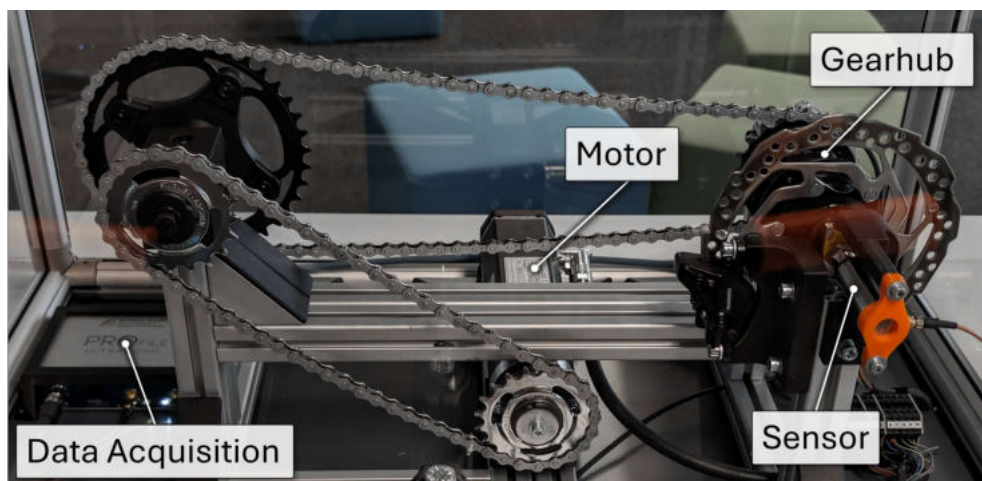


Figure 3.1: Experimental setup of the the gear demonstrator, including the gearhub, motor, data acquisition system, and sensor. The motor drives the system at 1.4 R/s, with power transmitted through chains and gears. The Shimano Nexus 3-speed internal geared hub SG-3D55 is monitored using a Vallen VS12-E sensor and the PROfile Ultrasonic acquisition system provided by BCMtech.

The gear under investigation is the Shimano Nexus 3-speed internal geared hub SG-3D55 [72]. It is designed for a wide range of applications, including bicycles and light industrial machinery, making it a versatile test subject. With three internal gears, this hub provides a simple yet sufficiently complex system to test various acoustic monitoring techniques effectively and should serves as an example and as a foundational model for further investigations into other gear mechanics.

The gear hub is driven as part of a structure involving different gears, modelled after bicycle mechanics. The initial rotational frequency is provided by a motor, PLG 63 EP from Dunkermotoren [73], and is maintained constantly at 1.4 Hz. Power transmission occurs through chains and gears. Since the small gears all have 20 teeth, the gear hub is driven at the same rate as provided by the motor.

The Shimano Nexus 3-speed internal geared hub SG-3D55 translates the input rotational speed into three distinct output speeds, corresponding to its three gears. When the driven rotational frequency is 1.4 Hz, the output speeds for each gear are listed in Table 3.1.

Table 3.1: Gear Ratios and Corresponding Rotational Speeds

Gear	Gear Ratio	Rotational Frequency (Hz)
1st (Low Gear)	0.74:1	1.036
2nd (Direct Drive)	1:1	1.4
3rd (High Gear)	1.36:1	1.904

Sensor Selection

For the gearbox test bench a commercial data acquisition system, the PROfile Ultrasonic [74], was used provided by BCMtec.

Selecting the right AE sensor and mounting it in the optimal position are crucial for meeting these requirements and accurate monitoring. Proper placement maximizes signal capture and minimizes interference, leading to reliable fault detection and effective maintenance.

Although the input shaft maintains a constant rotational speed across different gears, the acoustic signals change primarily due to the varying gear ratios. Each gear ratio affects how the load and stress are distributed among the gears, altering the dynamics of gear meshing and the interaction between the components of the gearbox. These changes lead to distinct patterns in the acoustic emissions, with different gears producing unique frequency signals. Thus, the sensor should be positioned close to the area where the gears mesh, typically on the outer housing near the sun gear, planet gears, or ring gear. This location allows the sensor to capture the acoustic signals generated by the interaction of the gear teeth, which are critical for detecting the current gear.

This placement ensures that the sensor captures the critical acoustic emissions related to gear shifts, without picking up too much of the background emissions that remain unchanged across gear switching and thus do not contribute to the classification.

To achieve this, the sensor was mounted on a screw axial to the gear hub as shown in Figure 3.1. To maintain consistent contact pressure, a size-adjustable fixture was designed for the sensor. The pressure can be adjusted using two screws. To ensure uniform coupling

3 Experimental Setup

of the ultrasonic waves, Korasilon Paste, a silicone lubricant from Kurt Obermeier GmbH, was used as the coupling agent between the gear hub and the sensor.

The focus of this investigation is to develop a low-maintenance model that is robust over time, rather than an optimized model that performs extraordinarily well with the test data but tends to deteriorate over time without thorough maintenance. To achieve long-term reliability, algorithm optimization was prioritized over sensor selection. While the choice of sensor is important, the goal was to create an algorithm adaptable across different sensors, including those that may not be specifically optimized. Therefore, two available sensors are compared.

Two sensors were available within the research group: the Vallen S12-E and the Vallen VS45-H, whose specifications are compared in Table 3.2. The frequency response of the sensors are illustrated in Figure 3.2 and Figure 3.3, respectively. The horizontal axis represents the frequency of the acoustic emission signal and vertical axis shows the amplitude of the sensor's response in decibels (dB) relative to 1 V per μbar . This is a measure of how sensitive the sensor is at detecting signals at different frequencies.

The Vallen S12-E operates within a frequency range of 7 kHz to 58 kHz, making it specialized for detecting low-frequency acoustic emissions. Its frequency response shows a drop below -75 dB from 15 kHz to 20 kHz, but it remains stable between 21 kHz and 45 kHz, with a peak at 12 kHz reaching -62 dB.

This characteristic is particularly beneficial for detecting large, low-frequency events, such as those associated with low gear meshing frequencies and potential structural issues within the gear hub. This sensor's focus on low frequencies also makes it more robust in environments outside of controlled settings, where high-frequency noise could interfere with signal clarity.

Table 3.2: Comparison of Vallen S12-E and Vallen VS45-H Ultrasound Sensors

Specification	Vallen S12-E	Vallen VS45-H
Frequency Range (fPeak) [kHz]	7 to 58 (12)	20 to 450 (280)
Operating Temperature [°C]	-5 to +85	-20 to +100
Capacity [pF]	159	270
Weight [g]	154	36
Size (D x H) [mm]	20.3 x 59.0	20.3 x 22.0

Conversely, the Vallen VS45-H has a broader frequency range from 20 kHz to 450 kHz, enabling it to capture both low and high-frequency signals. The frequency response dips below -75 dB around 120 kHz and 230 kHz but maintains consistent sensitivity above -65 dB

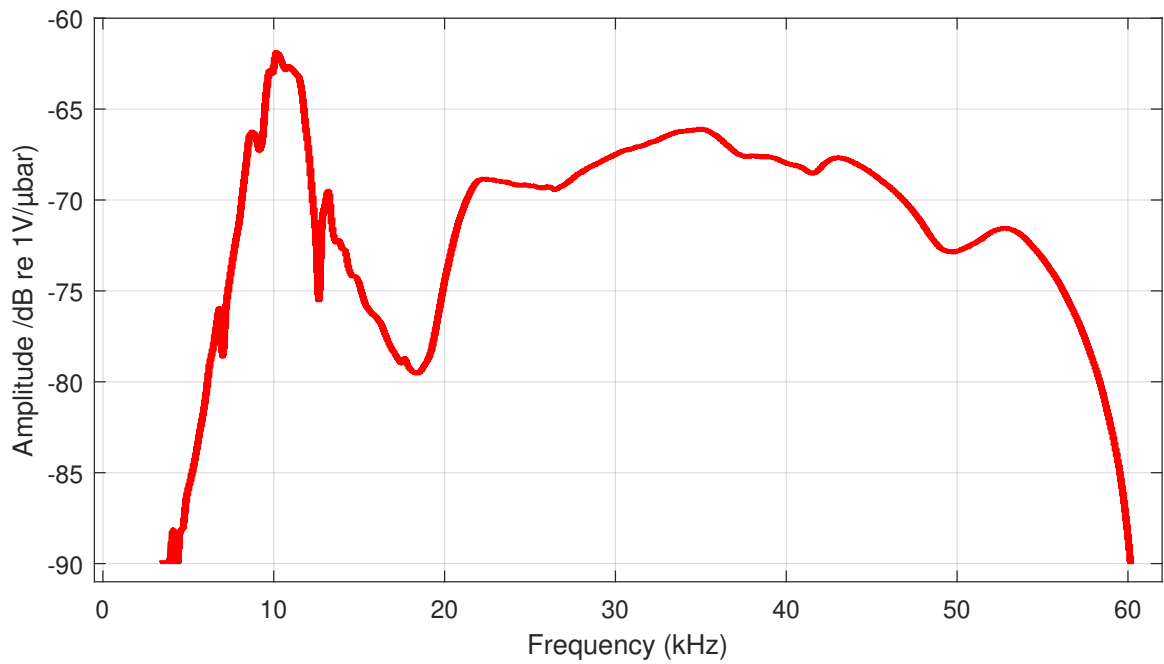


Figure 3.2: Frequency response of the Vallen S12-E sensor. The data is retrieved from the datasheet provided by Vallen[75].

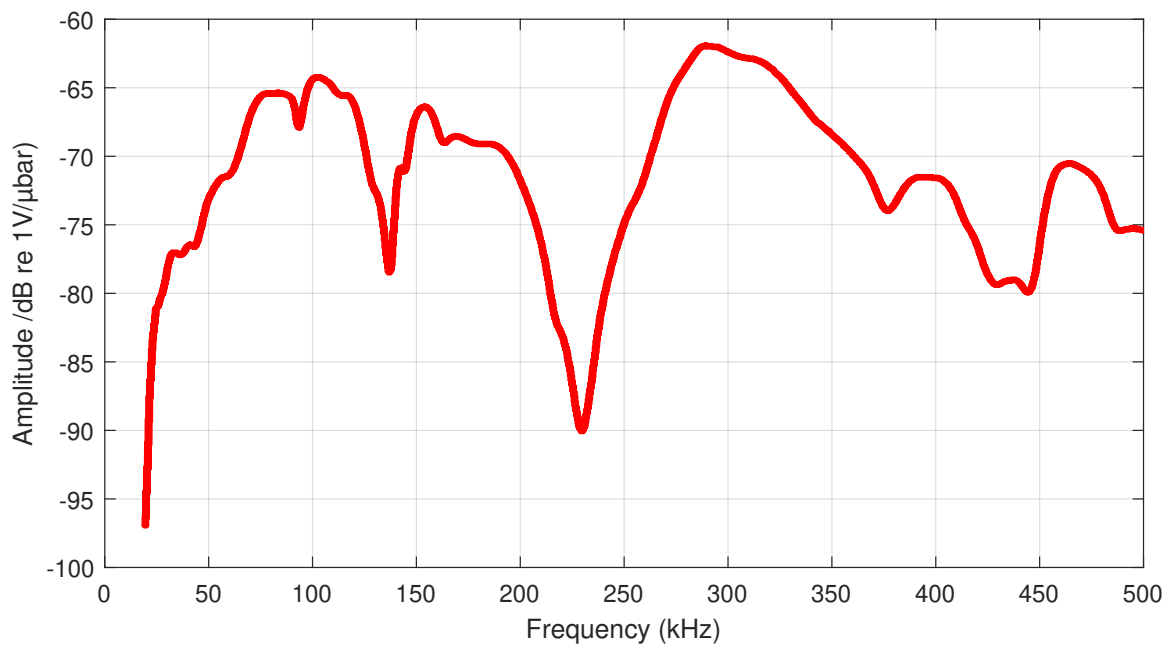


Figure 3.3: Frequency response of the Vallen VS45-H sensor. The data is retrieved from the datasheet provided by Vallen[76].

3 Experimental Setup

around 100 kHz and between 270 kHz and 330 kHz, with a peak at 280 kHz at -62 dB. This broad range allows the VS45-H to detect a wide spectrum of signals, including subtle high-frequency emissions that might indicate early-stage wear or minor defects, making it highly versatile for a variety of applications.

The choice between these sensors depends on which frequency range is most critical for distinguishing operating states of the gear hub and which range might be disruptive and should be avoided. If the frequency range of interest can be well-defined, a specialized sensor, like the Vallen S12-E, with its sensitivity range tailored to the important frequencies could be beneficial. However, if a broader monitoring capability is desired, the Vallen VS45-H may be more suitable, albeit potentially requiring subsequent digital filtering to focus on the relevant frequency range.

Without prior knowledge of the specific frequency range of interest, each sensor is installed to record a test data set with the setup running in Gear 1 and Gear 2. This test data provides a foundation for running several tests, including a comparison of the frequency spectra and prediction accuracy of machine learning models.

For effective classification, it is advantageous that the frequency spectra of different gears show clear distinctions. Significant spectral differences between the gears enhance the classifier's ability to identify which gear is operating based on the acoustic emissions. If the spectral differences are minimal, the classifier may struggle to differentiate between gears, leading to lower accuracy.

One method to evaluate a sensor's ability to distinguish between different gears is by comparing the spectra measured for each gear. The greater the differences between these spectra, the more likely it is that features and predictive models can identify distinguishing characteristics between the gears. To quantify this distinction, the RMS of the differences between the spectra of the two gears is calculated. The spectra and the absolute difference between these are illustrated in Figure 3.4. A higher RMS value indicates greater overall spectral differences, which can improve the classifier's performance by providing clearer features for distinguishing between gears.

The Vallen S12-E sensor achieved a higher RMS value and shows especially in the frequency range from 15 kHz to 40 kHz a higher separation between the spectra compared to the Vallen VS45-H.

To further validate the suitability of the sensors, a simple classification model is developed using the standard features listed in Table 3.3.

Since the model needs to quickly identify the current gear, the frame size from which one value per feature is calculated and classified should be less than 100 ms. An initial sweep through several machine learning models based on 50 ms frame sizes identified the support vector machine (SVM) with a linear kernel as the most suitable model, achieving the highest accuracy.

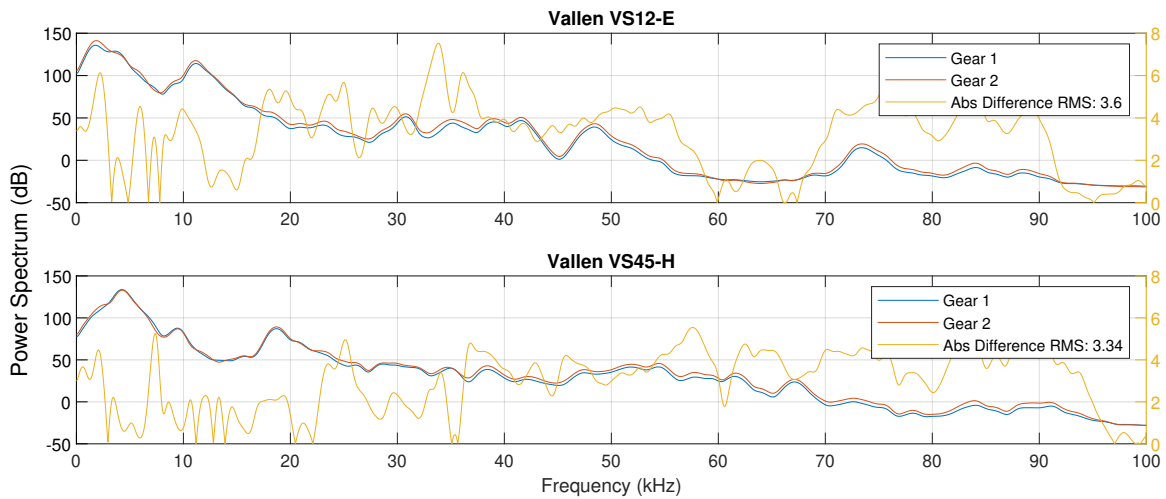


Figure 3.4: Comparison of the power spectra for Gear 1 and Gear 2 using the Vallen VS12-E (top) and Vallen VS45-H (bottom) sensors. The blue and red lines represent the power spectra for Gear 1 and Gear 2, respectively. The yellow line shows the absolute difference between the spectra of Gear 1 and Gear 2. The RMS value of the absolute difference is 3.6 for the VS12-E sensor and 3.34 for the VS45-H sensor. The VS12-E sensor demonstrates clearer distinctions between the gears, as indicated by the higher RMS difference.

Table 3.3: List of standard features.

Standard Frequency Features

MeanFrequency	BandPower
MedianFrequency	OccupiedBandwidth
PeakAmplitude	PowerBandwidth
PeakLocation	

Standard Time Features

Mean	RMS
StandardDeviation	ClearanceFactor
CrestFactor	ImpulseFactor
PeakValue	ShapeFactor
SINAD (Signal-to-Noise and Distortion ratio)	SNR (Signal-to-Noise Ratio)

To refine the optimal frame size range, additional tests were conducted using the SVM model, varying the frame sizes, as illustrated in Figure 3.5. The VS12-E sensor consistently showed higher accuracy than the other sensor across all frame sizes. The accuracy of the VS12-E sensor starts relatively high and increases steadily as the frame size increases, eventually stabilizing around 93 % as the frame size approaches 0.1 s. The accuracy of the VS45-H sensor shows a slower increase and stabilizes around 80 %, with a less pronounced improvement as the frame size increases compared to the VS12-E.

The increase in accuracy with increasing frame sizes can be attributed to the larger amount of data available for feature extraction in each frame. Larger frame sizes provide more data points, leading to more reliable and stable feature values. This stability enhances the

3 Experimental Setup

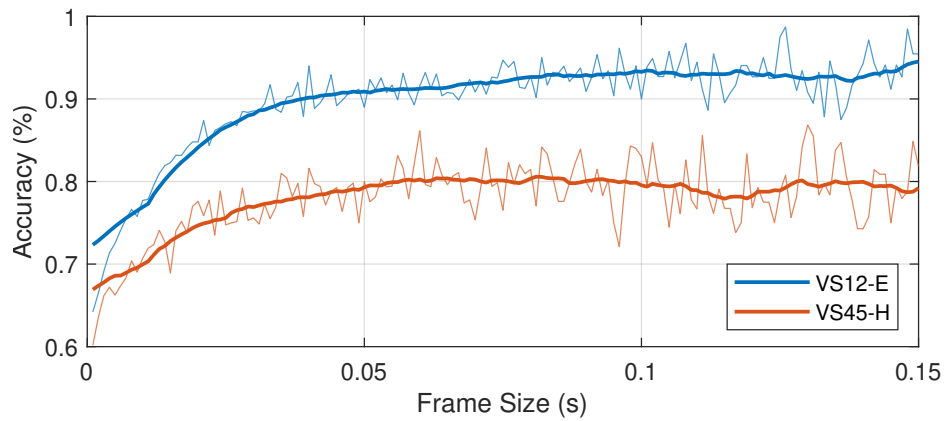


Figure 3.5: Accuracy comparison of gear classification using the Vallen VS12-E and Vallen VS45-H sensors across different frame sizes calculated 1 ms steps. The blue line represents the accuracy achieved with the VS12-E sensor, while the orange line represents the accuracy with the VS45-H sensor. The more transparent lines show the actual data points, whereas the full-color lines represent the moving mean of the data.

classifier’s ability to make accurate decisions. However, it is important to balance frame size with the need for real-time responsiveness, as larger frame sizes may introduce delays in classification.

The VS12-E sensor reaches a high accuracy level of around at 0.1 s. This frame size provides a reasonable trade off between performance and accuracy capturing enough data to ensure stable and reliable feature extraction without introducing significant delay or computational overhead. In addition it showed clearer distinctions between the spectra for Gear 1 and Gear 2, expressed by a slightly higher RMS value.

Based on these test further work was conducted using the Vallen VS12-E with a frame size of 0.1 s .

3.2 Setup for Rheological Investigations

To enable simultaneous acquisition of rheological and acoustic measurements, the MCR 302 rheometer (Anton Paar GmbH, Austria) was equipped with an ultrasonic measurement system developed at the University of Augsburg [34]. The monomer ϵ -caprolactam (AP-NYLON®) from L. Brüggemann GmbH & Co. KG (Germany) was used as the starting material for the polymerization to polyamid 6, with hexamethylene-1,6-dicarbamoyl-caprolactam (BRUGGOLLEN® C20P from L. Brüggemann GmbH & Co. KG, Germany) serving as the activator of the reaction. The polymerization reaction is described in more detail in [77, 78]

Figure 3.6 shows the test head of the rheometer. The sample is placed between two plates. To ensure an ideal polymerization reaction, an inert nitrogen environment is created using a protective hood.

The lower plate, whose temperature can be controlled via an integrated Peltier element and cooling water system, is statically installed in the rheometer.

The upper plate oscillates in the form of rotational oscillation around its own axis for measurement. This allows the viscosity of the sample to be determined with the aid of prior calibration.

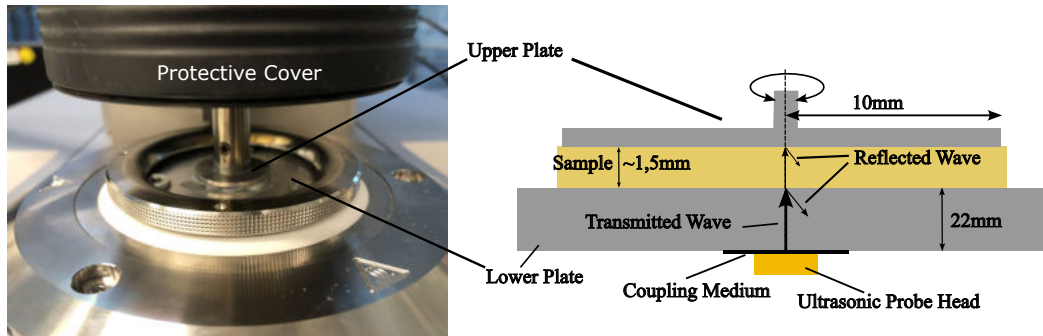


Figure 3.6: Left: Photography of the rheometer setup. Right: Schematic drawing of the setup. A sample is placed between the upper and lower plate. The ultrasonic sensor is mounted to the lower plate [79].

For the ultrasonic measurement, as shown in Figure 3.7, an ultrasonic probe head was mounted to the underside of the lower plate using a coupling medium (KORASILON® medium-viscosity paste, Kurt Obermeier GmbH & Co. KG). The sensor holder was adapted to the geometry of the rheometer and the probe head, and it was additively manufactured from stainless steel.

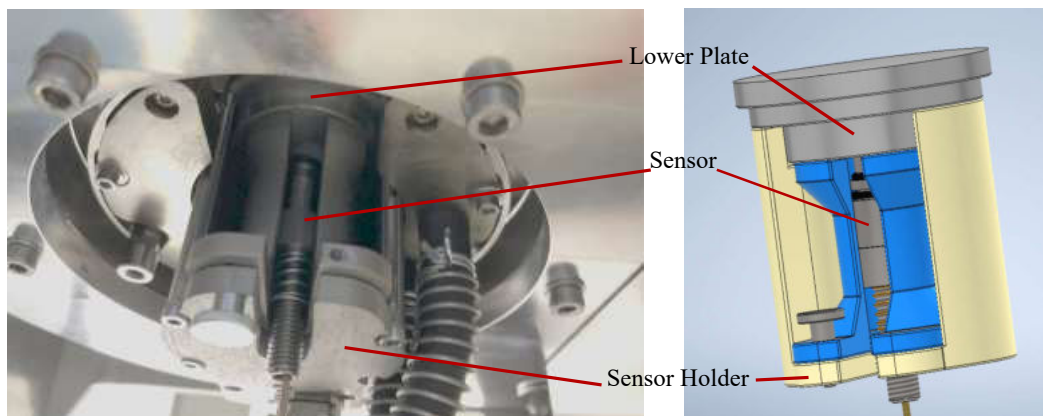


Figure 3.7: Left: Photography of the sensor holder mounted to the rheometer sample plate compared to the corresponding CAD-Model (right) of the sensor holder [79].

At the beginning of the measurements, the rheometer was heated to 120°C and maintained at this temperature for 10 min to achieve a stable temperature in the measurement setup. The sample, in the form of solid pellets, was then positioned between the plates and melted. To start the measurement, the upper plate was moved to a gap distance of about 1.5 mm, which was automatically adjusted during the measurement to maintain continuous contact

with the sample throughout the polymerization [79].

Both viscosity and ultrasonic measurements were then initiated, with the rheometer's temperature being ramped up to 160°C at a rate of 20 K/min. The oscillation of the upper plate was controlled via the Rheocompass software (Anton Paar GmbH, Austria) and was performed at a frequency of 1 Hz, with a shear deformation logarithmically decreasing over time from 10 % to 0.1 %.

To monitor the ongoing polymerization using US data a relationship between viscosity and the state of polymerization needs to be determined.

In [80], research was conducted using the same rheometer and settings to explore the relationship between the residual monomer content, indicating the stage of polymerization, and the viscosity. The conversion was determined by analysing the residual ϵ -caprolactam in quenched polyamid 6 samples using a method developed in [78], as shown in Table 3.4.

The conversion was measured in 100 s intervals from 250 s to 650 s after the start of the

Table 3.4: Conversion at different times after the start of polymerization [80].

Seconds	Conversion (%)
250	63.93
350	91.84
450	98.17
550	98.40
650	98.42

measurement. It was found that after 250 s, the conversion rate was 64 %, and it rapidly increased to 91 % and 98 % at 350 s and 450 s, respectively. Considering a maximum conversion rate of 99 %, the polymerization process converges and reaches a plateau around 450 s.

This setup and procedure ensure the accurate capture of both rheological and acoustic data allowing for a comprehensive analysis of the polymerization process and the monitoring of material changes through variations in the ultrasonic signal.

3.3 Infusion and Injection Processes: VAP and T-RTM

The VAP is a technique used in composite manufacturing where a vacuum is applied to a dry fibre preform to draw resin into the preform, ensuring complete impregnation.

The T-RTM process involves injecting a polymer melt into a mould containing a dry fibre preform. The polymer is driven by a pressure gradient, filling the mould and impregnating the fibre preform.

The VAP and T-RTM are both advanced manufacturing processes used in composite material production.

VAP involves infusing resin into a fiber preform under vacuum, which ensures a high-quality finish with minimal voids, while T-RTM focuses on injecting thermoplastic resin into a mold containing the fiber preform, allowing for quicker production and recyclability. The main difference lies in the type of resin used and the method of infiltration, with VAP emphasizing vacuum-assisted resin flow and T-RTM using pressure-driven injection. In the following both processes are described in more detail.

Vacuum Assisted Process (VAP)

The VAP is a vacuum infusion technology initially developed by EADS Deutschland GmbH for industrial applications. Unlike other vacuum infusion methods, such as Vacuum Assisted Resin Infusion (VARI), VAP offers superior reproducibility, uniform part thickness, and low porosity in composite parts [81].

The VAP setup, illustrated in Figure 3.8, involves a single-sided mould covered with a dry-fibre textile preform. Auxiliary materials such as peel ply, perforated release film, and flow media are used to facilitate resin distribution on the preform's surface and ensure easy release after curing. The entire layup is sealed with a semi-permeable membrane (VAP membrane), which allows degassing over the whole surface while preventing resin penetration. The setup is then covered with a vacuum film and sealed to the mould. Applying a vacuum defines the preform cavity and compacts the preform, creating a pressure gradient between the inlet and the cavity that drives the resin into the preform [82].

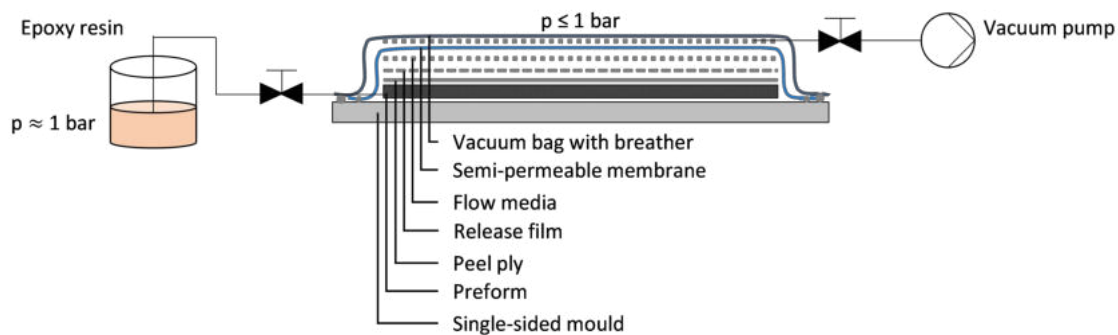


Figure 3.8: Vacuum assisted process - materials and setup according to [83].

Darcy's law, which describes the flow of fluids through porous media [84], can be used to characterize infusion processes. Flow front propagation, a key aspect of these processes, serves as a critical parameter for effective process monitoring and quality control. For setups with transparent vacuum bags, visual inspection methods, such as cameras, can be used to monitor the flow front effectively.

However, in cases involving opaque inserts, complex sub-structures made of different materials, or closed-mould applications, visual inspection is not feasible. In such scenarios,

3 Experimental Setup

non-visual inspection techniques become essential to ensure accurate monitoring and control of the flow front.

In this study, a camera-based flow front detection method was employed as a reference technique for validating the reconstruction algorithm. To this end, the conducted infusion test primarily served to generate a reference data set for assessing the accuracy of the developed flow front model. To maintain consistency and comparability, flow front monitoring of the VAP process was also carried out using the same camera-based inspection method. The material to be impregnated was a carbon fiber preform with dimensions of 300×600 mm, placed on a transparent glass plate as part of the VAP setup (see Figure 3.9). Resin EPIKOTE RIMR135 and curing agent RIMH1366 (HEXION) were used, with the curing process carried out at room temperature.

The visible contrast between the wetted and non-wetted areas of the preform allowed for clear detection of the flow front propagation, as illustrated on the right side of Figure 3.9.

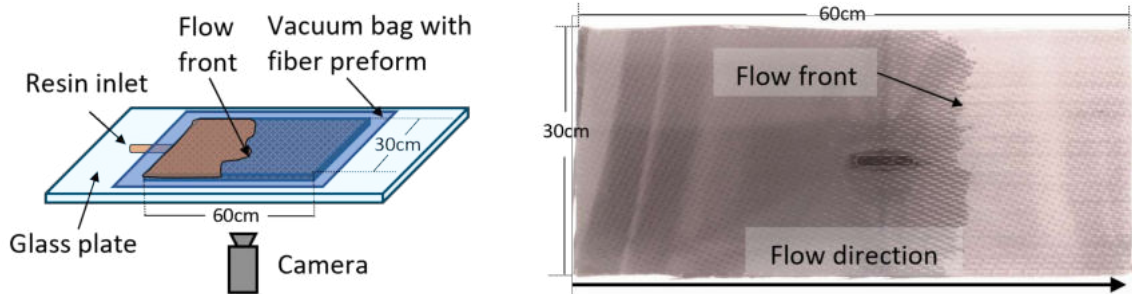


Figure 3.9: Setup of VAP infusion with camera for flow front detection (left). Flow front on bottom side of the textile preform (right).

The resin infusion was recorded with 1 fps and a resolution of 1280×720 px.

Thermoplastic Resin Transfer Molding Process (T-RTM)

T-RTM is a manufacturing process where thermoplastic resin is injected into a mold containing a dry fiber preform, resulting in a composite part after curing.

It is used for producing high-performance composite materials in industries such as automotive and aerospace. T-RTM is special compared to other manufacturing methods due to its recyclability, reduced cycle times, and the ability to produce tougher, more impact-resistant parts.

Figure 3.10 provides an general overview of the four stages of the T-RTM process described in [85] from which the data for this study is derived.

1. Preparation and Evacuation: In the initial stage of the T-RTM process, a dry fibre preform is prepared and manually cut to fit the mold. The preform, typically made of

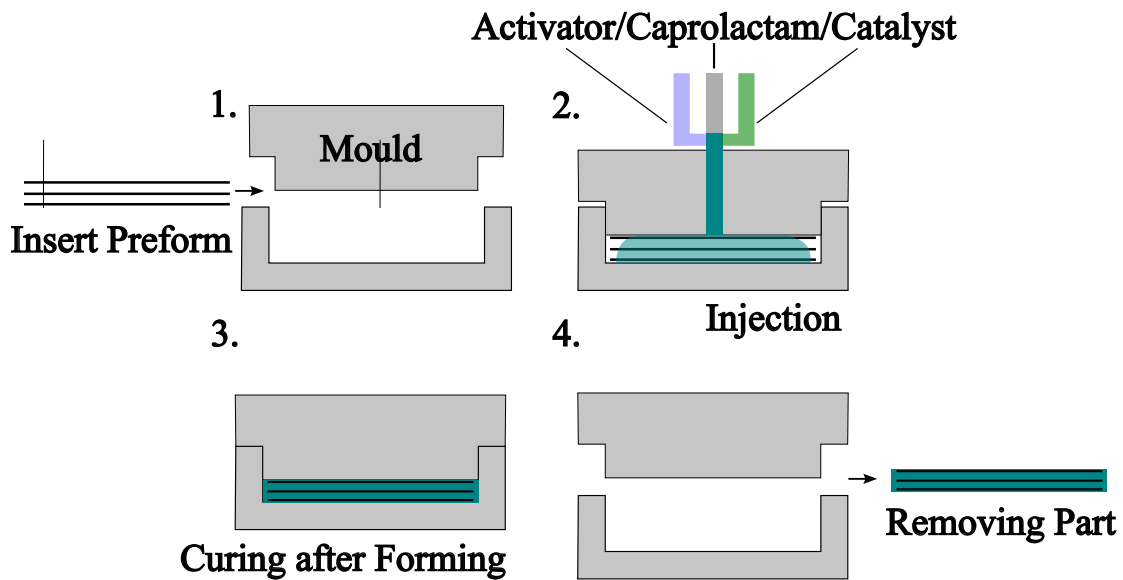


Figure 3.10: Schematic representation of the four stages in the T-RTM process: (1) Insertion of the preform into the mold, (2) Injection of the activator, caprolactam, and catalyst, (3) Curing after forming, and (4) Removal of the finished composite part.

materials like glass or carbon fibre textiles, is then carefully positioned within the mold. This precise placement is crucial for ensuring uniform resin distribution during subsequent stages.

Once the preform is properly positioned, the mold is heated to a designated temperature, around 150°C. The mold is then closed, and a vacuum is applied, serving two primary purposes: removing moisture from the preform to prevent defects during polymerization, and enhancing the permeability of the preform to ensure better resin flow and impregnation.

2. **Injection:** In the third stage, the resin or polymer is injected into the mold under pressure. This step involves driving the resin into the preform using a pressure gradient, which ensures that the resin thoroughly impregnates the fibre network. The injection phase is critical for achieving complete wetting and uniform distribution of the resin throughout the preform.
3. **Curing:** Finally, the preform undergoes curing, where it is fully polymerized or hardened under controlled conditions. This stage involves maintaining pressure and temperature to ensure that the polymerization process completes effectively, resulting in a solid, consolidated composite part.
4. **Removing the final part:** After complete curing and cooling down of the final part, the press can be opened to remove the part.

The specific materials and sensors used in the experiments conducted within the MAI CC4 CosiMo project are detailed in the following.

Using an injection machine from Krauss Maffei Technologies, Germany, and following the

3 Experimental Setup

CAPROCAST technology patented by Tecnalia, Spain, ϵ -caprolactam is injected into a glass fiber preform, where it polymerizes into polyamide 6. Strong bases, such as alkali metals, act as initiators to form free ϵ -caprolactam anions, which cause ring-opening anionic polymerization through nucleophilic attacks on other caprolactam monomers. Detailed overviews of the T-RTM process and the reaction kinetics of the polymerization can be found in [85–87].

The mold is a 0.5 m \times 1.1 m steel tool designed as a chicane component to introduce complexity, simulating a battery casing. Various geometries were integrated into the tool to study their impact on the flow front and overall process. For comprehensive in-line monitoring, analysis, and understanding of the process, a sensor network was developed and integrated into the tool. This network comprises various types of sensors, including 57 ultrasonic sensors, 8 dielectric analysis (DEA) sensors, 4 temperature sensors, and 4 pressure/temperature sensors [85]. However, the focus of this work is on the ultrasonic sensors.

The primary component of the ultrasound sensor was a piezoelectric plate, which was affixed to a 3D-printed adapter and mounted on the tool holder. The plate was bonded to a plastic spacer using a high-temperature resistant adhesive and was permanently secured to the holder after curing in an oven. The assembly process concluded with the precise alignment and screwing of the sensors into the mold halves. Figure 3.11 schematically represents the sensor integrated into the tool.

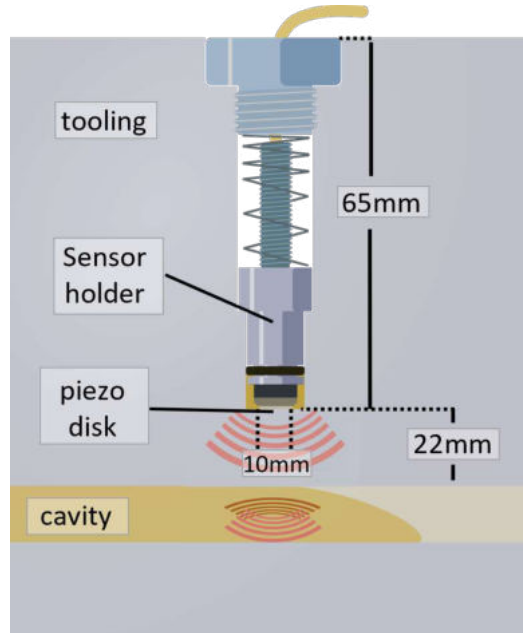


Figure 3.11: Illustration of the sensor integrated into the tool, according to [85].

Figure 3.12 illustrates the schematic of the sensor network integrated into the tool. The dimensions of the tool are specified as 50 cm by 110 cm, and the thickness of the resulting

battery casings ranges from 2.5 mm to 15 mm, as indicated in Figure 3.12. These thicknesses correspond to the cavity thickness when the press is fully closed.

The sensors were systematically arranged in a fine-mesh, equidistant grid to ensure comprehensive coverage and to further enhance the monitoring capabilities, additional sensors were strategically placed in areas with complex geometry. This strategic placement allows for detailed analysis and better detection of variations in the flow front, particularly in regions where the flow behaviour might be more intricate.

Most of the ultrasonic sensors were positioned on the top side of the component to perform pulse-echo measurements. This positioning was chosen because, in the given experimental setup, the flow front propagation primarily occurs on the top side. By concentrating the sensors in this critical area, enables high-resolution data and precise monitoring of the flow front as it progresses during the manufacturing process.

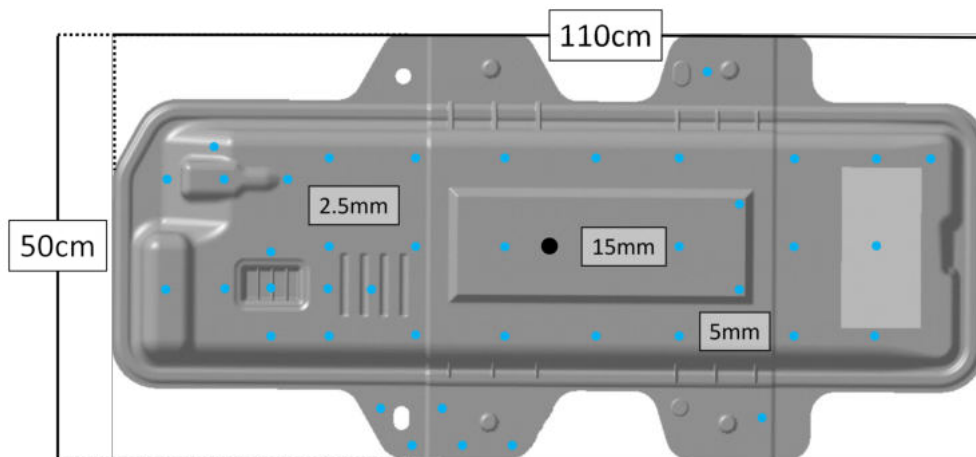


Figure 3.12: Illustration of the tool and the integrated US-sensors.

The remaining 10 sensors were installed on the opposite side, aligned with selected sensors on the top side, to perform transmission measurements. These transmission measurements can provide insights into the shape of the flow front and potentially allow for the extraction of other parameters, such as sound velocity.

However, for the purpose of flow front reconstruction presented here, the transmission measurements are not relevant.

To integrate the sensors into the tool, holes were milled, and the sensors were equipped with springs to ensure consistent contact pressure throughout the process. For optimal distance from the cavity, consider the sensor's near-field length N and avoid overlapping echoes in the received signal. Based on the material values presented in Table 3.5 the near-field length N of the sensor with a piezoelectric diameter of 10 mm is calculated to be $N = 8.5$ mm.

3 Experimental Setup

Table 3.5: Relevant material parameters, the Speed of Sound c , Attenuation a , density ρ and acoustic impedance Z .

# Layer, Material	c ($\frac{m}{s}$)	a ($\frac{dB}{mm}$)	ρ ($\frac{g}{cm^3}$)	Z ($\frac{kg}{m^2 \cdot s}$)
1, Steel	5900	0.01	7.8	46.02×10^6
2, Caprolactam	1400	0.07	1.1	1.54×10^6
3, Steel	5900	0.01	7.8	46.02×10^6

The measurement principle for detecting the flow front is illustrated in Figure 3.13. The emitted ultrasonic waves are depicted by yellow arrows, with the size of the arrows qualitatively representing the energy of the ultrasonic signals. The orange region between the black tooling represents the fluid, which moves to the left and gradually impregnates the preform. The orange-brown gradient illustrates different stages of polymerization.

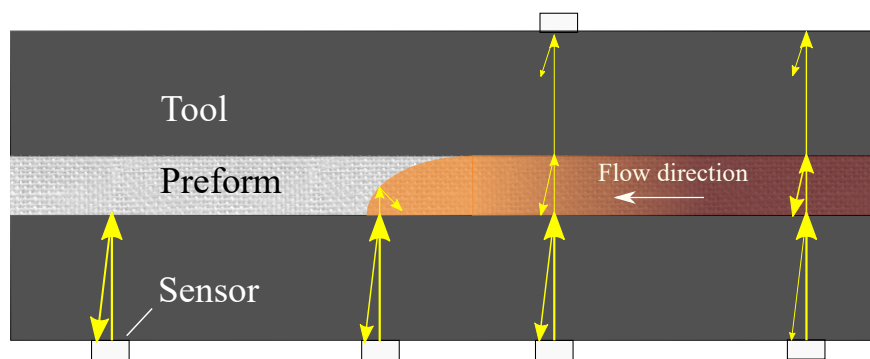


Figure 3.13: Exemplary illustration of the signal progression in the T-RTM experiments. As the impregnation progresses and varying degrees of polymerization occur, the reflection conditions change, altering the characteristics of the reflected ultrasonic waves. According to [10].

The emitted ultrasonic waves travel through the tool until they reach the interface between the tool (steel) and the cavity containing the preform (air). At this interface, most of the waves are reflected back due to the difference in acoustic impedance between steel and air.

When the flow front reaches the interface, the reflection conditions change significantly. The wetting of the preform increases its acoustic impedance at the interface.

This increased impedance leads to a stronger transmission of the ultrasonic signal through the interface and a simultaneous decrease in the intensity of the reflected pulse.

Multiple reflections can occur at the upper part of the tool, creating a cascade of main echoes in the captured signal. The transmitted wave then travels further and encounters another interface at the lower surface of the cavity, where it undergoes partial reflection. Due to the high attenuation of the impregnated preform, echoes from reflections at the lower part of the preform are challenging to extract, as they are often weak and difficult to distinguish from the noise.

To ensure clear detection of the flow front, the received ultrasonic signals are processed as follows: The signals are filtered with a 1 MHz high-pass filter to remove low-frequency

noise. They are then amplified by 40 dB using an instrumentation amplifier to enhance the signal strength. Finally, the signals are digitized at a sampling rate of 20 MS/s for detailed analysis.

3.4 Data Acquisition System and Sensor Placement

For the rheometer and the T-RTM experiments, the measurement system and sensors developed by Linscheid [34] were utilized. The ultrasonic probe, shown in Figure 3.14 used consists of a piezoelectric ceramic disc (type PRYY-0227, PICeramic) with a thickness resonance frequency of 2 MHz.

The probe is housed in a steel casing with a thread, a damping component, and a spring that ensures constant contact pressure for sensor coupling. The probe serves both as a sensor for incoming sound waves and as a pulse generator for generating ultrasonic waves.

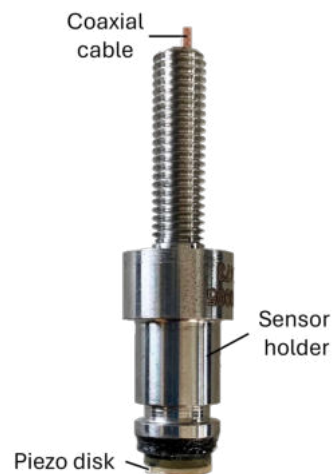


Figure 3.14: Photography of the sensor assembly showing the coaxial cable, piezo disk, and sensor holder.

The sensor is connected via the coaxial cable to a hardware module, which primarily consists of selection, filtering, and amplification circuits, as well as a microcontroller. The measurement computer digitizes and stores the measurement data and allows the hardware module to be controlled via the software SBench 6 (Spectrum Instrumentation GmbH, Germany).

An external control board drives the pulser and performs analogue pre-processing of the signals. The pulser consists of a MOSFET-driven spike pulse generator and an expander-limiter design, which excites the sensors with a 12 V spike pulse of approximately 300 ns length without overloading the preamplifier. The acquired echo signal is filtered with a 1 MHz high-pass filter and amplified by 40 dB using an instrumentation amplifier (AD8421 from Analogue Devices). This signal is then digitized at 20 MS/s using a streaming system

(M2p.5923-x4, Spectrum Instrumentation GmbH) [85].

For the ultrasonic measurement in the pulse-echo method, ultrasonic pulses are generated at intervals of 21 ms. The signal is stored for further processing in a 1 ms time window following the pulses. The intervals between the individual pulse-echo events do not provide useful information and are therefore not stored to reduce data volume. This principle is schematically illustrated in Figure 3.15 according to [79].

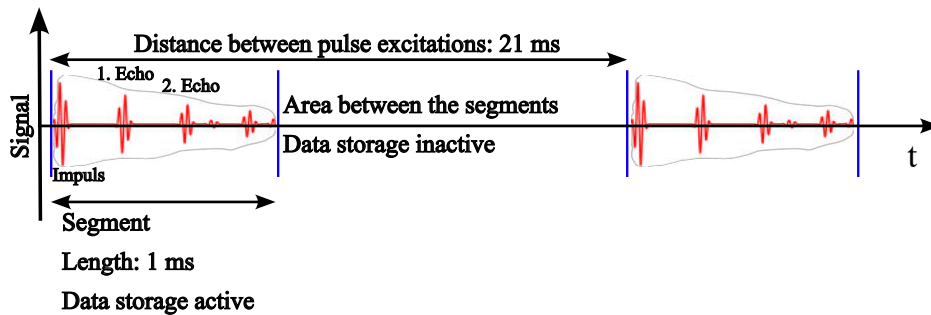


Figure 3.15: Diagram illustrating the timing and signal processing of pulse excitations with 1 ms active data storage segments and 21 ms intervals between pulses. The inactive data storage areas and corresponding echo signals are also shown.

Next, consider a typical use case for Pulse-Echo Measurements which is relevant for the following sections.

Principle of Pulse-Echo Measurement in Multilayer Structures

Many applications of pulse-echo measurements involve multilayer structures. A multilayer structure typically consists of a specimen to be investigated placed between two known materials, often with the same material used for both the top and bottom layers (i.e., Material 3 = Material 1).

For instance, for the processes described in the following, such as VAP, T-RTM, and the rheometer experiments the material of interest is sandwiched between two layers. The theoretical signal progression of an ultrasonic pulse introduced into a three-layer multilayer structure is illustrated in Figure 3.16. The ultrasonic probe head emits a pulse, generating main echoes (1st Main Echo and 2nd Main Echo) and secondary echoes as the waves reflect at material interfaces. The amplitude of the signal is plotted against time, highlighting the detection of the echoes at different time intervals.

In this setup, vertically coupled sound waves pass through Material 1 and encounter the first interface. At this interface, the incoming wave packet is partially reflected and partially transmitted. The reflected sound waves at this point generate a pronounced main echo cascade in the signal. Similarly, at the second interface between Material 2 and Material 3,

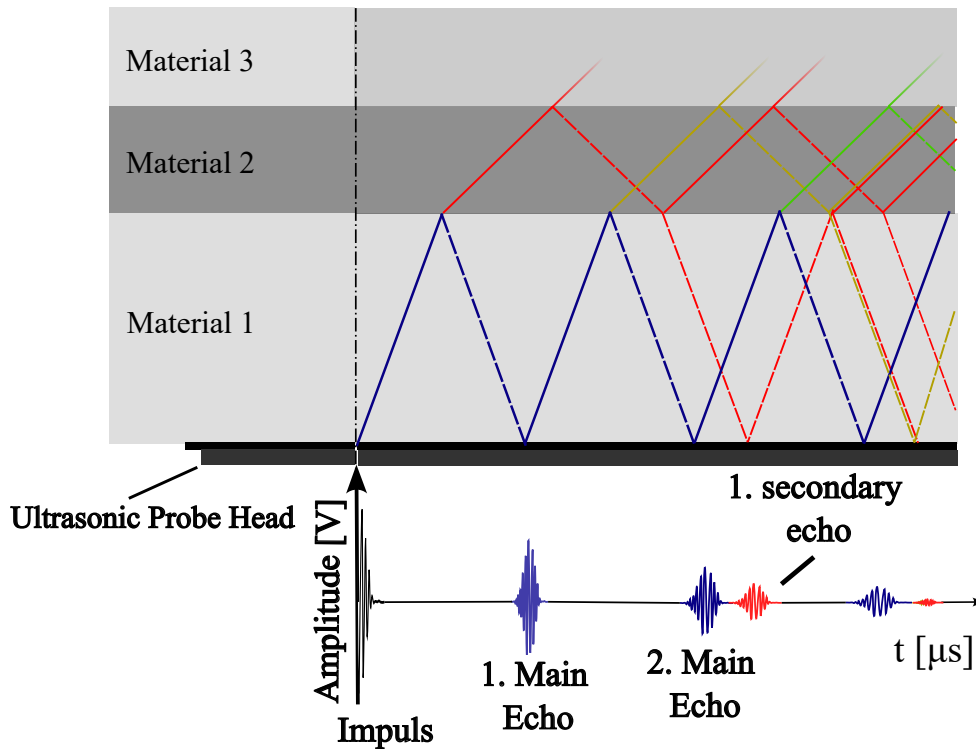


Figure 3.16: Schematic of ultrasonic pulse-echo measurements illustrating the propagation of ultrasonic waves through three distinct materials. According to [10]

the signal is again reflected and transmitted. These reflected sound waves, referred to as secondary echoes, appear as dampened echoes in the further course of the signal recording. Figure 3.16 depicts the sound paths in blue and red, with the paths transmitted into Material 3 being neglected for simplicity.

The strength of the main echoes depends on the reflection factor R between Material 1 and Material 2. This factor, determined by the acoustic impedance of Material 1 and Material 2, is given by the equation:

$$R = \frac{p_r}{p_0} = \frac{Z_2 - Z_1}{Z_2 + Z_1} \quad (3.1)$$

where p_0 is the sound pressure of the incoming wave, and p_r is the sound pressure of the reflected wave. Since the sound impedance depends on the material properties, changes in the reflection factor affect the ultrasonic signal.

Appropriate analysis methods can thus monitor material changes, such as polymerization or changes in contact conditions between the materials, by observing alterations in the ultrasonic signal.

Sensor Placement

Effective impulse-echo measurements rely on back reflected ultrasound or echoes, that occur at boundaries where there is a sudden change in acoustic impedance, such as interfaces between different materials. This method is particularly advantageous in processes characterized by layered or 'sandwich' structures. The ultrasound waves, when transmitted into a sandwich structure, are reflected at the interfaces between different materials which makes it easier to detect and characterize the internal structure, including the thickness of layers and the presence of defects.

To optimize sensor setup or evaluate the material's condition and properties, it is beneficial to consider the theoretical model of the expected received signal. The comparison between the theoretical model and the received signal can facilitate the signal interpretation where specific characteristics of the received signal such as amplitude variations, time of flight differences, or frequency shifts can be correlated with potential issues within the material. To achieve this objective, an application was developed using MATLAB 2022b, designed to predict impulse-echo measurements for a generic sandwich structure with an adjustable number of layers. The principle of the calculation method is based on [10]. The tool enables the customization of the sandwich structure's composition by allowing users to employ individual impulses and to specify the number of layers, each with its thickness and its material properties such as density, sound velocity and attenuation factor. Figure 3.17 illustrates the scheme of a three-layer sandwich structure, the reflections and transmission of the sound beam at the interfaces and the relevant input parameter of the model.

The tool can be used to optimize sensor placement, focusing particularly on the length

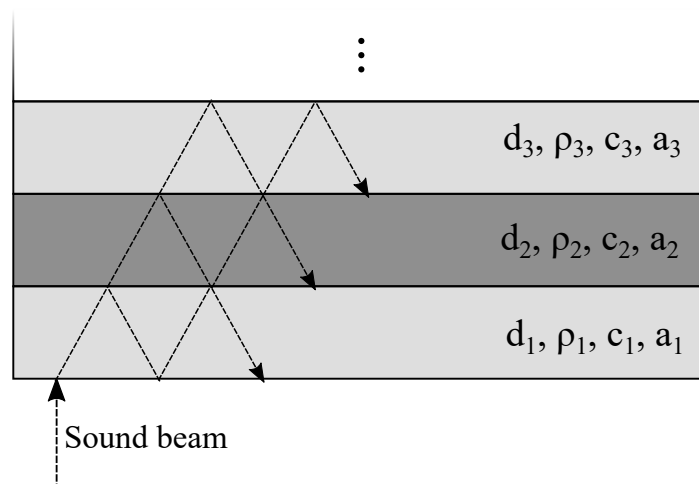


Figure 3.17: Schematic illustration of a ultrasound path travelling through a sandwich structure of three layers.

of the 'delay line', the path before the ultrasound waves reach the actual area of interest. In the figure the delay line can be defined as the first layer and strongly influences the composition of the received signal. It should be chosen adequately for a effective signal

analysis.

For a suitable choice of length and material for the delay line there are mainly three things to consider:

1. **Signal clarity:** An optimal delay line length, applied before ultrasonic waves reach the material of interest, can effectively separate signals from the material's surface from those generated by internal features, defects, or unwanted multiple reflections. This separation makes it easier to interpret the amplitudes or time-of-flight data and accurately locate and characterize internal defects. Specifically, when testing sandwich structures in impulse echo mode, the back wall echo contains valuable information about the physical state of the material under examination. For instance, the time of flight and the amplitude of the back wall echo are indicative of the material's properties and thickness as these characteristics are determined through the sound velocity and attenuation factor. Thus, for straight-forward signal analysis, it is beneficial to obtain a clear back wall echo without any overlap of the main echoes in the received signal.
2. **Control over beam spread and focusing:** To further facilitate signal interpretation it is practical to align areas of maximum sound pressure with regions of the material of greatest interest. Ensuring that critical areas are subjected to the highest levels of ultrasonic energy enhances the likelihood of detecting anomalies or variations in material properties and thereby contributing to more reliable signal interpretations.
3. **Surface coupling:** To adapt the delay line transducers can be equipped with specialized sensors mounting, typically made from materials with low adsorption coefficient or specifically tailored to the process materials to minimize or smooth the transitions of high acoustic impedance mismatches which could lead to undesired intense reflections.

Alternatively, when geometrically feasible, the delay line can be seamlessly integrated into the process apparatus through adjustments to the process geometry. This integration offers the advantage of minimizing interfaces, and thus reducing disruptive reflections and enhancing signal clarity.

To ensure effective transmission of ultrasonic waves between the transducer and the material it is important to select appropriate coupling media. The couplant, typically a gel, liquid, or paste, is applied to eliminate air gaps that could hinder sound wave propagation [20].

Figure 3.18 illustrates the effect of varying the delay line thickness, d_1 , on the composition of the received signal, while keeping all other parameters constant. The figure shows the paths of ultrasonic waves traveling through a two-layered sandwich structure with different lengths of the bottom layer, defined as the delay line. The horizontal axis represents time, and the path of the back-wall echo is highlighted in white.

Below the sandwich structure, the corresponding acoustic signal is shown as received by a sensor attached to the lower surface of the first layer. The first peak represents the

3 Experimental Setup

excitation impulse, while the main echoes in the signal are reflections from the interface between the first and second layers. The time interval t_1 between these echoes is directly influenced by the thickness of the delay line, d_1 .

The main echoes arise due to repeated reflections at the first interface. The length of the delay line determines the time interval t_1 between these echoes, which can be calculated using the equation

$$t_1 = \frac{2d_1}{c_1}, \quad (3.2)$$

where c_1 is the sound velocity. Consequently, the longer the delay line d_1 the greater t_1 . Similarly, the thickness of the second layer determines the time of flight of the first back wall echo, given by

$$t_2 = t_1 + \frac{2d_2}{c_2}. \quad (3.3)$$

Based on the initial pulse duration T relations between the given parameters can be defined to make sure the back wall echo occurs between the first and second main echo without overlap. Thus, to prevent that the back wall echo overlaps with the first main echo the condition

$$d_2 > T \cdot c_2 \quad (3.4)$$

must be satisfied, which is independent of the delay line d_1 . Consequently, for small d_2 a sufficiently short T is necessary to fulfil this condition.

To avoid overlap with the second echo, the condition

$$d_1 > \left(\frac{c_1}{c_2} d_2 + \frac{c_2 T}{2} \right) \quad (3.5)$$

must be met for the delay line d_1 .

Often, the first layer can be easily adjusted to enhance inspection of the second layer. Thus

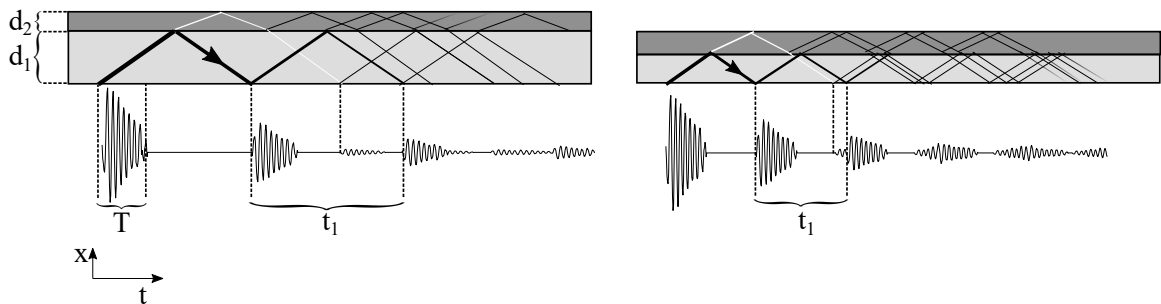


Figure 3.18: Impact of varying the delay line length d_1 on the received signal.

for optimization, the delay line can be designed in a way to ensure that the focal point of the sound source is aligned within the second layer. Since the focal length of the ultrasonic source corresponds to the near field length N it depends on the delay line length d_1 of the given setup as detailed in Equation 2.23.

Consequently, the length of the delay line and the thickness of the second layer are interde-

pendent and require mutual adjustment. To identify a suitable set of parameter avoiding overlapping of the echoes consider that the maximum thickness $d_{2,\max}$ of layer 2 for a given delay line is dictated by Equation 3.5. The lower limit is defined by Equation 3.4 which only depends on the impulse length in the given material and thus constant for varying delay line lengths.

The MATLAB app visualizes these restrictions in a graph to assist in a graphical identification of suitable parameter combinations. This approach is demonstrated in Figure 3.19 for a two-layered sandwich structure with parameters listed in Table 3.6 and a near field length of $N = 25$ mm. The green region on the graph highlights feasible combinations of d_1 and d_2 that ensure a received signal without any overlap between the main echo and the backwall echo. The red line marks the position of the near-field length within the second layer and serves as a visual guide to easily identify suitable parameter combinations.

In particular, if the focal length of the sensor $N = 25$ mm should fall within the second layer, only the combinations above the black line are available. Consequently, the combinations meeting both conditions must be chosen within the area bordered by the black dotted line. To illustrate the case of determining an ideal delay line consider Figure 3.20. If the thickness of layer 2 is fixed for example at 5 mm a horizontal line can be drawn at $d_2 = 5$ mm to find the corresponding d_1 for the intersection to the upper limit. The delay length ensuring no overlapping echoes should therefore be at least 11.5 mm and ideally, with the focal length within the second layer at least 20 mm.

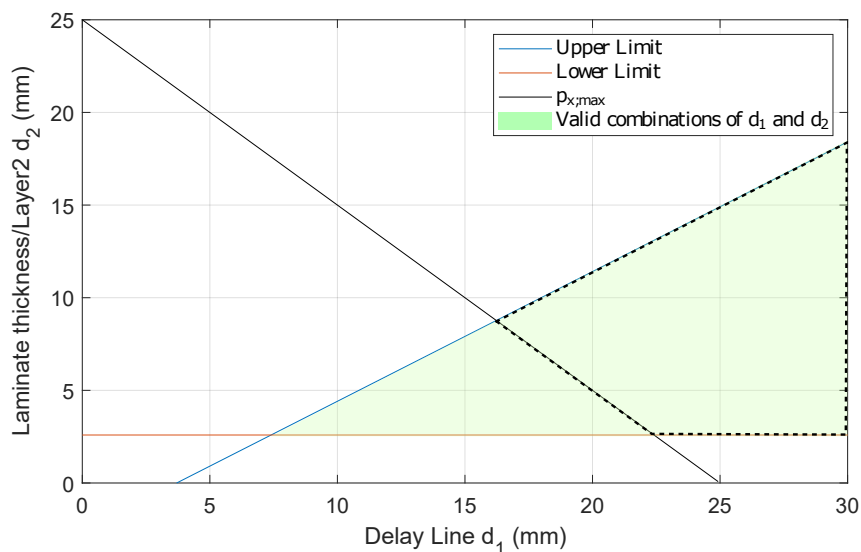


Figure 3.19: Graphical illustration to support the choice of a suitable delay line length. The upper limit follows Equation 3.5, while the lower limit is given by Equation 3.4 with a pulse length of $T = 3.7 \mu\text{s}$. The black line indicates the position of maximum sound pressure in Layer 2.

To identify a suitable delay length for the T-RTM experiments refer to Figure 3.21. The thickness of the part corresponds to the second layer. As indicated in Figure 3.12 the part

3 Experimental Setup

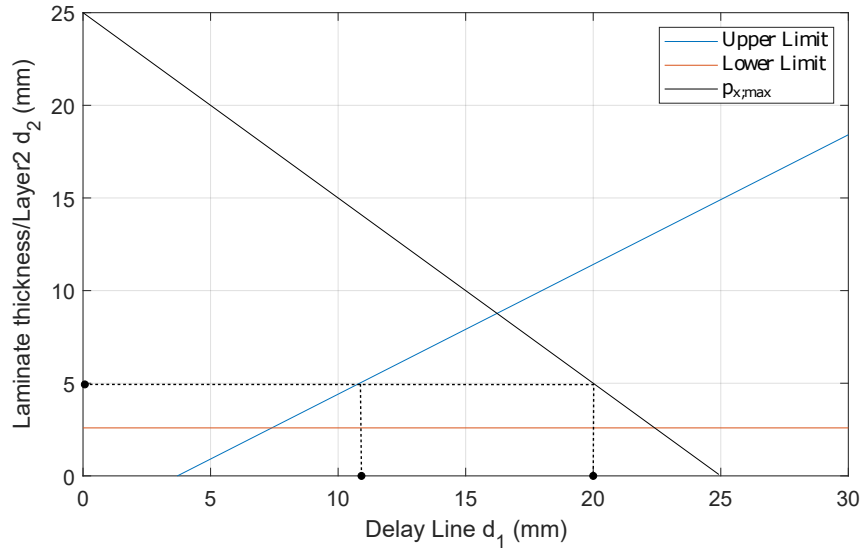


Figure 3.20: Graphical illustration of determining ideal delay line length.

Table 3.6: Parameters used for creating the graph in Figure 3.19.

Layer	Speed of Sound ($\frac{m}{s}$)	Attenuation ($\frac{dB}{mm}$)	Density ($\frac{g}{cm^3}$)
1	2000	0.01	7.8
2	1400	0.07	1.1

features areas with thicknesses of 2.5 mm, 5 mm, and 15 mm.

To avoid overlap between the main echoes and the first secondary echo can be graphically determined. Thus, the delay length d_1 should be > 33 mm and > 22 mm for a thickness $d_2 = 5$ mm and $d_2 = 2.5$ mm, respectively. Due to geometrical and technical restriction the necessary delay length for laminate thicknesses 15 mm is not feasible.

The focal length of the sensor is calculated to be $N = 8.5$ mm. There is no setting for which the focal length falls within the second layer while avoiding overlapping echoes.

However, due to the large attenuation of the caprolactam infused fibre, it is not expected to receive signals reflected from the backwall echo for thicknesses $d_2 \leq 5$ mm which might disturb the main echoes.

Thus, a uniform distance for the delay line of 22 mm is chosen. This is a compromise between signal clarity and attenuation: it is the shortest delay length to avoid overlapping echoes for thicknesses of 2.5 mm, where a backwall echo is expected, and at the same time reducing attenuation from geometrical spreading in comparison to longer lengths.

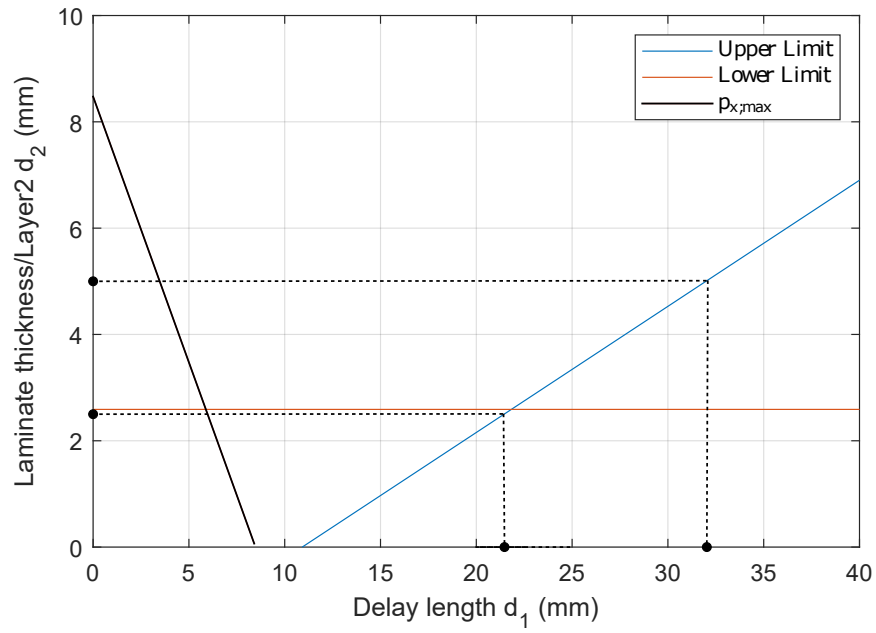


Figure 3.21: Illustration of determining suitable delay line lengths for laminate thicknesses $d_2 = 5$ mm and $d_2 = 2.5$ mm.

The rheometer experiments were initially planned to validate the rheological quantities derived from the ultrasound data collected during the T-RTM experiments. To ensure consistency and facilitate direct comparisons between the two setups, the same delay lengths and sensor configurations used in the T-RTM experiments were applied to the rheometer experiments.

4 Enhanced Techniques for Ultrasound based Condition Monitoring

This chapter begins with an overview of condition monitoring (CM) systems, highlighting their physical and non-physical components. A key challenge in these systems is signal degradation caused by sensor wear, environmental variability, and external noise, which can compromise reliability. Before detailing the enhanced techniques, the chapter addresses these challenges and introduces strategies to ensure robust, low-maintenance monitoring through optimized feature selection and advanced diagnostic modelling.

Many CM systems [88–91], including the ones discussed here, can be divided into physical and non-physical components. Figure 4.1 shows an overview of typical CM systems. The physical components include the monitored asset, such as a machine, system, or process, where measurable phenomena (e.g., vibrations, acoustic emissions, or temperature changes) arise. These phenomena are acquired via sensors and digitized for further processing. The non-physical components consist of the software infrastructure responsible for processing the digitized signals, ultimately delivering classifications and predictions about the system’s condition. These predictions are based on diagnostic models that assess the state of the monitored asset connected to variations in the digitized signal.

These variations in the digitized signal can typically be traced back to three sources:

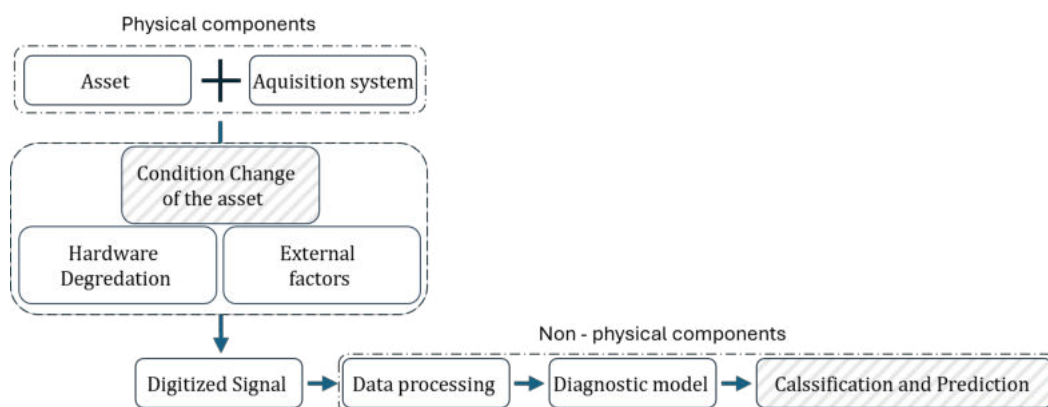


Figure 4.1: Outline of condition monitoring systems.

- Hardware degradation, such as sensor wear or interference from electronic devices in the acquisition system.

- External factors, including environmental variability.
- Actual changes in the condition of the asset, which represent the desired signal changes to be classified and predicted.

Thus, to ensure robust classification and prediction, it is critical to maintain the physical components regularly. This includes tasks such as sensor calibration to minimize signal degradation caused by factors other than actual condition changes in the asset.

While eliminating all sources of signal variation unrelated to the asset's condition is particularly challenging, especially in the long term, optimizing the non-physical components contribute to achieve accurate and robust predictions. Key strategies include:

- Designing data processing pipelines and diagnostic models that account for signal degradation not associated with condition changes in the asset.
- Frequent retraining for diagnostic models and redesign of the data processing pipeline as needed.

Establishing a solid data foundation reduces the frequency of retraining, improves long-term reliability, and decreases hardware maintenance demands. The first part of this chapter focuses on optimizing feature selection and adaptation to enable a reliable and low-maintenance CM system.

A major threat to CM accuracy is the misinterpretation of signal disturbances, such as sensor degradation or external interference. Understanding the causes of these disturbances is essential for selecting features that are robust to signal degradation.

However, signal distortions often result from multiple overlapping factors, making it difficult to isolate individual causes. To study these effects, we propose a controlled approach using synthetically degraded signals.

This approach introduces artificially generated disturbances into signals after preprocessing (e.g., filtering). This ensures that the evaluation targets the resilience of extracted features, rather than the preprocessing methods. The goal is to identify features that remain stable under realistic disturbances.

Synthetic noise is used to simulate various real-world challenges and allows systematic testing of model robustness. In this context, noise refers to any unwanted signal variation, such as environmental or electronic interference [92, 93]. According to [92, 94], noise can be categorized into:

- Steady Noise: Constant continuous sound with minimal fluctuations in sound pressure, as observed for example in gearboxes.

- Non-Steady Noise: Includes fluctuating noise with continuously changing noise levels as grinding or welding and intermittent noise which alternates between background and elevated levels like machinery acting in work cycles.
- Impulsive Noise: Short bursts (≤ 1 s), categorized as sharp sounds or industrial impacts (e.g. press, material handling), defined by peak pressure, rise time, and duration.

The noise intentionally added to the signal should simulate potential real-world challenges and provide valuable insights into the model's reliability and performance. A technique is proposed to generate such disturbances:

- A straightforward approach is to generate random noise as a foundation using tools such as MATLAB's pseudorandom number generator [95].
- To customize the synthetically generated noise for specific applications, two techniques can be applied independently or in combination:
 - Modifying the amplitude probability density function (PDF) in the time domain.
 - Modifying the power spectral density (PSD) in the frequency domain.

Following this approach the following common types of noises can be generated [96, 97]:

- Gaussian noise, defined as random noise with a PDF in the time domain corresponding to Gaussian distribution
- White Noise. Signals, especially those transmitted over long distances (e.g., satellite, cellular networks), are often subject to random noise due to factors like thermal noise and electromagnetic interference.

Due to its prevalence, Gaussian noise is an inherent part of nearly all signals. For example, additive white Gaussian noise (AWGN), is widely used to model thermal noise, noise due to electrical components and is often an issue in image processing [98, 99].

- Linearly Changing Noise: In this approach, the amplitude of the probability density function (PDF) is linearly modified over time. This method simulates a consistent trend of signal degradation, such as the gradual loss of sensitivity in a sensor or the progressive wear and tear of equipment over time.
- Sinusoidal Signals with Varying Frequencies and Amplitudes: Introducing narrow-band sinusoidal signals as noise can effectively simulate specific real-world interferences, such as power line disturbances in electronic circuits or mechanical vibrations in machinery. By adjusting the frequencies and amplitudes of these signals, the noise can be tailored to mimic various interference patterns and conditions.
- Coloured noise: To generate more tailored noise, the frequency spectrum can be modified to follow a specific function of frequency. An example is flicker noise (or $1/f$

noise), which is observed in a variety of dynamic systems, including electrical circuits. It manifests as electrical noise in the current through resistors or as fluctuations in other physical quantities or "process variables" across various devices and systems. Such noise has been extensively studied in physical, electronic, and other systems [100, 101]

Example: Impact of Signal Degradation on Features and Classification Models

To demonstrate the impact of introducing such disturbances to a signal consider Figure 4.2. In the first column, the top plot shows an acoustic signal superimposed with Gaussian noise. The signal is recorded by an acoustic sensor mounted on a gearbox to monitor its operational state, which changes at $t = 0.5$ s from State 1 to State 2.

The middle and bottom plots display the RMS and partial power features, which are extracted from the signal superimposed with the noise.

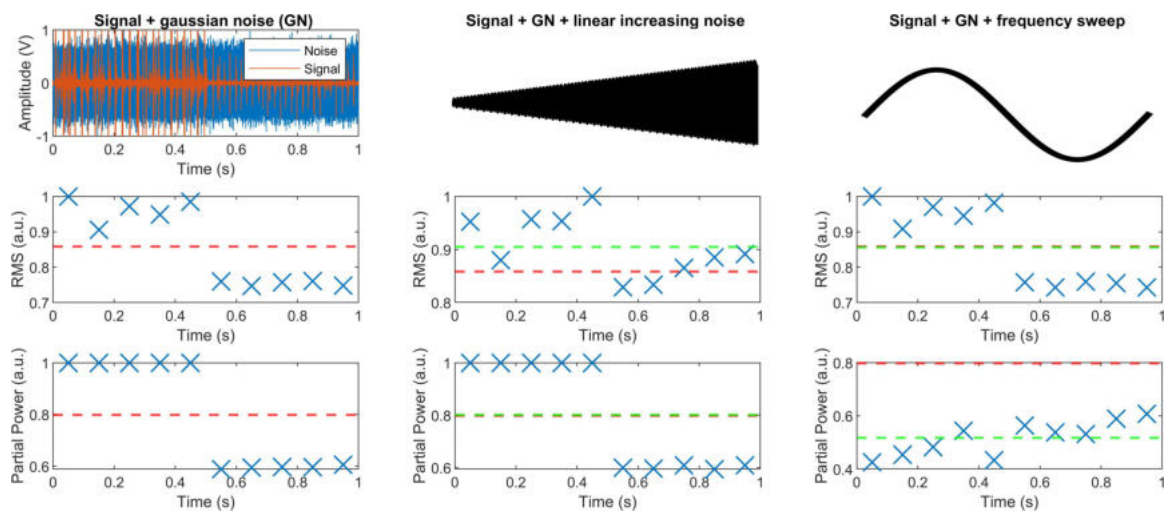


Figure 4.2: Illustration of the impact of various types of noise on extracted features and their distributions.

The red dashed line in the feature represents potential boundaries for state classification and should demonstrate how simple machine learning models make classification decisions based on these individual features. The middle and right columns illustrate changes in these features when linear increasing noise and a superimposed frequency sweep are introduced. The green dashed line highlights a new decision boundary value adapted to the corrupted signal.

The boundary values B can be defined based on the mean values of each state N and are calculated as:

$$B = \frac{mean_{N=1} + mean_{N=2}}{2}, \quad (4.1)$$

This boundary value emphasizes the clustering observed in the feature plots. In the left column, representing the signal with only Gaussian noise, this boundary is marked as a red dashed line. The clustering is clearly visible for both features. For the RMS and

partial power features, values above the boundary correspond to State 1, while values below it correspond to State 2. These features, along with the boundary value, form the basic principle of simple models for predicting and classifying the current State of the signal.

Despite the Gaussian noise, the data points of both features in the first column show clear clustering, indicating a reliable ML - model for classification.

In the second column, in addition to Gaussian noise linear increasing noise is added to the signal. In the RMS feature values a slight upward trend can be identified with rising noise levels, leading to less distinct separation between State 1 from 0 s to 0.5 s and State 2 from 0.5 s to 1 s. Using the previous boundary value, indicated by the red dashed line, would lead to misclassifications. However, adapting this boundary value, corresponding to retraining the machine learning model, can correct for the rising noise levels and restore nearly full classification accuracy.

In contrast, the partial power feature remains largely unchanged. It is defined as the percentage of energy within a specific frequency band relative to a predefined, broader frequency range. One key reason for its robustness against noise is that random noise tends to distribute energy uniformly across the entire frequency spectrum. As a result, while the total energy of the signal may increase due to the added noise, the proportion of energy within the specific frequency band compared to the total energy remains relatively stable. This self-normalizing characteristic ensures that the partial power feature is less sensitive to the overall increase in energy caused by the noise.

Thus, for the partial power feature the initial and newly calculated boundary value does not change a lot. Both lines clearly separate the data points. Thus, after adding the noise there is no need to recalculate the value which is representative to retraining a predictive model. This underlines the robustness of the partial power feature against the nature of the added noise. However, while the partial power feature generally shows robustness against noise with even PSD due to its self-normalizing nature, there are specific circumstances where it may become less stable compared to the RMS feature.

For instance, if the noise includes harmonics or specific tones that align with the frequency band of interest, the energy within that band will increase disproportionately, causing instability in the partial power feature. This type of frequency-specific interference can be synthetically added by introducing a chirp signal to the recorded data. A chirp signal is a type of frequency-modulated signal where the frequency varies linearly or non-linearly over time. In the example provided, the MATLAB chirp function [102] is used to generate an artificial signal in which the frequency linearly sweeps from 20 kHz to a higher value of 80 kHz over the whole duration of 1 s.

The results are shown in the right column of Figure 4.2. The added chirp signal causes disturbances in the partial power feature due to shifts in the power spectrum across frequencies.

In contrast, the RMS feature, which measures the total energy of the signal across all

frequencies, is less susceptible to these frequency-specific disturbances. RMS provides a more generalized measure of signal strength and remains more stable in the presence of frequency-specific interference.

These examples illustrate the importance of appropriate feature selection in signal analysis. They highlight how essential it is to include a combination of features in the model to ensure robustness against a variety of effects. Thus, by selecting a mix of features that complement each other, the model can leverage the strengths of each feature while compensating for their individual weaknesses.

All features rely on specific settings or parameters that can be fine-tuned to achieve a strong correlation with the desired response variable. One crucial parameter for all features is the position and length of the time snippets. The ultrasound signal is divided into these snippets, with each snippet generating a data point through feature extraction functions. Additionally, features like partial power require further settings, such as the definition of frequency bands. These parameters must be carefully selected based on the application's specific conditions, as they have a significant impact on the quality of the calculated features.

In this chapter, a feature adaptation process is outlined which is designed to achieve the highest possible correlations with the desired process variables. This step ensures that the features are closely aligned with the variables to be monitored and set a optimal foundation for predictive models or a subsequent selection process.

Next, a systematic selection process is introduced for identifying the best features from a predefined list. This approach helps in narrowing down the most relevant features, optimizing the predictive accuracy of the models.

Finally, while predictive models may accurately forecast process variables, one limitation of ultrasonic sensors are their spatial constraints. Due to the limited field of view of these sensors, the information they capture is localized and cannot fully cover the entire geometry of the area being monitored. Therefore, it is important to gather information about the areas between the sensors. In the last section, an approach for interpolating this information is described by considering the relationship between the geometry and the sensor measurements. This method allows for a more comprehensive understanding of the monitored space, despite the spatial limitations of the sensors.

4.1 Feature Adaption

As established in Subsection 2.3.5., the feature extraction process involves several parameters, such as the snippet length, which serves as a general parameter across all features,

and individual parameters, like frequency ranges for partial power features. Selecting the appropriate features for a specific application is crucial, but equally important is the adaptation of these parameters to suit the application's requirements. This section proposes an iterative method for effectively adapting these parameters.

The proposed feature adaptation method, illustrated in Figure 4.3, consists of four, iterative key steps designed to optimize feature extraction parameters for a specific application:

1. Select parameters for the features.
2. Calculate the features based on the selected parameters.
3. Assess feature performance:
 - a) Choose a suitable assessment method.
 - b) Calculate a performance score for the feature.
4. Assign a score to the parameter combination and visualize the results.

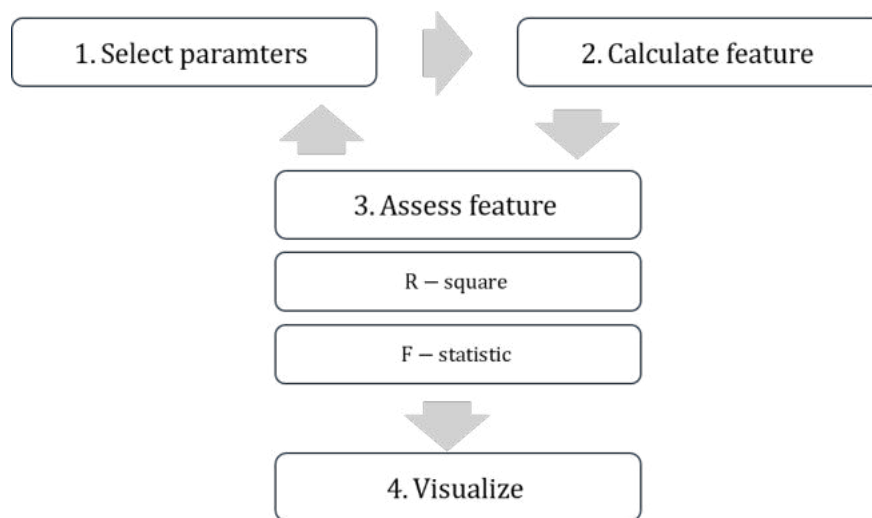


Figure 4.3: Outline of the proposed feature adaptation method, illustrating parameter selection, feature calculation, performance assessment, and visualization.

The process begins with selecting the parameters for the features. These parameters, such as snippet length or frequency ranges, serve as the basis for feature extraction and need to be carefully chosen to ensure compatibility with the data and application goals.

Next, the selected parameters are used to calculate the features, generating measurable outputs based on the input data. This step involves applying the feature extraction methods to the dataset, producing feature values that will later be evaluated for their effectiveness. The third step is to assess the performance of the extracted features.

Useful methods to assess the correlation between feature and response variable can be

categorized in continuous and discrete response variables:

- For continuous variables the R-square value is used to quantitatively measure of how well the feature explains the variance in the response variable, with values ranging from 0 to 1 indicating the proportion of explained variance. R-squared represents a normalized measure of similarity between quantities, independent of direct or indirect nature of the correlation [103, 104].
- For discrete variables the F-statistic can be used to compare the variances between groups of a categorical response variable. The feature value are assigned to the corresponding groups and then ANOVA (Analysis of Variance) [105] can be applied to determine if there are significant differences between the means of different groups. A higher F-value suggests a significant relationship or separation between groups of the response variable based on the defined feature.

It is essential to select an appropriate assessment method tailored to the specific analysis. This evaluation provides quantitative feedback on how well the parameter choices contribute to correlations to the response variable and thus meaningful feature extraction.

Finally, the calculated performance scores are assigned to the corresponding parameter combinations and visualized. Visualization helps to identify trends, robust parameter ranges, or areas of potential overfitting.

This visual feedback facilitates quick interpretation and iterative adjustments to refine the parameter settings, ultimately improving the feature extraction process.

To illustrate the application of this approach, the following section presents its implementation on a dataset collected under controlled environmental conditions. By applying the method to a well-structured dataset, this example offers a clear and practical demonstration of how the approach can identify meaningful patterns

Example: Application to a Gear Hub

Consider an ultrasound signal of a bicycle gear hub as shown in Figure 4.4. During the first two seconds, the gear is in a loaded state, and for the last two seconds, it is unloaded. The figure shows analyses highlighting the variations in power distribution across different frequency ranges under different loading conditions, aiding in the detection and monitoring of mechanical states.

The task is to distinguish between the states based on appropriate feature selection. This process is illustrated using the partial power feature, for which suitable frequency intervals need to be defined. The figure demonstrates the impact of parameter selection on the

feature's quality to distinguish between the states.

For instance, the interval set from 0 kHz to 5 kHz does not show any clear distinctions, however the other frequency intervals show a clear rise around 2 seconds which indicates a change in the gear. This highlights the importance of appropriate parameter selection. Careless selection of frequency intervals can result in poor features that do not contribute effectively to distinguishing the appropriate state. Therefore, a suitable method must be applied to assess the usefulness of the features in predicting the state of the gear hub.

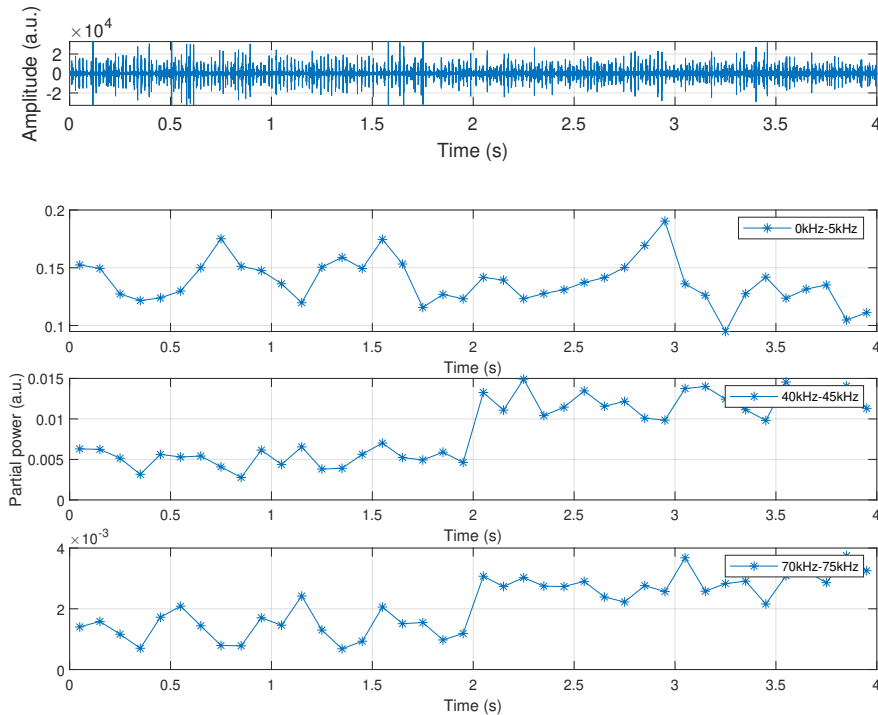


Figure 4.4: Feature extraction of ultrasound signals for process monitoring. The top plot displays a ultrasound signal in time domain of a gear hub over 4 seconds, while under load for the first 2 seconds. The bottom three plots illustrate the partial power within specific frequency bands: 0 KHz – 5 kHz, 40 KHz – 45 kHz and 70 KHz – 75 kHz.

The feature adaption process is illustrated by applying it to optimize these frequency ranges of the partial power feature.

It is necessary to develop a method to quantitatively assess the quality of features in distinguishing between states. For this purpose, the R-squared value for continuous variables or the F-value for discrete response variables is used to assess the correlation to the feature. The parameter settings of the frequency ranges are systematically rastered, and the F-value is calculated for each combination to identify suitable settings. In the case of a large number of features and parameters to be optimized, this process can be accelerated using optimization algorithms. For instance, gradient descent can efficiently navigate the parameter space to find the optimal settings by iteratively adjusting the parameters in the direction that minimally reduces the error. This method can significantly reduce the computational load

and time required to find the best parameter combinations compared to a rastering approach.

The upper plot in Figure 4.5 illustrates the F-value for the partial power feature with different frequency intervals of width 5 kHz. The partial power value corresponds to the percentage energy content within the defined frequency band. Two areas are visible with higher F-values: from 35 kHz to 45 kHz and from 70 kHz to 85 kHz. Higher F-values suggest a stronger relationship between the frequency range and the response variable.

The plot in the centre illustrates the power spectrum in decibels, comparing the unloaded and loaded conditions across frequencies from 0 to 100 kHz. The background colour of the bottom plot corresponds to the F-values from the top plot, with black indicating low F-values and red indicating high F-values. It shows that the higher F-values correspond with the highest differences in the power spectrum of the loaded and unloaded states. However, considering decibels as a unit, the correlation is related to the relative difference rather than the absolute difference between the power spectra.

The bottom plot compares the relative difference with the absolute difference of the power spectrum between the unloaded state P_U and the loaded state P_L . The highest absolute difference is below 10 kHz while the high values visible in the relative difference (left axes, blue) corresponds with the higher F-values.

This means that when analysing features in decibels, the focus should lie on how much the feature's value changes relative to its previous value. Large relative changes are more prominent in decibel measurements, making them more useful for distinguishing between different states of the gear hub.

This leads to potential conclusions; for example, initial parameter settings for partial power features could be guided by frequency intervals where the spectra of different states are most distinguishable. While this might seem intuitive, this example illustrates how the approach can uncover correlations or provide general guidelines for interpretation and quick parameter adjustments.

Furthermore, areas of good performance indicate robust parameter settings, while small areas might signal overfitting. Robust parameter settings are characterized by wide frequency intervals where high F-values are consistently observed. These wide areas suggest that the selected parameters are not overly sensitive to small variations in the data, indicating that the features are reliable and can generalize well to new data. Conversely, small areas of high performance might signal overfitting, where the parameters are tuned too precisely to the training data, capturing noise rather than the underlying signal. Overfitted models often perform poorly on new, unseen data because they lack generalizability.

4.2 Feature Selection

Initially, using features that are robust against application-specific disturbances helps mitigate the effects of these deteriorations and reduces the need for frequent retraining. To

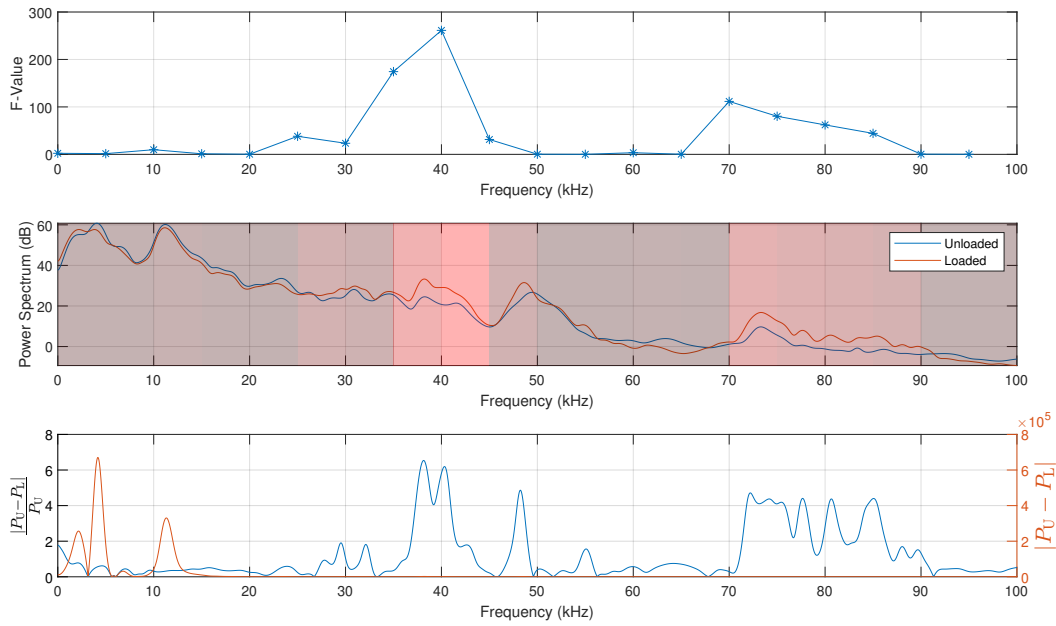


Figure 4.5: Comparison of the F-value (top) and the corresponding power spectrum at a loaded and unloaded state (middle) and its differences (bottom).

address this, a procedure is proposed for selecting methods to identify suitable features for this task.

The proposed method relies on a variety of analytical models that deliver scores to evaluate the effectiveness of each feature. These scores are then compared to those obtained through time-efficient feature selection methods, as described in Section 2.3.

In this context, the selection process based on a model that evaluates feature permutations is referred to as feature model selection (FMS), while the process of selecting features using standard feature selection algorithms is termed standard feature selection (SFS). The final scores derived from these methods are denoted as s_{FMS} and s_{SFS} , respectively. This dual approach ensures a comprehensive evaluation of features, balancing computational efficiency and robustness against disturbances.

Figure 4.6 and Figure 4.7 provide an outline of the processes, serving as a guide to follow the explanations outlined in each step. The main steps of the proposed FMS-method are as follows:

1. Selecting an extensive feature list: In addition to standard features and general features from repositories, application-specific features can be specifically designed to suit the problem at hand.
2. Preselecting features for efficiency: To reduce computational costs, consider preselecting a subset of features from the extensive list. Depending on available resources, select N features to proceed with further analysis.

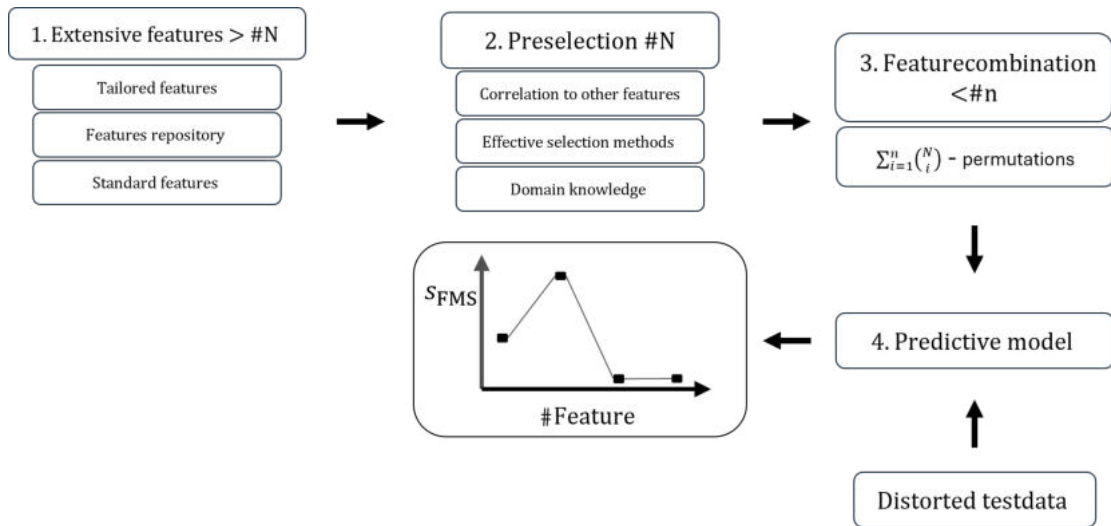


Figure 4.6: Overview of the proposed feature model selection approach (FMS).

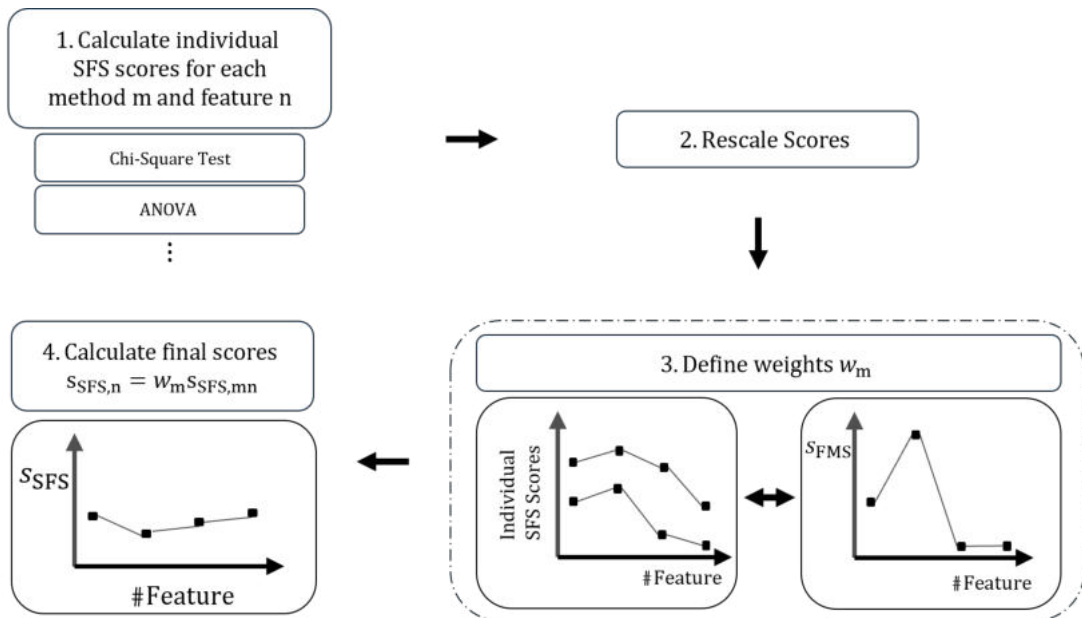


Figure 4.7: Overview of the standard feature selection approach (SFS).

3. Creating feature combinations: Generate all possible combinations of the preselected features with a maximum of n features per combination. A value of $n = 3$ has been shown to be sufficient, yielding $C = \sum_{k=1}^n \binom{N}{k}$ combinations in total.
4. Building predictive models and scoring features: Train predictive models for each feature combination and use the resulting accuracies to assign scores to the participating features. This process results in overall scores $S_{FMS,i}$ for each individual feature i . Additionally, the test data can be intentionally distorted to evaluate the robustness of features and tailor the scores to specific application needs.

For the SFS method, the following steps are proposed:

1. Calculate Scores: Compute the scores $s_{\text{SFS},m}$ for each feature i using each selection method m separately.
2. Rescale Scores: Since the scales of these scores can vary widely across methods, rescale the scores for each method to be comparable to each other, e.g. to the interval 0-1.
3. Optional: Weight Methods: Introduce weights w_m for each method m to control their influence on the overall feature scores. This allows to emphasize methods that are more relevant to the specific application. A strategy for determining these weights is proposed later in this chapter.
4. Combine Scores: The final scores $s_{\text{SFS},i}$ for each feature i is then calculated via $s_{\text{SFS},i} = w_m s_{\text{SFS},im}$.

FMS and SFS offer complementary approaches to feature selection. The FMS approach, while computationally intensive due to the need to train a large number of models, provides significant advantages. These include a thorough consideration of feature interactions by using a myriad of different feature combinations, direct alignment with the desired result, and the ability to customize the test data. This customization allows the selection process to be tailored for robustness against specific conditions under which the data is recorded.

In contrast, SFS is a far more computationally efficient process, making it better suited for applications where rapid calculations are required. By introducing weights w_m into the SFS process, the efficiency of SFS can be combined with the thoroughness of FMS. These weights can be derived from initial FMS results, aligning the SFS process with the scoring insights obtained through FMS.

Notably, while FMS needs to be run once to compute the weights and scores, the resulting weights can be reused for subsequent feature sets or similar applications. This reuse reduces the need to repeat the computationally expensive FMS process. For instance, in this work, weights derived from an acoustic signal analysis of a gear demonstrator could potentially be applied to other applications involving similar gear mechanics. This integration not only enhances scalability but also ensures an effective balance between the thoroughness of FMS and the efficiency of SFS.

The following describes the FMS process, including the determination of appropriate values for the weights w_m and the maximum number of features, n , per combination.

The process begins with an extensive selection of features, either sourced from repositories or specifically designed for the application. Domain knowledge is essential for identifying and creating relevant features, leveraging insights into the system being analysed. Features can be derived from the time domain, frequency domain or time-frequency domain (see section 2.3) ensuring a comprehensive and application-specific feature set.

Since predicting which features will be most valuable is inherently difficult, this initial list should be broad, exceeding the maximum number of features N that will undergo thorough testing.

The second step is to limit the sheer number of possible features to a manageable maximum of N features, depending on the application and available computational power. This step narrows down this list to a more focused set of features. For a suitable preselection of features, consider the computation time, correlation to other features and efficient, standard selection methods (FS) as described in section 2.3.

For large datasets, when simplicity and speed are crucial for a quick and straightforward assessment of feature importance, using individual filter methods like R-squared or ReliefF can be effective. These methods are computationally less intensive and can provide a good initial understanding of feature relevance, helping to focus on a smaller subset of potentially important features for further analysis.

For a more thorough analysis, a combination of tests, following the SFS-approach without applying weights, can be favourable. Using multiple methods can help validate the importance of features. If a feature is consistently identified as important across different methods, it is more likely to be genuinely relevant, rather than a result of overfitting. This is particularly useful in complex datasets where single methods might miss important features. Combining feature selection methods can help mitigate the biases introduced by any single method. For instance, some methods might perform well with linear relationships, while others might capture non-linear interactions or local structures.

This process ensures that the final ranking of feature importance considers the diverse strengths of different methods while allowing for adjustments based on the specific needs of the application. Combining methods provides a more balanced and comprehensive feature selection, reducing the risk of bias and improving the robustness of the results.

Once an extensive feature list is prepared, the selection process is refined by creating predictive models based on various permutations of n features. These models are then tested based on signals with additional disturbances, such as artificially introduced noise or degraded signals.

Since the model's accuracy can be influenced by the interactions between features, it's crucial to account for these interdependencies. To minimize the effect of feature interactions and obtain an individual score for each feature, multiple models are created, each incorporating different combinations of features.

Training separate models for each feature permutation reduces the bias stemming from interrelations among the features. This approach allows for obtaining authentic individual scores for each feature. However, the model itself can introduce bias due to its reliance on specific inherent data structures. Depending on available computational resources, this bias can be further reduced by using different models to calculate the scores

For example, given N features and n as the maximum number of features per combination, the total number of combinations is

$$C = \sum_{k=1}^n \binom{N}{k}. \quad (4.2)$$

For each combination an analytical model is created, delivering a score based on its accuracy. The score for each feature is then derived by averaging the accuracies of all models that include that feature, ensuring that the rating reflects the feature's true predictive value across various model scenarios.

The number of possible combinations of N features increases rapidly when considering all possible combinations, i.e., $n = N$, as described by Equation 4.2. However, it may be sufficient to limit the maximum number of features per combination to a value n smaller than N . While this approach does not evaluate every possible feature combination, selecting an appropriately high value for n can ensure that further increases in n have negligible impact on the resulting scores. In such cases, training models with up to n features is sufficient to achieve reliable and meaningful results.

To find a suitable value for n , Figure 4.8 plots the FMS scores s_{FMS} for $N = 20$ features and for models trained with $n = 1 \dots 5$ features. Particularly for small n , an increase leads to a general rise in the FMS scores because larger feature combinations provide the predictive model with more information.

Assume that the purpose of the selection process is to identify the best features in the prepared set. Then, instead of focusing on the absolute scores of individual features, it is particularly important to consider how the features perform relative to each other. The decisive information lies in the changes in relative accuracies, not in their absolute values.

This means that if the scores s_{FMS} of all features increases by the same factor as n increases, no additional information is gained for distinguishing between features. In such a case, further increasing n becomes redundant, as it does not contribute to improving the feature selection process.

To address this, an improvement rate for each feature i , dependent on n , is defined using the following equation:

$$\text{IR}(i, n) = \frac{s_{\text{FMS},i,n+1}}{s_{\text{FMS},i,n}} \quad (4.3)$$

The scores $s_{\text{FMS},i,n}$ for $n = 1 \dots 5$ are shown in Figure 4.8.

The standard deviation of $\text{IR}(i, n)$ for constant n is defined as:

$$\sigma_{\text{IR}}(n) = \sqrt{\frac{1}{m} \sum_{i=1}^m (\text{IR}(i, n) - \bar{\text{IR}}(n))^2} \quad (4.4)$$

with $\overline{IR}(n)$ as the mean improvement rare across all features i for a specific n .

Consider a case where the scores $s_{FMS,i,n}$ improve by the same factor as n increases. Then it follows that the $\sigma_{IR}(n)$ is equal to 0, indicating that no additional information is available to evaluate the relative importance or interdependence of the individual features.

Thus, $\sigma_{IR}(n)$ serves as a suitable measure of the additional information gained when increasing n compared to $n - 1$. A lower standard deviation indicates smaller relative changes between the scores s_{FMS} , suggesting diminishing returns from increasing n .

The corresponding graph, illustrated in Figure 4.9, shows $\sigma_{IR}(n)$ alongside the number of combinations c . For $n = 3$, the standard deviation drops below 0.02. Considering the rapid rise in the number of combinations for $n = 4$ and the relatively modest additional information gained per combination, it is advisable to limit calculations to $n = 3$ for computational efficiency.

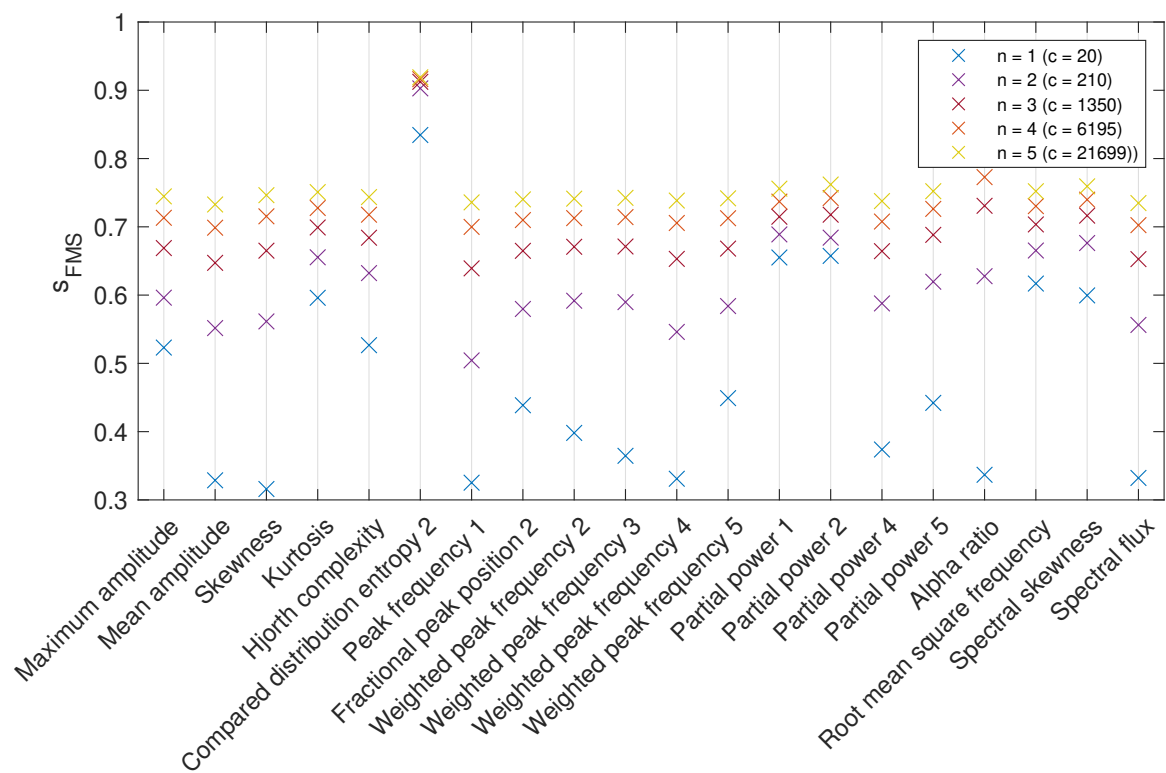


Figure 4.8: Average accuracy of SVM models attributed to the corresponding features. n designates the maximum number of features used for the model.

Example: Determining Weights w_m for an Acoustic Signal from a Gear Hub

Figure 4.10 illustrates the determination of the weights for ANOVA and Discriminit Analysis based on standard features and acoustic data obtained from the gear demonstrator which setup is described in the application section.

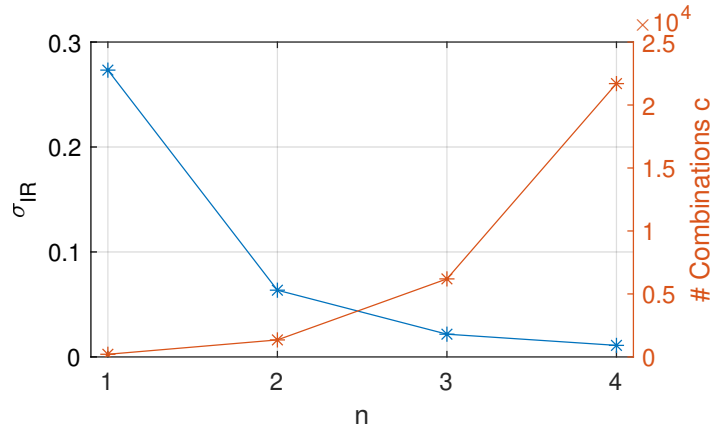


Figure 4.9: Standard deviation plotted versus n which designates the maximum number of features used to train the SVM models.

The top plot shows the scores assigned by an SVM model trained on subsets of three features each. The middle plot displays scores from ANOVA1 analysis, while the bottom plot presents scores from Discriminant Analysis. The features are listed along the x-axis, and their respective scores are plotted on the y-axis. Additionally, the table on the right provides R and R-squared values between the features- and the SVM-scores.

At first the scores are calculated via each scoring algorithm separately and rescaled between 0 and 1. The weights w_m of the feature selection method m are now based on the strength of similarity between the method and the SVM scores. Here the Pearson correlation, also known as the R-value is used for a quantitative measurement of the similarity or the linear correlation.

The Pearson correlation coefficient, $\rho(A, B)$, between two variables A and B is given by

$$\rho(A, B) = \frac{1}{N-1} \sum_{i=1}^N \left(\frac{A_i - \mu_A}{\sigma_A} \right) \left(\frac{B_i - \mu_B}{\sigma_B} \right), \quad (4.5)$$

where μ_A and σ_A are the mean and standard deviation of A , respectively, and μ_B and σ_B are the mean and standard deviation of B [104, 106].

4.3 Global Reconstruction

Measurements in process monitoring are often limited by both the geometric constraints of the investigated process and the physical constraints of the sensors. Each sensor's specific characteristics, such as range, accuracy, and sensitivity, result in localized measurements that cannot fully capture the entire process with a finite number of sensors.

These localized measurements are inherently influenced by the surrounding environment. In theory, information about the surroundings could be inferred by analyzing these localized

4 Enhanced Techniques for Ultrasound based Condition Monitoring

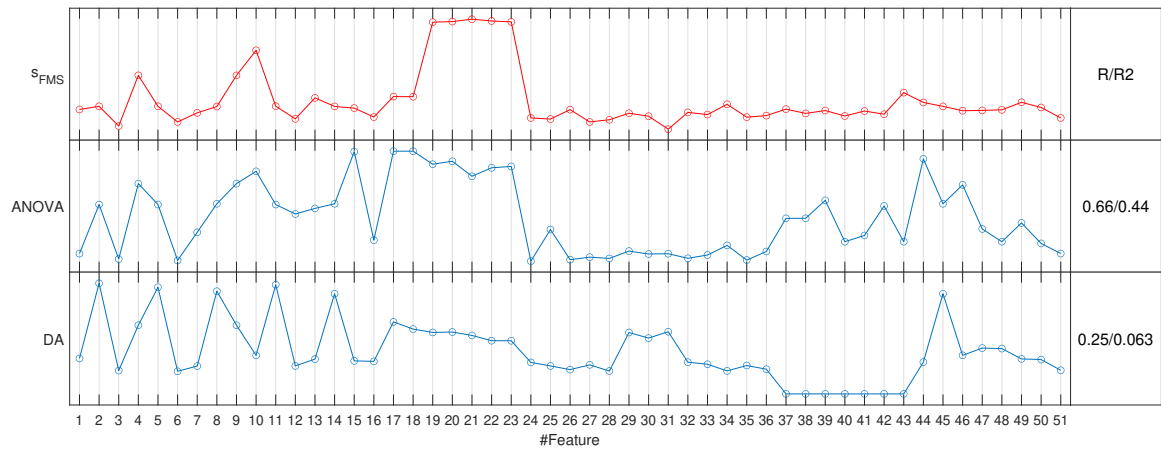


Figure 4.10: Comparison of FMS scores and SFS method, specifically ANOVA and discriminant analysis (DA).

measurements and understanding their physical dependencies. However, limitations in physical understanding and the precision of measurement hardware often prevent achieving the desired accuracy

Consider an active ultrasound measurement using a piezoelectric disc transducer. As described in [20], the ultrasonic beam emitted by the transducer has a finite spread and directivity, meaning the beam's energy is concentrated within a specific angle. Beyond this angle, the intensity decreases significantly, limiting the sensor's effective measurement range to a certain volume directly in front of it. The angle and range of the beam's coverage area depend on the transducer's design and the frequency of the ultrasonic waves. Additionally, as the waves travel through the investigated material, they experience attenuation, which further diminishes the effectiveness of the ultrasonic measurements with increasing distance from the source.

To address this issue and expand the area of investigation, sensor networks are often employed [107, 108]. By integrating multiple sensors, these networks enhance data collection coverage, offering a more comprehensive view of the target area. However, the deployment of sensor networks is experimentally challenging due to limited placement space, potential sensor interference, and the rising financial costs associated with additional sensors. Consequently, gaps in information may arise between sensors. The challenge then lies in accurately inferring the data within these gaps to create a continuous measurement profile.

One potential solution involves considering physical properties of the environment to simulate continuous measurements using the locally restricted measurements as starting points. However, this can be complicated. Defining a physical model tailored to the specific application is necessary, and the boundary conditions must be well understood. Often, simplifications need to be made, potentially making simulations inaccurate.

Therefore, it is desirable to develop a model that is generally applicable without the need for designing intricate physical models for each specific application. Such a model should leverage the locally restricted measurements of the sensor data and clearly accessible local boundary conditions, such as the space or form in which the physical variable changes.

A common situation in condition monitoring involves a binary state change that propagates through space over time, which needs to be continuously monitored in space. Simple cases include a medium spreading in space whose location-specific arrival times (0: medium not present, 1: medium present) should be monitored, as in the injection and infusion experiments discussed later in detail here.

This can be extended to various physical variables such as temperature T gradually changing over time where a threshold T_S should not be exceeded (0: $T \leq T_S$, 1: $T > T_S$).

In the following, a reconstruction method is proposed capable of making predictions for the area between the sensors for such applications. By integrating geometric information and the interrelations of sensor data, a reconstruction algorithm can be created to interpolate and extrapolate measurements across the entire spatial domain. This approach can significantly enhance the reliability and utility of sensor networks in various applications, providing a comprehensive overview of the monitored environment without the need for exhaustive physical modelling.

The reconstruction algorithm aims to estimate and interpolate the spatial data between sensor locations within a given area. This process involves several steps, and it utilizes the principles of graph theory to efficiently compute the desired values.

The first step in the reconstruction method is to prepare and parametrize information which can be deduced from the recorded data and from the geometry of the process. This should include:

- Spatial boundaries: The physical limits of the area under investigation.
- Sensor positions in space: The locations where sensors are placed.
- Localized sensor data: The measurements recorded by the sensors.

The relevant parameters for the reconstruction are listed in Table 4.1 and Figure 4.11 provides an illustration of the graph necessary for the reconstruction. The corresponding input data must be assigned to the parameters, and following the reconstruction process, the output data can be obtained as a result. The parameters and their respective meanings are detailed below.

For the graph and to digitize the space and its boundaries, define nodes distributed throughout the space, each with corresponding spatial coordinates $x_{1,2,3}$. These nodes, denoted as N_j act as a scaffold at which the data is of interest and should be calculated. Each node N_j holds the spatial information $x_{1,2,3}$ and connects it to the calculated or reconstructed data t_j .

Essentially, this data corresponds to the time of a state change from 0 to 1.

The nodes' distribution pattern should be adapted according to the specific application and the desired resolution. For instance, denser node placement can provide higher resolution in areas requiring detailed analysis.

To avoid introducing bias into calculations due to preferred orientations, an unstructured mesh based on Delaunay triangulation is advantageous. In structured meshes, the alignment of the grid can inadvertently influence the results, especially in scenarios where the physical phenomena being modelled do not align with the mesh's regular grid structure. This can lead to anisotropy, where the properties appear to vary depending on the direction.

The connection lines between the nodes form a triangular mesh are denoted as the edges E_n . The Euclidean distances d_n between connected nodes can be extracted from the geometry of the process.

In addition to the Euclidean distances, the reconstruction algorithm assigns time weights T_n to the edges E_n . These weights represent the time that passes between the change of states of the connected nodes. The challenge is to define these time weights T_n so that the final reconstructed times t_j align with the measured times \bar{t}_i at the sample points S_i . The weight function with its input parameters ϵ , δ , and R provides a customizable relationship between the sample points and the remaining nodes. This allows for the incorporation of geometric and physical boundary conditions into the reconstruction process.

Graph theory provides a useful mathematical framework for bundling the available information and efficiently calculating the desired times. In graph theory, a graph consists of nodes connected by edges, and various algorithms can solve problems related to paths, connectivity, and network flow [109].

Figure 4.11 illustrates a network of nodes (black dots) connected by edges (lines), with sample points S_1 and S_2 indicating sensor locations. The goal is to reconstruct the times t_j at each node using the graph.

Table 4.1: Relevant parameters for the reconstruction.

Symbol	Name	Input data	Output data
•	Node N_j	Local coordinates $x_{1,2,3}$	Reconstructed times t_j
—	Edge E_n	Euclidean distances d_n	Time distance T_n
○	Sample point S_i	Measured time \bar{t}_i	
	Weight function w_{in}	ϵ, δ, R	

To calculate t_j efficiently, the shortest path algorithm is used from graph theory. This algorithm finds the shortest path between nodes based on the assigned weights. In this

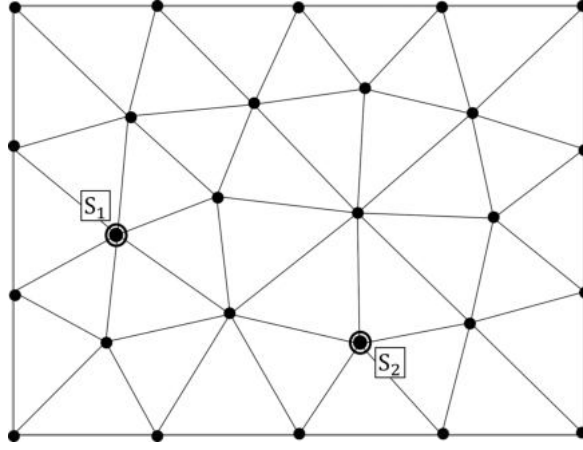


Figure 4.11: A graph representation illustrating the nodes, edges, and sample points in a sensor network. The black dots represent nodes, the lines represent edges connecting the nodes, and the circles labelled S_1 and S_2 represent sample points. This structure is used to reconstruct arrival times and infer spatial data between the sensors.

context, the shortest path algorithm calculates t_j by finding the shortest time-weighted path between nodes based on the time weights T_n . Mathematically, this can be expressed as:

$$t_j = \text{shortestpath}(T_n) \quad (4.6)$$

To use Equation 4.6 the times T_n need to be calculated. This process involves utilizing the given parameters, geometric information, and sensor data to accurately determine the time it takes for a state change to propagate across the network of nodes.

First, the geometric information is incorporated by considering the distances between nodes. Each edge E_n connecting two nodes has a corresponding Euclidean distance d_n , which is used in the equation:

$$T_n = \frac{d_n}{v_n} \quad (4.7)$$

T_n , is the time it takes for the state change to travel along edge E_n , and v_n has units of meters per second (m/s), which can be interpreted as the speed at which the change moves along the edge.

Next, the velocity v_n are adapted by incorporating the influence of the sensor data using the following equation:

$$v_n = \frac{w_{in} \bar{v}_i}{\sum_i w_{in}} \quad (4.8)$$

\bar{v}_i [m/s] are assigned to each sensor i . While it may seem intuitive to interpret these as local, point-specific velocities, they do not necessarily correspond to the true local velocity at which the state change propagates through the space. This discrepancy arises because, typically, only a limited number of sample points are available. Consequently, the reconstruction algorithm tends to favour \bar{v}_i that reflect broader, averaged velocities over larger areas, for more accurate results.

w_{in} represents a weight matrix that determines the influence of sensor i on edge n . The entries of the weight matrix can be controlled with parameters ϵ , δ and R . These parameters allow to adapt the weight matrix according to the geometry of the area and the distribution of the sensors. By carefully tuning these parameters, the influence of each sensor on the corresponding edges can be adjusted, ensuring that the reconstructed data accurately reflects the spatial layout and sensor placements.

In conclusion, it can be inferred that the desired arrival times $t_j(\bar{v}_i, w_{in}, d_n)$ are a function of the average velocities \bar{v}_i , the weight matrix entries w_{in} , and the distances d_n .

While w_{in} and d_n can be determined based on the geometry and sensor distribution, finding the optimal values \bar{v}_i might not be as straightforward.

To determine these parameters, the boundary condition can be used that the measured values \bar{t}_i at the sensor locations should coincide with the calculated values $t_{j=i}(\bar{v}_i, w_{in}, d_n)$. This means that the reconstructed times at the sensor locations should match the actual measured times. Ideal values for \bar{v}_i minimize the error function:

$$f(\bar{v}_i) = (\bar{t}_i - t_i(\bar{v}_i, w_{in}, d_n))^2, \quad (4.9)$$

This function represents the squared difference between the measured time \bar{t}_i and the calculated time $t_i(\bar{v}_i, w_{in}, d_n)$. Minimizing this error function, ensures that the calculated values are as close as possible to the measured values.

To start the optimization process, the average speed $\bar{v}_{i,0} = \frac{d_i}{\bar{t}_i}$ is used as an initial guess. Equation 4.8, Equation 4.7, and Equation 4.6 are subsequently utilized to calculate t_i in Equation 4.9, as well as the remaining times t_j , thereby providing the complete set of information required for the reconstruction results.

The main parameters to consider are the nodes and edges of the mesh and the parameters ϵ , δ and R of the weight function. The following section describes the process for determining suitable parameters to optimize the results.

Mesh Resolution

Creating a mesh with nodes and edges discretizes continuous space, which is necessary for computation. However, the discretizing process introduces approximation errors.

A suitable mesh should not be too dense, as this would be computationally expensive. Conversely, it should not be too sparse, as this would result in a low resolution of the results and inaccurate representation of the space.

Therefore, mesh resolution becomes a critical parameter, typically involving a trade-off between accuracy and computational efficiency.

Concerning accuracy, consider Figure 4.12, which illustrates a path of unit length composed

of N edges. The corresponding equations to calculate the errors are shown in Table 4.2.

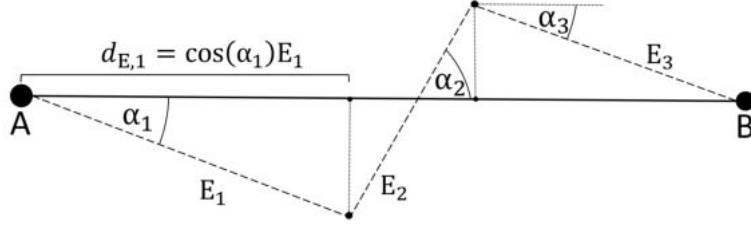


Figure 4.12: Illustration of the inaccuracies introduced by meshing. The solid line represents the actual shortest path between two points A and B in space. The dashed line represents the shortest path along the edges $E_{1,2,3}$ of a graph. The angles $\alpha_{1,2,3}$ represent the deviation of each edge from the shortest path.

Table 4.2: Equations for the error introduced through meshing.

# Edges	Average Error per Edge	Error of Path	Avg Angle
$N = 3$	$\frac{1}{N} \sum_{i=1}^N \frac{E_i - d_{E,i}}{d_{E,i}}$	$\frac{\sum_{i=1}^N (E_i - d_{E,i})}{\sum_{i=1}^N d_{E,i}}$	$\frac{1}{N} \sum_{i=1}^N \alpha_i$

Due to the finite number of nodes and edges, the graph discretizes physical space, introducing inaccuracies. As the length of the edges E_i do not necessarily coincide with the corresponding direct Euclidean distances $d_{E,i}$, the shortest path function produces an error $e[\%]$.

Increasing the number of edges N reduces the error. However, $e(N)$ shows a converging behaviour while the computational effort rises with increasing N . Therefore, there should be a magnitude of N beyond which a further increase does not effectively contribute to a higher accuracy given the rising computational costs.

The following present a mathematical analysis to assess an appropriate magnitude for the edge length. A useful quantity to choose a reasonable edge length L_E is the decrease of the average error per computational minute.

For a first estimation, consider a circle-shaped area of radius R . The error e_p of a path from the centre to the nodes on the boundary of the circle is given by

$$e_p = \frac{\sum_{i=1}^N (E_i - d_{E,i})}{\sum_{i=1}^N d_{E,i}} = \sum_{i=1}^N \left(\frac{1}{\cos(\alpha_i)} - 1 \right), \quad (4.10)$$

With $d_{E,i} = \cos(\alpha_i)E_i$ follows that e is a function of the angle α between the graph's edges E_i and the direct Euclidean path $d_{E,i}$.

Figure 4.13 shows the course of the relevant quantities presented in Table 4.2 over the number of edges N_E per path. As the curves monotonically decrease for $N > 10$, a correction factor C can be introduced to minimize the error. For example, consider a graph whose longest path is composed of 250 edges. According to Figure 4.13, the average error per

edge is $AE_E(N_E) > 3.8\%$, $N_E \in [0, 250]$, which makes $C = 0.038$ a reasonable value for the correction factor. Thus multiplying $\frac{1}{1+C}$ with the Euclidean distances assigned to the graph's weights can mitigate the overestimation of the direct path. Note that in the equation for the error of path, the smaller the error of edges the higher their weight in the calculation. Therefore it follows: Error of path \leq Average Error per Edge.

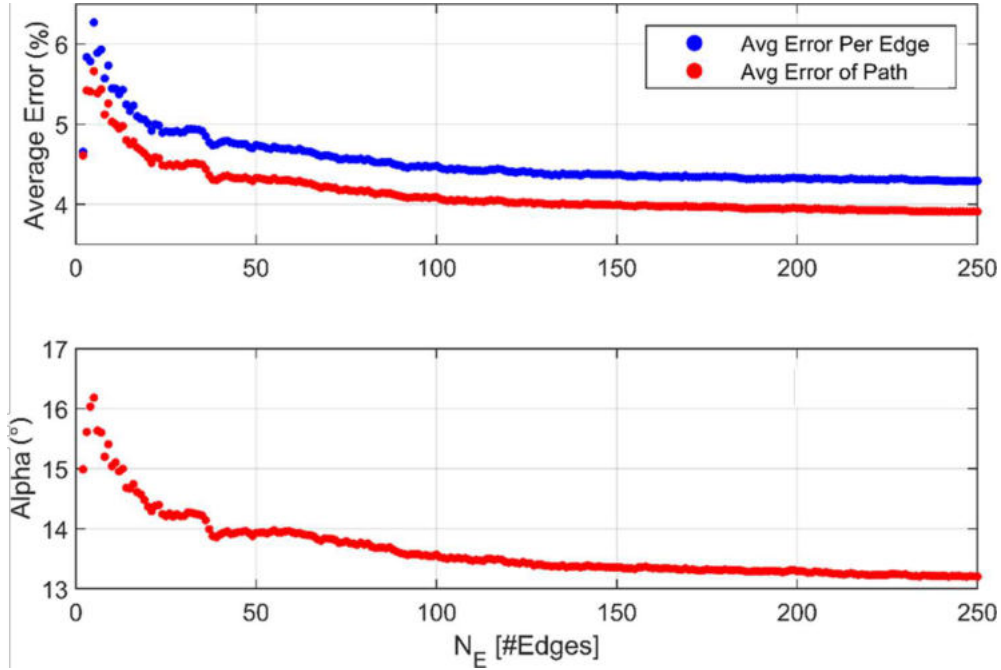


Figure 4.13: Average Errors of a path with N edges calculated using equations from Table 4.2. based on a graph generated by Delaunay triangulation applied to a 2D surface.

Figure 4.14 shows the error of a path for different C , additionally illustrating the case of overcorrecting for $C = 7\% > 3.8\%$. Here, instead of decreasing, the error shows increasing behaviour with rising N_E . Using Figure 4.13 for the identification of a suitable correction term helps to reduce the error to under 2% $N_E \in [0, 250]$ and creates an optimal foundation for the reconstruction.

As shown, with an increasing number of edges per path, the curves gradually flatten. That is, in the limit of finer meshes, the error decreases slower. At the same time, computational effort increases. To obtain a reasonable assessment for computation time, consider an area A with the longest direct path L within this area.

With the average edge length L_E and faces in triangular shapes of area $F_A = \frac{\sqrt{3}}{4} L_E^2$, the number of faces N_F of the graph can be calculated via

$$N_F = \frac{A}{F_A} \tag{4.11}$$

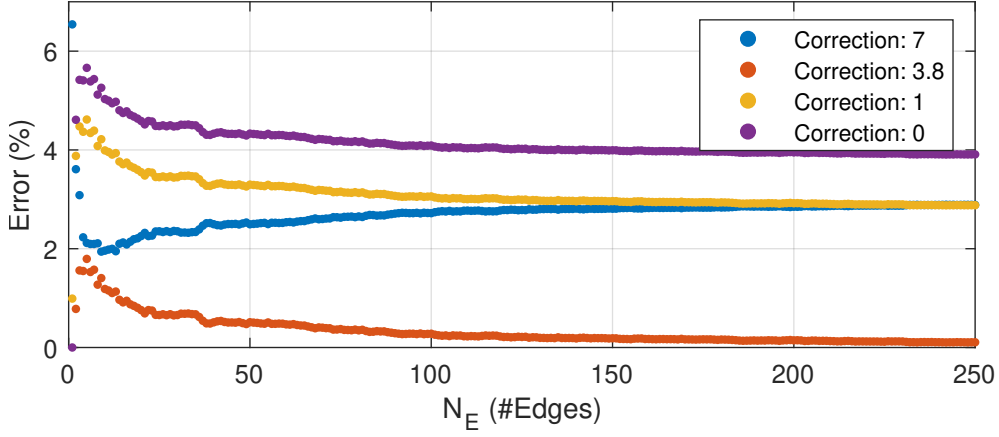


Figure 4.14: Error of a path composed of N edges using different Correction values C .

Figure 4.15 presents the computation time to create a graph of N_F faces. It is important to note that the computation time of the reconstruction algorithm itself is not considered in this context; rather, we focus solely on the creation of the mesh, which is typically generated once for a given geometry. However, regarding the reconstruction computation, it has been demonstrated that the computational time is primarily influenced by the choice of optimization algorithm and the number of variables involved, which directly corresponds to the number of sample points. In this study, we utilize MATLAB's built-in function `fminsearch` [110, 111] to determine the optimal solution. A comprehensive analysis of the impact of sample points and mesh nodes on computational efficiency is subject to further investigation in future work. A polynomial fit of grade 4,

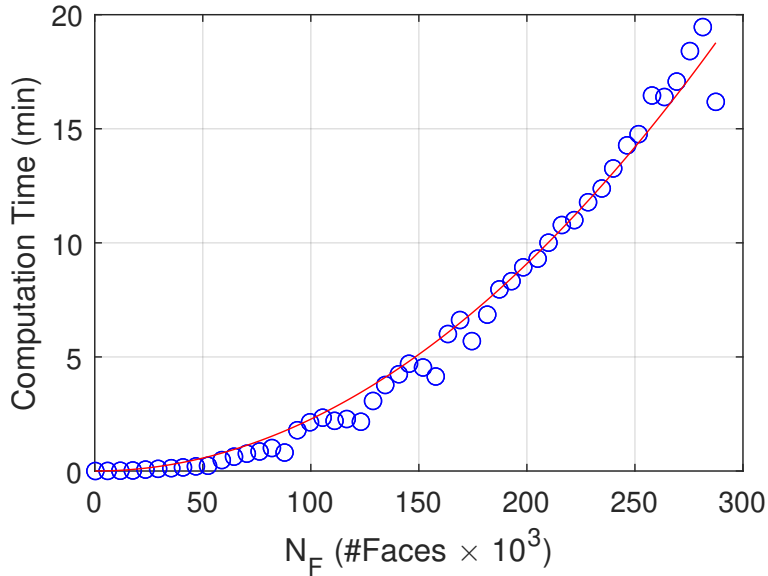


Figure 4.15: Improvement of the accuracy per computational minute over the number of faces N_F .

$$\text{Computation Time} = CT(N_F) = \sum_{i=0}^4 a_i N_F^i, \quad (4.12)$$

is used to assess the grade of dependency between the computation time and the number of faces in the graph. The boundary conditions for the computational time entail f_{CT} and $f'_{CT} > 0$, for $N_F \in [0, \infty)$, with $a_i > 0$ and $i = [0, 1 \dots 4]$. The least square fit yields:

Table 4.3: Least square fit parameters for computation time dependency.

Parameter	Value
a_0	1.36×10^{-46}
a_1	1.13×10^{-14}
a_2	1.09×10^{-8}
a_3	2.89×10^{-33}
a_4	5.33×10^{-23}

The value a_2 is more than six orders of magnitude larger than the others, suggesting a quadratic dependence. Thus, as a first approximation, the computation time CT for an area A and edge length L_E can be estimated by

$$CT(L_E) \approx 1.09 \times 10^{-8} N_F^2 = 1.09 \times 10^{-8} \frac{A^2}{\left(\frac{3}{4} L_E^2\right)}, \quad (4.13)$$

which is indicated as a red line in the graph.

A useful quantity to choose a reasonable mesh size is the decrease of the average error per computational minute. This quantity is denoted as the improvement rate IR, which helps identify the mesh resolution beyond which any further increase is not justified by the computational effort required for the marginal improvement in accuracy. Considering a path composed of N_E edges, the improvement rate is defined as:

$$IR = \frac{AE_P(N_E) - AE_P(N_E + 1)}{CT(N_E + 1) - CT(N_E)}, \quad (4.14)$$

where $AE_P(N_E)$ is the average error of path from Figure 4.13 and $CT(N_E)$ the computational time.

To assess a suitable range for L_E , consider a circle-shaped area with radius R . With the centre as the starting point of the paths, this surface serves as an upper limit for regular 2D shapes. Since the absolute error increases with the length of the path considered, we focus on the longest direct path within the area. Here, the longest path corresponds to R and is composed of N_E edges with length L_E . As a approximation these parameters are related via $N_E = \frac{R}{L_E}$.

Using a circle-shaped area $A = \pi L^2 = \pi N_E^2 L_E^2$ as an upper limit for regular 2D shapes, Equation 4.13 yields

$$CT(N_E) = 1.09 \times 10^{-8} \cdot 16\pi^2 \cdot N_E^4. \quad (4.15)$$

The corresponding curve for $IR(N_E)$ is illustrated in Figure 4.16, and depending on the necessary resolution, it helps to identify an upper limit of N_E for a time-efficient creation of

the graph. For instance, considering a geometry with a longest path of 1 m, the improvement rate of accuracy significantly decreases beyond an edge length of $L_E = \frac{L}{N_E} = \frac{2\text{m}}{200} = 1\text{ cm}$.

After choosing an appropriate mesh and graph, the following section presents further insight into the weight function and the identification of its suitable parameters.

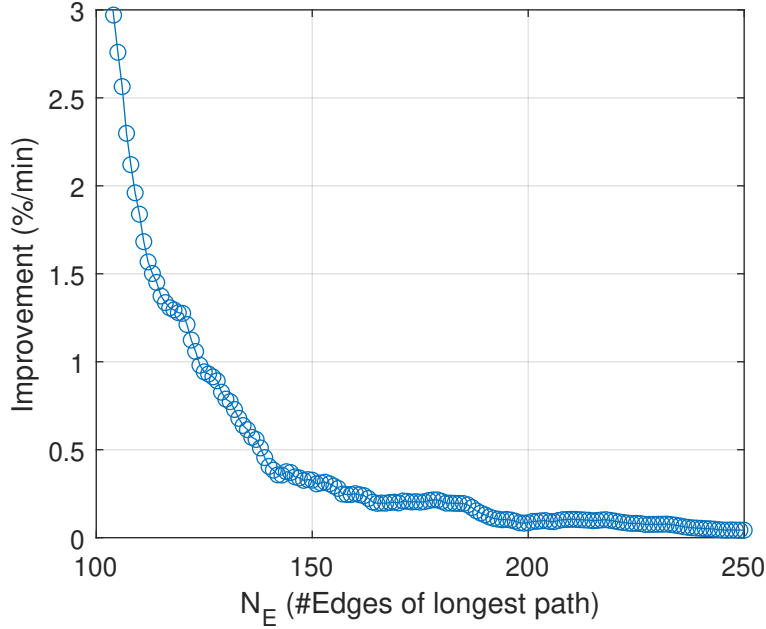


Figure 4.16: Improvement of the accuracy per computational minute over N_E . N_E represents the number of edges of the longest, direct path between two nodes.

Optimizing the Weight Function

For improved reconstruction of the flow front, it is favourable to adapt the weight function for the specific problem. Here, a guideline on how to identify appropriate parameters with respect to the given geometry is presented.

The weight matrix w_{in} consists of a radial w_{rad} and angular w_{ang} contribution and is defined as:

$$w_{in} = \frac{w'_{in}}{\max_i(w'_{in})}, \quad (4.16)$$

where

$$w'_{in} = w_{rad,in} + R \cdot w_{ang,in}. \quad (4.17)$$

The radial and angular weights are given by:

$$w_{rad,in} = \frac{1}{1 + \left(\frac{1}{\epsilon} - 1\right) \left(\frac{x_{in}^2}{d_A}\right)}, \quad (4.18)$$

$$w_{\text{ang},\text{in}} = 1 - \sin^{\delta} \left(\frac{\phi_{\text{in}}}{2} \right), \quad (4.19)$$

with x_{in} as the distance between sensor i and edge n . ϕ_{in} is the angle between edge n and the connecting line of the source, the origin of the state change propagation, and sensor i , illustrated in Figure 4.17.

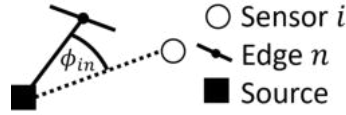


Figure 4.17: Definition of angle ϕ_{in} used to calculate w_{ang} .

The parameters ϵ and δ are used to adapt the radial weight w_{rad} and the angular weight w_{ang} , respectively. R controls the angular weight's contribution to the total weight w_{in} . The average distance of the sample points d_A is defined by its spatial distribution, thus constant for a given setup.

Figure 4.18 shows w_{rad} and w_{ang} for various parameters. The parameter $\epsilon \in [0, 1]$ corresponds to the value at the average distance $w_{\text{rad},\text{in}}(x_{\text{in}} = d_A)$. Thus, decreasing ϵ narrows the radial influence of the sensors, and vice versa. Decreasing $\delta \in [0, \infty]$ focuses the influence on angles close to 0° and 360° .

Finally, increasing R shifts the focus on w_{ang} , while a decrease below 1 emphasizes w_{rad} .

Figure 4.19 shows the weight matrices $w_{\text{rad},\text{in}}$, $w_{\text{ang},\text{in}}$ and w_{in} for a rectangular shape and 10 sample points. w_{rad} and w_{ang} are independent of the sample points. However, following Equation 4.17, w'_{in} considers the relation of the sample point distributions autonomously, resulting in robust results for varying sensor setups. For example, as shown in Figure 4.19, the weight function for the sensor marked in red is particularly deformed by the adjacent sensors, taking into account their influence in nearby areas according to the relative orientation to the injection point.

Despite the self-adapting nature of the weight matrix, a careful selection of the parameters increases the accuracy of the results. To this end, it is useful to estimate appropriate arrival times $\bar{t}_{j,\text{Ref}}$ for every node as a reference. This can be achieved by assuming reasonable flow front velocities from which $\bar{t}_{j,\text{Ref}}$ can be derived or, alternatively, by conducting a reference experiment.

With the average velocities assigned to the sample points, the arrival times $\bar{t}_{j,\text{calc}}$ can be calculated using Equation 4.6, Equation 4.7 and Equation 4.8. With the error function in Equation 4.20, $\bar{t}_{j,\text{calc}}$, which depend on the weight function's parameters, can be compared with $\bar{t}_{j,\text{Ref}}$.

$$f(w_{\text{tot},\text{in}}) = \left(\bar{t}_{j,\text{calc}}(w_{\text{in}}) - \bar{t}_{j,\text{Ref}} \right)^2. \quad (4.20)$$

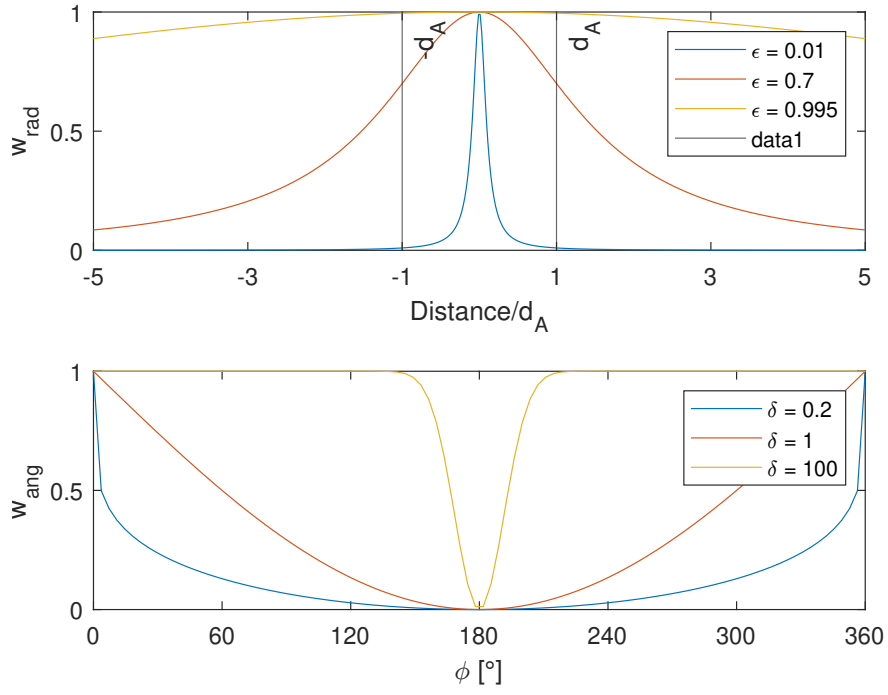


Figure 4.18: Radial w_{rad} and angular weight w_{ang} for different parameter ϵ and δ .

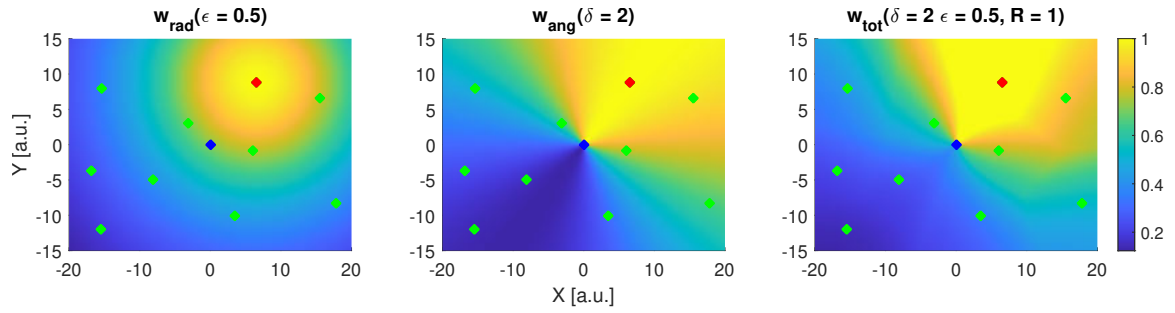


Figure 4.19: 2D illustration of the weight functions for the sample point marked in red. The green dots indicate the rest of the sample points and the blue dot the injection point.

Minimizing $f(w_{\text{tot,in}})$ should then deliver suitable parameters for $w_{\text{in}}(\epsilon, \delta, R)$.

5 Application

In this chapter, the three approaches introduced in Chapter 4 are demonstrated using the experimental setups described in Chapter 3.

First, the adaptation process is applied to the rheometer experiments to illustrate how features can be optimized to assess rheological parameters. These insights are then transferred to the T-RTM experiments, where the approach is used to evaluate the state of polymerization.

Next, the feature selection approach is tested on the gear demonstrator, using data collected over a period exceeding one year. This approach aims to identify the most relevant features to ensure high prediction accuracy throughout this extended timeframe.

Finally, the reconstruction method is validated using the VAP experiments. Then, the algorithm is applied to the more complex T-RTM process to reconstruct the temporal progression of the flow front.

5.1 Feature Adaption: Rheological Measurements

In this section, the application of the proposed feature adaptation method to rheological measurements is demonstrated. A rheometer (see Chapter 3) is equipped with an ultrasound sensor to enable the simultaneous acquisition of ultrasound and rheometer data. The goal is to adapt the extracted features from the ultrasound data to align as closely as possible with the rheometer measurements. This demonstrates that the ultrasound data contains information about the rheological processes in the sample, laying the foundation for measuring rheological changes in the sample using ultrasound sensors, instead of relying on labor-intensive rheometer experiments.

The setup consists of a multilayer structure, and the impulse echo method is used for ultrasound data acquisition (see Chapter 3).

To analyse the signal, consider the signal profile shown in Figure 3.16, where materials 1 and 3 correspond to the lower and upper plates of the rheometer, and material 2 represents the sample under investigation. In time-domain feature extraction, applying a time gate helps isolate critical portions of the signal while excluding irrelevant data. A time gate defines specific limits, retaining only the desired segment of the signal for analysis. This approach improves the relevance and accuracy of feature extraction by focusing on key components, such as the first echo in ultrasound data, while discarding the rest.

As illustrated in Figure 5.1, the ultrasound signal at $T = 2$ min is segmented using a time gate, keeping only the relevant portion. This gated segment is then processed to extract a feature, which can be tracked over time to provide insights into the underlying processes. By focusing on specific signal segments, the gate concept optimizes feature extraction, emphasizing the most informative parts of the data.

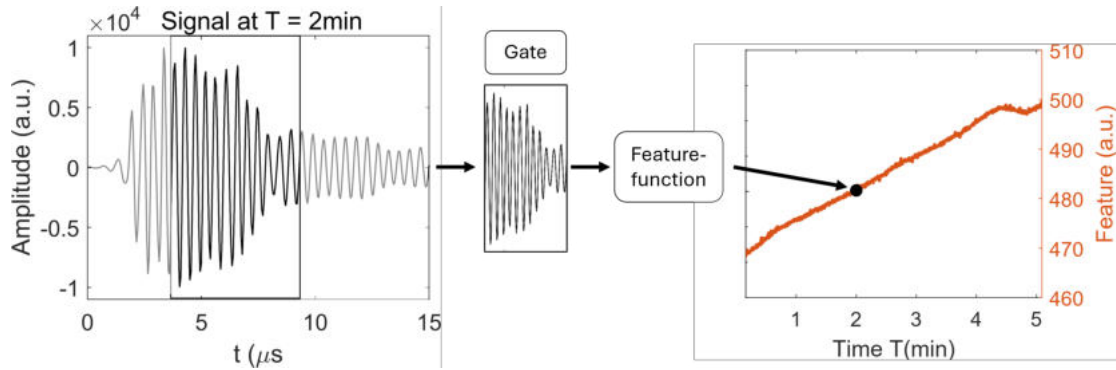


Figure 5.1: Schema of feature extraction using the gate concept.

Similarly, in the frequency domain, spectral energy regions (partial powers) can be analysed. These regions represent the proportion of energy within a selected frequency range relative to the total energy of the signal. The specific frequency ranges to be analysed should be chosen based on the task and the effects under investigation.

Combining empirical knowledge with a preliminary analysis of the ultrasonic signals and their frequency spectra can lead to a well-informed estimation of appropriate parameter settings for gates and frequency ranges.

In practice, however, the clear identification of echoes in the time domain can be complicated by interfering reflections, deviations in sensor alignment and coupling, and other measurement artefacts. This highlights the importance of robust feature extraction methods that can withstand these influencing factors.

Systematic variation of gate positions and frequency ranges contributes to the further optimization and interpretation of ultrasonic signals. This approach ensures that the extracted features remain reliable and meaningful despite the presence of potential disturbances in the measurement environment.

To determine the optimal parameters for feature calculation, follow the approach outlined in the previous chapter. Figure 5.2 specifically illustrates this process for the parameter of the gate. The process begins by varying the gate's start position and width. Features are extracted from the gated segment and compared to reference measurements, such as rheological data, to evaluate how effectively the gated data captures meaningful physical phenomena. A score is then calculated to quantify this comparison, and the results are visualized iteratively in a heatmap to identify the optimal gate settings. The focus is on two specific features for deeper investigation: partial power and RMS.

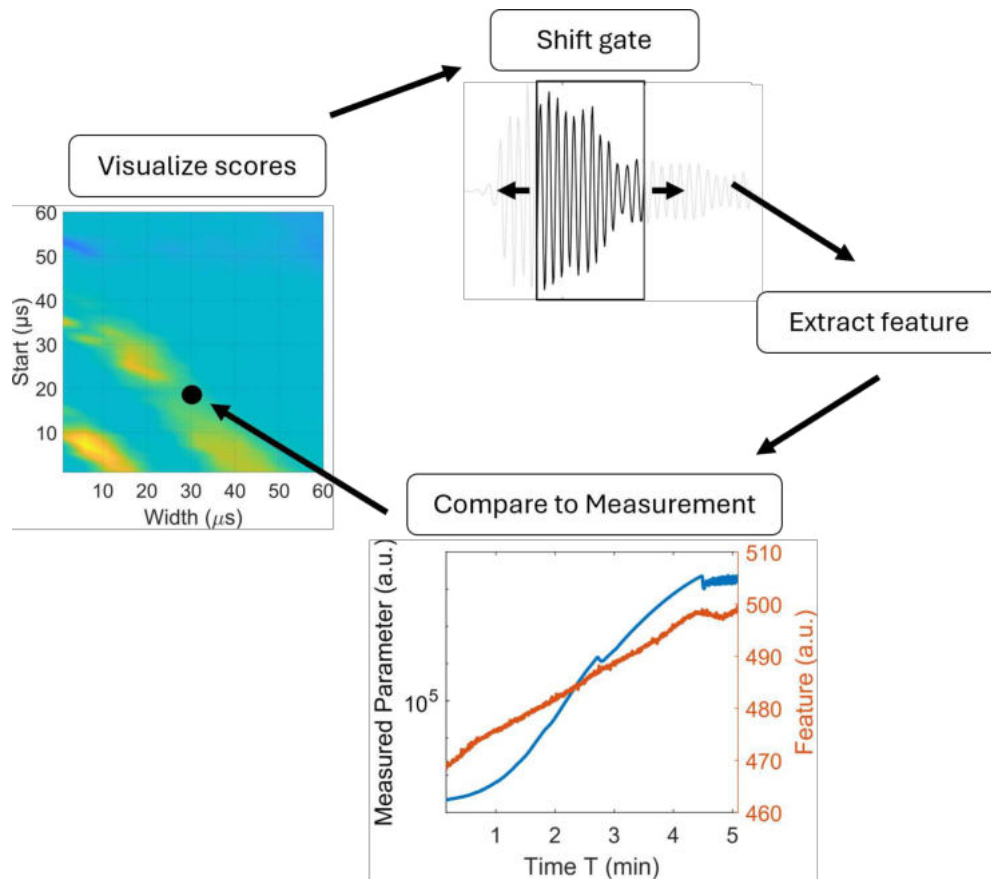


Figure 5.2: Workflow for optimizing gate settings and feature extraction.

Partial power feature is chosen as a representative for a frequency domain feature because it offers the flexibility to adapt its parameters, specifically the length and starting point of the frequency intervals to be investigated. This allows us to tailor the feature extraction to the most relevant frequency ranges. In contrast, a feature in the time domain can be extracted from a gate where both the starting point and length can be varied.

The RMS feature was chosen by a preliminary evaluation with random gate settings and various time domain features. For a specific gate position, the feature that showed the highest correlation (R-value) to the rheometer measurements was awarded a point. The results of this evaluation are illustrated in Figure 5.3, highlighting the RMS value with the highest score.

To determine the optimal frequency range for calculating partial powers using the R-value as the evaluation criterion, the length and starting point of the frequency range were systematically varied within the ultrasonic sensor's operating range of 1.4 MHz to 3 MHz. To simplify the process and reduce the degrees of freedom, the time gate used for calculating partial power was fixed, spanning the entire signal segment.

For each parameter setting, calculate the partial power feature and its corresponding R-value relative to the logarithmic progression of viscosity, as stronger correlations were generally

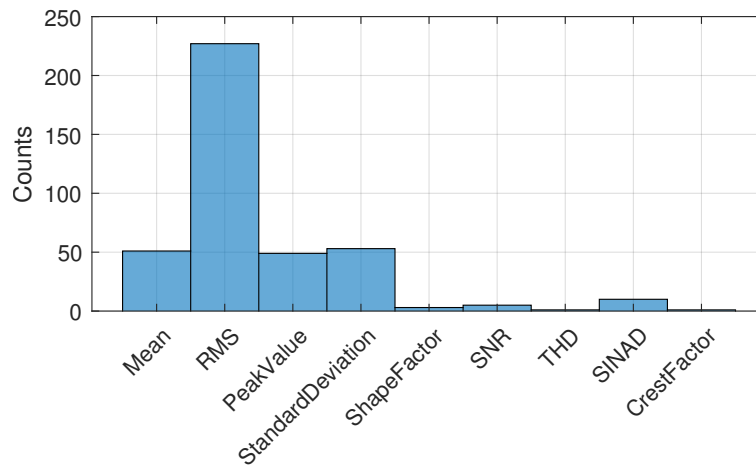


Figure 5.3: Each point is assigned the feature with the highest absolute R-value at a fixed gate position. The histogram illustrates the distribution of points across randomly varied gate positions.

observed compared to a linear progression. Similarly, R-values for the RMS feature were calculated by varying the time gate.

The R-values are depicted in Figure 5.4 and Figure 5.5 for the partial power and RMS-feature, respectively as functions of both the frequency and time windows. To facilitate the distinction of high R-values, a bilogarithmic colour scale is used. This colour scale helps in identifying the maximum values in the diagram. A high R-value indicates a strong correlation with the measured viscosity, with the sign indicating whether the correlation is positive or negative.

A notable observation in Figure 5.4 is the linear distribution of the maximum positive R-values. These values consistently show that the frequency range ends uniformly around 2.2 MHz. The starting value, however, can be chosen flexibly without a significant drop in the R-value. Therefore, the frequency ranges with high correlation to the rheological measurement values encompass the sensor's natural frequency and the lower frequencies. For comparison, the ultrasonic pulse and its corresponding frequency spectrum in an empty measurement without a sample are shown in Figure 5.6.

Large negative R-values are observed with a variable length frequency window starting at approximately 2.2 MHz. Consequently, to achieve strong correlations with the rheological measurements, it is advantageous to set the start or end of the frequency window at 2.2 MHz. When the frequency window includes ranges both above and below this frequency, the negative and positive contributions to the spectral energy density compete, resulting in a decrease in correlation. This pattern is consistently observed across various rheometer experiments, suggesting a general recommendation for the bounds of spectral energy densities. However, further research is needed to extend these findings beyond the specific experimental setup used here.

Additional studies on the dependencies between spectral energy densities and the resonance

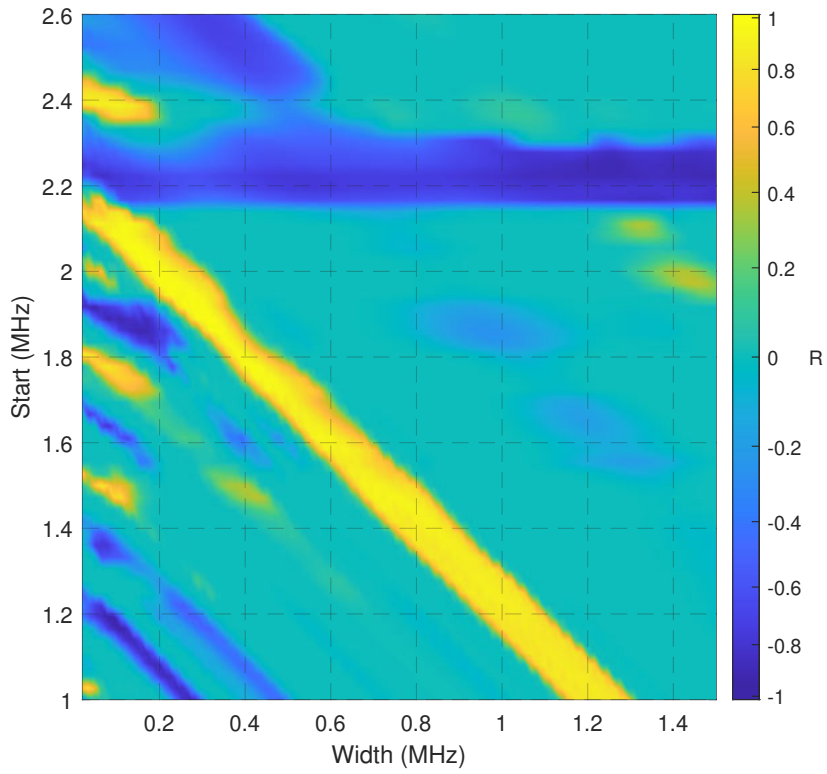


Figure 5.4: R-values on a bilogarithmic colour scale for the partial power feature as a function of the frequency window.

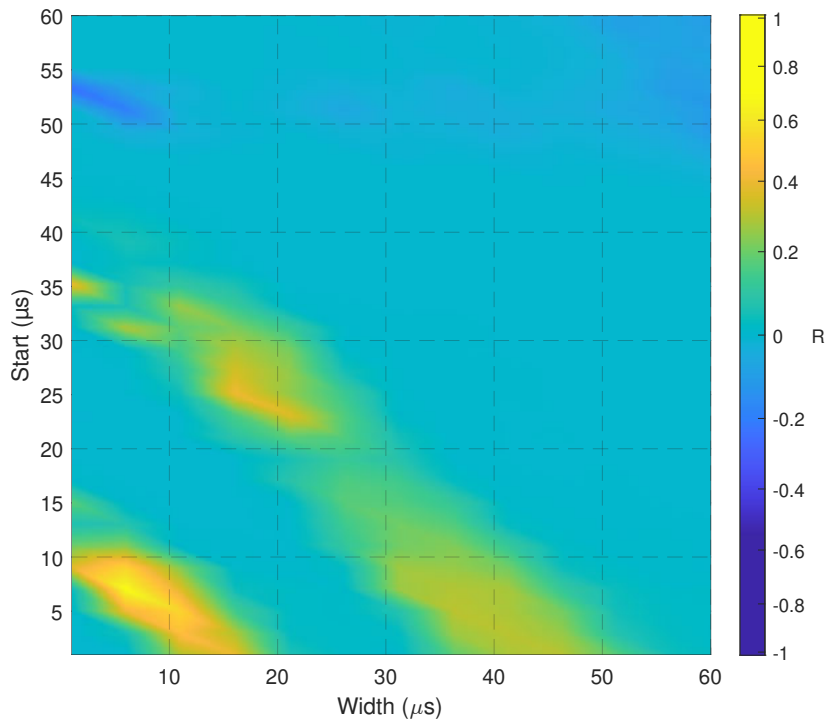


Figure 5.5: R-values on a bilogarithmic colour scale for the RMS depending on the gate position and width.

frequency of the ultrasonic sensors can lay the groundwork for adaptive algorithms that automatically determine suitable parameters. This could lead to more efficient and accurate analyses across different experimental conditions and setups.

The reduction in the energy content of higher-frequency ultrasound waves with increasing viscosity and ongoing polymerization aligns with thermoelastic dissipation. This phenomenon results in increasingly stronger damping of higher-frequency ultrasound waves [20].

Figure 5.5 shows the results for the R-value obtained from varying the gate parameters for the RMS feature. The highest values are concentrated at start times and gate widths between $1\ \mu\text{s}$ and $10\ \mu\text{s}$, with maximum values around $7\ \mu\text{s}$ and $6\ \mu\text{s}$, respectively. The calculated travel times for the first and second main echoes are approximately $7\ \mu\text{s}$ and $14\ \mu\text{s}$ after pulse emission, theoretically placing the first main echo within the gate range. However, this echo is not clearly identifiable in the signal shown in Figure 5.6.

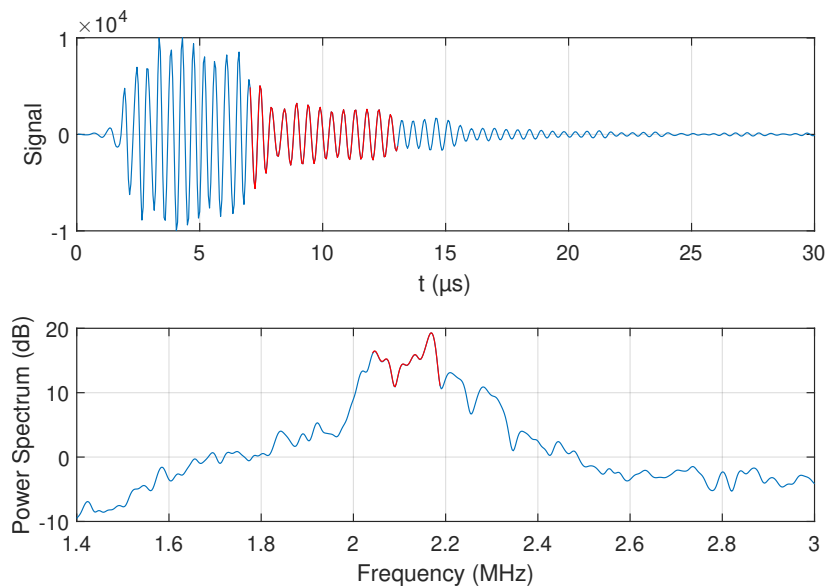


Figure 5.6: Impulse and frequency spectrum of the ultrasound sensor used. The areas marked in red are within the time or frequency window ideal for the RMS and partial power feature.

Figure 5.7 and Figure 5.8 compare the partial power feature and RMS with the measured viscosity, using parameter settings deemed optimal based on the result plots in Figure 5.4 and Figure 5.5. Generally, the partial power exhibit higher correlations. The increase in the RMS value reflects a rise in echo amplitude, caused by altered reflection conditions due to the progressing polymerization.

In Figure 5.9 and Figure 5.10, the partial power and RMS values, with the identified optimal parameters, are applied to another experiment. Despite the disassembly and reassembly of the experimental setup and the associated readjustment of the sensor, a high correlation, particularly of the spectral energy density with the progression of viscosity, is observed.

5.1 Feature Adaption: Rheological Measurements

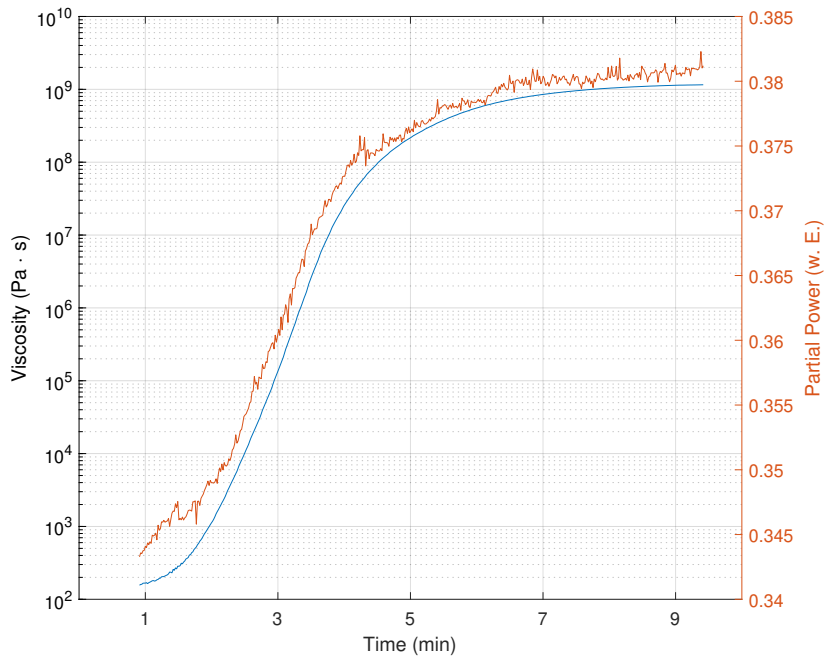


Figure 5.7: Temporal progression of the Partial Power feature in a frequency window from 2.05 MHz to 2.19 MHz compared to the logarithmically plotted viscosity.

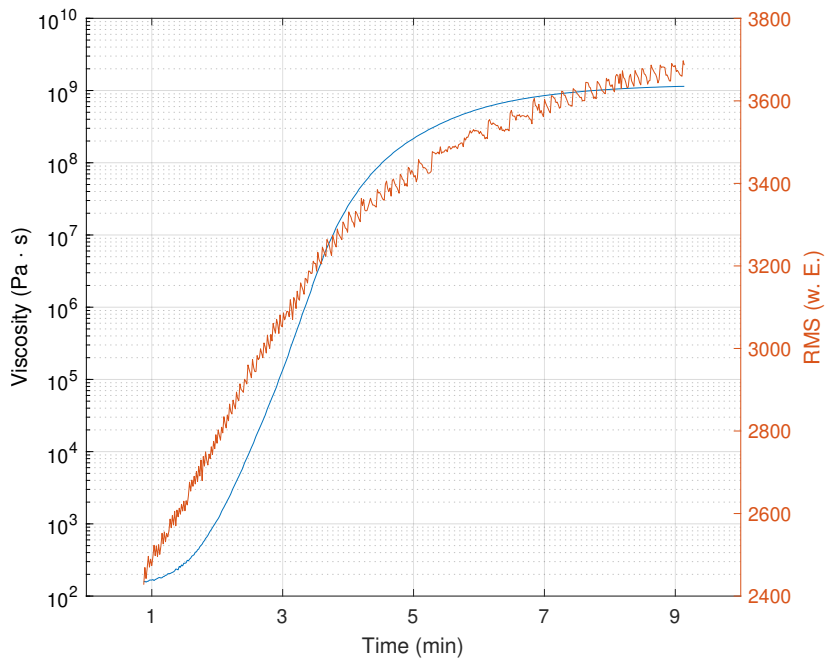


Figure 5.8: The temporal progression of the RMS value in a time window from $7 \mu\text{s}$ to $13 \mu\text{s}$ after pulse emission compared to the logarithmically plotted viscosity.

This enables the estimation of the temporal changes in viscosity based on ultrasonic measurements, allowing for the monitoring of the saturation behavior of the polymerization reaction. This is especially valuable for industrial processes like the T-RTM process.

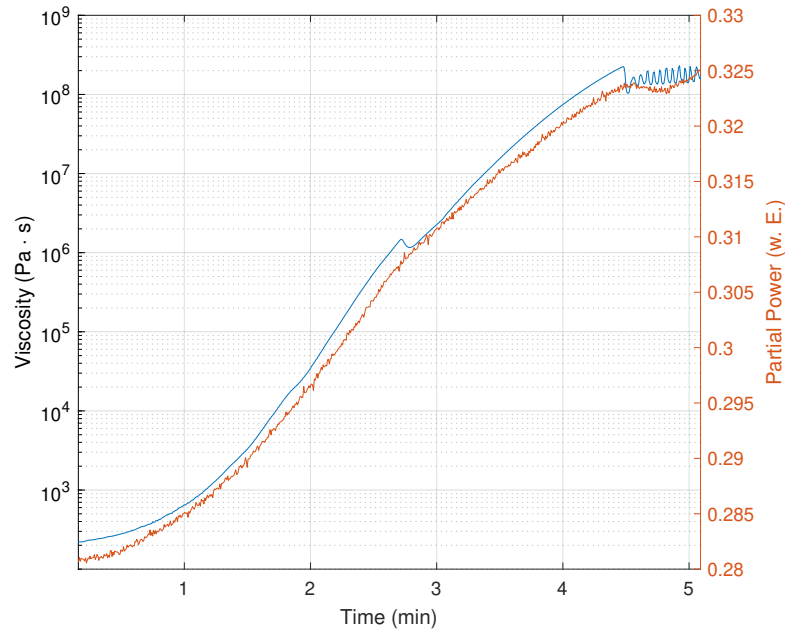


Figure 5.9: Temporal progression of the partial power feature for a different measurement and with the same settings for the frequency window as in Figure 5.8.

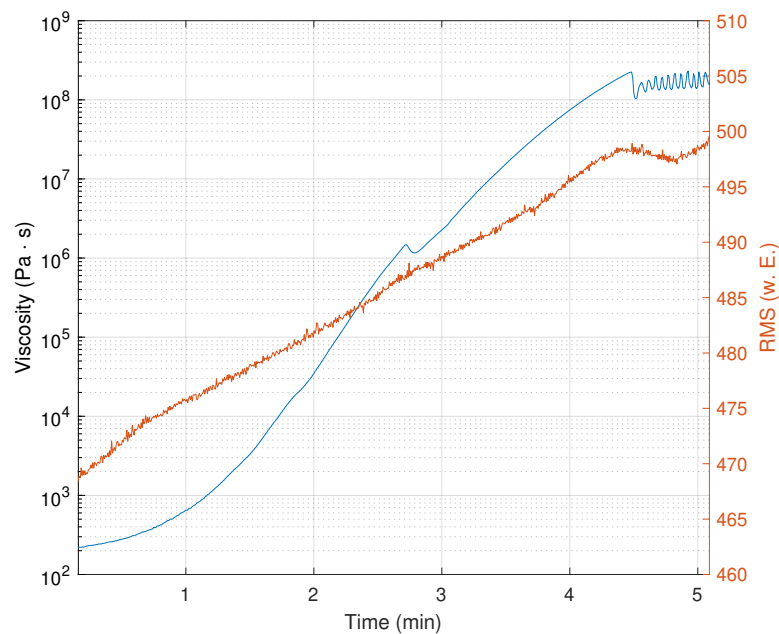


Figure 5.10: The temporal progression of the RMS value for a different measurement and with the same settings for the time window as in Figure 5.8.

To investigate whether the feature parameters identified could be applied across different experiments for this specific US-sensor, the same parameters identified for the rheometer experiments are used and applied to the T-RTM process.

In the T-RTM experiments there is no sensor available to directly measure the degree of polymerization as a benchmark measurement. However, the tool was equipped with DEA sensors. In [78, 85] it has been shown that based on the DEA data, it was possible to deduce a conversion factor α to assess the time of sufficiently advanced polymerization. In the following this time can be used as a benchmark.

Here the task was to monitor the ongoing polymerization in the T-RTM process using US data. In previous experiments, described in Chapter 3 a relationship between viscosity and the state of polymerization was identified and since it was established that viscosity can be tracked using US data, it should be therefore possible to assess the polymerization process through the US data.

These previous findings can be compared to the measurements of this work, as the same experimental setup was used. Figure 5.11 compares the viscosity and the partial power feature to the measured conversion ratio, which is defined as 1 - rest monomer content. The curves show similar behaviour with the plateau of the viscosity marking the point when the polymerization accelerates.

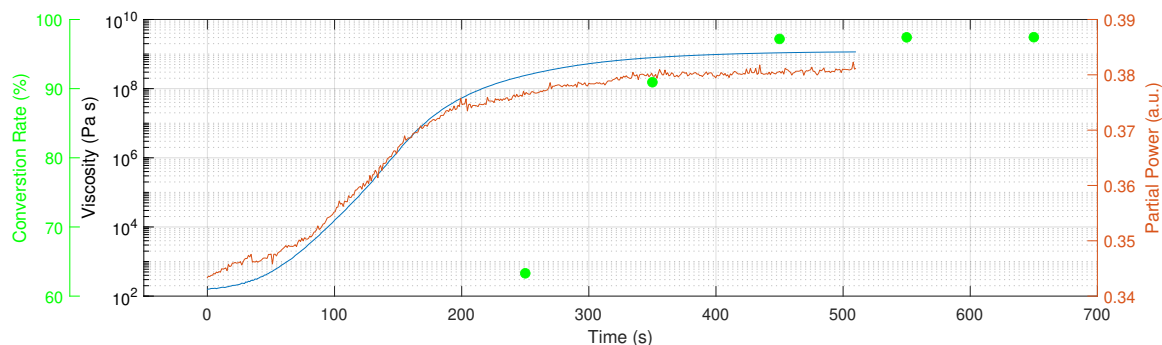


Figure 5.11: Comparison of the measured viscosity, the partial power features and the conversion of ϵ -caprolactam found in [80].

The data shows a rapid increase followed by saturation, indicating that viscosity and partial power, as well as the conversion, reach a plateau, although at slightly different times.

To establish a relationship between the partial power feature and the state of polymerization, the time shift between the curves needs to be assessed. For this purpose consider Figure 5.12. The upper plot compares the normalized partial power feature with the conversion rate. The first measurement point is defined above 98 % conversion as the time at which polymerization is sufficiently advanced for practical applications like T-RTM, occurring at 450 s. The point where the normalized partial power value consistently exceeds 0.9 is defined as

the beginning of its saturation phase .

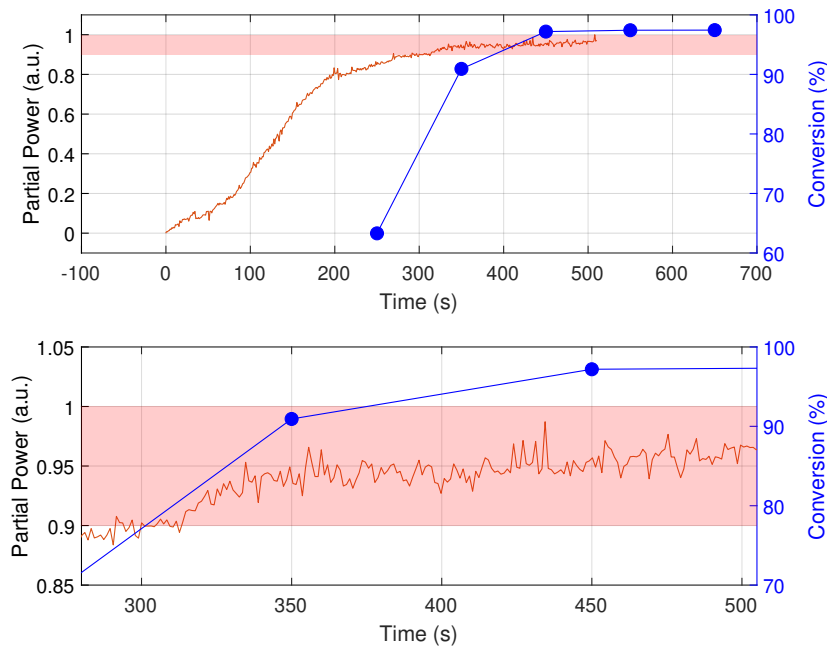


Figure 5.12: Relationship between partial power and polymerization state. The upper plot compares normalized partial power with conversion rate, showing a time shift between partial power saturation and when conversion exceeds 98 %, marking sufficient polymerization. The lower plot zooms in on critical time points.

The lower plot in Figure 5.12 provides a close-up view of the area of interest to facilitate easier identification of critical times. At around 315 s, the partial power begins the saturation phase.

This means that after the partial power value stabilizes, it takes an additional 135 s for the polymerization to reach its saturation level.

Next, the aim was to apply these observations to the T-RTM process. The application should test the approach's applicability beyond the rheometer experiment.

However, the general applicability of such an estimation face challenges like:

- **Material and scalability:** Although the same material is used, there are significant differences in size.
- **Temperature profile:** Both experiments target the same final temperature (around 160 degrees Celsius), but with different heating rates.
- **Process dynamics:** The T-RTM process involves more material and dynamic conditions compared to the small static samples in rheometer tests.

For validation, the conversion times for the T-RTM process, estimated in [85], are used. The dielectric signals from DEA-sensors have been combined with a reaction kinetic model

based on quasi-isothermal differential scanning calorimetric investigations. This allows to monitor the conversion during polymerization, achieving a degree of conversion of 98.5 % approximately 342 s after injection.

This value is defined as the target value and compared with the expected value derived from the partial power features. Figure 5.13 illustrates this comparison process.

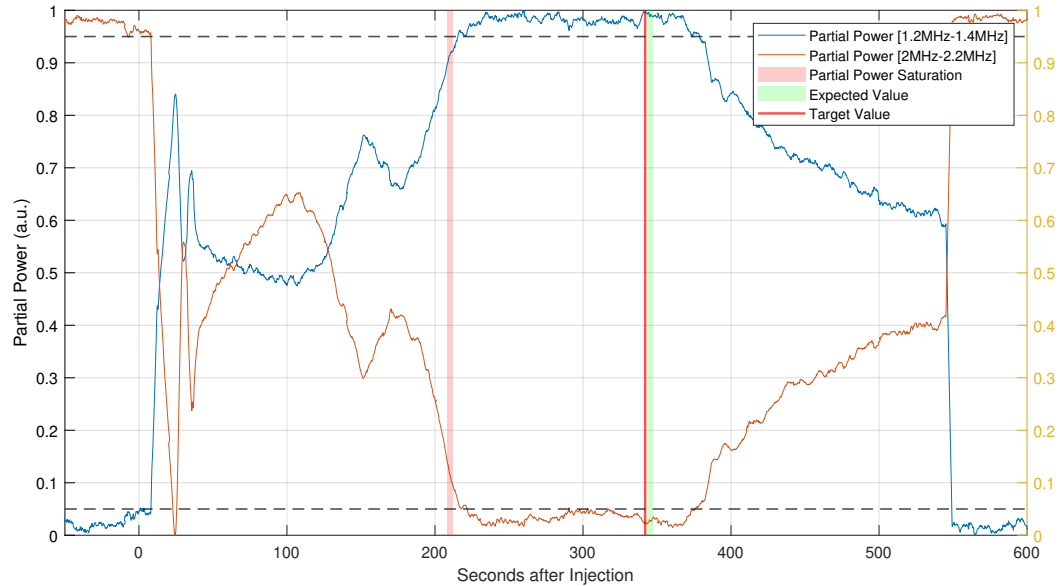


Figure 5.13: Determining the polymerization time based on partial power features.

Based on the r -values tested, limits are established for the partial power. Applying the 90 % threshold method, the time of reaching the saturation value is determined, which is around 210 s. The estimated time shift to complete polymerization was assessed to be 135 s, leading to an expected saturation point of polymerization around 345 s. This compares well with the expected value at 342 s, indicating a good assessment.

5.2 Feature Selection: Gearbox Test Bench

Here, the Feature Model Selection (FMS) and Standard Feature Selection (SFS) approaches (see Chapter 4) are demonstrated using the gearbox test bench (see Chapter 4). The necessary data for applying and validating these methods was collected over an extended period of more than one year. During each data collection session, the test bench was operated in three different gears. The goal is to identify robust features using FMS and SFS that can reliably distinguish between these gears across all datasets and throughout the entire timeline.

Before thoroughly assessing the performance of each individual feature, the proposed selection method is tested on preselected features listed in Table 5.1.

The features in this list were selected based on following considerations. Part of this list

comprises frequently used features with proven performance in various applications (AE) [22, 34, 90]. For instance, in [34] these features were successfully utilized for analysing acoustic emission signals during drilling processes.

To these features, common statistical features are incorporated, that are fast to compute. These features allow for efficient analysis while maintaining high relevance to the signal characteristics.

Additionally, features commonly used in other fields, such as the Hjorth parameters in electroencephalography (EEG), are included. Initially employed in medical electroencephalography signals, Caesarendra et al. [66] suggested that these features could be effectively used for condition monitoring [67].

Additionally, as proposed in [112] Spectral Negentropy is included, which measures the spectrum of the negentropy of the squared envelope and its spectrum, which is reported to capture the impulsive nature of faults in frequency bands.

Finally, features are considered that analyse the underlying data distribution, including Compared Distribution Entropy 1-2, Compare Gaussian Fit, Compare Extreme Value Fit, and Compare Uniform Fit. Compared Distribution Entropy calculates the change in kernel-smoothed distribution entropy when ignoring 20 % or 30 % of outlier values from a dataset, while the other features evaluate how well a dataset fits Gaussian, Extreme Value, and Uniform distributions. These features were identified through the Highly Comparative Time-Series Analysis (HCTSA) and have shown good performance in feature selection methods.

To assess the importance of individual features, the feature selection method outlined in section 4.2 was followed. Figure 5.14 shows the general approach, while Figure 5.15 illustrates a specific example using the RMS feature.

The evaluation involved determining the performance of each feature using a Support Vector Machine (SVM) model. Specifically, models were created for every possible combination of feature subsets containing one to three features, drawn from a preselected list of 51 features in Table 5.1.

This approach resulted in the generation of $\sum_i^3 \binom{51}{i}$ unique models, allowing for an in-depth examination of how various feature combinations performed in distinguishing between the different gears. Each model's performance was assessed based on the percentage of correct predictions it produced.

To tailor the evaluation results to specific needs, test datasets with either natural or artificially introduced distortions can be chosen. This customization helps identify features that perform particularly well in handling specific types of distortion, providing insights into their robustness and suitability for varying conditions.

To calculate the contribution of a specific feature, only the models in which that feature was included were considered. The performance scores of these models were averaged and assigned exclusively to that specific feature. This ensured that each feature's score reflected only the instances where it was actively contributing to the model's predictions.

Table 5.1: Overview of Features and Domains.

No.	Feature	Domain	Notes
1	Maximum amplitude	Time	FS
2	Root mean square (RMS)	Time	AE
3	Mean amplitude	Time	AE
4	Mean absolute amplitude	Time	AE
5	Standard deviation	Time	FS
6	Skewness	Time	FS
7	Kurtosis	Time	FS
8	Energy	Time	FS
9	Sum absolute amplitude	Time	AE
10	Sum root amplitude	Time	AE
11	Root energy amplitude	Time	AE
12	Crest factor	Time	FS
13	Clearance factor	Time	FS
14	Hjorth activity	Time	Proven in EEG analysis [66]
15	Hjorth mobility	Time	Proven in EEG analysis [66]
16	Hjorth complexity	Time	Proven in EEG analysis [66]
17	Compared distribution entropy 1-2	Time	Assesses change in distribution entropy
19	Compare gaussian fit	Time	Evaluates Gaussian distribution fit
20	Compare extreme value fit	Time	Evaluates Extreme Value distribution fit
21	Compare uniform fit	Time	Evaluates Uniform distribution fit
22	Spectral entropy	Frequency	Captures impulsive nature of faults [112]
23	Spectral negentropy	Frequency	Measures spectrum negentropy [112]
24	Peak frequency 1-5	Frequency	AE
29	Fractional peak position 1-3	Frequency	AE
32	Weighted peak frequency 1-5	Frequency	AE
37	Partial power 1-6	Frequency	AE
43	Alpha ratio	Frequency	FS
44	Spectral mean	Frequency	FS
45	Spectral mean square	Frequency	FS
46	Spectral centroid	Frequency	FS
47	Root mean square frequency	Frequency	AE
48	Root variance frequency	Frequency	AE
49	Spectral skewness	Frequency	FS
50	Spectral kurtosis	Frequency	FS
51	Spectral flux	Frequency	FS

The averaged scores, based on the prediction accuracy, were then used to rank the features.

Figure 5.16 illustrates the results of investigating the features' robustness against artificially introduced noise. For this purpose, the model is trained on undisturbed, recorded data and tested on unseen data, which was artificially corrupted by introducing random noise with different levels L . L represents the percentage of the root mean square (RMS) of the

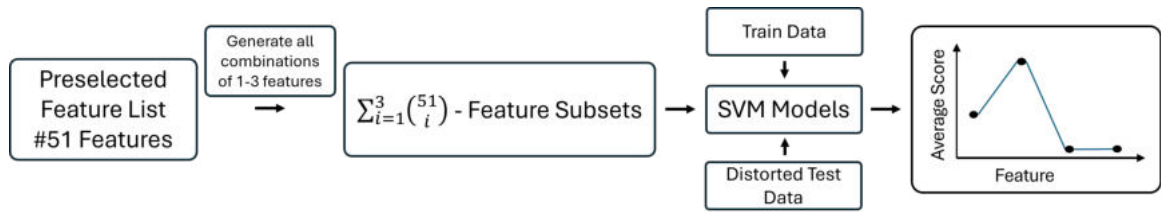


Figure 5.14: General approach for feature selection: generating SVM models for all combinations of 1-3 features from a preselected list of 51 features to compute average scores for each feature.

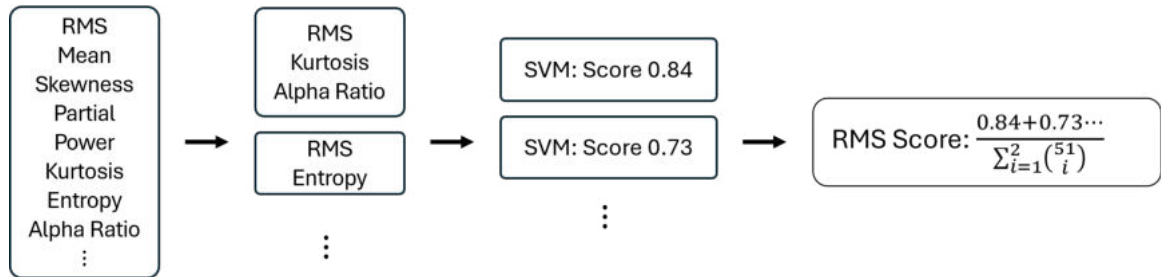


Figure 5.15: Evaluation of the RMS feature in combination with other features using SVM models to calculate predictive performance scores.

initial signal, with values ranging between $L = 0\%$ and $L = 25\%$. The bottom plot shows the mean and standard deviation in blue for each features across the different noise levels corresponding to the upper plot. The standard deviation measures the extent to which the performance of features varies across different noise levels. Consequently, it can be used to quantify robustness against noise: the higher the standard deviation, the more susceptible the feature is to changes in noise levels.

A robustness score against noise is illustrated in orange circles. To define such a score, the mean value is incorporated to account for generally high performance across noise levels, while also favouring low standard deviations to ensure consistency and stability.

However, consider that features that already perform poorly at $L = 0\%$ have limited potential to experience substantial losses in accuracy. This can be described as a lower "fall height". Consequently, smaller standard deviations may be attributed to general low accuracies, rather than exclusively to the feature's robustness against noise. To account for this effect, the final scores are calculated for measuring noise robustness using the equation:

$$s_N = \text{mean} - \frac{\text{std}}{1 + \text{mean}} \quad (5.1)$$

Dividing the standard deviation by the mean value plus 1 before subtracting it from the mean value itself allows us to account for the fall height effect. Since mean values range between 0 and 1, adding 1 to the mean before division ensures that the term $\frac{\text{std}}{1 + \text{mean}}$ increases monotonically with the mean. This approach prevents features with initially low values but high variability from being unfairly advantaged or disadvantaged in the final scoring.

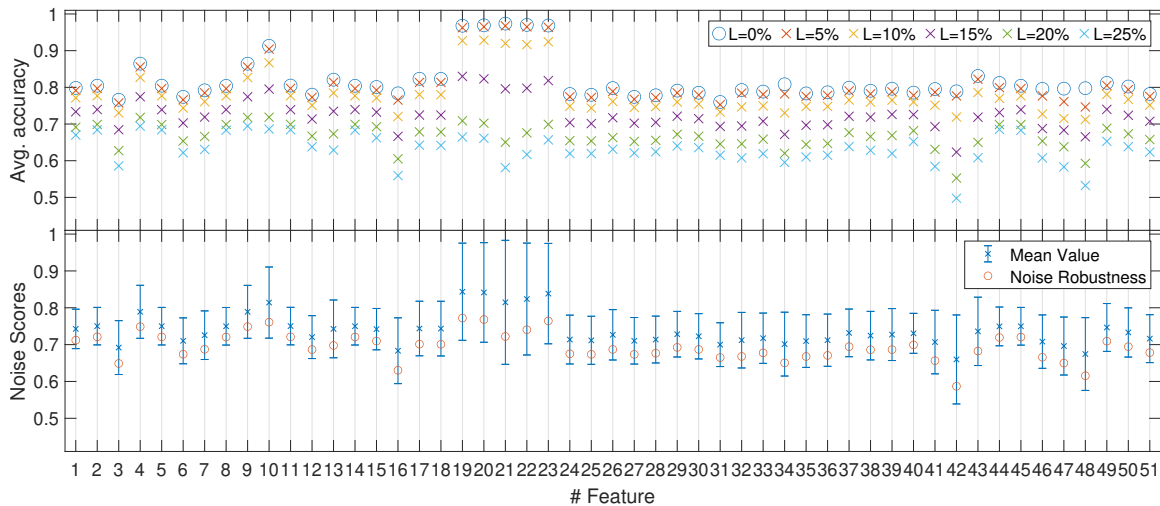


Figure 5.16: Evaluation of noise influencing feature performance. The top plot shows the average accuracy of various features across different noise levels. The bottom plot presents the corresponding mean values and its standard deviations in blue. The orange circles show the noise robustness score calculated via Equation 5.1.

For low to medium noise levels $L \leq 20\%$ the distribution features achieve the best scores. They perform exceptionally well in the absence of noise but show a higher drop in performance as noise increases. This is represented by high standard deviation values.

The sum root amplitude starts with a high value for the noise-free signal and maintains the highest values even for larger noise levels $< 20\%$.

The spectral mean exhibits very small standard deviations and good performance under high noise levels. This indicates that the spectral mean is a stable feature, showing consistent performance with minimal variation, even as noise increases.

The majority of features show a similar trend: decreasing scores with increasing noise levels. This trend highlights the general challenge of maintaining model accuracy as the noise in the data increases. Features with smaller error bars in the robustness noise plot are more reliable as they demonstrate consistent performance across varying noise levels.

Next, following the same approach but instead of using artificial corrupted data as test data, data recorded at a later time is employed.

As a result of extensive use, the gear demonstrator exhibited visible signs of wear, such as usage marks and chain abrasion. Additionally, the sensor position and screws on the holder were intentionally left unadjusted, further contributing to the investigation of the features' performance under conditions of wear and tear.

These factors altered the signal characteristics, against which the features should demonstrate robustness.

The expectation is that, compared to artificially adding noise, through these time-induced changes, the test data is much closer to a real world scenario. The algorithm might identify signal characteristics that change unpredictably over time, which are not reliable for robust classification, and avoid relying on them. Instead, it would focus on the stable characteristics that are still useful for accurately classifying the gears.

Figure 5.17 illustrates the results of investigating the features' robustness against this real signal degradation over time. For improved visualization in the graph, only four dates were selected, including the training data. The additional measurements are illustrated later on. The top plot shows the average accuracy of various features tested on subsequent data. The bottom plot presents the corresponding mean values, standard deviations and the final scores calculated via Equation 5.1

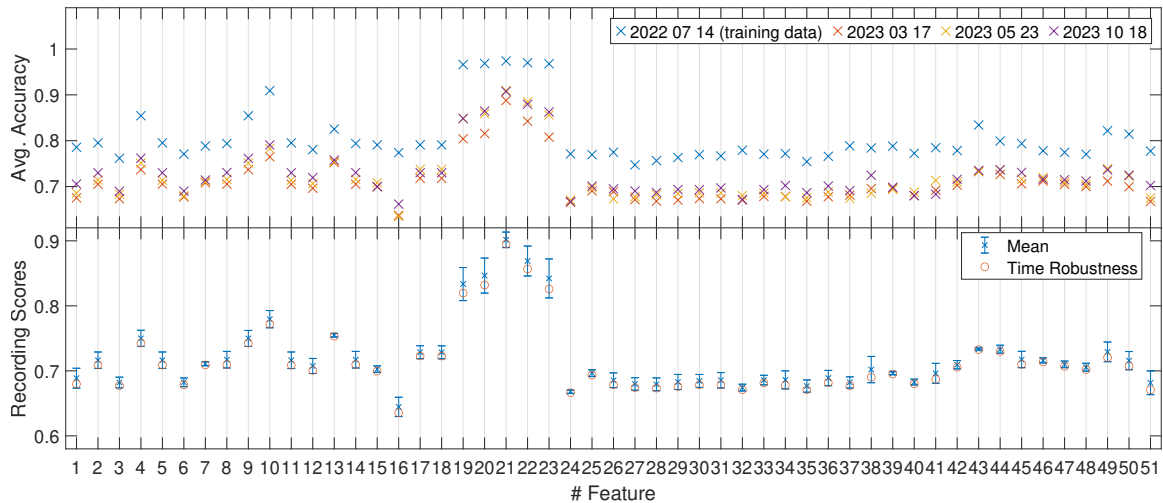


Figure 5.17: Evaluation of wear and tear influence over time on feature performance. The legend displays the date and the number of days elapsed since the previous one.

Contrary to the expectation that predictive power would continuously decrease, there is no clear trend observed across all features. Initially, the model shows signs of degradation, but after additional time has passed, several features show recovery. One possible explanation is that patterns in the data that the model was previously trained on reappeared in the later dataset, enabling the model to regain predictive accuracy. This recurrence of familiar patterns may help the model recalibrate or re-align with the underlying data structure, temporarily boosting performance.

The "distribution features", compared distribution entropy 1 & 2, compared extreme value fit, compare uniform fit and specifically compare Gaussian fit, achieve the highest score with a low standard deviation, indicating strong performance and stability over time. The Sum Root Amplitude feature also stands out with higher values.

Figure 5.18 compares the result of data that solely deteriorated over time from Figure 5.17 with robustness scores of artificially corrupted data of Figure 5.16. In both scenarios, the distribution features exhibit the highest scores. However, in the case of artificially introduced noise, this is less pronounced.

On the other hand, several frequency features, such as root variance frequency, root mean square frequency, spectral centroid, and alpha ratio partial power 5 & 6, perform relatively poor in terms of robustness scores when artificial noise is introduced compared to the

scores from time-induced deterioration.

For the other features, despite varying test conditions, the scores exhibit a similar trend, suggesting that artificially introduced noise generates dependency patterns comparable to those produced by time-induced distortions. Using artificial noise could be advantageous, as collecting data over time and waiting for natural deterioration is significantly more time-consuming. Thus, replacing natural degradation with artificially introduced noise could serve as a practical alternative, yielding comparable relative scores. However, further investigation is necessary to clarify several influencing factors, such as the specific application contexts, the nature of time-induced distortions and the type of artificial noise used.

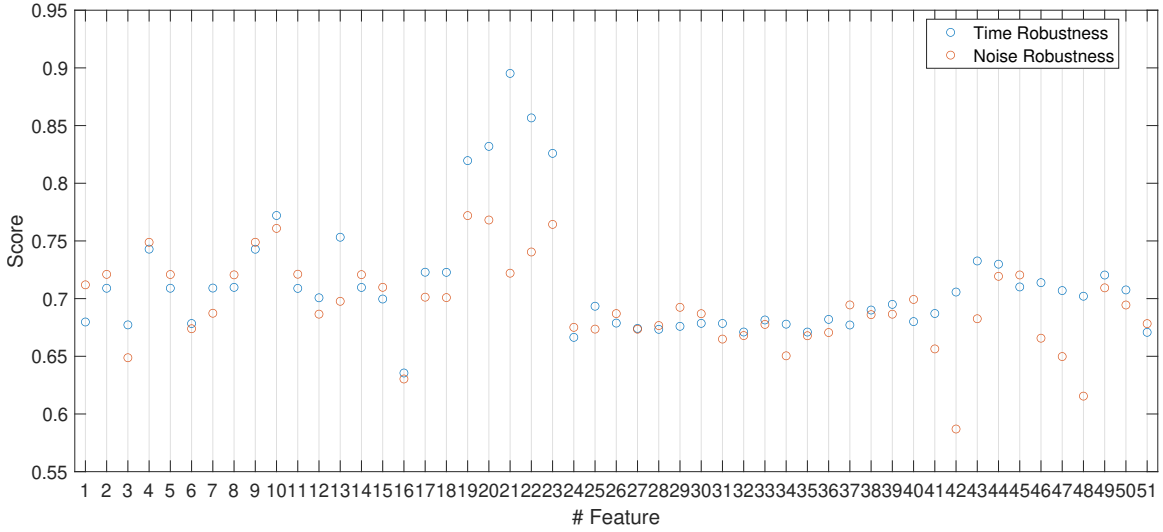


Figure 5.18: Comparison of Time and Noise Robustness Scores. The plot shows robustness scores for each feature, with blue circles representing robustness to degradation over time and orange circles indicating robustness against artificially introduced noise. Higher scores suggest greater feature reliability in maintaining predictive performance under the respective conditions.

Considering that for N features it is necessary to train $\sum_i^3 \binom{N}{i}$ models, it is not suitable for a quick feature selection. A conventional, yet faster method, which avoids training numerous models, is to use the standard feature selection algorithms presented in the previous chapter. To bundle these algorithms, thus reducing bias introduced when using only one method, 15 algorithms are employed to calculate scores s_{ji} for each algorithm j and feature i . For each feature 15 scores are obtained from each selection algorithm.

For each method the scores are rescaled on a scale from 0 to 1 for each feature individually:

$$r_{ji, \text{rescale}} = \frac{s_{ji} - \min_j(s_{ji})}{\max(s_{ji}) - \min(s_{ji})} \quad (5.2)$$

Then the average score for each feature is calculated as follows:

$$s_i = \text{mean}_j(r_{ij}) \quad (5.3)$$

5 Application

Because the algorithms operate on different scales, rescaling scores before averaging ensures that each method has an equal influence on the final score.

The result is illustrated in Figure 5.19. For the specific selection algorithms refer to Figure 5.20.

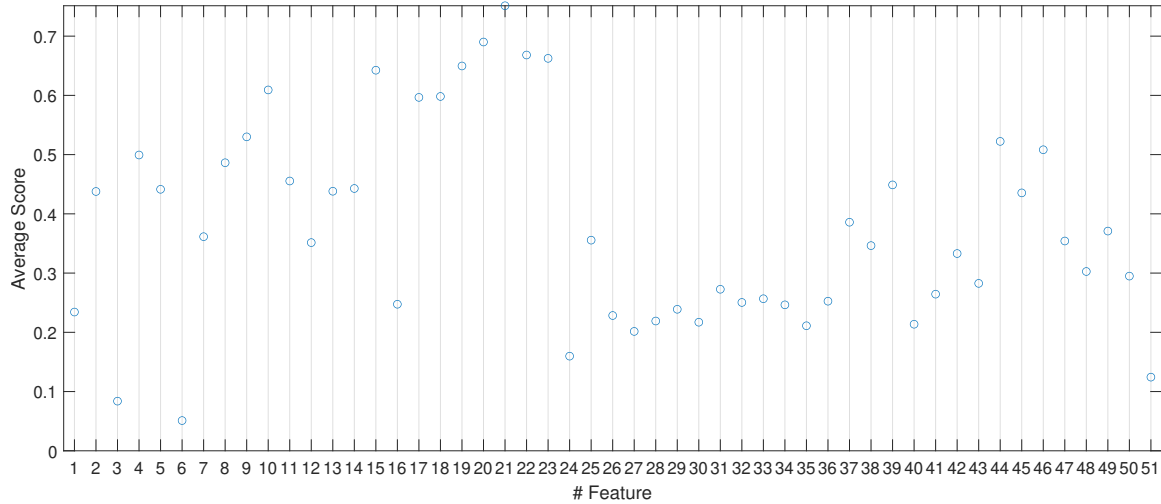


Figure 5.19: Average Score of the 15 Feature selection algorithms.

Again, the distribution features and the sum root amplitude show high scores with the compared gaussian fit achieving the highest score.

However, in this selection process using standard algorithms (SFS), although time-efficient, the selection cannot be adjusted to prioritize signal degradation caused by wear and tear or increasing noise levels, as it is possible in the previous Feature Model Selection (FMS) process through feature permutation and the use of various datasets.

To combine the benefits of FMS, which adapts to noise and wear effects, with the effectiveness of SFS, the weights w_j are calculated for each algorithm j . These weights are used to derive a weighted average, favouring the algorithms that tend to highlight similar features as the FMS method. If this similarity arises from fundamental patterns in the datasets, making these weights applicable for general gearbox measurements beyond the specific application. Using the weights, instead of just using Equation 5.2 and Equation 5.3 the final scores can then be calculated via:

$$s_i = \frac{\sum_j w_j s_{ji}}{\max_j(s_{ji})} \quad (5.4)$$

The weights and the comparison between SFS and FMS is illustrated in Figure 5.20. The figure shows the feature scores for the SFS methods and for the FMS algorithm using SVM models and artificial noise. The R-square value is then used to compare the scores of each

SFS method with the FMS scores. The Chi-Square Test yielded highest R-value.

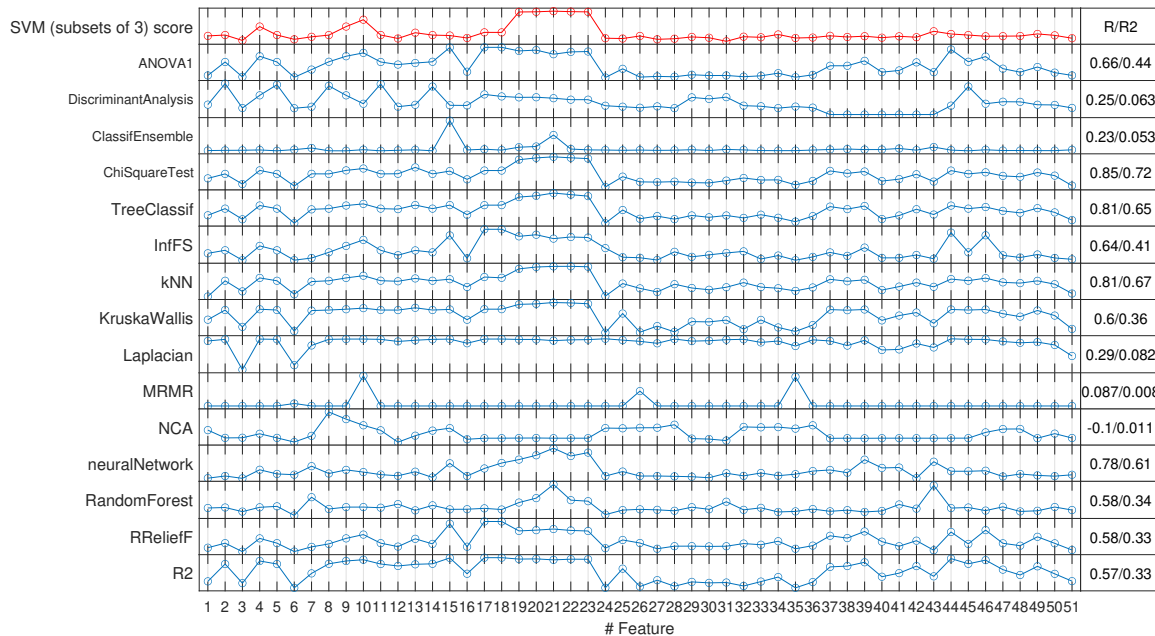


Figure 5.20: Comparison of the SVM scores with the scores of fast feature selection algorithm. The top plot shows the SVM score for each feature and the lower plots show individual feature scores. The corresponding R and R-square values between each algorithm and the SVM scores are listed on the right with R-square value being used as the final weight assigned to each method.

Figure 5.21 compares the final scores for each method and feature. The scores are rescaled between 0 and 1 for comparison across all 15 selection algorithms. Compared to the unweighted FS scores, the weighted FS scores emphasize the distribution features, maintaining their high values while many other features see a decrease.

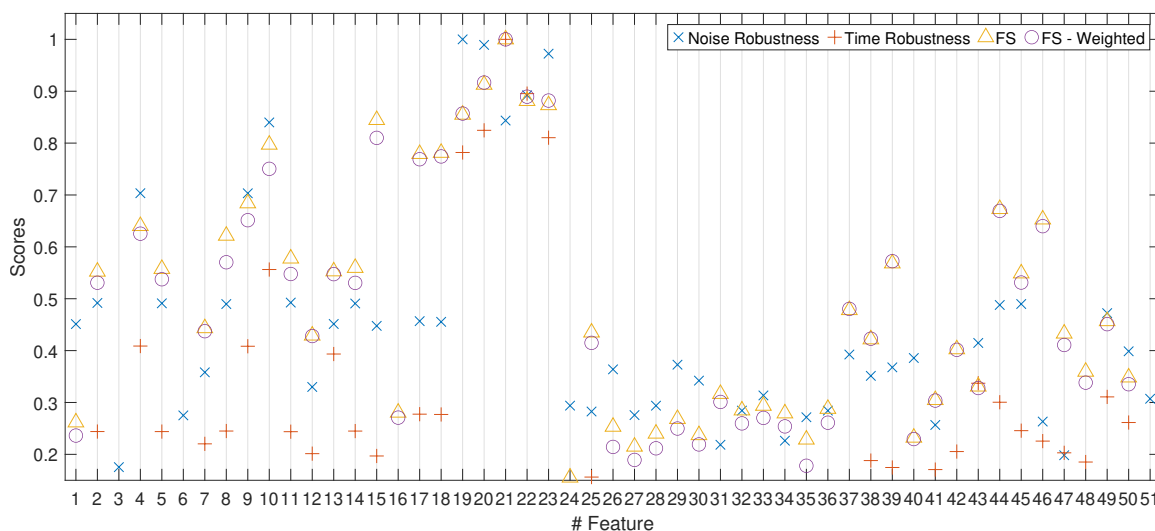


Figure 5.21: Comparison of different scores.

Since the weights were designed to adjust toward the noise robustness results, the weighted FS scores should align more closely with the noise robustness scores. This general tendency is indeed observable. To quantify this, the RMS difference between the noise robustness scores and the unweighted and weighted FS scores are calculated, respectively. The RMS value decreased from 0.39 to 0.36 after introducing the weights, confirming this shift.

After rating the features a further step is to identify the optimal number of features. Several studies [18, 113, 114] describe the benefits of reducing the feature dimensionality across several fields: Reducing features in classification problems can significantly enhance model performance by minimizing overfitting, which helps the model generalize better to new data. It simplifies the model, making it faster to train and easier to interpret, while also lowering computational costs.

However theoretically determining the optimal number of features for a specific case is not straightforward [115]. To identify the optimal number for this application, an experimental approach is chosen to evaluate prediction accuracies across different sizes of feature subsets. Starting with models based on a single feature, extra features are sequentially added in the order of their robustness scores. The results are illustrated in Figure 5.22.

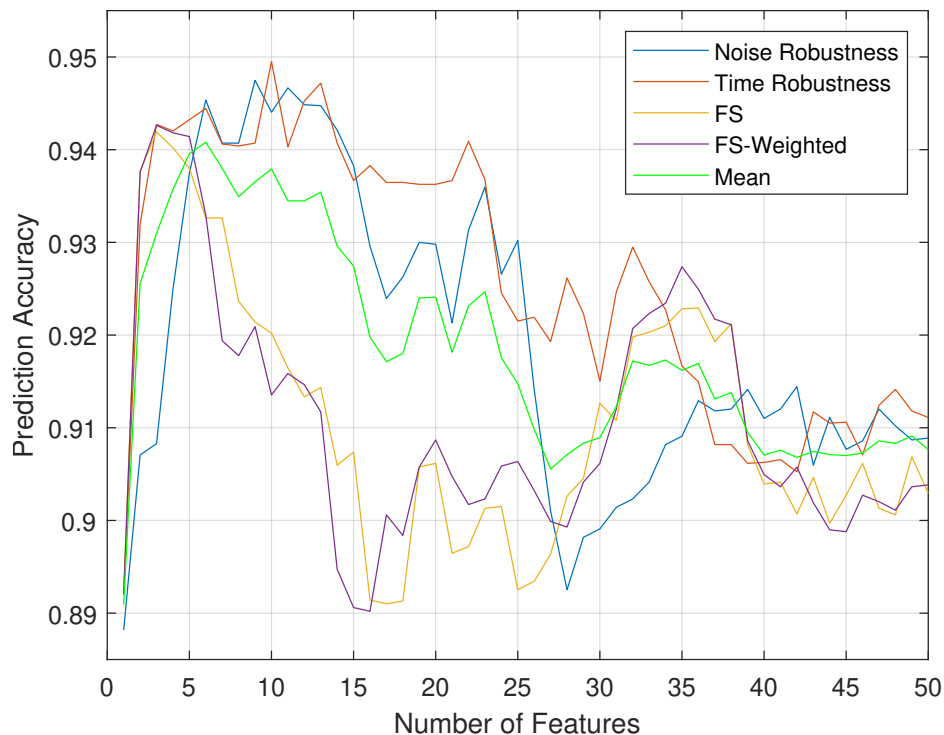


Figure 5.22: Prediction accuracy for varying number of features. The features were added consecutively corresponding to the SVM Time, SVM Noise, the weighted and unweighted FS scores. The mean does only take the unweighted FS scores into account in order to avoid overvaluing the results of the FS scores.

All methods show that the initial few features are crucial, as most accuracy gains occur within the first 5 to 10 features. Adding more features beyond this point (around 10-20)

leads to accuracy declines or fluctuations, suggesting that additional features may introduce noise or overfitting and reducing the model's generalization capability.

The investigations in [113] on the effect of number of features on classification of roller bearing faults confirm these findings and show good high accuracies for < 10 features using SVM and PSVM models.

Thus, the different scores are compared based on SVM models with 5-10 features and calculated the corresponding mean values. Figure 5.23 illustrate these values with the standard deviations, indicated by dotted lines in the respective colors.

The dates of the data are plotted on the x-axis in equidistant steps, regardless of the actual recording dates. While it may be useful to plot the results against a variable linked to the expected deterioration of the demonstrator, such as its usage and strain, a neutral approach with equidistant steps is chosen for clarity. Although the elapsed days and external visitor use of the demonstrator were recorded, many unregistered factors—such as internal tests, relocations, and exhibitions—also contributed to signal deterioration. Specific events, like impacts during relocations or improper use by external visitors, may have caused abrupt changes in the recorded data, accelerating deterioration. Consequently, defining a reliable measure to accurately represent wear and tear is challenging, making the neutral, equidistant approach a practical choice for an overview.

However, as elapsed days and the number of external visitors are undeniably linked to wear, Figure 5.24 additionally displays the measurements on the corresponding x-scales.

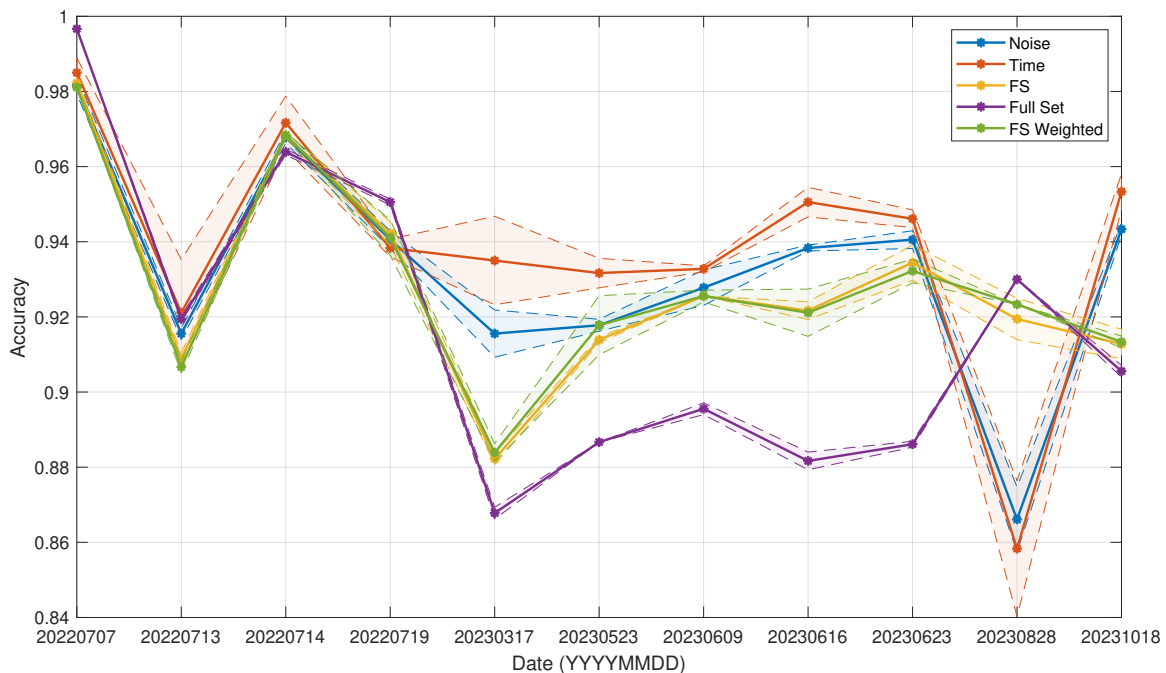


Figure 5.23: Prediction accuracy for the SVM models trained on the first data set at 2022-07-07 and tested on the other. The number of features used to train the models are varied from 5 to 10. The mean value are then illustrated with the solid line, and the dotted line represent the standard deviation.

5 Application

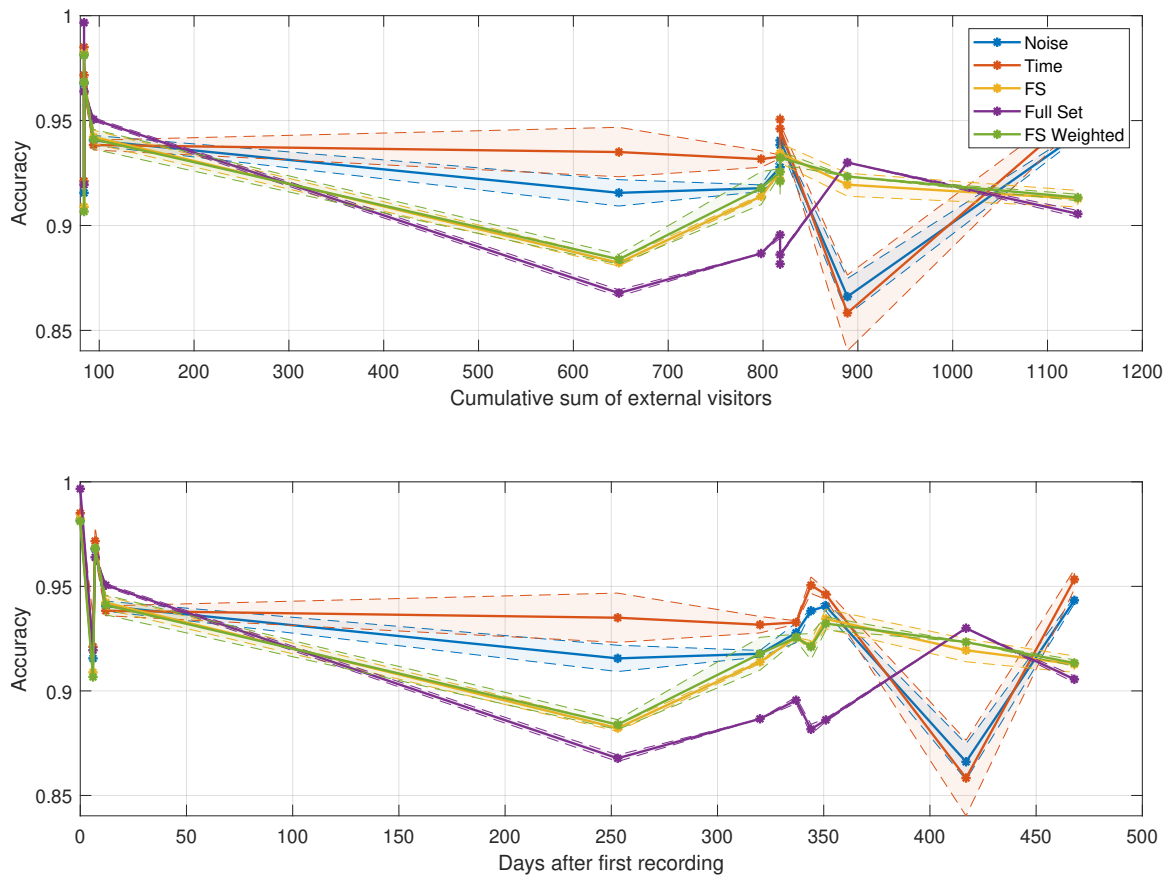


Figure 5.24: Analog to Figure 5.23 but with different x - scales.

All methods showed improvement compared to using the full set of 51 features. The highest scores were achieved by the SVM-Time scores. It is important to note that the datasets from 2023-03-17, 2023-05-23, and 2023-10-18 were used to identify these scores, which may introduce a bias towards better results.

However, the remaining, unseen datasets still delivered the best results, confirming the robustness and effectiveness of the SVM-Time scores.

The second-best scores are based on the SVM-Noise scores. This is a good result as the only dataset used to identify these scores was recorded on 2022-07-07.

The FS method also achieved improved results compared to the full dataset and was fine-tuned by the weighted FS scores. Using these weights across different applications assume the FMS scores as a benchmark indicating robustness and resistance to both artificial noise and other signal degradation effects.

This is justified for two main reasons: firstly, by specifically using modified testing data to create scores that are robust against intended modifications; and secondly, by the high accuracy demonstrated in the figure.

The accuracies for the data recorded on 2023-08-28 are notably reversed compared to other datasets, with a conspicuous peak observed when using the entire feature set. Since the full

feature set generally yields the worst average performance, it can be inferred that the model may have selected features that capture random effects rather than robust characteristics. This selection likely resulted from the high accuracy achieved in the training data from 2022-07-07, which was influenced by these random effects. Consequently, the peak observed in the 2023-08-28 dataset could be due to the recurrence of these random characteristics identified during the training phase

Furthermore the dataset recorded on 2023-08-28 may have issues related to data quality. This could include noise, missing values, or other anomalies that were not present in the other datasets. Such issues can significantly impact the performance of the other SVM models.

In summary, every method shows improvement over using the full set of 51 features. The highest scores are achieved by the SVM-Time method, which consistently delivers better results even when applied to unseen datasets. This indicates that the scores identified are effective in improving accuracy. The second-best performance comes from the SVM-Noise method, which is particularly noteworthy as it only relies on the initial dataset recorded on 2022-07-07 for score identification. The FS method also shows improved results compared to using the full feature set, and these results are further refined by applying the weighted FS scores.

5.3 Global Reconstruction

This section explores the application of the global reconstruction algorithm to two specific processes: the VAP and the T-RTM process. In both cases, accurately predicting and controlling the flow front, the leading edge of fluid as it infiltrates the fibre preform, is crucial to ensuring the quality and integrity of the final composite material.

Monitoring and controlling the flow front dynamics is essential for two main reasons [10, 116]:

- Complete wetting: Ensures that the entire preform material is adequately impregnated with resin or polymer melt.
- Avoiding pores: Prevents the formation of air bubbles, which can lead to defects in the final composite material.

During both processes, it is crucial to ensure that the entire preform material is wetted, consolidated, and chemically cured.

To understand the physical characteristics of liquid composite moulding processes, such as vacuum infusion and injection moulding consider Darcy's law [84]:

$$\frac{Q}{A} = u = -\frac{K}{\mu} \frac{dp}{dx} \quad (5.5)$$

The Darcy velocity, u is defined as the quotient of the volumetric flow rate Q and the flow area A . This velocity depends on the permeability K of the impregnated fibre preform, the viscosity μ of the liquid and the pressure gradient $\frac{dp}{dx}$.

The permeability is influenced by the architecture of the textile preform and the degree of compaction when vacuum is applied and the viscosity is mainly influenced by the liquid's temperature. The pressure gradient is determined by the pressure difference between the cavity (vacuum) and the resin pot. This pressure difference is typically the ambient pressure for resin infusion or approximately 5 bar for transfer injection moulding [84, 117].

The complexity of flow front dynamics, influenced by factors such as pressure gradients, fluid viscosity, and fibre architecture, presents significant challenges for accurate prediction through theoretical models or simulations. These models and simulations are heavily dependent on physical domain knowledge and precise physical parameters, which are not always readily available.

As a result, the VAP and the T-RTM processes serve as excellent examples of where the global reconstruction method could be particularly beneficial, offering valuable insights into the critical variable of flow front dynamics. Unlike other methods, the primary advantage of this reconstruction technique is that it relies solely on sensor measurements and geometrical relationships to accurately reconstruct the flow front dynamics.

Using a simple, flat tooling setup, the VAP experiments provide a controlled environment to test the basic functionality of the algorithm for reconstructing resin propagation. This setup allows for comprehensive data recording, which is crucial for validating the algorithm. In contrast, applying the algorithm to the T-RTM process involves highly complex tooling and limited monitoring capabilities, serving as a field test of the algorithm's robustness.

However, it is important to note that while comparing these methods, their differing application areas must be considered. The reconstruction method is not designed to predict process dynamics but rather to function as a measurement tool.

For the VAP process, a triangular mesh grid consisting of 30,000 nodes with a maximum edge length of 0.28 cm is fitted to the tool's surface, which measures 30×60 cm.

The arrival times \bar{t}_i are automatically extracted from a recorded image sequence and assigned to the corresponding nodes i .

Using MATLAB 2023a, a flow front detection method was developed. It identifies the boundary of the resin flow front by comparing the current image to a reference image recorded earlier. The contrast between the reference and the current picture is calculated by taking the absolute difference in the luminance channel.

This contrast image is converted into a binary image using a threshold value τ , where pixel values $\leq \tau$ are assigned 1, and values $> \tau$ are assigned 0. Based on experimental

optimization, the threshold τ is set to one-quarter of the maximum contrast value.

To improve the binary image, noise is removed and morphological closing are applied using a disk-shaped structuring element, which fills small holes and gaps. The boundaries of the connected components are detected using MATLAB's built-in function 'bwboundaries' [118]. The largest boundary is selected as the flow front boundary.

The time t of a current recording is then assigned to the pixels within the flow front boundary, which have changed between the current and its previous recordings. This time t is defined as the arrival time.

Figure 5.25 illustrates the process of identifying the arrival times for the flow front. The figure shows a camera recording, zoomed in on the flow front. The boundary of the flow front at $t = 30$ s is highlighted in red. Noticeably, there are isolated fluid segments that advance ahead of the main flow front, visible as slight discolourations. These segments are correctly detected and disregarded by the algorithm.

An earlier recording, taken 1 s prior, depicts the flow front's boundary outlined in green. Nodes that fall between the red and green boundaries are assigned an arrival time of $t = 30$ s. This intermediate region is marked in blue within the figure.

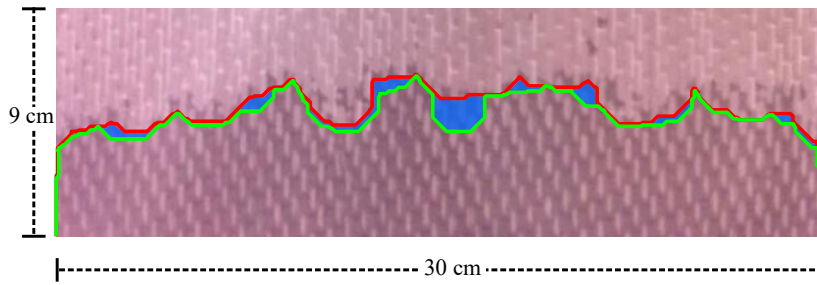


Figure 5.25: Photography of a VAP experiment and identification of flow front. The red boundary marks the current flow front. The green boundary represents its position one recording earlier. The area enclosed in between these boundaries is marked in blue.

This comprehensive spatial data enables an effective examination of different virtual sensor setups. In the absence of physical sensors, arrival times are extracted from chosen nodes corresponding and treated as measurements of virtual sensors. The grid and the extracted arrival times, representing virtual sensor data, were used as initial parameters for the flow front reconstruction.

Finally, a comparison of the recorded data with the results of the reconstruction allows for verification of the algorithm. A measurement for the global average time difference between recorded and reconstructed data is calculated per node using the equation:

$$f = \frac{\sum_i |\bar{t}_{i,\text{Recorded}} - \bar{t}_{i,\text{Reconstructed}}|}{\text{Number of Nodes}} \quad (5.6)$$

After choosing 16 nodes as sample points with their extracted arrival times and using Equation 4.20 an appropriate parameter set for the weight function w_{in} , see Equation 4.16, is identified, listed in Table 5.2

Table 5.2: Parameter values for VAP and T-RTM processes.

Parameter	VAP	T-RTM
ϵ	0.01	0.02
δ	35	20
R	5	4

Applying the reconstruction algorithm as described in the previous chapter delivers the results represented in Figure 5.26. It illustrates the boundaries of the recorded flow front in green for times t ranging between 50 s and 250 s. In correspondence to these times the contour of the reconstructed flow front is illustrated in red. The background, represented as a greyscale metric, visualizes the deviation between reconstructed and recorded arrival times using the formula $|\bar{t}_{j,Reconstructed} - \bar{t}_{j,Recorded}|$. The average absolute delay is $f = \pm 4.6$ s, which is, in comparison to the total time of the process of 278 s, a percentage deviation of 1.7 %.

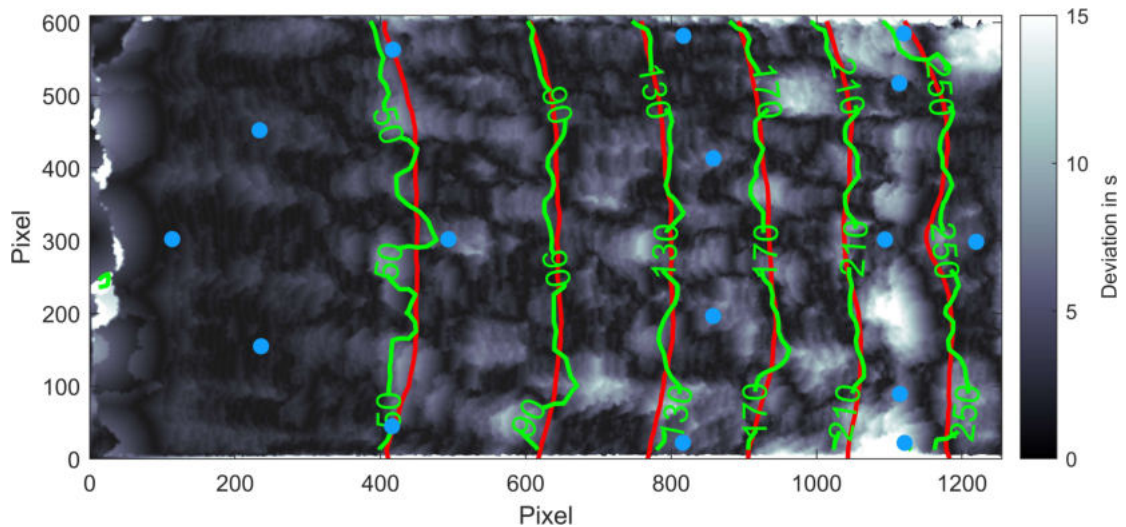


Figure 5.26: Contour plot showing the absolute deviation between the recorded and reconstructed arrival times. Blue dots indicate the locations of the sample points. Contour lines represent the flow front based on recorded arrival times (green) and reconstructed arrival times (red) across observation periods ranging from 50 s to 250 s.

The calculated flow front interpolation offers deeper insights into the process, highlighting locations that are difficult to impregnate. This demonstrates the algorithm's adaptability, as it can be fine-tuned by adjusting the weight parameters as previously described.

The application of the algorithm to the VAP process demonstrated its efficacy, showing an

average temporal deviation of just 1.7% compared to the total process time. This level of accuracy enables the detection of deviations and anomalies in the flow front based on the reconstructed data.

In the experiment illustrated in Figure 5.26, the algorithm's ability to handle typical phenomena such as wrinkled flow fronts and dragging along the edges was tested. These issues arise due to variable permeability of the preform and increased friction. The resolution of the interpolated flow front is dependent on the density of the sensor network, as the estimation relies on information from surrounding sensors, which is managed by the weight function.

By identifying potentially critical areas, strategic sensor placement can enhance the accuracy of the calculated flow front. E.g. to address the common issue of lagging flow fronts along the edges observed in the VAP experiments, additional sensors were placed near the edges, as shown in Figure 5.26. This setup allowed the reconstruction to accurately present the flow front propagation.

However, some deviations occurred due to the wrinkled flow front, which could not be fully captured by the algorithm because the average distance between sensors was smaller than the wrinkled structure of the flow front. To resolve this issue, a significantly higher number of sample points would be required in these locations to provide the necessary input data for accurate interpolation.

In the following section, the application of the reconstruction algorithm to the data recorded by the ultrasonic (US) sensors during the T-RTM experiments is described. Since the flow front dynamics in these experiments cannot be optically tracked and validated, all information regarding the flow front relies solely on the sensor data. Therefore, as a crucial first step, the ultrasonic signals recorded during the T-RTM experiments are analyzed by comparing them with machine data and other sensor readings, such as pressure data, to understand how the US signals correspond to events during the T-RTM process.

To illustrate this analysis, refer to Figure 5.27, which compares the press position with the RMS values extracted from the US signals. The red-shaded interval indicates the time period during which the injection occurs. The process begins with the tool being closed to approximately 3.5 mm above complete closure to facilitate vacuuming. This initial closure helps in evacuating the cavity to reduce moisture and improve permeability. After evacuation, the tool is further closed to a 2 mm gap, which is the set position for the injection phase.

This step is also visible in the RMS as the preform gets compressed and pushed against the tool surface, altering the reflection conditions.

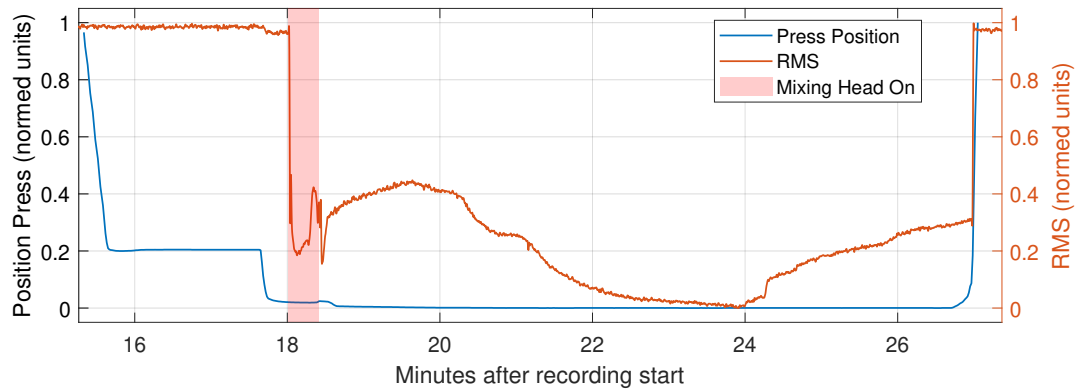


Figure 5.27: Illustration of the RMS-feature extracted from a US-Signal and tool position during resin injection.

The injection of the resin starts at this point. Shortly after the injection begins, there is a sudden drop in the RMS value. This drop corresponds to the arrival of the flow front and the abrupt change in reflection conditions due to the resin wetting the preform.

During the injection phase, the RMS shows considerable fluctuations. These fluctuations could be attributed to the high pressure gradients and uneven spread of the flow front as the resin advances.

For example, as observed in the VAP experiments, illustrated in Figure 5.25, the flow front can initially wet the pores between the fibre bundles before gradually impregnating the bundles themselves. This uneven progression can lead to air entrapment within the preform, causing intermittent changes in the reflection conditions.

Additionally, varying permeability of the preform introduces localized differences in flow speed and direction, which contribute to the irregular shape of the flow front.

Figure 5.28 presents a representative set of RMS values extracted from recorded ultrasonic signals, highlighting the typical characteristics observed during the flow front detection process and their comparison with pressure data. The figure illustrates the dependency of the ultrasonic signals on changing reflection and transmission conditions at the cavity's surface, as well as their correlation with the pressure variations within the cavity.

The figure demonstrates the RMS dependency on pressure, which arises from changes in the reflection coefficient induced by pressure. This occurs because the pressure alters the material properties, such as the density of the material, which influences the acoustic impedance and therefore the reflection indices. Another factor is the changes in contact that occur. The preform is not necessarily completely flat, lacking full contact with the cavity. Applying pressure can flatten the preform, increasing the contact with the cavity and thus altering the reflection conditions.

The pressure is monitored using sensors located on the surface of the cavity. The positions of the relevant sensors, which are strategically integrated into the tool, are depicted in

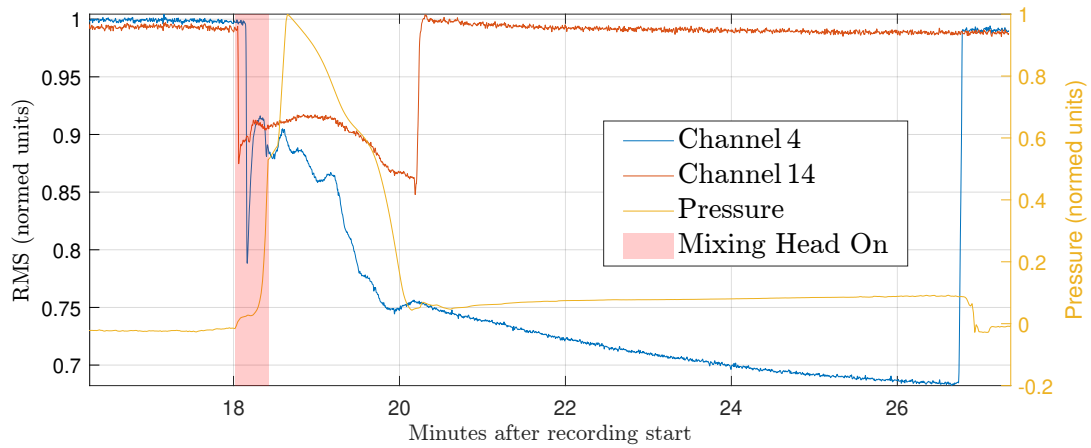


Figure 5.28: Illustration of the behaviour of the RMS of two channels and pressure over time during a composite manufacturing process. The y-axis on the left represents the RMS and the y-axis on the right represents the pressure. The red-shaded area indicates the time period when the mixing head is on.

Figure 5.29.

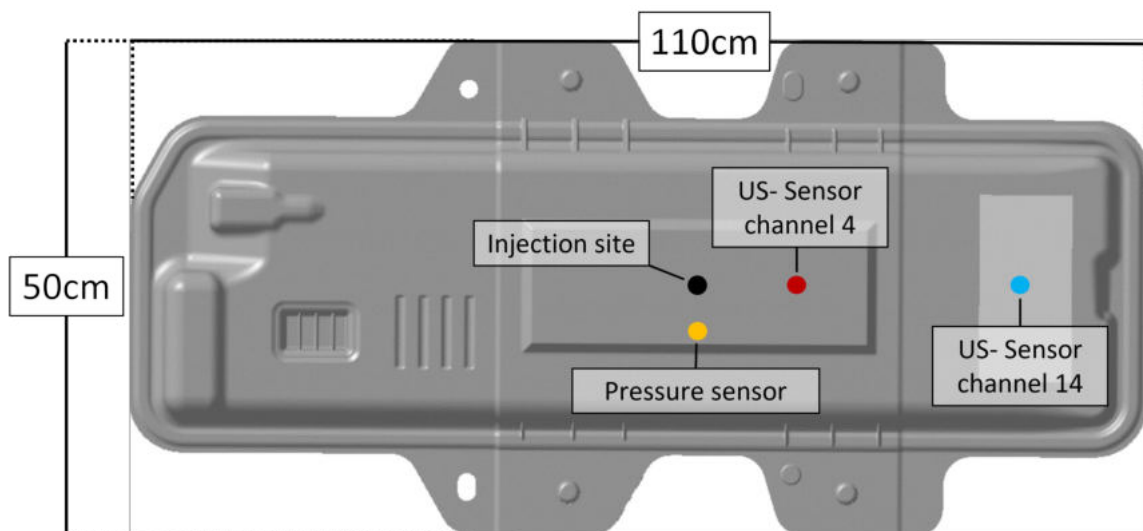


Figure 5.29: Sensor positions within the tool layout.

The pressure curve captures the key stages of the process. Initially, there is a sharp rise in pressure, corresponding to the activation of the mixing head, indicated by the start of the red shaded area. After the injection ceases, further closure of the cavity from 3.5 mm to 2 mm results in an additional pressure increase, reaching its peak value. During polymerization, mold shrinkage effects cause a gradual pressure drop. Over the subsequent 5-minute dwell period, the matrix polymerizes, attaining its final stiffness. Any irregularities in the pressure during this phase are attributed to the polymerization process. Finally, in the last step, the tool is opened, and the fully polymerized part is manually removed. [86]

The red and blue curves, representing the RMS of the ultrasound signals, remain relatively stable before the injection process begins. Immediately after the activation of the mixing head, both channels exhibit a sharp decrease in amplitude. This decrease occurs sequentially, reflecting the temporal order corresponding to the distance from the injection point. This behaviour suggests a significant change caused by the arrival of the flow front, resulting in a sudden alteration in the reflection conditions. Channel 14 shows minor fluctuations but remains relatively stable compared to Channel 4.

The fluctuations in the RMS of Channel 4 begin with the injection phase and the rising pressure. When the pressure drops and stabilizes, the fluctuations stabilize as well. The RMS extracted from the signal of Channel 14 shows a different behaviour, the RMS abruptly rises sharply to the initial value, indicating a return to the initial reflexion conditions which could be interpreted as a complete loss of contact between the impregnated preform and the surface.

During the high pressure gradients the RMS show rather unpredicted behaviour in comparison to the low gradient zones. This underlines the influence of the pressure on the US-signals.

After the injection, the RMS value stabilizes somewhat, indicating that the flow front dynamics have slowed down as polymerization begins. The resin solidifies, and the system reaches a more stable state. Following the injection, the RMS value stabilizes, indicating that the flow front dynamics have slowed down as the polymerization process begins. As the fluid solidifies, the system transitions to a more stable state, with fewer changes in reflection conditions and less fluctuation in the ultrasonic signal. Gradually, the RMS value converges, suggesting the completion of the polymerization process.

In general, there are three trends observed in the signals throughout the experiments. The figure Figure 5.30 depicts three distinct types of RMS value behaviours during the T-RTM process, each corresponding to different physical phenomena within the system.

- Abrupt, complete increase: The RMS value shows a sudden and complete rise. This behaviour could be indicative of a sudden detachment of the preform from the cavity surface, possibly due to stresses that are abruptly released. Such a sharp increase in the signal suggests that the resin has caused an immediate change in the reflection conditions, reflecting a rapid interaction with the preform.
- Gradual increase: The RMS value gradually increases to its maximum value. The gradual rise in the signal following the arrival of the flow front suggests a slow detachment of the preform from the surface, potentially due to material shrinkage. As the resin impregnates the preform, it may cause the preform to slowly lift away from the tool surface, leading to incremental changes in the acoustic impedance and a corresponding gradual increase in the RMS value.

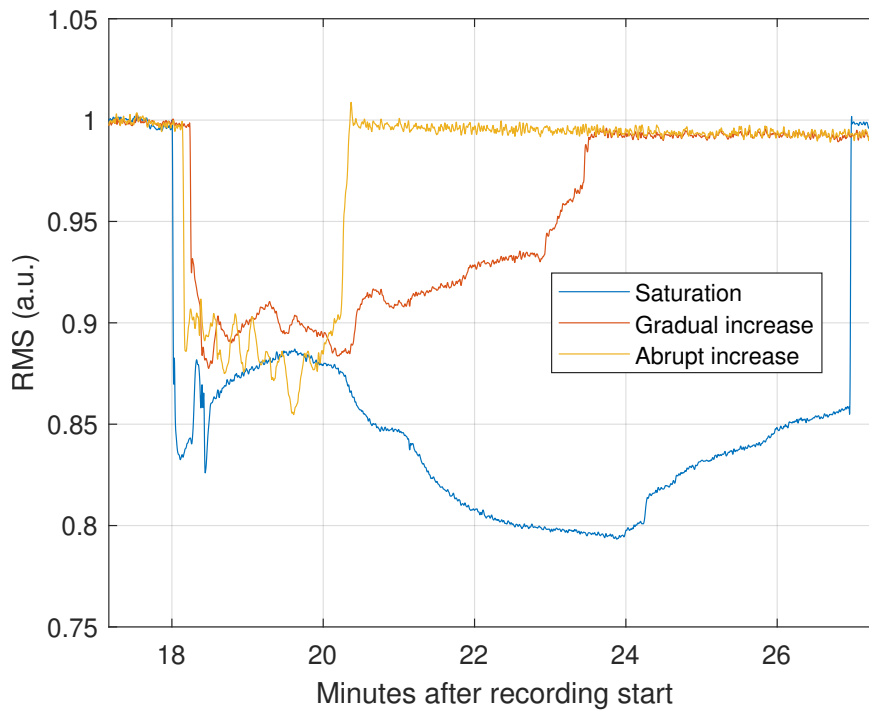


Figure 5.30: Illustration of three distinct RMS value behaviours during the T-RTM process, each reflecting different physical phenomena.

- **Saturation behaviour:** The signal initially rises and then slowly decreases over time, reaching a stable plateau. The initial abrupt decrease indicates the arrival of the flow front, while the gradual, steady decrease over time (up until around 24 min) likely corresponds to the ongoing polymerization process. The absence of abrupt changes such as pressure drops or sudden detachment of the preform suggests a stable interaction between the resin and the preform, with the steady signal decrease reflecting the progress of polymerization and eventual stabilization.

The T-RTM experiment does not allow for optical validation, making it difficult to ascertain that the initial abrupt drop in ultrasonic signals is due to the arrival of the flow front. To address this, validation experiments were conducted using the same sensors and a transparent plexiglass as a tool, for which custom 3D-printed sensor holders were designed.

For practicality and cost-effectiveness, vegetable oil was used instead of ϵ -caprolactam. Since the primary objective was to validate the arrival of the flow front, vegetable oil served as a suitable substitute. The polymerization process was not a concern in this context. Using Equation 2.16 Table 5.3 compares the theoretical reflection index values with those derived from the material parameters of Table 5.4.

The acoustic impedance of plexiglass is closer to that of oil than to that of steel, resulting in significantly lower reflection values for validation trials with plexiglass. Although there are differences in viscosity and corresponding reflexion indices between oil and caprolactam,

Table 5.3: Reflection indexes for various material pairs and the ratio of the echoes amplitude before and after the flow front arrival of caprolactam and oil (Air/Caprolactam) and (Air/Oil) which is given by the division of the corresponding reflexion indices.

Material Pair	Reflection Index	Ratio
Steel/Air	1.0000	-
Steel/Caprolactam	0.9363	0.9363
Plexiglass/Air	0.9997	-
Plexiglass/Oil	0.4694	0.4695

Table 5.4: Sound velocities, densities, and impedances for various materials [20, 119].

Material	Velocity of Sound (m/s)	Density (g/cm ³)	Sound Impedance (Pa·s/m)
Caprolactam	1330	1.1	1463
Steel	5700	7.8	44460
Plexiglass	2700	1.2	3240
Air	340	0.0012	0.408
Oil	1300	0.9	1170

which can cause absolute differences in the signals, the critical factor for detection is the relative drop rates in the RMS value, making oil an appropriate replacement.

In [120], various methods for flow front detection based on ultrasonic signals were examined and validated through camera recordings. The following methods were compared, focusing exclusively on the RMS value due to its straightforward interpretability. When the preform is wetted, the RMS value typically drops because the liquids used generally have an acoustic impedance closer to the tooling than air. And since air has a much lower acoustic impedance compared to the tooling, a drop in the reflection index occurs, leading to a decrease in the amplitude of the reflected signal and, consequently, the RMS value. Therefore, methods were developed to identify the time of this abrupt drop, corresponding to the flow front arrival. The straightforward interpretation of the RMS value offers a significant advantage over other features, where interpretation and general method development for flow front detection are not as straightforward.

- **Threshold method:** This method involves normalizing the RMS value based on the average signal value before the flow front arrives. The flow front arrival is detected when the RMS value drops below a predefined threshold. The method proved effective in detecting the flow front within the visually determined arrival time range. Using different thresholds (e.g., 0.9, 0.95, 0.99) allowed for flexibility in adjusting detection sensitivity. Signal smoothing was applied to minimize noise, enhancing the method's performance.
- **Differentiation method:** This approach involves numerically differentiating the RMS value to detect abrupt changes associated with the flow front arrival. The differ-

entiation process highlights sharp drops in the signal. The algorithm searches for the minimum value in the differentiated signal, which corresponds to the flow front arrival. While the method successfully identified the flow front, it was sensitive to noise and required signal smoothing for optimal performance. It struggled with gradual changes and was less effective for slower flow front movements.

- Change point detection method: MATLAB's `ischange` function [121] was used to identify change points in the signal. The function splits the signal into segments at points of abrupt change, optimizing the segmentation based on a cost function. This method provided more precise detection compared to the threshold and differentiation methods but was computationally intensive and required careful parameter tuning.

All methods were tested with RMS values extracted from various gate positions and lengths. Ultimately, it was decided to continue with the threshold method due to its ease of application, robust results, and minimal need for parameter adjustments across different experiments and sensors. A threshold value of 0.95 consistently yielded reliable results.

After validating the reconstruction algorithm, it was applied to the T-RTM process. In this process, the solid steel tooling hinders optical monitoring. However, the results of the reconstructed flow front are compared with the manufactured parts from successful or prematurely aborted experiments.

For the complex T-RTM mold, the mesh used as a base for the graph is fitted to the tooling's CAD model, consisting of 130,000 nodes with a maximum edge length of 1 cm. Table 5.2 lists the parameters for the weight function, and Figure 5.31 presents the reconstruction of an experiment, enabling an estimation of the flow front during the process.

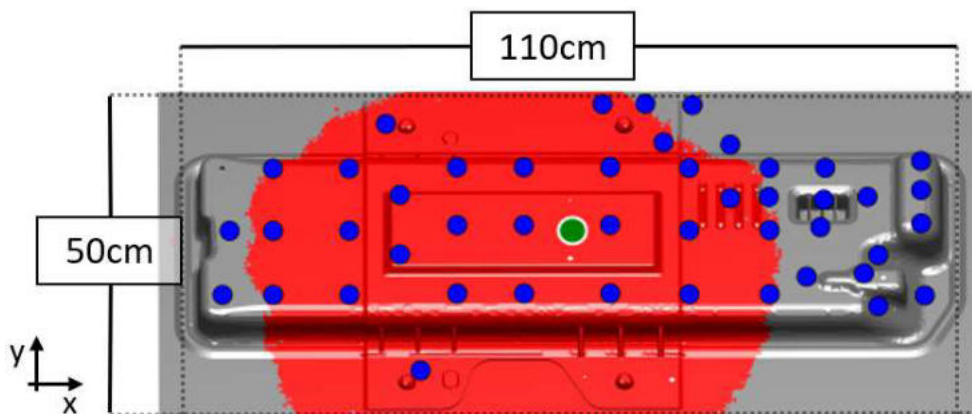


Figure 5.31: Illustration of the reconstructed flow front (red) applied to the T-RTM process. The blue dots represent US-sensor locations.

Figure 5.32 illustrates an unfinished component where the experiment had to be aborted because the catalyst was depleted during the injection process. The fibre preform was therefore partly impregnated, providing snapshots of the flow front. Despite this interruption,

it can be inferred that the flow front propagation followed similar global trends to those observed in other experiments, as the other parameters, such as temperature and pressure, remained within the expected ranges.

In general, a preferred direction of propagation can be observed. In Figure 5.32, the flow front predominantly moved along the negative x-direction (west). This preference might be due to the resin encountering fewer obstacles when moving along the negative compared to the positive x-direction. Additionally, the flanges were more effectively wetted. These trends were deduced from the unfinished parts as illustrated in the Figure 5.32.

Furthermore, this assumption is reinforced by the recurrent dry spots along the right edge of the component, indicating slower wetting rates in this direction.

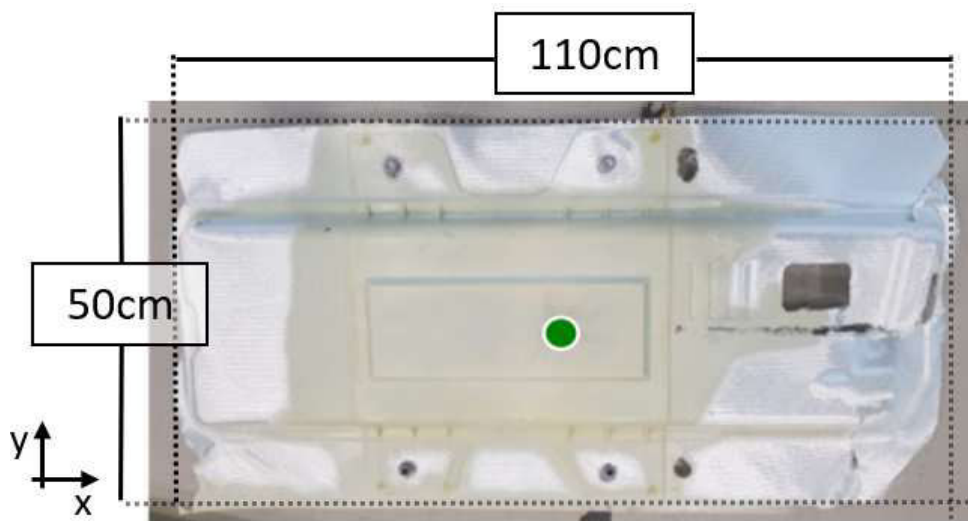


Figure 5.32: Photography of a unfinished part. The figure shows the preferred flow direction of the resin.

To mitigate this issue, strategic cuts were made in the preform, as depicted in the Figure 5.32. These cuts aimed to improve resin distribution and reduce the occurrence of dry spots. These dry spots are clearly visible in manufactured parts as well as in the reconstructions. Figure 5.33 compares the reconstruction of a successful experiment with the corresponding manufactured part, highlighting a location of crucial interest where dry spots frequently occurred. This location correlates with conspicuously long impregnation times estimated by the flow front reconstruction demonstrating that even smaller critical areas can be identified.

However, spatially localized effects, such as the flow channel formations observed in Figure 5.31, may remain undetected by the algorithm if the sensor network is unfavourably distributed.

These flow channels are often associated with tight curvatures in the mold, which can cause compressions and wrinkling in the preform. Detecting irregularities in the flow pattern requires strategically placing sensors in critical areas to capture detailed data. However,

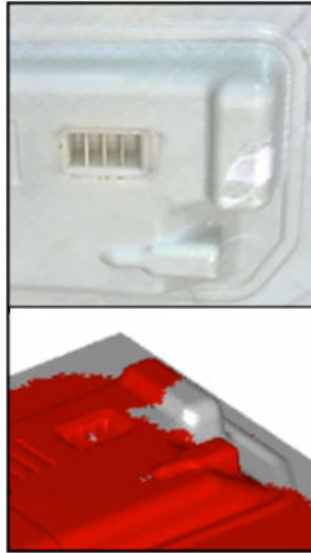


Figure 5.33: Comparison of a manufactured part (top) with its reconstruction (bottom).

in some cases, the small surface areas and sharp radii in these regions may make sensor placement challenging or even infeasible. Despite these limitations, optimizing sensor placement can significantly enhance the algorithm's ability to analyze flow front dynamics, ultimately improving quality control and the efficiency of the T-RTM process.

6 Discussion

This chapter presents an overview of the three advanced processing techniques proposed in this work: the Feature Adaption Approach, the Feature Selection Approach, and the Global Reconstruction Algorithm. For each method, the objectives and methodology are summarized, highlight the key findings. Finally, limitations and challenges are discussed considering scalability, accuracy and propose potential strategies for addressing these challenges in future research.

6.1 Feature Adaption

Objective and Methodology

The primary objective of the feature adapting approach is to optimize feature extraction parameters for ultrasound-based process monitoring to enhance the accuracy and predictive power of the monitoring system. This involves dynamically adapting the parameters of features to suit specific applications, which is crucial given that the optimal parameters can vary significantly from one application to another.

The adaptation of features from ultrasound-based measurements plays a critical role in the accuracy and robustness of process monitoring systems. Feature adaptation ensures that key aspects of the signal are preserved and enhanced in variable environments, which is particularly important in industrial applications where noise, environmental variability, and complex material interactions can impact the reliability of the extracted features.

Many features, whether simple or complex, require predetermined parameters such as frame size length, partial power limits, etc. These parameters are critical in defining the feature extraction process.

Through this approach the aim was to optimize process monitoring and set a foundation for robust analytical models. This involves a systematic approach to adjusting and validating feature parameters to achieve the best correlation with the desired physical properties, such as viscosity, curing degree, or polymerization progress.

For the experimental setup a rheometer equipped with an ultrasonic measurement system is used. The setup includes a piezoelectric ceramic transducer for both emitting and receiving ultrasound signals. The signals are collected during the polymerization process of ϵ -Caprolactam to Polyamide-6, with the rheometer providing reference viscosity measure-

ments.

Ultrasound signals are captured at regular intervals. These signals are then preprocessed using digital filtering techniques to enhance signal quality by removing noise and irrelevant frequency components. After that the features are extracted.

The focus was on partial power features (representative of the frequency spectrum) and RMS (root mean square) as a time-domain feature.

- Partial Power: Ratio of the energy in specific frequency bands to the full energy.
- RMS: This measures the signal amplitude over time, providing insights into the overall energy and consistency of the ultrasonic signal.

These were chosen for their ease of interpretability, which is essential for practical applications. This simplicity helps to understand optimization process and to judge if the features generalize well across different conditions, avoiding the risk of overfitting. This is a major concern when tailoring features too specifically to an application.

The methodology involves varying the parameters of the selected features and calculating the Pearson correlation coefficient (R-score) with the desired outcome (e.g., viscosity measured by the rheometer). This iterative process helps in identifying the optimal parameter settings that provide the highest correlation with the monitored property.

For partial power features, the frequency bands are varied to find the most responsive range and for RMS, different time windows are tested to capture the most significant signal segments.

Overfitting occurs when the model or features are too closely tailored to the training data, resulting in poor generalization to new data. By interpreting the R-scores general patterns to avoid overfitting can be identified. For example, for the rheometer experiments it can be deduced, that the optimal frequency ranges for the partial power feature consistently ended at about 2 MHz - 2.2 MHz. This frequency correlates with the sensor's eigenfrequency.

To validate this approach, it was applied to the T-RTM process, where monitoring polymerization is crucial. In this context, the same material, ϵ -Caprolactam, was used as in the rheometer experiments. This application aims to investigate if the findings from the laboratory-controlled rheometer experiments can be effectively translated to entirely different setups within industrial environments.

Key findings

The methodology successfully identified parameter settings that achieve high correlations between features and desired process variables while also providing insights into the underlying physical principles. By carefully interpreting and visualizing the results, it becomes

possible to uncover physical correlations, providing insights that can be applied across various applications.

Specifically, the study found significant correlations between the extracted ultrasound signal features and the viscosity measurements obtained from the rheometer. Notably, the partial power feature consistently showed high correlation values across different experiments, demonstrating its reliability in tracking changes in viscosity. A deeper analysis of the correlation values revealed relationships with the sensor characteristics. For instance, the optimal parameter setting for the partial power feature consistently showed that the frequency window ended around 2.2 MHz.

This pattern, observed across different experiments, provided a general recommendation for the limits of spectral energy densities. The consistent finding that the optimal frequency window aligned with the sensor's resonance frequency indicated that the method was not overfitting to the noise or random fluctuations. This finding is opposed to a random value caused by overfitting but a constant property of the sensor and could be a general frequency range applicable to different applications.

This approach is further investigated if it can be applied to more complex, non-laboratory processes. Therefore, the findings on viscosity tracking from the rheometer experiments were evaluated for their applicability to T-RTM experiments. In T-RTM, an important aspect for efficient production is accurately determining the time of full polymerization. Achieving full polymerization ensures that the final composite material exhibits the desired mechanical properties and structural integrity.

Based on this work, a relationship between polymerization and viscosity could be established. It could be observed that the time to reach full polymerization often shows a delay compared to the time required to achieve a constant viscosity. By calculating this time shift and leveraging the established correlation between viscosity and ultrasound (US) signal features, the time to full polymerization can be assessed solely based on US data.

The results of this approach showed excellent agreement with more complex methods that combine simulation models and DEA data. This validation demonstrates that this ultrasound-based monitoring technique can reliably predict the time of full polymerization, simplifying the monitoring process while maintaining accuracy. This approach not only enhances the efficiency of the T-RTM process but also underscores the potential of ultrasound monitoring as a versatile tool in various industrial applications.

In general, the success of ML-based approaches is highly dependent on the quality and relevance of the features used in the model. Features represent the underlying patterns or properties in the data, and if they are not well-defined or relevant, the algorithms may struggle to make accurate predictions [122–124].

Proper feature engineering, therefore, becomes essential. Extensive research exists on feature selection methods, such as filtering, wrapper methods, and embedded techniques, which help in selecting or ranking features from an existing pool [61, 122, 124]. These methods mainly aim to reduce dimensionality and improve model performance by focusing on the most informative features. In this work, however, we not only apply feature selection techniques but also focus on optimizing individual features before they are selected. Thus using Pearson correlation the individual features are evaluated and optimized based on their relationship with the target variables, ensuring that the features are meaningful and contribute to model accuracy.

It is logical to first optimize and properly define features before selecting them because the quality of the features directly influences the effectiveness of feature selection techniques. If the features are poorly defined or improperly tuned, even a well-performing selection method might overlook their potential value. By optimizing features beforehand, we ensure that they reflect the most relevant aspects of the process, making feature selection more efficient and accurate.

Adapting individual features in this way has three primary benefits:

- Revealing the physical background and interpretation of the process and signal.
- Obtaining strong correlations with the desired variables.
- Improving the foundation for ML model performance.

Limitations

- Specific focus of study: Although the findings from the rheometer experiments and their application to the T-RTM process are promising and accurate, further research is needed to validate the method's applicability to other materials and processes. Since this study focused on a specific polymerization process and material system, additional experiments are essential to confirm the robustness of the approach. To broaden the application scope, future work should include testing the developed methods on a wider range of materials and manufacturing processes. This would help in establishing the generalizability and robustness of the techniques. To this end improving applicability and facilitate industrial implementation, developing adaptive algorithms that can automatically adjust feature extraction parameters in real-time based on changing process conditions will enhance the practicality and efficiency of ultrasound-based monitoring systems.
- Computational intensity: The iterative optimization process for feature extraction parameters can be computationally intensive, potentially limiting its use in real-

time industrial applications. Further optimization of this approach, including the integration of techniques such as parallel computing, could significantly enhance computational efficiency.

Currently, this method is best suited for offline application as a tool to refine features and improve the corresponding predictive model. By applying the method beforehand, it can also aid in uncovering the underlying physical principles of the process by identifying optimal parameter settings, thereby enabling robust feature selection.

- Complexity of quantitatively predictions: The method has been shown to qualitatively monitor rheological properties effectively. As a next step, appropriate models with optimized features as input parameters can be developed to provide not only qualitative predictions but also quantitative determinations of rheological measurements. To quantitatively predict process variables or material properties from ultrasound measurements, machine learning (ML) and deep learning (DL) approaches can be employed. However, these methods require a robust and extensive data foundation, which can be costly and time-consuming to generate.

Alternatively, mathematical models such as physical inversion models [125] can be developed. However, constructing accurate physical models and identifying reliable correlations is also a challenging and resource-intensive task. These models are highly dependent on process variables such as pressure and temperature, and their complexity increases significantly in real-world applications, where sound wave paths are non-linear or pass through multiple material interfaces [123, 126].

To address these challenges, refining the feature adaptation approach by simultaneously optimizing multiple parameters presents a promising alternative. By adapting features to strongly correlate with the desired properties, this approach can uncover simple and effective mathematical relationships for predicting process variables, reducing reliance on extensive theoretical modeling.

6.2 Feature Selection

Objective and Methodology

In many cases, the primary issue with machine learning models is not the initial accuracy achieved but rather the robustness of the model as conditions change over time. This is also known as data drift, where the statistical properties of the target variable shift due to environmental or operational changes, making long-term model accuracy harder to maintain. [19]. This can occur due to the model focusing on noise or other properties that are not constant over time, thereby failing to generalize well to new data.

To mitigate these issues, analytical models require high maintenance, including regular retraining, updating training data and adaptive learning techniques.

While the aforementioned methods are essential, the approach discussed here aims to complement them by reducing maintenance efforts and extending intervals between retraining or supporting adaptive learning techniques. The feature selection approach focusses on enhancing the robustness and accuracy of predictive models by carefully selecting and optimizing features. This approach integrates both common feature selection algorithms [71, 124, 127] and model-based permutation methods to create a comprehensive feature selection framework.

The methodology is as follows:

1. **Preselection Features:** Depending on computational resources an initial extensive list of features is compiled from various sources, including domain knowledge and previous successful applications.
2. **Feature Model Selection (FMS):** This method involves training separate models for each possible combination of features and averaging their accuracy scores. While it provides a direct link between feature scoring and model performance, it is computationally intensive. To tailor the scores for robustness, introduce synthetically distorted data customized for the application or use data recorded later in time that exhibits real signal degradation. This approach ensures that the selected features remain effective under various conditions, enhancing the overall reliability of the model. However, this approach, especially with a large number of features, can be computationally demanding. Additionally, datasets containing real degraded data might not always be readily accessible.
3. To combine the benefits of the FMS method while maintaining an efficient selection algorithm, utilize weighted standard feature selection algorithms (SFS). The weights, derived from FMS and calculated only once, are used to adjust the importance of features within the SFS algorithms, thereby enhancing robustness. This approach retains the accuracy and reliability of FMS and can be efficiently applied to larger feature sets.

To test this method, a setup for gearbox monitoring was constructed, allowing us to configure three different gears in a controlled environment. The setup was equipped with an ultrasound sensor and the trained ML model is expected to identify these gears based on the recorded ultrasound data and selected features.

Over time, it is anticipated that the prediction power of the model will decline due to wear, mechanical misalignment and changes in environmental conditions. This can lead to altered acoustic emission patterns or degradation of the acoustic signal. To evaluate the selected features and their performance under the influence of a degraded signal, the setup was deliberately not readjusted or maintained.

Key Findings

Using the recorded data from this setup, the proposed selection methods can be applied and compared to standard feature selection algorithms. To do this, 51 features are preselected out of which the best n features are identified by each corresponding algorithm. The number of features n was varied from 7 to 14 to minimize bias and ensure a comprehensive evaluation. The features were selected based on the following methods:

1. FMS: Based on artificial corrupted data with random noise.
2. FMS: Based on recorded data later in time.
3. Standard Feature Selection Methods.
4. Weighted Feature Selection Methods
5. All 51 features.

For each method, the selected features are used to train SVM models on previously recorded data. Then the models' prediction accuracy was tested on data recorded at a later time to evaluate their performance under real signal degradation conditions. The results showed that, on average, except for one dataset, every selected feature set performed better than using the full set of 51 features. This indicates that feature selection plays a crucial role in improving model accuracy and robustness.

Disregarding the single anomaly, it was found that the proposed feature selection methods outperformed the standard feature selection algorithms. The FMS model based on recorded data from a later time achieved the best performance. This suggests that features identified using naturally degraded data provide a more realistic and effective selection for long-term model reliability.

Overall, this study demonstrates the effectiveness of combining FMS with weighted standard feature selection methods to enhance feature robustness and model accuracy, even in the presence of signal degradation. This approach offers a practical solution for improving the performance of machine learning models in real-world applications where data quality may deteriorate over time.

Limitations

- Dependence on temporal data: The best-performing model, the Feature Selection Model (FMS), which was based on recorded data from a later time, benefited from prior exposure to the data. This exposure allowed the model to learn patterns of degradation and recognize specific characteristics that are crucial for robust feature selection. Consequently, the model had an inherent advantage, as it could identify and adapt to these patterns more effectively than models trained on earlier or synthetic data with noise.

Despite the advantage of prior exposure, the model also demonstrated superior performance on new, unseen data. This indicates that the model has not only learned to identify critical patterns in the training data but has also developed a level of robustness that enables it to generalize to other data variations. This suggests that the model's feature selection process is highly effective at capturing the essential characteristics required for accurate predictions, even under data variability.

To achieve the best possible results, it is crucial to record data over time. In real-world applications, data availability for the FMS approach can be limited, particularly in industrial systems where degraded data is scarce due to the need for maintaining optimal conditions. In such cases, synthetic corrupted data with noise can be employed. Methods based on artificially corrupted data with random noise and weighted feature selection methods also showed improved robustness compared to standard feature selection models. These methods provide an advantage because they avoid selecting features based solely on correlations, instead focusing on capturing deeper, more meaningful relationships.

So far, simple techniques such as superimposing white noise was used. By introducing more sophisticated disturbances based on physical considerations—such as expected frequency shifts—the feature selection process can be further enhanced. This allows the simulation of potential degradation scenarios, providing a more comprehensive basis for robust feature selection.

- **Causal understanding:** In the proposed approach, the aim was to tailor a feature selection algorithm specifically to the given application without requiring a full understanding of the physical relationships. The proposed method allows users to adapt the algorithm to work with synthetic corrupted data or data exposed to degradation over time, ensuring that the selected features are robust to this type of perturbation. The standard feature selection algorithms typically select features based on correlations between predictive features and the target variable. However, correlations only indicate how often features occur with the corresponding target variable, without uncovering deeper or causal relationships.

However, as shown in [128, 129], correlation between shoe size and reading ability in children or between being in bed and dying are not causally meaningful predictors. These examples illustrate that relying solely on correlations can result in predictors that lack robustness and interpretability.

Thus, for robustness, it is beneficial to understand the physical relationships and cause-and-effect dynamics underlying the data, leading to more prudent feature selection. However, identifying these relationships is not always straightforward due to complex dependencies, environmental factors, uncontrollable conditions, and unknown physical parameters. These complexities make it challenging to fully understand the underlying causal mechanisms, particularly in real-world applications. The problem of unstable feature selection has also been highlighted in recent de-

velopments, where causality-based feature selection methods are being developed. These methods aim to identify features that directly influence the outcome, rather than relying on mere correlations [128–130].

Causality-based features have a direct cause-and-effect relationship with the target variable, making them more reliable than correlated features. Various methods of causal feature selection, such as Bayesian networks and Markov boundary theory, help identify features relevant for predicting the target variable. These methods can be broadly categorized into constraint-based approaches, such as the Markov blanket, which represents the minimal set of variables that render the target variable conditionally independent of the rest, and score-based approaches, which use statistical measures (e.g., likelihood, BIC) to find the best causal relationships, often based on Bayesian networks.

These causality-based methods could be combined with the current approach. For instance, instead of weighting standard feature selection methods, weighted causality-based feature selection methods could be employed. Alternatively, they could be used as pre- or post-processing steps to enhance the robustness of feature selection.

Incorporating these advanced methods offers a more robust feature selection process that goes beyond correlation, making it flexible and adaptable to various complex real-world data scenarios.

- **Model longevity:** A critical question remains of how long will the model maintain this robustness. As the system continues to degrade and new patterns emerge, the model's ability to adapt and remain accurate will be tested. Further investigation is necessary to confirm the model's robustness over extended periods. Specifically, long-term testing with data recorded over longer timeframes will help determine how well the model maintains its performance as new degradation patterns develop.
- **Computational intensity:** Addressing the issue of computational efficiency, optimizing the code can significantly reduce computation time. Techniques such as parallel processing, multi-core processors, distributed computing, and GPU acceleration can speed up the process and improve scalability.
- **Application breadth:** The methods can be tested across different applications. Future research should investigate their performance in general gearbox configurations and other industrial applications. This would involve validating the robustness and adaptability of selected features and weights across various scenarios and equipment to ensure their broad applicability.

6.3 Global Reconstruction

Objective and Methodology

In process monitoring, data collection is often confined to the detection range and sensitivity of the sensors. The primary goal of the proposed reconstruction method is to leverage this limited, localized sensor data to generate comprehensive, full-coverage information, which is essential for thorough and optimal monitoring.

This research focuses on the propagation of flow fronts, as seen in injection and infusion processes like T-RTM and VAP. In these manufacturing processes, accurately monitoring and understanding flow fronts is crucial for ensuring product quality and process efficiency. The study illustrates how the proposed method is used for flow front reconstruction addressing challenges posed by sparsely distributed sensors and complex geometries. Especially in processes like the T-RTM process, where visual inspections are not feasible, such data reconstruction simplifies automated process monitoring and subsequent diagnosis of process anomalies.

The global reconstruction algorithm's methodology involves the following key steps which are illustrated in Figure 6.1:

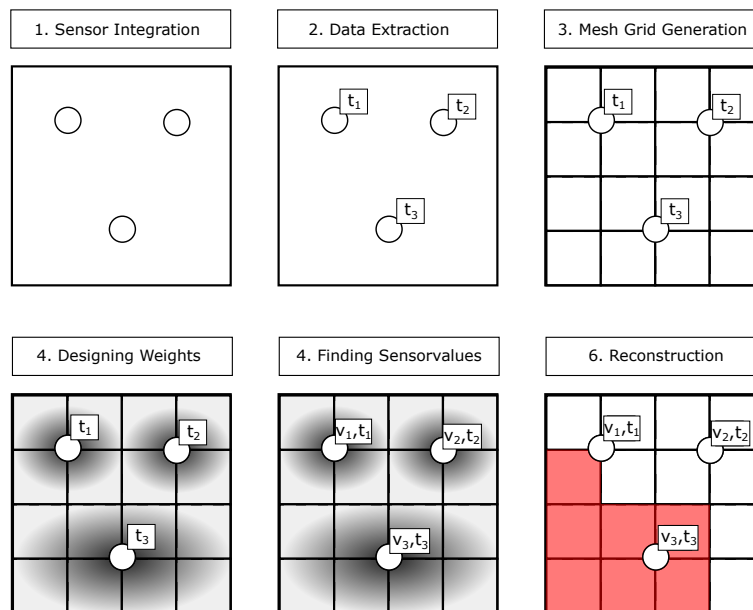


Figure 6.1: Illustration of the global reconstruction algorithm steps: (1) Strategic Sensor integration into the process geometry. (2) Relevant data is extracted. (3) A mesh grid is generated to represent the process geometry. (4) Weight functions are optimized for accurate representation. (5) Sensor values are optimized to minimize error. (6) The data is reconstructed based on the determined parameters.

1. Sensor integration: A network of sensors is strategically integrated into the process with minimal interference.

2. Data Extraction: Higher-level information of interest, such as the flow front arrival times $t_{1...3}$, is extracted from the acquired data.
3. Mesh grid generation: A triangular mesh grid is generated to cover the relevant geometries of the process. The size of the mesh is adapted to balance efficiency and accuracy. The extracted information from the previous step is assigned to the corresponding nodes representing.
4. Weight function design: A weight function is tailored to the geometry, with parameters optimized by assigning expected values for the propagating variable, such as flow front velocity. Iterative adjustments are made to minimize error, and the parameter set with the lowest error is chosen for the next steps.
5. Sensor values optimization: The final step involves determining sensor values that, in combination with the weight function, enable full reconstruction. Optimal sensor velocities are found by fitting the reconstruction to the measurements $t_{1...3}$ as boundary values. Minimizing the error yields the parameters $v_{1...3}$. In the context of reconstructing the flow front, these values correspond to velocities, consistent with the units involved.
6. Reconstruction: When the crucial parameter, such as mesh grid, weight function and sensor values are determined, the data can be reconstructed and for each node. For instance, the flow front can be visualized by couriering the areas for which the majority of corresponding nodes indicate its arrival.

Key Results

Using sensor networks, the reconstruction algorithm is adaptable to various applications and geometries through a careful selection of parameters.

The presented applications of the algorithm demonstrate its effectiveness in monitoring flow front propagation. Particularly, the focus is on processes such as the VAP and T-RTM and have demonstrated the algorithm's effectiveness in capturing the flow front.

In the T-RTM experiments, where large-scale observation is challenging, the reconstruction method helped to identify critical areas that are not directly detectable during the process. Based on these insights, proactive interventions were successfully implemented in subsequent experiments to prevent defects, such as dry spots, and optimize production.

Thus the identification of critical spots in the T-RTM process, and the low temporal deviation achieved in the VAP, 1.7% compared to the total process time, demonstrate the algorithm's potential for real-world applications.

In addition to geometric information, the algorithm requires only the arrival times of the flow front extracted from the sensor data. Without any assumption about the underlying

physics, the algorithm provides a generic method for reconstructing propagating mediums. With the adaptable weight function, the fundamentals of the algorithm extend beyond flow front simulations and can be applied to a variety of processes and diverse geometries without needing extensive modifications.

In the T-RTM process, which involves a two-stage polymerization with a complicated viscosity profile and permeability variations influenced by press pressure and fold formation, traditional simulations can be extremely challenging. The reconstruction algorithm, however, provides a straightforward and effective overview of the flow front dynamics.

Thus, the algorithm is capable to provide insights into the process efficiently.

For instance, it can quickly deliver the preferred directions of flow propagation even without conducting abortive tests, the algorithm would have identified the preferred flow front propagation directions in the T-RTM process. And it can highlight critical areas, such as the frequently observed dry spots, by analyzing the extended wetting times. This allows for proactive adjustments and optimizations in the manufacturing process.

This issue of flow front estimation has been addressed by combining pressure sensors with neural networks and physics simulation [131]. Other approaches [132, 133] use pressure sensors with flow front modelling based on Darcy's Law.

This approach suggests a generic algorithm for estimating a propagating quantity and applies it to reconstruct the flow front in infusion and injection moulding processes. Therefore, no physics-based simulation or alongside modelling of the actual process is required. The algorithm is based on graph theory, using the geometrical boundary conditions and the arrival time of the flow front at individual sensors. Given that the applied sensors can properly detect the arrival time of the flow front, the algorithm is independent of the specific sensor type.

It should be noted, however, that the reconstruction algorithm is not intended to replace simulations. Simulations require detailed knowledge of physical material parameters and are primarily used before the process to conduct feasibility studies and make preventive adjustments. The flow front algorithm, on the other hand, is applied post-process to provide recommendations for subsequent experiments by interpreting the results and identifying critical areas.

Limitations

While the reconstruction algorithm offers significant advantages for monitoring and control in composite manufacturing processes, it also has several limitations that must be acknowledged. Despite these limitations, the reconstruction algorithm developed for detecting and analyzing flow front propagation in composite manufacturing processes holds significant potential for advancing industrial practices. There are several key areas in which

further development contribute to to fully realize the algorithm's capabilities and extend its applicability:

- **Dependence on Sensor Placement:** The accuracy and reliability of the reconstruction depend on the strategic placement and density of the sensors. Inadequate sensor coverage, particularly in complex geometries or critical areas, can lead to inaccuracies in the reconstructed data. Critical areas with high complexity require a higher density of sensors to capture the details of the flow front accurately. This need for extensive sensor networks can increase costs and complicate the setup. Future work should focus on integrating advanced sensor technologies and optimizing sensor networks. This includes exploring new sensor types that provide higher resolution and sensitivity, as well as employing machine learning techniques to optimize sensor placement dynamically. By refining the sensor network, the accuracy and reliability of the flow front reconstruction can be significantly improved.
- **Sensitivity to Initial Parameter Settings:** The performance of the reconstruction algorithm is sensitive to the initial parameter settings of the weight function and sensor velocities. Incorrect parameterization can result in significant deviations from actual values, necessitating careful calibration and optimization.
- **Post-Process Application:** The reconstruction method is typically applied post-process, meaning it cannot provide real-time monitoring or immediate feedback during the manufacturing process. This limitation restricts its ability to facilitate on-the-fly adjustments and corrections. For real-time applications, the algorithm would need to be integrated with real-time data acquisition systems and control frameworks, which could introduce additional technical challenges. Developing real-time monitoring and feedback systems is a critical next step. Implementing the algorithm in a real-time framework will allow for continuous monitoring of the manufacturing process, enabling immediate detection and correction of anomalies. This will not only enhance process control but also reduce the likelihood of defects, improving overall product quality.
- **User-Friendly Interface and Visualization Tools:** Creating a user-friendly interface and advanced visualization tools will make the algorithm more accessible. By providing intuitive visualizations and easy-to-use controls, users can better understand the flow front dynamics and make informed decisions during the manufacturing process.
- **New Applications:** While the algorithm has shown promise in VAP and T-RTM processes, exploring its application in other manufacturing methods and industries can uncover new opportunities. Adapting the algorithm to different materials, processes, and industry requirements will test its utility.

7 Summary and Outlook

The primary challenge addressed in this dissertation was to improve the effectiveness of ultrasound-based process monitoring systems, ensuring they maintain accuracy and robustness even under complex and variable industrial conditions.

Several key challenges in advancing process monitoring were identified and addressed:

- **Feature Adaption:** The parameters of the extracted features are optimized to better capture relevant process variables, thereby increasing the precision and reliability of the monitoring system. This approach ensures that the features used are finely tuned to the specific conditions of each application, allowing for more accurate predictions.
- **Feature Selection:** Recognizing that many predictive models experience performance degradation over time, the focus was placed on selecting features that are not only relevant but also resilient to changes and drifts in operational conditions. An innovative aspect of this approach is that the selection algorithm can be customized to the specific application by individually choosing the test datasets. This allows for the selection of features that are particularly robust against the challenges presented in the test datasets. As a result, the long-term effectiveness of the monitoring systems can be maintained, even as the industrial environment evolves.
- **Due to the physical limitations of sensor placement,** techniques were developed to reconstruct data from regions beyond the immediate reach of sensors. This innovation expands monitoring coverage, ensuring that critical areas are not overlooked despite sensor constraints. The algorithm operates independently of physical models or simulations, enhancing the sensor-acquired data. It can be effectively applied without relying on often difficult to determine physical parameters of the processes.

These approaches help to enhance the accuracy and resilience of monitoring systems. By combining customizable feature engineering with data reconstruction, it becomes possible to effectively operate even with limited sensor access, thereby increasing the systems' versatility and adaptability across a broader range of industrial applications.

While the contributions of this work represent significant progress, there remain numerous opportunities for further advancement in ultrasound-based monitoring systems. The complexity and creativity inherent in data acquisition, processing, and interpretation offer multiple avenues for development. Various techniques have emerged for the detection of anomalous sounds, such as Autoencoders, which are unsupervised neural networks that

learn to reconstruct input data, thereby identifying abnormal operations. Another approach is Gaussian Mixture Model-Based Anomaly Detection, which models the distribution of normal acoustic features to identify anomalies based on the low probability of a data point fitting within this distribution. [15, 89] .

Recent enhancements extend beyond just processing and interpretation techniques. There is also significant potential in improving the quality of raw data, advancing sensor technology, and refining data processing methods. For instance, Phased Array Ultrasonic Testing (PAUT), as demonstrated in [134], offers substantial advantages over conventional Single Element Ultrasonic Testing (SEUT) in inspecting composite materials. PAUT's ability to focus signals, reduce noise, and detect smaller defects with higher accuracy makes it a superior choice in many applications.

So far there have been significant advancements across various areas of ultrasound-based monitoring, ranging from the development of advanced sensor technologies to improvements in data acquisition hardware and the emergence of sophisticated processing techniques. These progressions have collectively enhanced the capabilities and applications of ultrasound monitoring systems.

However, future research and applications should not merely focus on individual advancements but rather aim to integrate these developments to fully unlock the potential of ultrasound-based monitoring systems. The real challenge lies in navigating the broad and complex field of ultrasound monitoring. Thus, it is essential to not only focus on specific areas of this expansive field but also to determine and combine the most suitable approaches for each unique application.

Navigating this "jungle" of recent innovations requires a strategic approach, where the goal is to maximize the effectiveness, precision, and reliability of ultrasound-based monitoring systems. By carefully selecting and integrating the best advancements, tailored to the specific demands of each application, the full potential of these systems can be realized.

Glossary

C_{iklm}	Elasticity tensor. 6, 7, 150
E_n	Edges of the graph. 150
E	Young's modulus. 7, 150
G	Shear modulus. 7, 150
N_j	Nodes of the graph. 150
N	Near field length. 10, 150
R	Parameter to control the angular weight contribution. 88, 89, 96, 98, 124, 150
R	Reflection factor. 150
S_i	Sample points of the graph. 150
T	Transmission factor. 150
Z	Sound impedance. 150
δ	Parameter to control the characteristics of angular weight. 88–91, 96–98, 124, 150, 170
ϵ	Parameter to control the characteristics of radial weight. 88–91, 96–98, 124, 150, 170
ν	Poisson ratio. 7, 150
σ_{ik}	Stress tensor. 6, 150
p	Sound pressure. 150
s_{FMS}	Final feature score based on feature model selection approach. 80, 83, 84, 150
s_{SFS}	Final feature score based on standard feature selection approach. 80, 150
t_j	Reconstructed time values [s]. 150
w_{in}	Weight function defining the contribution of sample point i to node n in the graph. 124, 150
$x_{1,2,3}$	Local coordinate [m]. 150

Acronyms

ANOVA	Analysis of Variance. 39, 40, 86, 150, 170
CM	condition monitoring. 1, 3, 4, 38, 150
DFT	discrete Fourier transform. 19–21, 150
FFT	fast Fourier transform. 19, 20, 36, 150
FMS	feature model selection. 80–83, 86, 150, 170
FT	Fourier transform. 15–17, 19, 27, 28, 150
NDT	non destructive testing. 2, 5, 150
RMS	root mean square. 31, 34, 36, 48–50, 100–106, 126, 150, 168, 171
SFS	standard feature selection. 80–82, 86, 150, 170
SHM	structural health monitoring. 2, 150
T-RTM	thermoplastic resin transfer moulding. 43, 52–56, 58, 99, 106–108, 121, 122, 124, 125, 128, 129, 131, 133, 144–147, 150, 169, 172
US	ultrasound. 43, 107, 150
VAP	vacuum assisted process. 43, 52–54, 99, 121–126, 144, 145, 147, 150, 169, 172

References

- [1] P. Glavič, Z. N. Pintarič, and M. Bogataj, “Process design and sustainable development—a European perspective”, *Processes* **9**, 148 (2021).
- [2] Y. S. Perera, D. Ratnaweera, C. H. Dasanayaka, and C. Abeykoon, “The role of artificial intelligence-driven soft sensors in advanced sustainable process industries: A critical review”, *Engineering Applications of Artificial Intelligence* **121**, 105988 (2023).
- [3] P. Bradu, A. Biswas, C. Nair, S. Sreevalsakumar, M. Patil, S. Kannampuzha, A. G. Mukherjee, U. R. Wanjari, K. Renu, B. Vellingiri, et al., “Recent advances in green technology and Industrial Revolution 4.0 for a sustainable future”, *Environmental Science and Pollution Research* **30**, 124488 (2023).
- [4] Z. M. Çınar, A. Abdussalam Nuhu, Q. Zeeshan, O. Korhan, M. Asmael, and B. Safaei, “Machine learning in predictive maintenance towards sustainable smart manufacturing in industry 4.0”, *Sustainability* **12**, 8211 (2020).
- [5] *DIN ISO 17359: Condition monitoring and diagnostics of machines - General guidelines*, Deutsche Norm, Replaces DIN ISO 17359:2003-11 (Deutsches Institut für Normung e.V., 2011).
- [6] M. S. Reis and G. Gins, “Industrial process monitoring in the big data/industry 4.0 era: From detection, to diagnosis, to prognosis”, *Processes* **5**, 35 (2017).
- [7] A. Razek, “Monitoring Complexity in Clean Energy Systems Applications”, *Clean Energy and Sustainability* **2**, 10007 (2024).
- [8] D. Wu, W. Qu, Y. Wen, Y. Zhang, and B. Liang, “The Application, Challenge, and Developing Trends of Non-destructive Testing Technique for Large-scale and Complex Engineering Components Fabricated by Metal Additive Manufacturing Technology in Aerospace”, *Journal of Nondestructive Evaluation* **43**, 86 (2024).
- [9] M. Gupta, M. A. Khan, R. Butola, and R. M. Singari, “Advances in applications of Non-Destructive Testing (NDT): A review”, *Advances in Materials and Processing Technologies* **8**, 2286 (2022).
- [10] N. Liebers, “Ultraschallsensorgeführte Infusions-und Aushärteprozesse für Faserverbundkunststoffe”, *PhD Thesis*, (2018).
- [11] D. Chauveau, “Review of NDT and process monitoring techniques usable to produce high-quality parts by welding or additive manufacturing”, *Welding in the World* **62**, 1097 (2018).

- [12] Y. Yu, X. Cui, Z. Liang, X. Qing, and W. Yan, “Monitoring of three-dimensional resin flow front using hybrid piezoelectric-fiber sensor network in a liquid composite molding process”, *Composites Science and Technology* **229**, 109712 (2022).
- [13] Z. Yang, H. Yang, T. Tian, D. Deng, M. Hu, J. Ma, D. Gao, J. Zhang, S. Ma, L. Yang, et al., “A review on guided-ultrasonic-wave-based structural health monitoring: From fundamental theory to machine learning techniques”, *Ultrasonics* **133**, 107014 (2023).
- [14] B. Luijten, N. Chennakeshava, Y. C. Eldar, M. Mischi, and R. J. van Sloun, “Ultrasound signal processing: from models to deep learning”, *Ultrasound in medicine & biology* **49**, 677 (2023).
- [15] G. Jombo and Y. Zhang, “Acoustic-based machine condition monitoring—methods and challenges”, *Eng* **4**, 47 (2023).
- [16] S. Hassani and U. Dackermann, “A systematic review of advanced sensor technologies for non-destructive testing and structural health monitoring”, *Sensors* **23**, 2204 (2023).
- [17] M. Kuhn and K. Johnson, *Feature engineering and selection: A practical approach for predictive models* (Chapman and Hall/CRC, 2019).
- [18] R. Zebari, A. Abdulazeez, D. Zeebaree, D. Zebari, and J. Saeed, “A comprehensive review of dimensionality reduction techniques for feature selection and feature extraction”, *Journal of Applied Science and Technology Trends* **1**, 56 (2020).
- [19] F. Bayram, B. S. Ahmed, and A. Kassler, “From concept drift to model degradation: An overview on performance-aware drift detectors”, *Knowledge-Based Systems* **245**, 108632 (2022).
- [20] J. Krautkrämer and H. Krautkrämer, *Ultrasonic testing of materials* (Springer Science & Business Media, 2013).
- [21] L. P. Feigen, *Physical characteristics of sound and hearing*, Vol. 28, 2 (Elsevier, 1971), pp. 130–133.
- [22] M. Sause, *Identification of failure mechanisms in hybrid materials utilizing pattern recognition techniques applied to acoustic emission signals* (mbv, Mensch-und-Buch-Verlag, 2010).
- [23] B. A. Auld, *Acoustic fields and waves in solids* (Krieger Publishing Company, 1973).
- [24] F. I. Fedorov, *Theory of elastic waves in crystals* (Springer Science & Business Media, 2013).
- [25] J. L. Rose, *Ultrasonic waves in solid media* (Acoustical Society of America, 2014).
- [26] H. Stenzel, *Leitfaden zur Berechnung von Schallvorgängen* (Springer-Verlag, 2013).
- [27] W. P. Mason, *Physical acoustics and the properties of solids* (van Nostrand, 1958).
- [28] T. Cox and P. d’Antonio, *Acoustic absorbers and diffusers: theory, design and application* (CRC press, 2016).

- [29] G. Wissmeyer, M. A. Pleitez, A. Rosenthal, and V. Ntziachristos, “Looking at sound: optoacoustics with all-optical ultrasound detection”, *Light: Science & Applications* **7**, 53 (2018).
- [30] H. Selim, M. Delgado-Prieto, J. Trull, R. Pico, L. Romeral, and C. Cojocar, “Defect reconstruction by non-destructive testing with laser induced ultrasonic detection”, *Ultrasonics* **101**, 106000 (2020).
- [31] Y. Yao, Y. Pan, and S. Liu, “Power ultrasound and its applications: A state-of-the-art review”, *Ultrasonics sonochemistry* **62**, 104722 (2020).
- [32] G. Gautschi, “Background of Piezoelectric Sensors”, in *Piezoelectric Sensorics* (Springer, Berlin, Heidelberg, 2002).
- [33] B. Landolt, “Numerical data and functional relationships in science and technology”, *Magnetic and Another Properties of Oxides and Related Compounds*. (1978).
- [34] F. Linscheid, “Entwicklung eines Zustandsüberwachungssystem durch Kombination von akustischen Überwachungsverfahren.”, *Thesis*, (2022).
- [35] P. R. Stepanishen, “Pulsed transmit/receive response of ultrasonic piezoelectric transducers”, *The Journal of the Acoustical Society of America* **69**, 1815 (1981).
- [36] P. Franček, A. Petošić, M. Budimir, and I. Hrabar, “Electrical resonance/antiresonance characterization of NDT transducer and possible optimization of impulse excitation signals width and their types”, *NDT & E International* **106**, 29 (2019).
- [37] R. Bracewell and P. B. Kahn, “The Fourier transform and its applications”, *American Journal of Physics* **34**, 712 (1966).
- [38] A. V. Oppenheim, *Discrete-time signal processing* (Pearson Education India, 1999).
- [39] M. Unser, “Sampling-50 years after Shannon”, *Proceedings of the IEEE* **88**, 569 (2000).
- [40] M. Frigo and S. G. Johnson, “FFTW: An adaptive software architecture for the FFT”, in *Proceedings of the 1998 IEEE International Conference on Acoustics, Speech and Signal Processing, ICASSP’98* (Cat. No. 98CH36181), Vol. 3 (IEEE, 1998), pp. 1381–1384.
- [41] S. Haykin and B. Van Veen, *Signals and systems* (John Wiley & Sons, 2007).
- [42] A. S. Sedra and K. C. Smith, *Microelectronic circuits* (Holt, Rinehart & Winston, 1987).
- [43] J. G. Proakis, *Digital signal processing: principles, algorithms, and applications, 4/E* (Pearson Education India, 2007).
- [44] C. E. Shannon, “Communication in the presence of noise”, *Proceedings of the IRE* **37**, 10 (1949).
- [45] R. L. Allen and D. Mills, *Signal analysis: time, frequency, scale, and structure* (John Wiley & Sons, 2004).

- [46] N. Abdennour, T. Ouni, and N. B. Amor, “The importance of signal pre-processing for machine learning: The influence of Data scaling in a driver identity classification”, in 2021 18th International Conference on Computer Systems and Applications (AICCSA) (IEEE, 2021), pp. 1–6.
- [47] A. A. Torres-Garcia, O. Mendoza-Montoya, M. Molinas, J. M. Antelis, L. A. Moctezuma, and T. Hernandez-Del-Toro, “Pre-processing and feature extraction”, in *Biosignal processing and classification using computational learning and intelligence* (Elsevier, 2022), pp. 59–91.
- [48] L. He and B. Feng, “Time–Frequency Domain Analysis”, in *Fundamentals of Measurement and Signal Analysis* (Springer, 2022), pp. 143–160.
- [49] H. Schmickler, “Time-domain and Frequency-domain Signals and their Analysis”, *arXiv preprint arXiv:2009.14544* (2020).
- [50] M. G. Pecht and M. Kang, “Machine Learning: Data Pre-processing”, in *Prognostics and Health Management of Electronics: Fundamentals, Machine Learning, and the Internet of Things* (IEEE, 2019).
- [51] S. Khalid, T. Khalil, and S. Nasreen, “A survey of feature selection and feature extraction techniques in machine learning”, in 2014 science and information conference (IEEE, 2014), pp. 372–378.
- [52] J. P. Kumar, P. S. Chauhan, and P. P. Pandit, “Time domain vibration analysis techniques for condition monitoring of rolling element bearing: A review”, *Materials Today: Proceedings* **62**, 6336 (2022).
- [53] N. Rajapaksha, S. Jayasinghe, H. Enshaei, and N. Jayarathne, “Acoustic analysis based condition monitoring of induction motors: A review”, in 2021 IEEE Southern Power Electronics Conference (SPEC) (IEEE, 2021), pp. 1–10.
- [54] A. Kumar and R. Kumar, “Role of signal processing, modeling and decision making in the diagnosis of rolling element bearing defect: a review”, *Journal of Nondestructive Evaluation* **38**, 5 (2019).
- [55] K. Lu, J. X. Gu, H. Fan, X. Sun, B. Li, and F. Gu, “Acoustics based monitoring and diagnostics for the progressive deterioration of helical gearboxes”, *Chinese Journal of Mechanical Engineering* **34**, 1 (2021).
- [56] C. Malla and I. Panigrahi, “Review of condition monitoring of rolling element bearing using vibration analysis and other techniques”, *Journal of Vibration Engineering & Technologies* **7**, 407 (2019).
- [57] K. Skowronek, T. Barszcz, J. Antoni, R. Zimroz, and A. Wyłomańska, “Assessment of background noise properties in time and time–frequency domains in the context of vibration-based local damage detection in real environment”, *Mechanical Systems and Signal Processing* **199**, 110465 (2023).

- [58] M. Vishwakarma, R. Purohit, V. Harshlata, and P. Rajput, "Vibration analysis & condition monitoring for rotating machines: a review", *Materials Today: Proceedings* 4, 2659 (2017).
- [59] D. G. Manolakis and V. K. Ingle, *Applied digital signal processing: theory and practice* (Cambridge university press, 2011).
- [60] S. Mallat, *A wavelet tour of signal processing*, 1999.
- [61] W. Jia, M. Sun, J. Lian, and S. Hou, "Feature dimensionality reduction: a review", *Complex & Intelligent Systems* 8, 2663 (2022).
- [62] B. D. Fulcher and N. S. Jones, "hctsa: A computational framework for automated time-series phenotyping using massive feature extraction", *Cell systems* 5, 527 (2017).
- [63] A. Jović, K. Brkić, and N. Bogunović, "A review of feature selection methods with applications", in 2015 38th international convention on information and communication technology, electronics and microelectronics (MIPRO) (Ieee, 2015), pp. 1200–1205.
- [64] S. Brugger, "Ultrasound-based Condition Monitoring of Gearboxes", *MA thesis, University Augsburg*, (2024).
- [65] W. K. Mutlag, S. K. Ali, Z. M. Aydam, and B. H. Taher, "Feature extraction methods: a review", in *Journal of Physics: Conference Series*, Vol. 1591, 1 (IOP Publishing, 2020), p. 012028.
- [66] W. Caesarendra and T. Tjahjowidodo, "A review of feature extraction methods in vibration-based condition monitoring and its application for degradation trend estimation of low-speed slew bearing", *Machines* 5, 21 (2017).
- [67] B. Hjorth, "EEG analysis based on time domain properties", *Electroencephalography and clinical neurophysiology* 29, 306 (1970).
- [68] W. Yang, P. J. Tavner, C. J. Crabtree, Y. Feng, and Y. Qiu, "Wind turbine condition monitoring: technical and commercial challenges", *Wind energy* 17, 673 (2014).
- [69] A. May, D. McMillan, and S. Thöns, "Economic analysis of condition monitoring systems for offshore wind turbine sub-systems", *IET Renewable Power Generation* 9, 900 (2015).
- [70] D. McMillan and G. W. Ault, "Quantification of condition monitoring benefit for offshore wind turbines", *Wind engineering* 31, 267 (2007).
- [71] I. Guyon and A. Elisseeff, "An introduction to variable and feature selection", *Journal of machine learning research* 3, 1157 (2003).
- [72] Shimano, *Nexus 3-speed Internal Geared Hub SG-3D55*.
- [73] D. GmbH, *PLG 63 EP - Industry Compatible Planetary Gearbox ()*.
- [74] BCMtec AG, *PROfile Ultrasonic Product*.

- [75] Vallen Systeme GmbH, *VS12-E Acoustic Emission Sensor Data Sheet*, Vallen Systeme GmbH, Accessed: 2024-08-21, 2019.
- [76] Vallen Systeme GmbH, *VS45-H Acoustic Emission Sensor Data Sheet*, Vallen Systeme GmbH, Accessed: 2024-08-21, 2015.
- [77] S. Kurt, “Kalorimetrische und rheologische Untersuchung der anionischen Polymerisation von Caprolactam zu Polyamid-6”, *Thesis*, (2021).
- [78] S. Kurt, J. Maier, R. Horny, S. Horn, D. Koch, and J. Moosburger-Will, “Determination of the residual monomer concentration of caprolactam in polyamide-6 using thermogravimetric analysis coupled with Fourier transform infrared spectroscopy gas analysis”, *Journal of Applied Polymer Science* **138**, 50730 (2021).
- [79] M. Achzet, B. Schaller, T. Schlech, F. F. Linscheid, and M. G. Sause, “Ultraschallbasierte Untersuchung rheologischer Eigenschaften von Polymeren für die Prozessüberwachung”, (2023).
- [80] F. Suarez, “Monitoring real time dielectric and rheological properties of the anionoc polymerization from caprolactam to polyamide 6 at the rheometer”, *MA thesis, University of Augsburg*, (2022).
- [81] A. Hindersmann, “Confusion about infusion: An overview of infusion processes”, *Composites Part A: Applied Science and Manufacturing* **126**, 105583 (2019).
- [82] J. Filsinger, T. Lorenz, F. Stadler, and S. Utecht, *Method and device for producing fiber-reinforced components using an injection method*, Generic, 2005.
- [83] J. Faber, A. Huber, and M. Kupke, “Manufacturing study on CFRP rear pressure bulkhead using vacuum assisted process (VAP)”, (2022).
- [84] A. Scheidegger, *The physics of flow through porous media* (University of Toronto press, 1957).
- [85] J. Faber, M. Vistein, A. Chaloupka, M. Achzet, F. Linscheid, S. Kurt, and M. Sause, “Sensor-based process monitoring of in-situ polymerization in T-RTM manufacturing with caprolactam”, (2021).
- [86] T. Stefani, J. Faber, and D. Henning, “Introducing thermoplastics to serial production: Thermoplastic resin transfer molding using caprolactam”, (2020).
- [87] S. Kurt, T. Bratzdrum, A. Chaloupka, S. Horn, and J. Moosburger-Will, “Isothermal anionic polymerization of caprolactam to polyamide-6: Kinetic modeling and application for production process”, *Journal of Applied Polymer Science* **140**, e54320 (2023).
- [88] R. Qi, J. Zhang, and K. Spencer, “A review on data-driven condition monitoring of industrial equipment”, *Algorithms* **16**, 9 (2022).
- [89] Q. R. Luong, T. Schlech, F. F. Linscheid, M. Achzet, and M. G. Sause, “Echtzeitfähige Analyse hochfrequenter Ultraschalldaten zur Überwachung von Fertigungsprozessen”, (2023).

- [90] C. Baumeister, T. Schleich, M. Achzet, Q. R. Luong, F. Linscheid, B. Brück, and M. Sause, *Akustische Überwachung des Werkzeugverschleißes bei der zerspanenden Bearbeitung* (Universität Augsburg, 2023).
- [91] R. Teti, K. Jemielniak, G. O'Donnell, and D. Dornfeld, "Advanced monitoring of machining operations", *CIRP annals* **59**, 717 (2010).
- [92] C. H. Hansen, *Fundamentals of Acoustics* (Wiley, Hoboken, NJ, USA, 1999).
- [93] A. Demir and A. Sangiovanni-Vincentelli, *Analysis and simulation of noise in non-linear electronic circuits and systems*, Vol. 425 (Springer Science & Business Media, 2012).
- [94] *Acoustics – Noise emitted by machinery and equipment – Rules for the drafting and presentation of a noise test code*, International Organization for Standardization, 1996.
- [95] I. The MathWorks, *Random Numbers (rand) Function*, version R2023a, MATLAB Base Functionality, The MathWorks, Inc.
- [96] H. Zhivomirov, "A method for colored noise generation", *Romanian journal of acoustics and vibration* **15**, 14 (2018).
- [97] S. V. Vaseghi, *Advanced digital signal processing and noise reduction* (John Wiley & Sons, 2008).
- [98] A. C. Bovik, *The essential guide to image processing* (Academic Press, 2009).
- [99] S. Iqbal, T. M. Khan, K. Naveed, S. S. Naqvi, and S. J. Nawaz, "Recent trends and advances in fundus image analysis: A review", *Computers in Biology and Medicine* **151**, 106277 (2022).
- [100] V. Radeka, "1/f noise in physical measurements", *IEEE Transactions on Nuclear Science* **16**, 17 (1969).
- [101] P. Bak, C. Tang, and K. Wiesenfeld, "Self-organized criticality", *Physical review A* **38**, 364 (1988).
- [102] I. The MathWorks, *Chirp Signal Generation (chirp) Function*, version R2023a, Signal Processing Toolbox, The MathWorks, Inc.
- [103] R. A. Fisher, "Statistical methods for research workers", in *Breakthroughs in statistics: Methodology and distribution* (Springer, 1970), pp. 66–70.
- [104] I. The MathWorks, *Correlation Coefficient (corrcoef) Function*, version R2023a, MATLAB Base Functionality, The MathWorks, Inc.
- [105] I. The MathWorks, *Analysis of Variance (anova) Function*, version R2023a, Statistics and Machine Learning Toolbox, The MathWorks, Inc.
- [106] K. Pearson, "VII. Note on regression and inheritance in the case of two parents", *proceedings of the royal society of London* **58**, 240 (1895).

- [107] S. Stieber, A. Hoffmann, A. Schiendorfer, W. Reif, M. Beyrle, J. Faber, M. Richter, and M. Sause, “Towards real-time process monitoring and machine learning for manufacturing composite structures”, in 2020 25th IEEE International Conference on Emerging Technologies and Factory Automation (ETFA), Vol. 1 (), pp. 1455–1458.
- [108] M. Achzet, T. Schlech, F. F. Linscheid, J. Faber, and M. G. Sause, “Ultraschallbasierte prozessüberwachung am beispiel eines T-RTM prozesses”, (2022).
- [109] L. Volkmann, *Fundamente der Graphentheorie* (Springer-Verlag, 2013).
- [110] I. The MathWorks, *Multidimensional unconstrained nonlinear minimization (fminsearch) Function*, version R2023a, Optimization Toolbox, The MathWorks, Inc.
- [111] J. C. Lagarias, J. A. Reeds, M. H. Wright, and P. E. Wright, “Convergence properties of the Nelder–Mead simplex method in low dimensions”, *SIAM Journal on optimization* **9**, 112 (1998).
- [112] M. A. Ugwiri, M. Carratú, V. Paciello, and C. Liguori, “Benefits of enhanced techniques combining negentropy, spectral correlation and kurtogram for bearing fault diagnosis”, *Measurement* **185**, 110013 (2021).
- [113] V. Sugumaran and K. Ramachandran, “Effect of number of features on classification of roller bearing faults using SVM and PSVM”, *Expert Systems with Applications* **38**, 4088 (2011).
- [114] D. Theng and K. K. Bhoyar, “Feature selection techniques for machine learning: a survey of more than two decades of research”, *Knowledge and Information Systems* **66**, 1575 (2024).
- [115] J. Hua, Z. Xiong, J. Lowey, E. Suh, and E. R. Dougherty, “Optimal number of features as a function of sample size for various classification rules”, *Bioinformatics* **21**, 1509 (2005).
- [116] K. Tifkitsis and A. A. Skordos, “Real time uncertainty estimation in filling stage of resin transfer molding process”, *Polymer Composites* **41**, 5387 (2020).
- [117] A. George, “Optimization of resin infusion processing for composite materials: simulation and characterization strategies”, *PhD thesis, Stuttgart, Univ., Diss., 2011*, (2011).
- [118] I. The MathWorks, *Boundary Tracing in Binary Images (bwboundaries) Function*, version R2023a, MATLAB Image Processing Toolbox, The MathWorks, Inc.
- [119] TDI Process Measurement, *Liquid Sound Speed Charts*, <https://tdi-pm.com/images/tdi/PDF/Resources-Brochures/Liquid-Sound-Speed-Charts.xls>.
- [120] B. Schaller, “Ultraschallbasierte Prozessüberwachung von Injektionsverfahren”, *University Augsburg* (2023).
- [121] I. The MathWorks, *Detect Changes in Data (ischange) Function*, version R2023a, MATLAB Base Functionality, The MathWorks, Inc.

- [122] Z. Ge, Z. Song, S. X. Ding, and B. Huang, “Data mining and analytics in the process industry: The role of machine learning”, *Ieee Access* 5, 20590 (2017).
- [123] A. L. Bowler, M. P. Pound, and N. J. Watson, “A review of ultrasonic sensing and machine learning methods to monitor industrial processes”, *Ultrasonics* 124, 106776 (2022).
- [124] G. Chandrashekar and F. Sahin, “A survey on feature selection methods”, *Computers & electrical engineering* 40, 16 (2014).
- [125] R. Challis, M. Povey, M. Mather, and A. Holmes, “Ultrasound techniques for characterizing colloidal dispersions”, *Reports on progress in physics* 68, 1541 (2005).
- [126] A. Simeone, E. Woolley, J. Escrig, and N. J. Watson, “Intelligent industrial cleaning: a multi-sensor approach utilising machine learning-based regression”, *Sensors* 20, 3642 (2020).
- [127] J. Li, K. Cheng, S. Wang, F. Morstatter, R. P. Trevino, J. Tang, and H. Liu, “Feature selection: A data perspective”, *ACM computing surveys (CSUR)* 50, 1 (2017).
- [128] K. Yu, X. Guo, L. Liu, J. Li, H. Wang, Z. Ling, and X. Wu, “Causality-based feature selection: Methods and evaluations”, *ACM Computing Surveys (CSUR)* 53, 1 (2020).
- [129] H. Liu and H. Motoda, *Computational methods of feature selection* (CRC press, 2007).
- [130] B. Schölkopf, “Causality for machine learning”, in *Probabilistic and causal inference: The works of Judea Pearl* (2022), pp. 765–804.
- [131] J. Zhu, D. Droste, A. Dimassi, and A. S. Herrmann, “A neural-network-assisted method for flow-front estimation in resin transfer molding using pressure sensors”, *Journal of Composite Materials* 56, 2979 (2022).
- [132] C. Di Fratta, F. Klunker, and P. Ermanni, “A methodology for flow-front estimation in LCM processes based on pressure sensors”, *Composites Part A: Applied Science and Manufacturing* 47, 1 (2013).
- [133] C. Di Fratta, G. Koutsoukis, F. Klunker, and P. Ermanni, “Fast method to monitor the flow front and control injection parameters in resin transfer molding using pressure sensors”, *Journal of Composite Materials* 50, 2941 (2016).
- [134] H. Taheri and A. A. Hassen, “Nondestructive ultrasonic inspection of composite materials: A comparative advantage of phased array ultrasonic”, *Applied Sciences* 9, 1628 (2019).

Acknowledgments

I express my gratitude to all the partners, specifically Faurecia, Krauss Maffei, SGL Technologies GmbH, Premium Aerotec, Siebenwurst, NETZSCH, KUKA, iba and the Deutsches Zentrum für Luft- und Raumfahrt involved in the MAI CC4 Cosimo project (NW-1803-0013) and the financial support provided by the program Neue Werkstoffe Bayern by the Bavarian State Ministry of Economic Affairs, Regional Development and Energy.

List of Figures

2.1	Differential three-dimensional element with the components of the stress tensor.	6
2.2	Schematic propagation of a longitudinal (left) and a transverse (right) wave along the wave vector \hat{k}_1, \hat{k}_2 and with the wavelengths λ_1, λ_2 , respectively.	8
2.3	Illustration of a sound beam partially reflected and transmitted at an interface.	9
2.4	Sound pressure p of a circular emitter following Equation 2.18. The distance is illustrated in units of the nearfieldlength N . The red solid line indicates the last maximum p_{\max} and the red dashed line indicating the approximation for large distances $> N$	11
2.5	The amplitude of p_{tot} over distance in units of the near field length N and for different attenuation factors α . Amplitude 100 % is arbitrarily set to p_0 . When $\alpha = 0$, it indicates pure geometric spreading, where p_{tot} equals p_{gs}	12
2.6	Illustration of the crystal lattice of BaTiO ₃ as an example of the perovskite structure [33].	13
2.7	Left: Graph of a continuous signal $x(t)$, plotted as a function of time t . Right: Corresponding FT $X(\omega) \leftrightarrow x(t)$ as a function of frequency ω . The frequency ω_c marks the largest frequency occurring in the spectrum.	16
2.8	Left: Graph of a discretized signal $x_s(t)$ with a sampling frequency of $\frac{1}{T}$. Right: Corresponding FT $X_s(\omega)$ for the case of $ \omega_c < \frac{1}{2T}$	17
2.9	FT $X_s(\omega)$ for the case of $ \omega_c > \frac{1}{2T}$ which results in aliasing and a distortion of the frequency spectrum.	18
2.10	Comparison of the rectangular, Hamming and Kaiser window. The sample length is arbitrarily set to 500.	19
2.11	Left: Rectangular window with cut-off frequency at f_c . Right: Corresponding inverse FT in the time domain.	22
2.12	Left: Discretized impulse response of the rectangular window. Right: Corresponding frequency response.	22
2.13	An overview of a signal processing workflow involving signal acquisition, preprocessing, and interpretation methods for accurate signal analysis and decision-making.	24
2.14	Signal preprocessing workflow, beginning with data organization and followed by feature extraction and selection, ultimately leading to signal interpretation.	25

List of Figures

2.15	Recorded acoustic signals of a bicycle hub monitored using an ultrasonic piezo sensor. Both graphs display the raw amplitude data over time. The bottom graph shows the same signal but additionally differentiates between signals recorded while the hub was in condition 1 (blue) and condition 2 (orange).	27
2.16	Above: Acoustic signal recorded from a bicycle hub, initially in an unloaded state for the first 2 s, followed by a loaded state from 2 s to 4 s. Below: The corresponding frequency spectrums for the unloaded and loaded states, illustrating the distinct acoustic differences of each condition.	29
2.17	The top graph displays the amplitude of the gear signal over time for loaded (orange) and unloaded (blue) states. The bottom figure shows a spectrogram of the signal.	30
2.18	Upper plot: Segmentation of a ultrasound signal of a gearbox into equally spaced time intervals Δt . For $t < 0.5$ s the gearbox operates in Gear 1 and switches to Gear 2 at $t = 0.5$ s. The middle and bottom panels show the extracted features.	32
3.1	Experimental setup of the the gear demonstrator, including the gearhub, motor, data acquisition system, and sensor. The motor drives the system at 1.4 R/s, with power transmitted through chains and gears. The Shimano Nexus 3-speed internal geared hub SG-3D55 is monitored using a Vallen VS12-E sensor and the PROfile Ultrasonic acquisition system provided by BCMtech.	44
3.2	Frequency response of the Vallen S12-E sensor. The data is retrieved from the datasheet provided by Vallen[75].	47
3.3	Frequency response of the Vallen VS45-H sensor. The data is retrieved from the datasheet provided by Vallen[76].	47
3.4	Comparison of the power spectra for Gear 1 and Gear 2 using the Vallen VS12-E (top) and Vallen VS45-H (bottom) sensors. The blue and red lines represent the power spectra for Gear 1 and Gear 2, respectively. The yellow line shows the absolute difference between the spectra of Gear 1 and Gear 2. The RMS value of the absolute difference is 3.6 for the VS12-E sensor and 3.34 for the VS45-H sensor. The VS12-E sensor demonstrates clearer distinctions between gears, as indicated by the higher RMS difference.	49
3.5	Accuracy comparison of gear classification using the Vallen VS12-E and Vallen VS45-H sensors across different frame sizes calculated 1 ms steps. The blue line represents the accuracy achieved with the VS12-E sensor, while the orange line represents the accuracy with the VS45-H sensor. The more transparent lines show the actual data points, whereas the full-color lines represent the moving mean of the data.	50

3.6	Left: Photography of the rheometer setup. Right: Schematic drawing of the setup. A sample is placed between the upper and lower plate. The ultrasonic sensor is mounted to the lower plate [79].	51
3.7	Left: Photography of the sensor holder mounted to the rheometer sample plate compared to the corresponding CAD-Model (right) of the sensor holder [79].	51
3.8	Vacuum assisted process - materials and setup according to [83].	53
3.9	Setup of VAP infusion with camera for flow front detection (left). Flow front on bottom side of the textile preform (right).	54
3.10	Schematic representation of the four stages in the T-RTM process: (1) Insertion of the preform into the mold, (2) Injection of the activator, caprolactam, and catalyst, (3) Curing after forming, and (4) Removal of the finished composite part.	55
3.11	Illustration of the sensor integrated into the tool, according to [85].	56
3.12	Illustration of the tool and the integrated US-sensors.	57
3.13	Exemplary illustration of the signal progression in the T-RTM experiments. As the impregnation progresses and varying degrees of polymerization occur, the reflection conditions change, altering the characteristics of the reflected ultrasonic waves. According to [10].	58
3.14	Photography of the sensor assembly showing the coaxial cable, piezo disk, and sensor holder.	59
3.15	Diagram illustrating the timing and signal processing of pulse excitations with 1 ms active data storage segments and 21 ms intervals between pulses. The inactive data storage areas and corresponding echo signals are also shown.	60
3.16	Schematic of ultrasonic pulse-echo measurements illustrating the propagation of ultrasonic waves through three distinct materials. According to [10]	61
3.17	Schematic illustration of a ultrasound path travelling through a sandwich structure of three layers.	62
3.18	Impact of varying the delay line length d_1 on the received signal.	64
3.19	Graphical illustration to support the choice of a suitable delay line length. The upper limit follows Equation 3.5, while the lower limit is given by Equation 3.4 with a pulse length of $T = 3.7 \mu\text{s}$. The black line indicates the position of maximum sound pressure in Layer 2.	65
3.20	Graphical illustration of determining ideal delay line length.	66
3.21	Illustration of determining suitable delay line lengths for laminate thicknesses $d_2 = 5 \text{ mm}$ and $d_2 = 2.5 \text{ mm}$	67
4.1	Outline of condition monitoring systems.	69
4.2	Illustration of the impact of various types of noise on extracted features and their distributions.	72

List of Figures

4.3	Outline of the proposed feature adaptation method, illustrating parameter selection, feature calculation, performance assessment, and visualization.	75
4.4	Feature extraction of ultrasound signals for process monitoring. The top plot displays a ultrasound signal in time domain of a gear hub over 4 seconds, while under load for the first 2 seconds. The bottom three plots illustrate the partial power within specific frequency bands: 0 KHz – 5 kHz, 40 KHz – 45 kHz and 70 KHz – 75 kHz.	77
4.5	Comparison of the F-value (top) and the corresponding power spectrum at a loaded and unloaded state (middle) and its differences (bottom).	79
4.6	Overview of the proposed feature model selection approach (FMS).	80
4.7	Overview of the standard feature selection approach (SFS).	80
4.8	Average accuracy of SVM models attributed to the corresponding features. n designates the maximum number of features used for the model.	84
4.9	Standard deviation plotted versus n which designates the maximum number of features used to train the SVM models.	85
4.10	Comparison of FMS scores and SFS method, specifically ANOVA and discriminant analysis (DA).	86
4.11	A graph representation illustrating the nodes, edges, and sample points in a sensor network. The black dots represent nodes, the lines represent edges connecting the nodes, and the circles labelled S_1 and S_2 represent sample points. This structure is used to reconstruct arrival times and infer spatial data between the sensors.	89
4.12	Illustration of the inaccuracies introduced by meshing. The solid line represents the actual shortest path between two points A and B in space. The dashed line represents the shortest path along the edges $E_{1,2,3}$ of a graph. The angles $\alpha_{1,2,3}$ represent the deviation of each edge from the shortest path.	91
4.13	Average Errors of a path with N edges calculated using equations from Table 4.2. based on a graph generated by Delaunay triangulation applied to a 2D surface.	92
4.14	Error of a path composed of N edges using different Correction values C .	93
4.15	Improvement of the accuracy per computational minute over the number of faces N_F	93
4.16	Improvement of the accuracy per computational minute over N_E . N_E represents the number of edges of the longest, direct path between two nodes.	95
4.17	Definition of angle ϕ_{in} used to calculate ω_{ang}	96
4.18	Radial ω_{rad} and angular weight ω_{ang} for different parameter ϵ and δ	97
4.19	2D illustration of the weight functions for the sample point marked in red. The green dots indicate the rest of the sample points and the blue dot the injection point.	97
5.1	Schema of feature extraction using the gate concept.	100

5.2	Workflow for optimizing gate settings and feature extraction.	101
5.3	Each point is assigned the feature with the highest absolute R-value at a fixed gate position. The histogram illustrates the distribution of points across randomly varied gate positions.	102
5.4	R-values on a bilogarithmic colour scale for the partial power feature as a function of the frequency window.	103
5.5	R-values on a bilogarithmic colour scale for the RMS depending on the gate position and width.	103
5.6	Impulse and frequency spectrum of the ultrasound sensor used. The areas marked in red are within the time or frequency window ideal for the RMS and partial power feature.	104
5.7	Temporal progression of the Partial Power feature in a frequency window from 2.05 MHz to 2.19 MHz compared to the logarithmically plotted viscosity.	105
5.8	The temporal progression of the RMS value in a time window from 7 μ s to 13 μ s after pulse emission compared to the logarithmically plotted viscosity.	105
5.9	Temporal progression of the partial power feature for a different measurement and with the same settings for the frequency window as in Figure 5.8.	106
5.10	The temporal progression of the RMS value for a different measurement and with the same settings for the time window as in Figure 5.8.	106
5.11	Comparison of the measured viscosity, the partial power features and the conversion of ϵ -caprolactam found in [80].	107
5.12	Relationship between partial power and polymerization state. The upper plot compares normalized partial power with conversion rate, showing a time shift between partial power saturation and when conversion exceeds 98 %, marking sufficient polymerization. The lower plot zooms in on critical time points.	108
5.13	Determining the polymerization time based on partial power features.	109
5.14	General approach for feature selection: generating SVM models for all combinations of 1-3 features from a preselected list of 51 features to compute average scores for each feature.	112
5.15	Evaluation of the RMS feature in combination with other features using SVM models to calculate predictive performance scores.	112
5.16	Evaluation of noise influencing feature performance. The top plot shows the average accuracy of various features across different noise levels. The bottom plot presents the corresponding mean values and its standard deviations in blue. The orange circles show the noise robustness score calculated via Equation 5.1.	113
5.17	Evaluation of wear and tear influence over time on feature performance. The legend displays the date and the number of days elapsed since the previous one.	114

5.18	Comparison of Time and Noise Robustness Scores. The plot shows robustness scores for each feature, with blue circles representing robustness to degradation over time and orange circles indicating robustness against artificially introduced noise. Higher scores suggest greater feature reliability in maintaining predictive performance under the respective conditions.	115
5.19	Average Score of the 15 Feature selection algorithms.	116
5.20	Comparison of the SVM scores with the scores of fast feature selection algorithm. The top plot shows the SVM score for each feature and the lower plots show individual feature scores. The corresponding R and R-square values between each algorithm and the SVM scores are listed on the right with R-square value being used as the final weight assigned to each method.	117
5.21	Comparison of different scores.	117
5.22	Prediction accuracy for varying number of features. The features were added consecutively corresponding to the SVM Time, SVM Noise, the weighted and unweighted FS scores. The mean does only take the unweighted FS scores into account in order to avoid overvaluing the results of the FS scores.	118
5.23	Prediction accuracy for the SVM models trained on the first data set at 2022-07-07 and tested on the other. The number of features used to train the models are varied from 5 to 10. The mean value are then illustrated with the solid line, and the dotted line represent the standard deviation.	119
5.24	Analog to Figure 5.23 but with different x - scales.	120
5.25	Photography of a VAP experiment and identification of flow front. The red boundary marks the current flow front. The green boundary represents its position one recording earlier. The area enclosed in between these boundaries is marked in blue.	123
5.26	Contour plot showing the absolute deviation between the recorded and reconstructed arrival times. Blue dots indicate the locations of the sample points. Contour lines represent the flow front based on recorded arrival times (green) and reconstructed arrival times (red) across observation periods ranging from 50 s to 250 s.	124
5.27	Illustration of the RMS-feature extracted from a US-Signal and tool position during resin injection.	126
5.28	Illustration of the behaviour of the RMS of two channels and pressure over time during a composite manufacturing process. The y-axis on the left represents the RMS and the y-axis on the right represents the pressure. The red-shaded area indicates the time period when the mixing head is on.	127
5.29	Sensor positions within the tool layout.	127
5.30	Illustration of three distinct RMS value behaviours during the T-RTM process, each reflecting different physical phenomena.	129
5.31	Illustration of the reconstructed flow front (red) applied to the T-RTM process. The blue dots represent US-sensor locations.	131

5.32	Photography of a unfinished part. The figure shows the preferred flow direction of the resin.	132
5.33	Comparison of a manufactured part (top) with its reconstruction (bottom).	133
6.1	Illustration of the global reconstruction algorithm steps: (1) Strategical Sensor integration into the process geometry. (2) Relevant data is extracted. (3) A mesh grid is generated to represent the process geometry. (4) Weight functions are optimized for accurate representation. (5) Sensor values are optimized to minimize error. (6) The data is reconstructed based on the determined parameters.	144